Modeling of Nonlinear Viscoelastic Solids with Damage Induced Anisotropy, Dissipative Rolling Contact Mechanics, and Synergistic Structural Composites

by

Gérard-Philippe Zéhil

Department of Civil and Environmental Engineering
Duke University

Date: _____

Approved:

_____
Henri P. Gavin, Supervisor

_____
Wilkins Aquino

_____
Cameron R. Dale Bass

_____
John E. Dolbow

_____
Xuanhe Zhao

Dissertation submitted in partial fulfillment of the requirements for the degree of Doctor of Philosophy in the Department of Civil and Environmental Engineering in the Graduate School of Duke University
2013

Abstract

Modeling of Nonlinear Viscoelastic Solids with Damage Induced Anisotropy, Dissipative Rolling Contact Mechanics, and Synergistic Structural Composites

by

Gérard-Philippe Zéhil

Department of Civil and Environmental Engineering
Duke University

Date: _____

Approved:

_____
Henri P. Gavin, Supervisor

_____
Wilkins Aquino

_____
Cameron R. Dale Bass

_____
John E. Dolbow

_____
Xuanhe Zhao

An abstract of a dissertation submitted in partial fulfillment of the requirements for the degree of Doctor of Philosophy in the Department of Civil and Environmental Engineering
in the Graduate School of Duke University
2013

Abstract

The main objectives of this research are: (i) to elaborate a unified nonlinear viscoelastic model for rubber-like materials, in finite strain, accounting for material softening under deformation, and for damage induced anisotropy, (ii) to conceive, implement and test, simple, robust and efficient frictional rolling and sliding contact algorithms, in steady-state, as alternatives to existing, general purpose, contact solving strategies, (iii) to develop and verify high fidelity and computationally efficient modeling tools for isotropic and anisotropic viscoelastic objects in steady-state motion, (iv) to investigate, numerically and through experimentation, the influence of various material parameters, including material nonlinearities such at the Payne effect and the Mullins effect, as well as geometric parameters and contact surface conditions, on viscoelastic rolling resistance, and (iv) to explore, analytically and through experimentation, the conditions under which favorable mechanical synergies occur between material components and develop novel composites with improved structural performances.

A new constitutive model that unifies the behavioral characterizations of rubber-like materials in a broad range of loading regimes is proposed. The model reflects two fundamental aspects of rubber behavior in finite strain: (i) the Mullins effect, and (ii) hyper-viscoelasticity with multiple time scales, including at high strain rates. Suitable means of identifying the system's parameters from simple uniaxial extension tests are explored. A directional approach extending the model to handle softening

induced anisotropy is also discussed.

Novel, simple, and yet robust and efficient algorithms for solving steady-state, frictional, rolling/sliding contact problems, in two and three dimensions are presented. These are alternatives to powerful, well established, but in particular instances, possibly 'cumbersome' general-purpose numerical techniques, such as finite-element approaches based on constrained optimization. The proposed algorithms are applied to the rolling resistance of cylinders and spheres.

Two and three-dimensional boundary element formulations of isotropic, transversely isotropic, and fully orthotropic, compressible and incompressible, viscoelastic layers of finite thickness are presented, in a moving frame of reference. The proposed formulations are based on two-dimensional Fourier series expansions of relevant mechanical fields in the continuum of the layers and support any linear viscoelastic material model characterized by general frequency-domain master-curves. These modeling techniques result in a compliance matrix for the upper boundary of the layers, including the effects of steady-state motion. Such characterizations may be used as components in various problem settings to generate sequences of high fidelity solutions for varying parameters. These are applied, in combination with appropriate contact solvers, to the rolling resistance of rigid cylinders and spheres.

The problem of a viscoelastic sphere moving across a rigid surface is significantly more complicated than that of a rigid indenter on a viscoelastic plane. The additional difficulties raised by the former may explain why previous work on this topic is so sparse. A new boundary element formulation for the multi-layered viscoelastic coating of a rigid sphere is developed. The model relies on the assumption of a relatively small contact surface in order to decouple equilibrium equations in the frequency domain. It is applied in combination with an adapted rolling contact solving strategy to the rolling resistance of a coated sphere.

New modeling approaches yielding rolling resistance estimates for rigid spheres

(and cylinders) on viscoelastic layers of finite thicknesses are also introduced, as lower-cost alternatives to more comprehensive solution-finding strategies, including those proposed in this work. Application examples illustrate the capabilities of the different approaches over their respective ranges of validity.

The computational tools proposed in this dissertation are verified by comparison to dynamic finite element simulations and to existing solutions in limiting cases. The dependencies of rolling resistance on problem parameters are explored. It is for instance shown that, on orthotropic layers, the dissipated power varies with the direction of motion, which suggests new ways of optimizing the level of damping in various engineering applications of very high impact. Interesting lateral viscoelastic effects resulting from material asymmetry are unveiled. These phenomena could be harnessed to achieve smooth and 'invisible' guides across three-dimensional viscoelastic surfaces, and hence suggest new ways of controlling trajectories, with a broad range of potential applications.

A new experimental apparatus is designed and assembled to measure viscoelastic rolling resistance. Experiments are conducted by rolling steel balls between sheets of rubber. Principal sources of measurement error, specific to the device, are discussed. Rolling resistance predictions are obtained using the computational tools presented in this dissertation, and compared to the measurements. Interesting conclusions are drawn regarding the fundamental influence of the Payne effect on viscoelastic rolling friction.

The work presented in this dissertations finally touches on the mechanical behavior of casing-infill composite tubes, as potential new lightweight structural elements. The axial behavior of composite circular tubes is addressed analytically. The influence of material parameters and geometry on structural performances are revealed and presented in original graphical forms. It is for instance shown that significantly improved overall stiffness and capacity at yield can be obtained using a moder-

ately soft and highly auxetic infill, which further highlights the need to develop new lightweight auxetic materials, without compromising their stiffness. It is furthermore concluded that limited mechanical synergies can be expected in metal-polymer composite tubes, within the linear range of the materials involved. This prediction is confirmed by a bending experiment conducted on an Aluminum-Urethane composite tube. The experiment however reveals unexpected and quite promising mechanical synergies under large deformations. This novel composite has a potential influence on the design and performance of lightweight protecting structures against shocks and accelerations due to impacts, which justifies that it be characterized further.

To all the uncovered mysteries, and to those that remain veiled.

To Chafika Nassar, Daniel Benoît, Georges Zéhil, Capt. Gérard Zéhil, Guy Zéhil, Hélène Flaifel Zéhil, Jean Khoury, Laure Khoury, Marwan Maalouf, May Maalouf, Mays El-Dairi, Michael Zalzal, Michèle Salwan, Mona Maalouf Khoury, Nehemtallah Maalouf, Nicole Salwan, Nisrine Khoury, Patrick Zéhil, Peter Zalzal, Renu, Rinalda Maatouk, Robert Khoury, Roger Zéhil, Rose Nassar, Saba, Sami Hobeich, Samia Hobeich, Samir Hobeich, Souhail Hobeich, Tony Salwan, and Zeina Maalouf Benoît.

To Asaad Bou Tanos, Athanasia Bou Tanos, Amale Azar, Annette Bassil, Carl Hamod, Chuck Yazbek, Claude Chouity, Charbel Ghanem, Daniel Balaban, Dorita Bou Tanos, Doumit Bou Tanos, Elias Bou Tanos, Elie Ghanem, Fadi Abboud, Georges El-Dairi (Joujou), Ghayas Yazbek, Henri Bassil, Jad Balaban, Jaqueline Bassil, Jihane Chebli, Joseph Azar, Julia Aoun, Juliette Azar, Karen Bassil, Laure Azar, Léna Yazbek, Makram Chebli, Micha Chouity, Mickette Chebli, Mounir Azar, Nadim Yazbek, Nagib Chouiti, Naji Abboud, Pierre Bou Tanos, Pierrette Bou Tanos, Rafik Azar, Rola Mazloum, Rony Ghaoui, Sandra Ghaoui, Salim Chebli, Samir Azar, Skandar Bassil, Tania Chouity, Tarek Azar, Thérèse Bou Tanos, Toufic Azar, Valéry Bijani, Walid Asmar, Wissam Ghanem, Woody Boueiz, and Ziad Azar.

To Adib Chkeyban, Antoine Azzam, Antoine Fargialla, Georges Salloum, Marlène Hneiné, Naim Chrabieh, Raja Fares, and Rizkallah Ghazal.

To fathers Victor Assouad, Roger Bassili, Paul Brouwers, Bernard Charvet, Jean

Dalmais, Pierre Lahoud, Bruno Pin, and Michael Zammit.

To Christophe Varin, Corine Khater, Hiba Berbery, Jackie Triolet Varin, Joe Taoutel, Marwan Antoun, Marwan Tzenios, Mike Ayvasian, Mona Chehab, Nagy Khoury, Nathalie Farah, Rodrigues Francis, Samar Baroody, Souraya Asmar, and Wassim Kreidi.

To Amin-André Hatem, Gergi El-Murr, Chef Jacques Triolet, Labib Nasr, Nadim Abboud, Nassib Nasser, Nicole Antoun, father Roger Kouyoumdji, Tony Feghali, and Youssef Asmar.

To Alain Samaha, Avona Eid, Charles Abou Aad, Dany Hanna, Dany Obeid, Dina Achy, Elie Haibi, Hani Aoun, Jean-Pierre Chamoun, Jihad Moubarak, Joe Bitar, Joe Sabbagh, Joseph Khawand, Margot Ghosn, Marianne Metni, Nader Sfeir, Nadine Malo, Nicolas Abdel-Nour, Raymond Mantoura, Raya Bitar, Raymond Najjar, Riad Chebli, Léa Roselyne Metni, Sami Kayat, Antoine Sacy, Victor Ghosn, and Walid Khairallah.

To Hyam Maatouk, Jihane Harb, Emile Abou Rahal, Najoie Abou Rahal, Rabih Nouh, Samantha Maatouk and Sarkis Maatouk.

To Andrea Faulkner-Pollard, Georges and Tony El-Turk and Kevork Kechichian.

To Alfred Hayek, Dany Mezher, Fadi Geara, Fouad Kaddah, Hugues Leroy, Ibrahim Assily, Marwan Brouche, Michel Chakar, Michel Issa, Muhsin Elie Rahhal, Nadim Choueiry, Ragi Ghosn, Rima Kilany, Roger Salloum, Said Bitar, Salim Salem, Sélim Catafago, Thierry Duval, Toufic Aaris, Wajdi Najem, Wassim Raphaël,

and William Habre.

To Boutros Chalouhy, Charbel Ghanem, Fouad Abou Chakra, Hares Zaidan, Issam Abou Antoun, Issam Makke, Jad Mezher, Karen Barmaki, Mario Maalouf, Maroun Rouhana-Moussa, Mary Saber, Maya Dourra, Monjed Ezzeddinne, Myriam Zaidan, Nadine Daccache, Nicolas Pérot, Rabih Saad, Rémi Ghosn, Rima Mouawad, and Talal Ghantous.

To Bertrand Lenoir, Claude Roy, Daniel Forestier, Frédéric Lambeaux, Marc Braun, Maurice Imbert, Michel Pages, Patrice Kirschner, Pierre Blondeau, Régis Boutes, and Sylvain Boireau.

To Alain Testu, Alexandre Glaros, Aurélie Ceux, Benoît Baudry, Chantal Dintzner, Christian Poumeau, Christian Ross, Edward Karim, François Grison, Frédéric Charles, Henri Ducrot, Henri Peudennier, Hussein Khalife, Imad Imad, Irina Popescu, Jean des Robert, Jean-Marc Viol, Julien Riedberger, Landry Jouval, Michel Vilmain, Michèle Saint-Dizier, Mona Fouladirad, Mounir Moustar, Nastaran Farzami Vivan, Philippe Varennes, Pierre Sainte-Rose, Robert Martin, Simone Waghon, Sophie Netter, Stéphane de Gail, Thomas Pradeau, Yéhia Khalife.

To Alain Guilloux, Alain Mézard, Alain Quenelle, Claude Servant, Emmanuel Bouchon, Florent Imberty, Jean-Armand Calgaro, Jean-Bernard Datry, Michel Virlogeux, Patrick le Chaffotec, and Evelyne Osmani.

To Kim, Pawin, Pawina and Srilak Jiramongkolchai, and to Sara and Sina Farsiu.

To all my colleagues, my peers, my teachers, my friends, and my loved ones.

Contents

List of Tables

List of Figures

Acknowledgements

I would like to express my gratitude to my advisor, Professor Henri P. Gavin, and to the members of my Ph.D. committee, Professors Wilkins Aquino, Cameron R. 'Dale' Bass, John E. Dolbow and Xuanhe Zhao, as well as to Professors Earl H. Dowell, Omar M. Knio, Jeff T. Scruggs, Thomas P. Witelski, and Dr. Olivier Le Maître, for the guidance and support that they provided during the course of my graduate studies at Duke University.

I also wish to thank Professors Dolbow and Gavin, the Director of Graduate Studies Professor J. Jeffrey Peirce, the Graduate School, the department of Civil and Environmental Engineering at Duke University and the department chair Professor John D. Albertson, for the role they played in securing the financial support of my research and for giving me the opportunity to pursue my 'delayed' academic endeavors, after several years of professional experience in the design and construction of bridges.

I am also grateful to Dianne Bennett, Ruby Nell Carpenter, Tiffany Casey, Rebecca Dupre, Stelian Igescu, Dwina Martin and Susan Williford for their friendliness, and for the assistance they provided me with in handling all kinds of administrative and logistical matters, at Duke. Thank you Ruby Nell for often telling me that I was "on top of things," it sure helped me staying there.

Many thanks to Professors Aquino and Zhao for granting me access to valuable computational resources that facilitated certain aspects of my research. Special

thanks to Michael R. Blagg and to Steven Earp for their technical support, as well as to Christine Larson who worked very hard, as a senior undergraduate, on setting the rolling resistance experiment. The contributions of the Fairprene company and of WorkSafe Technologies, who graciously provided sheets of Neoprene rubber, and Urethane rubber, respectively, for the rolling resistance experiment, are greatly appreciated. I am also grateful to Gregory Favaro from, CSM Instruments, for providing valuable information regarding features of the manufacturer's high temperature tribometer.

The work described in this document would not have been possible without the sacrifices of my mother May N. Maalouf, my father Captain Gérard G. Zéhil, the help of my brother Patrick G. Zéhil, and the unconditional love, understanding and support of my family and close friends. My special gratitude goes to Professor Mays El-Dairi for her help, and her constant care and support.

Additionally, I would like to thank Professors Marwan Brouche, Sina Farsiu, Fouad Kaddah, Dany Mezher, Muhsin Elie Rahhal, Wassim Raphaël, as well as Amy Allen, Dr. Chandra Annavarapu, Dr. Ian Cassidy, Max Coar, Dr. Anand Embar, Sara Farsiu, Dr. Scott Harvey, Dr. Kim Jiramongkolchai, Dr. Firas Khasawneh, Dr. Temesgen Kindo, Ismail Kuzucu, Steve Lattanzio, Quan Li, Jennifer Rinker, Craig Wasilewsky, Boya Yin, Ziyu Zhang, and many more, for their friendship and support.

Part of the material presented hereafter is based upon work supported by the National Science Foundation under Grant No. NSF-CMMI-0900324. Any opinions, findings, and conclusions or recommendations expressed in this material are those of the author and do not necessarily reflect the views of the National Science Foundation.

1

Introduction

1.1 Modeling of nonlinear viscoelastic solids with damage induced anisotropy

1.1.1 Unified isotropic modeling of rubbers

Several classes of models have been proposed to characterize the constitutive behavior of rubber-like materials (e.g. Boyce and Arruda, 2000). Micro-mechanical models are founded on the physics of polymer chains network and statistical methods (e.g. Arruda and Boyce, 1993; Drozdov and Dorfmann, 2004). Alternatively, phenomenological models rely on mathematical developments that are associated with conceptual representations or analogies with the purpose of replicating the material's behavior as observed at the macroscopic scale (e.g. Dorfmann and Ogden, 2004; Dorfmann and Pancheri, 2012; Gent, 1996; Hoo Fatt and Ouyang, 2007, 2008; Huber and Tsakmakis, 2000; Liu, 2010; Liu and Hoo Fatt, 2011; Ogden and Roxburgh, 1999; Pioletti et al., 1998). In some mixed approaches, constitutive equations are founded on macroscopic models that contain statistical parameters reflecting a certain representation of the microscopic structure (e.g. D'Ambrosio et al., 2008; De Tommasi et al., 2006; Horgan et al., 2004).

Most existing material descriptions were developed under specific loading conditions. For instance, in the work of Brown (1997), the nonlinear dynamic behavior of filled elastomers is characterized at small strain amplitudes. Alternatively, Hoo Fatt and Ouyang (2008) propose a finite strain constitutive model for virgin Styrene Butadiene rubber subjected to a high strain rate monotonic loading. Furthermore, Liu and Hoo Fatt (2011) present constitutive equations, in finite strain, for the dynamic response of rubber under cyclic loading while D'Ambrosio et al. (2008), De Tommasi et al. (2006) and many others (e.g Chagnon et al., 2004, 2006; Dorfmann and Ogden, 2004; Dorfmann and Pancheri, 2012; Horgan et al., 2004; Marckmann et al., 2002; Ogden and Roxburgh, 1999) focus on characterizing main features of the rate independent softening behavior of elastomers, i.e. the Mullins effect (Mullins, 1969). Valuable reviews of the Mullins effect as well as of existing viscoelastic and hyperelastic constitutive laws were provided by Diani et al. (2009), Boyce and Arruda (2000); Drapaca et al. (2007) and Marckmann and Verron (2006) respectively.

A careful inspection of the relevant literature furthermore reveals that a pertinent distinction can be made between: (i) models focusing on the rate independent softening behavior of the virgin material (e.g. D'Ambrosio et al., 2008; De Tommasi et al., 2006), (ii) models describing its instantaneous response at high strain rates (e.g. Hoo Fatt and Ouyang, 2007, 2008), and (iii) models relating the repeatable dynamic behavior of the non-virgin material under cyclic loading (e.g. Liu and Hoo Fatt, 2011).

However, in many applications, rubbers are exposed to diverse loading conditions acting on the material in different states. This is the case, for instance, of elastomeric structural bearings and expansion joints which are subjected to prescribed displacements and tractions of various origins. While applied loads of increasing amplitude damage the polymer chains network and cause material softening, intermittent unloading conditions associated with temperature fluctuations can induce partial heal-

ing of the network and material stiffening by reentanglement and recross-linking of the chains. At an appropriate time scale, part of the applied loads is monotonic and, depending on the previous loading history, may be acting on a partially healed polymeric network. Conversely, cyclic loads typically engage a repeatable behavior of the non-virgin material. Both monotonic and cyclic loads can be slowly varying thus generating an equilibrium behavior (e.g. prescribed displacements due to material shrinking, creep, or thermal strains), or change rapidly hence engaging an instantaneous and rate-dependent response (e.g. passing train, emergency breaking, accidental shock, turbulent wind, gust, or earthquake).

When rubber-like materials are subjected to mechanical loading cycles, their hyper-viscoelastic response experiences stiffness and damping degradations. Alternatively, full or partial recovery of the material's initial properties can occur following favorable changes in temperature and pressure. In many applications, the accurate prediction of such variations in the material's behavior is of paramount importance in addressing system reliability as well as human safety issues. Failing to account for such changes in behavior, with sufficient accuracy, can result in tragic outcomes with potentially disastrous consequences. Unfortunately, existing constitutive models have a restrictive range of application and a limited predictive ability. Because in engineering practice material characterizations are often used separately while most viscoelastic models do not track the variations in the material's behavior, current designs involving rate dependent responses tend to overlook the Mullins effect and therefore rely on inaccurate predictions of the levels of degradation. This trend is further enhanced by the fact that, despite the abundance of tentative theories, no consensus has been reached yet on the actual physical sources of the Mullins effect (e.g. Diani et al., 2009). Consequently, the softening of rubbers under first deformation is frequently ignored in practical analyses and no distinction is made between the primary response of the virgin material and its repeatable behavior under subsequent

loadings.

In the current state of engineering practice, the prediction of a system's response under combined loading regimes, engaging a rate-dependent response and a softening behavior simultaneously, requires combining separate material models, each addressing a different aspect of material behavior. However, constitutive model libraries in commercial codes are far from exhaustive. Model combination rules and modalities are also limited, sometimes poorly documented and therefore opaque to the user. These facts often result in poorly controlled modeling approximations which undermine prediction reliability and accuracy.

There are currently very few predictive models for the behavior of elastomers that also account for their degradation and can therefore be considered as potential candidates to be used for the safe design of engineered components. Three-dimensional finite strain behavioral laws comprising hyperelastic, viscoelastic and elastoplastic components were proposed by Lin and Schomburg (2003), Lion (1996) and Miehe and Keck (2000). These formulations are based on the theory of thermodynamics with internal state variables (Coleman and Gurtin, 1967) and retain different choices of such variables to characterize the evolution of internal dissipative processes. The Mullins stress-softening effect is assumed to act isotropically on all their components and it is accounted for within the framework of continuum damage mechanics (Kachanov, 1986; Lemaître, 1996) using a unique damage parameter. Despite their relative rheological completeness, these elaborate models continue to show notable imperfections in replicating true rubber behavior: common shortcomings in modeling the Mullins effect are described for instance by Diani et al. (2009) while further predictive limitations can be directly seen upon comparing observed and fitted behaviors (e.g. Lin and Schomburg (2003, figure 8);Lion (1996, figures 2.1 and 4.1)). Clearly, more alternatives are needed as much remains to be done in modeling elastomers.

In the absence of a unique and perfectly-accurate behavioral characterization of

rubber-like materials, it is clear that significant improvements in design efficiency as well as substantial reductions in engineering resources and computational costs may be achieved by the provision of a greater number of unified formulations, valid under multiple loading conditions. Developing such models further would also contribute to reaching higher levels of accuracy by eliminating the need for approximate prediction combination techniques.

In order to address these goals, alternative constitutive formulations must be considered and their modeling capabilities explored. Building on the current state of knowledge in modeling elastomers, we put forward, in Chapter 2 (Zéhil and Gavin, 2013f), a new, mixed, three-dimensional, constitutive description of rubbers, in finite strain. The proposed model is based on a careful selection of preexisting components accurately reflecting key rubber behavior in two different loading regimes: (i) the rate-independent softening under deformation, also known as the Mullins effect, and (ii) hyper-viscoelasticity, including high strain rates. This new model complements the set of existing mixed formulations and is believed to have a significant potential in meeting the aforementioned needs, particularly in applications involving those two regimes.

1.1.2 Mullins effect induced anisotropy

Based on considerations of material symmetry, but also on the implicit assumption of a directional network alteration (as opposed to an isotropic one), Horgan et al. (2004) argue that the damage associated with the Mullins effect is inherently anisotropic and briefly discuss a tensorial approach to account for this anisotropy. Experimental data (e.g. Dargazany and Itskov, 2009; Diani et al., 2006; Dorfmann and Pancheri, 2012; Itskov et al., 2006; Machado et al., 2012) confirm that stress softening introduces some anisotropy in the material response. Diani et al. (2006) and Dargazany and Itskov (2009) present micromechanical directional models to handle softening in-

duced anisotropy. The potential of several finite-directional models in reflecting the behavioral anisotropy induced by the Mullins effect in initially isotropic hyperelastic materials is tested by Gillibert et al. (2010), based on the models' initial anisotropy and their ability to replicate the behavior of a full (i.e. infinite-directional) network. Dorfmann and Pancheri (2012) build on the tensorial approach outlined by Horgan et al. (2004) and derive a simple phenomenological model accounting for stress softening and changes in material symmetry. The model applies, in its current form, to pure homogeneous deformations; however, it may be extended to more general loading conditions by the addition of an evolution law.

A possible directional approach to model the Mullins effect induced anisotropy is also presented in Chapter 2 (Zéhil and Gavin, 2013f). This approach preserves the main characteristics of the isotropic model proposed in the same chapter, such as the form of stored energy density, and the probabilistic approach to damage.

1.2 Dissipative rolling contact mechanics

1.2.1 Rolling Resistance

For diverse reasons, rolling resistance remains important to many engineering applications. From nanotechnologies and molecular dynamics (e.g. Lee et al., 2009) to various scale industrial applications and transportation purposes (e.g. Hall, 2001; Qiu, 2006, 2009), from earthquake hazards mitigation, to energy harvesting and sustainable development considerations (e.g. Sharp, 2009), depending on human's objectives and goals, rolling resistance may be fiercely avoided or eagerly sought and thus requires careful attention.

Rolling resistance has been, and still is, widely addressed in scientific literature. In 1785 experiments on friction were reported by Coulomb (1821) and Vince and Shepherd (1785). Further experiments led to significant progress during the 1950's and the early 1960's towards a better understanding of its complex nature, involving

surface contact phenomena as well as bulk properties of the interacting materials (Greenwood et al., 1961; Tabor, 1955). Hysteretic friction in the bulk is revealed in many works on nonstationary viscoelastic contact problems, in various settings (e.g. Barber et al., 2008; Chertok et al., 2001; Galin and Gladwell, 2008; Golden and Graham, 2001; Morland, 1967, 1968; Wang and Knothe, 1993). In particular, rolling friction of hard cylinders was approached in two dimensions using various methods (e.g. Hunter, 1961; Johnson, 1985; May et al., 1959; Morland, 1967; Pöschel et al., 1999) and its dependence upon physical parameters was modeled based on simplifying assumptions regarding the description of the foundation layer and/or the nature of contact interactions. A one-dimensional treatment of a hard sphere rolling on a viscoelastic half-space modeled using a 'Winkler' approximation was given by Flom and Bueche (1959). In the absence of surface friction, a "first-principle" (i.e. free of empirical parameters) continuum-mechanics expression of the rolling resistance coefficient was derived by Brilliantov and Pöschel (1998) for the rolling motion of a viscoelastic sphere on a hard plane, in quasi-static conditions, such that the total stress field may be considered as the sum of an elastic part and a dissipative part, and the vertical displacement field may be approximated by the corresponding result of the static problem.

More recently, numerical difficulties associated with enforcing frictional conditions on finite element models of hyperelastic tires rolling in steady state conditions on rigid surfaces, were tackled by Laursen and Stanciulescu (2006) and Stanciulescu and Laursen (2006). A full two-dimensional boundary element formulation for a hard cylinder rolling on a viscoelastic layer of finite thickness was introduced by Qiu (2006) while Persson (2010) presented an approach to calculate the rolling resistance of hard objects on viscoelastic solids using a static pressure distribution. More comprehensive solutions to the problem of rolling resistance in three dimensions, including frictional effects, remain however in need. Furthermore, the increasing complexity of numeri-

cal models requires investigating possible ways of reducing their computational costs and hence improving their efficiency.

1.2.2 Rolling contact mechanics

Contact problems involve surface to surface mechanical interactions between one or more physical bodies, which in general, are deformable. The contact surface as well as the corresponding boundary conditions are usually unknown and left to be determined as part of the solution. Mechanical behaviors of touching objects are defined by their various shapes, bulk material properties, surface characteristics and by external actions. These primary factors may in turn depend upon other physical parameters, such as temperature and time, but also upon the state of contact. Reciprocally, the mechanical response of each individual object has an influence on the dimensions of the contact surfaces as well as on the intensity and nature of surface interactions. Contact problems are hence characterized by intricate and highly nonlinear dependences. They are consequently regarded as being among the most difficult to model and solve (e.g. Zienkiewicz and Taylor, 2005).

Full analytical solutions to contact problems exist in some standard settings (e.g. Galin and Gladwell, 2008). Very useful asymptotic expansions have also been derived in limiting cases (e.g. Jaffar, 1997, 2008). However, more often than not, contact problems require numerical modeling and solution. Well established finite element methods are frequently used to this end while specific types of constraints arising from contact are commonly enforced using optimization techniques based on Lagrange multipliers and penalty methods. A dense review of some of the most successful finite element solving strategies can be found, for instance, in Zienkiewicz and Taylor (2005). Nevertheless, despite their power and broad scope of application, the fact remains that in many particular instances, the practical implementation of such methods can be unnecessarily complicated.

Simpler and more convenient alternatives exist, such as the approach proposed by Kalker (1979), which is based on the Hertz elastic theory of contact (Hertz, 1881). The high computational efficiency of such approaches results from the use of existing analytical solutions based on simplifying assumptions and therefore limiting their scope of application. In its original form, Kalker's approach assumes that the contact surface is elliptic and that the distribution of normal stresses is of the Hertz's form. Its current implementation in the "CONTACT" program (Vollebregt, 2012) relaxes these assumptions but still approximates the contacting bodies by linear elastic half-spaces to decouple the contact problem from the global simulation. In this context, surface displacements are estimated according to the analytical solution of Boussinesq and Cerruti (Love, 1927) for an elastic half-space. Kalker's contact theory relies on the principle of superposition and the reciprocity theorem. It is therefore limited to linear elasticity and secondarily, to linear viscoelasticity. The latter is applied only to the contact surface but not to the bulk of the contacting bodies. Instead, the responses of the bodies are approximated using the elastic half-space approach. In brief, the Kalker theory is based on the assumptions that the contacting bodies are linear elastic and that the contact surface is flat and small with respect to their typical dimensions. Many practical settings do not satisfy these assumptions, for instance, in the case of problems involving thin viscoelastic layers.

Chapter 3 (Zéhil and Gavin, 2013c) focuses on presenting simple, yet robust and efficient algorithms for solving steady-state, frictional, rolling (or sliding) contact problems, in two and three dimensions. The cores of the solvers rely on very general principles: (i) resolving normal and tangential motional conflicts between the contacting bodies, and (ii) eliminating unacceptable normal and tangential surface tractions. The proposed algorithms are formulated in the context of small deformations and applied to the cases of a rigid cylinder and a rigid sphere rolling on a linear viscoelastic layer of finite thickness, in two and three dimensions, respectively.

The formulations presented can be extended to handle stationary or steady-state rolling/sliding contact problems involving a deformable indenter or to more general settings, such as problems involving materials nonlinearities and large deformations.

1.2.3 Modeling of viscoelastic layers and coatings: Isotropic incompressible layers of arbitrary thickness

Many soft materials and rubber-like materials are nearly incompressible. In Chapter 4 (Zéhil and Gavin, 2013e), a three-dimensional boundary element formulation of an incompressible linear viscoelastic layer of finite thickness is presented, in a moving frame of reference. This formulation is applied, in combination with a contact solver from Chapter 3 (Zéhil and Gavin, 2013c), to build a full three-dimensional model for the resistance incurred by a rigid object (sphere) rolling/sliding on the layer, including surface friction. Inspired by the seminal work of Qiu (2006), we expand relevant mechanical fields in the continuum of the layer into two-dimensional Fourier series. The storage and loss moduli characterizing the constitutive behavior of linear viscoelastic materials, in the frequency domain, are used to relate the Fourier coefficients. The proposed formulation results in the assembly of a compliance matrix $\mathbf{C}$ characterizing the behavior of the layer's upper boundary, including the effects of steady-state motion. This compliance matrix may be used in any stationary or steady-state rolling/sliding contact problem-solving strategy. The proposed formulation is quite general and practical in that it accommodates any linear viscoelastic model, including experimental master-curves. In order to increase its computational efficiency, special attention is given to exploiting configurational similarities as well as symmetry.

Anisotropic compressible and incompressible layers of arbitrary thickness

The author's interest in rolling resistance initially stems from the exploration of new damping principles suitable for the seismic isolation of critical facilities. In a recent study (Harvey et al., 2013) conducted on a Ball-N-Cone$^{\text{TM}}$rolling isolation bearing (WorkSafe Technologies, 2012), we addressed the benefits of damping in rolling isolation systems. In order to limit the peak acceleration levels to which sensitive equipment may be subjected to during the course of an earthquake, higher levels of 'soft' damping can be achieved by increasing the resistance to rolling or sliding of their seismic isolation platforms. In practice, this damping principle can be implemented by inserting a dampening material between contacting components of the isolation system, in relative motion with respect to each other. For instance, in the case of rolling isolation bearings, viscoelastic rubber sheets can be inserted between the rigid roller (e.g. a sphere) and the hard surfaces on which the rolling occurs (e.g. 'dished' or bowl-shaped steel plates).

An early and approximate closed-form expression for the rolling resistance R_r incurred by a rigid sphere rolling on a *compressible* viscoelastic half-space was derived by Greenwood and Tabor (1958) who integrated, under the small strain assumption, the horizontal projection of the stationary normal stress distribution, as given by Hertz (1881), over the front half of the contact 'disk', and evaluated its work per unit distance of rolling. The proposed expression for rolling resistance is in good agreement with experimental results presented by the authors for spheres moving slower than at 1 cm/s under mean contact pressures below 2.76 MPa (i.e. 400 lb.in^{-2}). This expression may be re-written as follows

$$R_r \approx \alpha_{GT} \left(\frac{3^4}{4^7}\right)^{\frac{1}{3}} \left(\frac{1-\nu^2}{E}\right)^{\frac{1}{3}} \frac{P^{\frac{4}{3}}}{R^{\frac{2}{3}}}, \tag{1.1}$$

where P is the vertical load supported by the rolling sphere, and R stands for its

radius. Young's modulus E and Poisson's ratio ν of the layer's material, as well as the loss fraction α_{GT} of the input deformation energy are taken as constants. Flom and Bueche (1959) proposed an alternative simplified theory accounting for the influence of rolling speed and resulting in expressions that otherwise confirm, for intermediate values of the dynamic loss factor (known as $\tan\delta$), the dependencies of rolling resistance predicted by equation (1.1) on the vertical load P, the radius of the sphere R and the layer's stiffness. These expressions may be written in the generic form

$$R_r \approx \alpha_{FB} \left(\frac{1-\nu^2}{E} \right)^{\frac{1}{3}} \frac{P^{\frac{4}{3}}}{R^{\frac{2}{3}}}, \tag{1.2}$$

where, as noted by Lakes (2009), α_{FB} depends on $\tan\delta$ and therefore on the material parameters of the layer and on the rolling velocity V_s. Based on the simplifying assumption that the dynamic contact region has a similar size to that given by the static solution of Hertz, Lakes also noted that an upper bound for the viscoelastic rolling resistance of a rigid sphere is given by

$$R_r \approx \left(\frac{3}{4} \right)^{\frac{1}{3}} \left(\frac{1-\nu^2}{E} \right)^{\frac{1}{3}} \frac{P^{\frac{4}{3}}}{R^{\frac{2}{3}}}, \tag{1.3}$$

where E is interpreted as a dynamic modulus at a circular frequency ω, proportional to V_s/R. Expressions (1.1)-(1.3) are furthermore consistent in predicting that rolling resistance decreases with Young's modulus and that it is maximized by a Poisson ratio of zero. Hence, based on this simple and qualitative reasoning, it may be expected that relatively soft and compressible layers, with a Poisson ratio that is close to zero, would yield higher levels of resistance and damping than harder layers or layers made of incompressible materials ($\nu \approx 0.5$) such as rubbers.

The boundary element formulation presented in Chapter 3 (Zéhil and Gavin, 2013e) applies to *incompressible* and *isotropic* layers, which is practically the case

of most rubber-like materials. Compressible materials are however characterized by one additional frequency-dependent complex parameter, i.e. the complex Poisson ratio $\nu^*(\omega)$, and can not be modeled with this formulation. Extending the boundary element formulation to *compressible* layers is therefore needed. In Section 5.4, a compressible isotropic formulation is derived, in three dimensions, to answer this first need. This derivation is somewhat akin to that proposed by Persson (2001) based on Fourier transforms and applied in a simplified approach to the rolling resistance of hard cylinders and sphere on a viscoelastic layer (Persson, 2010). A two-dimensional formulation in plane strain is deduced in Section 5.7 to complement the incompressible formulations proposed by Qiu (2006, 2009).

Moving further, one may think of cork as an example of relatively soft material characterized by a Poisson ratio that is close to zero. In fact this material is used as a stopper for wine bottles because it shows very little lateral expansion when it is compressed. However, cork does not behave isotropically. Indeed, its prismatic cells are packed in columns in the radial direction, which constitutes a direction of symmetry of the cellular structure. Cork may therefore be modeled as a transversely isotropic medium (e.g. Rosa and Fortes, 1991). In order to achieve accurate rolling resistance predictions on viscoelastic materials such as cork, with different mechanical characteristics in the out-of-plane direction, the boundary element formulation must further be extended to polar anisotropic layers. This additional need is addressed in Section 5.5 where a three-dimensional transversely isotropic formulation is derived. This formulation is specialized further to plane strain in Section 5.8.

On the other hand, a hard-wearing layer cannot be too soft. Hence, there seems to be a tradeoff between high resistance to rolling and durability. Given the need to achieve optimal levels of damping under specific conditions (of seismic hazard for instance) while maintaining suitable service life expectancies, the future use of specially designed layers made of viscoelastic *metamaterials* cannot be excluded and

should therefore be prepared. Man-made materials, such as auxetic composites made of rubber-filled re-entrant honeycombs for instance, are often characterized by different mechanical properties in three orthogonal directions. Predicting the resistance of such materials to rolling and sliding would ultimately require extending the boundary element formulation to fully orthotropic layers. This need is fully addressed in Section 5.6.

Sphere with viscoelastic coatings

Viscoelasticity is a time-dependent model of material behavior capable of replicating the storage and restitution (elasticity), and the dissipation in the bulk at different internal rates (viscosity), of variable proportions of the deformation energy. Particles and solids of rounded shape presenting viscoelastic properties, or interacting mechanically with other viscoelastic entities, with or without direct contact, are involved in many aspects of science and technology, in various fields, and at different length-scales, from the smallest fundamental particles (e.g. Berg, 1999), to nano-materials and living cells (e.g. Bahadur and Schwartz, 2008; Bose et al., 2010; Coghill, 2012; Subramaniam et al., 2013; Xu and Shao, 2008), to various sorts of objects and systems at the human scale, such as the motion of rigid spheres in polymer gels (e.g. Hunter, 1968), the vibratory sorting of fruits and vegetables (e.g. Arnold, 1985), polymer-coated grinding spheres (e.g. Langus et al., 2011), rubber bullets (e.g. Bir et al., 2012), particle dampers (e.g. Els, 2009), structural damping fillers (e.g. Oyadiji, 1996), computer mouse-balls, spherical wheels for vehicles and robots (e.g. Wu and Hwang, 2008; Wu et al., 2011), flows of viscoelastic fluids around spheres (e.g. Atsbha, 1993), flows of granular materials (e.g. Yung et al., 2007; Zhou et al., 1999), human or animal joints (e.g. Esat and Ozada, 2010), and rolling balls in seismic isolation platforms (e.g. Harvey et al., 2013; Tsai et al., 2010), to the largest planets, and stars (e.g. Bambusi and Haus, 2012).

Among all possible types of static or dynamic interactions between one, two, a few, or even very large numbers of rounded entities, those involving contact are very common, and often accompanied by losses of mechanical energy. Upon rolling or sliding, mechanical energy is transformed into heat in the continuum of those of the interacting objects that are characterized by a viscoelastic behavior. This dissipative process in the bulk, known as viscoelastic "rolling resistance", or viscoelastic "rolling friction", is reflected by changes in the mechanical fields (i.e. the stresses and strains) across the contact interfaces, so as to resist the ongoing motion.

Problems related to the resistance incurred by rigid indenters, such as cylinders, spheres and cones, rolling or sliding on a viscoelastic plane, are addressed quite extensively in the scientific literature, both experimentally and from a modeling perspective, in two and three dimensions, and at different scales, such as in the works of Bueche and Flom (1959); Carbone and Putignano (2013); Chertok et al. (2001); Flom and Bueche (1959); Flom (1960); Galin and Gladwell (2008); Greenwood and Tabor (1958); Greenwood et al. (1961); Hunter (1961); Johnson (1985); Lee et al. (2009); May et al. (1959); Persson (2010); Pöschel et al. (1999); Qiu (2006); Tabor (1952, 1955); Zéhil and Gavin (2013e,c,d, 2014c), to cite a few (see Chapters 3, 4, 5 and 7). Alternatively, the rolling contact between viscoelastic cylinders, or between a viscoelastic cylinder and a rigid plane is analyzed for instance by Golden and Graham (2001); Kumar et al. (1988); Morland (1967, 1968); Munisamy et al. (1991); Nowell and Hills (1988); Oden and Lin (1986); Qiu (2009); Wang and Knothe (1993), while Hall (2001) presents a nice review of the fundamentals of rolling resistance from the perspective of the tire industry. However, quite surprisingly, problems involving the rolling/sliding friction of viscoelastic spheres have received far less attention.

To date, no work has ever addressed the modeling and the solving of the resistance incurred by a rigid sphere, covered with a viscoelastic coating, rolling or sliding, on a rigid plane. In Chapter 6 (Zéhil and Gavin, 2013b), we present a

novel three-dimensional boundary-element formulation that fully characterizes the mechanical behavior of the external boundary of a multi-layered viscoelastic coating attached to a hard rotating spherical core. The proposed formulation incorporates both the viscoelastic, and the inertial effects of the steady-state rolling motion of the sphere, including the Coriolis effect. The proposed formulation is based on Fourier-domain expressions of all mechanical governing equations. It relates two-dimensional Fourier series expansions of surface displacements and stresses, which results in the formation of a compliance matrix for the outer boundary of the deformable coating, discretized into nodes. The computational cost of building such a compliance matrix is optimized, based on configurational similarities and symmetry. The proposed formulation is applied, in combination with a rolling contact solving strategy, to evaluate the viscoelastic rolling friction of a coated sphere on a rigid plane. Steady-state results generated by the proposed model are verified by comparison to those obtained from running dynamic simulations on a three-dimensional finite element model, beyond the transient. A detailed application example includes a verification of convergence and illustrates the dependence of rolling resistance on the applied load, the thickness of the coating, and the rolling velocity.

1.2.4 Simplified approaches to rolling resistance

In many circumstances, a complete and perfectly accurate solution to the rolling contact problem is not necessary, hence justifying the search for cheaper computational means. This is particularly the case when only an estimate of the rolling resistance is sought. In Chapter 7 (Zéhil and Gavin, 2013d), we consider alternative approaches to the full three-dimensional model, providing rolling resistance estimates with an accuracy that is suitable for many engineering purposes. Chapter 7 clearly delineates two approaches to estimating the rolling resistance of a rigid sphere on a viscoelastic layer of finite thickness. In both approaches, the effects of slipping friction are

neglected.

In the "2D cylinder-based" approach, the sphere is conceptually sliced into a set of cylinders. The rolling resistance incurred by each cylinder is determined by solving a rolling contact problem in two dimensions. The foundation's behavior is described by a numerical compliance in plane strain. The 2D cylinder-based approach builds on results from Qiu (2006) and involves new approximate methods of extending two-dimensional models of rolling cylinders to modeling a rolling sphere in three dimensions. Three numerical methods of varying complexity and accuracy are presented for this approach.

In the "direct Fourier series" approach, rolling resistance is estimated by computing dissipated power, in the vertical direction, along the contact surface. This approach mainly relies upon the approximate assumption that the stationary vertical stress distribution, as well as the corresponding contact area, are unaltered by motion. Inspired by the recent work of Persson (2010) on rolling resistance, and building upon results from Zéhil and Gavin (2013e,c) (see Chapters 3 and 4), as well as on stationary contact results from Jaffar (1988, 1997, 2008), new expressions for the rolling resistance are derived, for different ranges of foundation thickness, in the form of direct Fourier expansions.

1.2.5 Rolling resistance experiment

Most documented experiments conducted to measure rolling and sliding resistances on rubber-like materials date back to the 1950's and the early 1960's. Tabor (1952) presented typical results for the resistance incurred by a hard sphere rolling, at moderate speed, on rubber layers of similar stiffness but of different resilience. He correlated the observed friction with the hysteresis losses in the bulk, which he evaluated analytically from the normal load. Sabey (1959) conducted skidding experiments of rubber samples of different resilience on hard surfaces of different roughness. These

experiments highlighted the fact that hysteresis losses in the bulk of the rubber contribute significantly to the total resistance to skidding. Bueche and Flom (1959) presented experimental results, of a hemispherically-ended steel rider sliding on lubricated Plexiglas and polyethylene, showing that rolling resistance results apply to lubricated sliding where surface frictions have been minimized.

Flom and Bueche (1959) proposed a simplified theory of rolling resistance featuring the importance of elastic hysteresis losses and predicted that, at increasing speed, the coefficient of rolling friction for a sphere should go through a maximum, this maximum being a known function of temperature. Independently, and at the same time, May et al. (1959) predicted a similar type of behavior, for a hard cylinder rolling on a viscoelastic material, from an alternative approach to rolling friction also based on hysteresis losses. The analysis was later extended in May et al. (1963) to predict the complex behavior of viscoelastic cylinders rolling between two hard surfaces.

In order to validate their theory, as presented in Flom and Bueche (1959), Flom (1960) used a rotating experimental device (see Figure 1.1) to measure the resistance incurred by three hard spheres rolling in circles on a sheet of rubber. The thicknesses of the elastomer samples were not reported by the authors. It should perhaps be assumed that the samples were chosen to be thick enough to behave as a half-space. Indeed, the viscoelastic model Flom and Bueche (1959) validated by this experiment was calibrated to yield the Hertzian solution (Hertz, 1881) in the static case. The range of rolling speeds that were considered in this study is moderate: roughly, 1 to 20 cm/s. The linear viscoelastic characterizations of the tested elastomers (unfilled butyl, Neoprene GN and silicone SE 450) were based on rudimentary rebound measurements, or on the use of early DMA properties from similar but unlikely identical materials found in the literature (e.g. Nolle, 1950). Nevertheless, despite the numerous assumptions involved, the authors reported a satisfactory agreement between

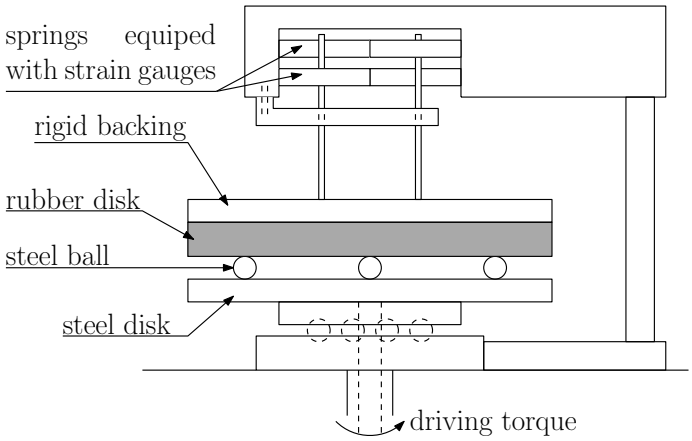

FIGURE 1.1: Experimental setup used by Flom (1960) to measure the rolling resistance of rigid spheres. Three identical balls are placed between a horizontal steel disk rotating at constant speed and a disk of rubber attached to a rigid backing. The latter can be loaded vertically. The balls are guided by a large circular groove in the lower disk. The rolling resistance incurred by the balls is deduced from the measured couple that prevents the upper disk from spinning.

their theory and the experiment.

More recently, Xu et al. (2007) presented an experimental apparatus (see Figure 1.2) that measures the steady-state coefficient of rolling friction of a squash ball on a conveyor belt, at moderate velocities. The setup was designed to fill an identified gap in the availability of accessible methods to perform rolling resistance experiments involving deformable spheres. It was later used in a classroom for teaching purposes. The different sources of power dissipation contributing to rolling resistance cannot be clearly distinguished using the proposed device. Indeed, energy losses occur not only in the bulk of the sphere, but also to some extent in the bulk of the deformable conveyor belt, and at the contact interface in case of slipping friction as well. Nevertheless, the experimental results presented by the authors, for the combined losses, revealed a linear dependence of the coefficient of rolling friction on the translational velocity, at moderate loads and rates of motion.

In 2010, Persson (2010) proposed the experimental setup illustrated in Figure 1.3

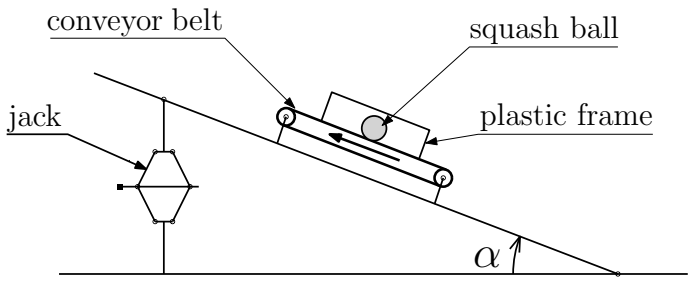

FIGURE 1.2: Experimental setup proposed by Xu et al. (2007) to measure the rolling resistance of a squash ball on a conveyor belt. Rolling resistance is determined by the angle α at which the conveyor belt must be inclined to achieve steady-state rolling conditions, at a given speed.

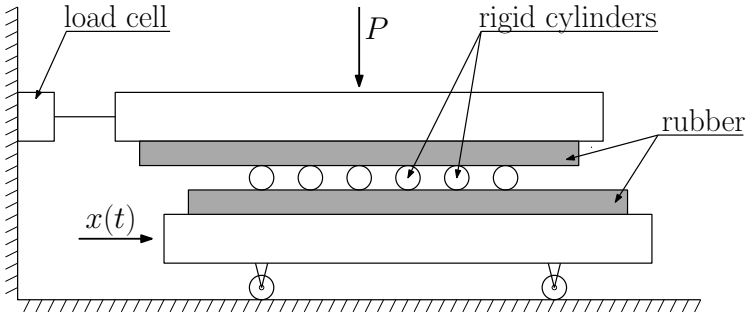

FIGURE 1.3: Experimental setup proposed by Persson (2010) to measure the rolling resistance of rigid cylinders. Similar sheets of rubber are attached to two horizontal and rigid plates. N identical rigid cylinders are set in parallel between the rubber sheets. The rolling resistance incurred by one cylinder subjected to the load P/N corresponds to the force measured on the upper block divided by N.

to measure the total resistance incurred by multiple rigid cylinders rolling between two rubber sheets (of constant Poisson's ratio), as a means to determine the viscoelastic complex modulus $E^*(\omega)$ of the rubber. However, the author does not describe an implementation of this setup.

In Chapter 8 we present an experimental apparatus designed to measure rolling resistance. The setup is used to determine the actual resistance to motion incurred by a rigid steel-ball rolling, in steady-state, between two sheets of rubber, bonded to horizontal steel plates. Several tests are conducted, involving different materials,

sheet thicknesses, balls diameters, applied weights, and prescribed rolling velocities. Rolling resistance measurements are compared to predictions obtained from linear viscoelastic characterizations of the materials involved, at different strain amplitudes, using the computational tools developed in Chapters 3 and 4 (Zéhil and Gavin, 2013e,c). An analysis of the principal sources of measurement error is presented and interesting conclusions are drawn regarding the importance of the Payne effect on rolling resistance predictions.

1.3 Synergistic Structural Composites

Composites play a key role in the ongoing race to develop new structural materials with improved characteristics for the various load bearing applications. The fundamental concept behind structural composites lies in the judicious combination of materials characterized by different and often complimentary properties, to achieve better overall performances.

From a structural perspective, relevant performance indicators include: (i) an improved structural efficiency characterized by higher stiffness-to-weight and strength-to-weight ratios, so as to satisfy conditions of deformability, serviceability, and resistance capacity, at reduced structural dimensions and weights, architectural constraints, and production costs, (ii) a higher damping to stiffness ratio, so as to improve the responses of structures to vibrations induced by dynamic loads, without compromising their structural efficiency, (iii) an improved structural safety, measured in terms of ductility, i.e. larger ratios of ultimate to yield deformations, and resistance capacities, (iv) improved application-specific performances such as resistances to fire, blasts, impacts, abrasion and shatter, cracking control, compactness, and reduced permeability, (v) an improved environmental impact, which implies a reduced consumption of energetic and material resources, an increased proportion of safe, environmental friendly, reusable or recyclable materials.

The most commonly used structural composites, in the broad sense, include: (i) reinforced concrete, prestressed concrete, and conventional steel-concrete composite structures, which combine, in quite brilliant ways, the good compressive behavior of concrete and tensile behavior of structural steel and/or steel cables, (ii) fiber reinforced concrete, where the tensile (among other) properties of the composite are improved by the added fibers, such as steel, glass, or synthetic (e.g. polypropylene) fibers, (iii) soil stabilizing and retaining structures such as reinforced earth, landslide mitigating structures comprising geosynthetics and geotextiles, vegetated cribbings, and gabion and rock matrix structures, (iv) soil reinforcing systems such as micro-piles, soil nails, jet grouted piles and vibro-replacement jet columns, (v) composites resulting from repairing techniques such as carbon fiber reinforcement systems, (vi) sandwich-structured composites and filled tubes.

The sandwich-structured composites, or sandwich panels, comprise two thin but stiff skins, such as metal sheets, to resist the bending moment, separated by a lightweight core material resisting the shear force. Depending on applications, the core of sandwich panels is often made of lightweight wood or relatively soft polymer foams, of conventional or re-entrant honeycomb structures, which may be filled to increase the damping properties of the composite, or alternatively, of stiffer polymers, such as polyurethane sheets. The patented "sandwich plate system", which comprises two metal plates bonded with a polyurethane elastomer core, has been studied extensively in the past few years (Braun et al., 2002; Kennedy et al., 2003; Teixeira de Freitas et al., 2010a,b, 2012a,b, 2013). The system is intended for use in a variety of applications including the construction and repair of structural floors, stadiums, ships, and bridges.

Filled tubes are generally constituted from an elongated tubular casing filled with a relatively softer material. These composites include: (i) concrete-filled, reinforced concrete-filled, prestressed concrete-filled, and expansive-cement-filled steel tubes,

which are broadly used in construction (e.g. Chang et al., 2009; Chung, 2010; Deng et al., 2011; Han, 2004), (ii) concrete-filled fiber-reinforced polymer tubes, which were reported to be effective in applications such as piling, poles, highway overhead sign structures, and bridge components (Ahmad et al., 2008a,b; Fam and Rizkalla, 2002; Fam and Cole, 2007; Naguib and Mirmiran, 2002; Shao and Mirmiran, 2005, e.g.), (iii) foam-filled aluminum, steel or composite tubes, or sandwich tubes, mainly used for energy absorption in applications involving very large deformation and high strain-rates, such as impacts (e.g. Fan et al., 2013; Niknejad et al., 2013; Reddy and Wall, 1988; Seitzberger et al., 2000; Strano et al., 2013; Yang and Qi, 2013), and (iv) epoxy polymer concrete-filled steel tubes, which were introduced and studied as potential earthquake resisting elements (Oyawa et al., 2001, 2004; Oyawa, 2007).

Unlike most types of sandwich panels, filled tubes take more or less advantage of the confining effect that the casing has on the infill. The differences between the mechanical properties of the two components influence the structural behavior of the composite. The compressibility of the infill, which may be seen as determined by its Poisson ratio, plays a key role in this regard.

Poisson's ratio has been the subject of an imposing number of papers, in the past two decades. Topics include: (i) general articles discussing Poisson's ratio and reviews on auxetic materials and their applications (e.g. Alderson, 1999; Alderson and Alderson, 2007; Baughman et al., 1998; Evans, 1990; Evans and Alderson, 2000; Greaves et al., 2011; Lakes, 1993a,b; Lakes and Wineman, 2006; Liu, 2006; Liu and Hu, 2010; Mott et al., 2008; Prawoto, 2012; Yang et al., 2004), (ii) developing techniques to produce novel substances, such as foams, with auxetic properties (e.g. Alderson and Evans, 1992; Caddock and Evans, 1989; Chan and Evans, 1997, 1999a,b; Chen and Lakes, 1991; Choi and Lakes, 1992b,a; Evans, 1989; Fozdar et al., 2011; Friis et al., 1988; Martz et al., 1996; Warren, 1990), (iii) developing new auxetic composites or studying composites with auxetic inclusions (e.g. Assidi and Ganghof-

fer, 2012; Hou et al., 2012; Milton, 1992; Wei and Edwards, 1998a,b; Zhang et al., 1998), (iv) proposing modes of deformation and micro-mechanisms presenting auxetic behaviors (e.g. Dirrenberger et al., 2011; Bezazi et al., 2005; Grima et al., 2005, 2007, 2013; Lira et al., 2009; Pasternak and Dyskin, 2012), (v) developing models for auxetic behavior, such as micro-structural models, or models based on homogenization (e.g. Alderson and Evans, 1993, 1995; Choi and Lakes, 1995; Dirrenberger et al., 2011; Evans and Caddock, 1989; Gaspar et al., 2003; Lee et al., 1996), (vi) studying empty and filled cellular structures, including conventional and re-entrant honeycombs, in relation to auxetic properties, and damping (e.g. Alderson et al., 2010b,a; Boucher et al., 2013; Grima et al., 2013; Lira et al., 2009; Murray, 2009; Murray et al., 2012; Prall and Lakes, 1997; Soman et al., 2012), (vii) studying auxetic fibers (e.g. Alderson et al., 2005; Simkins et al., 2005), (viii) studying auxetic behavior in nanomaterials (e.g. Hall et al., 2008), (ix) examining specific properties of auxetic materials, such as their indentation behavior or their viscoelastic response (e.g. Alderson et al., 1994; Chan and Evans, 1998; Evans and Alderson, 1992; Scarpa et al., 2005), and (x) studying the nonlinear behavior of auxetic materials and structures, such as their buckling behavior, or their elasto-plastic behavior (e.g. Dirrenberger et al., 2012; Obrecht et al., 2006). Materials with negative Poisson ratios remain at the center of many current research projects.

In Chapter 9 Zéhil and Gavin (2014b), we derive analytical expressions for the axial behavior of filled circular tubes, to develop physical insight into the mechanical interactions between the casing and the infill, in the linear range. These equations are presented in yet unpublished graphical forms, revealing the influence of dimensionless material and geometric parameters on the structural efficiency of the composite. It is for instance shown that significantly stiffer and stronger members can be obtained by filling the casing with a moderately softer, but highly auxetic, material. This observation further stresses the need for novel lightweight auxetic materials that

would remain stiff enough to be used in structural applications.

It is furthermore inferred that polymer-filled metallic tubes can present limited mechanical synergies in the linear range of the materials involved. This prediction is confirmed by a bending experiment conducted on a Urethane-filled Aluminum tube of square cross section. The experiment however reveals interesting mechanical synergies under large deformations.

2

Unified constitutive modeling of rubber-like materials under diverse loading conditions

2.1 Preamble

This chapter presents a new constitutive model that unifies the behavioral characterizations of rubber-like materials in a broad range of loading regimes. The proposed model combines a selection of existing components that are known to reflect, with suitable accuracy, two fundamental aspects of rubber behavior in finite strain: (i) rate-independent softening under deformation, also known as the Mullins effect, and (ii) hyper-viscoelasticity, including at high strain rates. The evolution model is further generalized to account for multiple rates of internal dissipation (or material time-scales). Suitable means of identifying the system's parameters from simple uniaxial extension tests are explored. Several aspects of the model's behavior are shown in virtual experiments of uniaxial extension, at different stretch rates. A possible directional approach extending the model to handle softening induced anisotropy is briefly discussed.

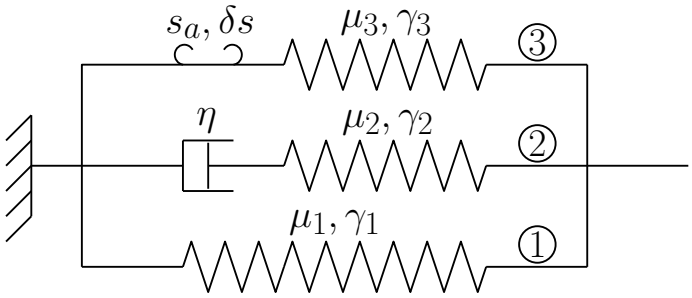

FIGURE 2.1: 1D representation of the full 3D prototypical model.

2.2 Proposed model

Building on the work presented in D'Ambrosio et al. (2008) and De Tommasi et al. (2006) for a low strain rate characterization of the Mullins effect, as well as on existing high-speed constitutive modeling approaches, as addressed for instance in Hoo Fatt and Ouyang (2008), the new prototypical model shown in Figure 2.1 is proposed as a unified description of the behavior of isotropic incompressible rubber-like materials, under multiple loading conditions.

The proposed model corresponds to an isotropic three-dimensional formulation in finite strain. Three model components contribute additively, in terms of stored energy and stress, to the global response: ① a permanent nonlinear hyperelastic component characterized by a stored energy function U_1, ② a permanent hyper-viscoelastic component characterized by a viscosity η and a stored energy function U_2 (i.e. a nonlinear Maxwell element), and ③ a non-permanent component composed of nonlinear hyperelastic links characterized by a distribution of activation and breaking thresholds, as well as a stored energy function U_3. The model is further generalized in Section 2.8 to include multiple components of type ② and a possible directional approach extending the model to handle softening induced anisotropy is briefly discussed in Section 2.9.

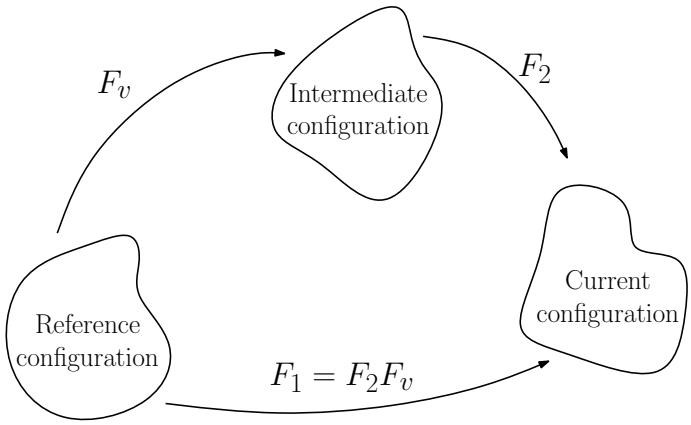

FIGURE 2.2: Multiplicative decomposition applying to links of type ②.

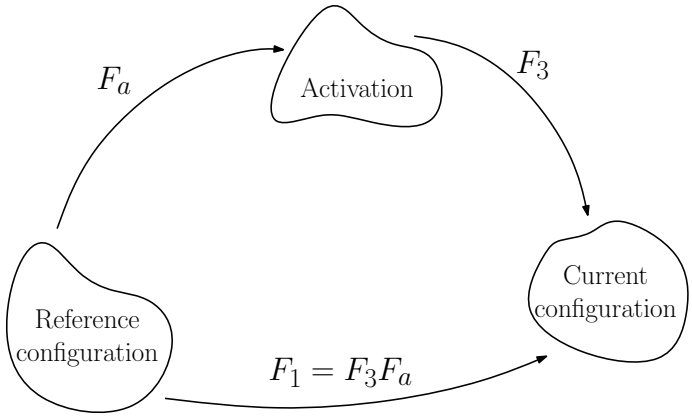

FIGURE 2.3: Multiplicative decomposition applying to links of type ③.

2.3 General kinematics

Addressing the hyper-viscoelastic component ② first, the total deformation gradient $\mathbf{F}_1$ is divided into a viscous component $\mathbf{F}_v$ and an elastic component $\mathbf{F}_2$ by means of a multiplicative decomposition

$$\mathbf{F}_1 = \mathbf{F}_2\mathbf{F}_v. \tag{2.1}$$

The intermediate configuration shown in Figure 2.2 is generally not kinematically consistent. It corresponds to locally relaxed elements of continuum which are conceptually isolated from each other. Furthermore, the intermediate configuration is not

unique: any combination of rigid body motions, in the local sense, would still yield an admissible alternative. Consequently, strain measures that are independent of the choice of intermediate configuration are used to describe the constitutive behavior of the material at hand.

Another set of multiplicative decompositions applies to the non-permanent links of type ③. As described in Figure 2.3, the global deformation gradient $\mathbf{F}_1$ of each activable link is written as

$$\mathbf{F}_1 = \mathbf{F}_3 \mathbf{F}_a, \tag{2.2}$$

where $\mathbf{F}_a$ is a partial deformation gradient that puts the link in a state of activation, while $\mathbf{F}_3$ corresponds to the complement of deformation associated with the strain energy U_3. The elastic energy stored in any given link of type ③ is lost when the link reaches a deformation gradient $\mathbf{F}_b$ putting it in a state of rupture.

2.4 Hyperelastic formulation

2.4.1 General theory

Assuming that each component undergoes an isochoric transformation, the invariant $J_j = \det(\mathbf{F}_j)$ is equal to 1, and the corresponding stored energy is a function of the first and second invariants of the appropriate measure of strain

$$U_j = U_j(I_{b_j}, II_{b_j}), \tag{2.3}$$

where $\mathbf{b}_j = \mathbf{F}_j \mathbf{F}_j^T$ is the left Cauchy-Green or Finger tensor associated with the transformation defined by $\mathbf{F}_j$. The hyperelastic formulation used in this work builds on the fact that, for each component $j \in \{1, 2, 3\}$, the rate of change of the Lagrangian Green strain tensor $\dot{\mathbf{E}}_j$ is work conjugate to the second Piola-Kirchhoff stress tensor

$\mathbf{S}_j$ (i.e. the pull-back of the Cauchy stress tensor $\boldsymbol{\sigma}_j$)

$$\left.\begin{aligned} \dot{U}_j &= \left(\frac{\partial U_j}{\partial \mathbf{E_j}}\right) \mathbf{:}\dot{\mathbf{E}}_j \\ \dot{U}_j &= \mathbf{S}_j \mathbf{:}\dot{\mathbf{E}}_j \end{aligned}\right\} \Rightarrow \left(\frac{\partial U_j}{\partial \mathbf{E_j}} - \mathbf{S}_j\right) \mathbf{:}\dot{\mathbf{E}}_j = 0. \tag{2.4}$$

Due to incompressibility, the rate of change of J_j, which can be expressed in terms of the right Cauchy-Green deformation tensor $\mathbf{C}_j = \mathbf{F}_j^T \mathbf{F}_j$, is equal to zero (e.g. Bonet and Wood, 2008)

$$\dot{J}_j = \left(J_j \mathbf{C}_j^{-1}\right) \mathbf{:}\dot{\mathbf{E}}_j = 0. \tag{2.5}$$

Comparing equations (2.4) and (2.5) shows that both left hand sides are collinear, which, for $J_j = 1$, yields the following expression of the second Piola-Kirchhoff stress in component j

$$\mathbf{S}_j = \frac{\partial U_j}{\partial \mathbf{E}_j} + p_j \mathbf{C}_j^{-1}, \tag{2.6}$$

where the coefficient of proportionality p_j corresponds to an undetermined pressure term arising from incompressibility. Alternatively, a generic form of the Cauchy stress tensor in each component j is obtained by pushing forward $\mathbf{S}_j$, in expression (2.6), to the current configuration and applying the chain rule to $\partial U_j / \partial \mathbf{E}_j$ (see appendix A.2)

$$\boldsymbol{\sigma}_j = 2\left(\frac{\partial U_j}{\partial I_{b_j}} + I_{b_j} \frac{\partial U_j}{\partial II_{b_j}}\right) \mathbf{b}_j - 2\frac{\partial U_j}{\partial II_{b_j}} \mathbf{b}_j^2 - p_j \mathbf{I}. \tag{2.7}$$

It should be noted that the term $-p_j \mathbf{I}$ in expression (2.7) does not always correspond to the full stress axiator (i.e. the spherical part of $\boldsymbol{\sigma}_j$).

2.4.2 Specialized formulation

Numerous expressions of stored energy density functions are proposed in the literature (e.g. Marckmann and Verron, 2006). The dependence of U_i on I_{b_i} was found

to be dominant in the case of incompressible rubber-like materials (e.g. Yeoh, 1990). The following form will be retained for the purposes of this work

$$U_j = \mu_j \left(I_{b_j} - 3\right)^{\gamma_j}, \tag{2.8}$$

where μ_j and γ_j are constant parameters, with $j \in \{1, 2, 3\}$. The underlying expression in (2.8) was reported capable of capturing the initially-stiff behavior of the material at high strain rates, without oscillating in the range of large deformations by Hoo Fatt and Ouyang (2008). Substituting (2.8) into (2.7) yields the corresponding Cauchy stress in each component

$$\boldsymbol{\sigma}_j = 2\mu_j\gamma_j \left(I_{b_j} - 3\right)^{\gamma_j - 1} \mathbf{b}_j - p_j\mathbf{I}. \tag{2.9}$$

2.5 Characterization of the non-permanent links

For simplicity, scalar activation and breaking criteria are retained for the non-permanent links: letting $s(\mathbf{F}_1)$ be a scalar function of the global deformation gradient $\mathbf{F}_1$, each link is activated when $s(\mathbf{F}_1)$ reaches its activation threshold s_a and breaks when $s(\mathbf{F}_1)$ exceeds its breaking threshold $s_b \geq s_a$. The active range of a non-permanent link is therefore characterized by the following expression

$$s_a = s(\mathbf{F}_1 = \mathbf{F}_a) \leq s(\mathbf{F}_1) \leq s(\mathbf{F}_1 = \mathbf{F}_b) = s_b, \tag{2.10}$$

where $\mathbf{F}_a$ and $\mathbf{F}_b$ correspond to the values taken by $\mathbf{F}_1$ when $s(\mathbf{F}_1) = s_a$ and $s(\mathbf{F}_1) = s_b$, respectively. Referring back to equation (2.2), the elastic deformation incurred by an active link is characterized by the partial deformation gradient $\mathbf{F}_3 = \mathbf{F}_1\mathbf{F}_a^{-1}$.

It is further assumed (see De Tommasi et al., 2006) that all the breakable links are active in a range of deformation of constant amplitude δs. Consequently, $s_b = s_a - \delta_s$ and only a marginal distribution needs to be defined for s_a. Figure 2.4 shows the proportions of active and broken links deduced from a generic probability density function $p(s_a)$ of the activation threshold: s_M is the maximum value taken by $s(\mathbf{F}_1)$

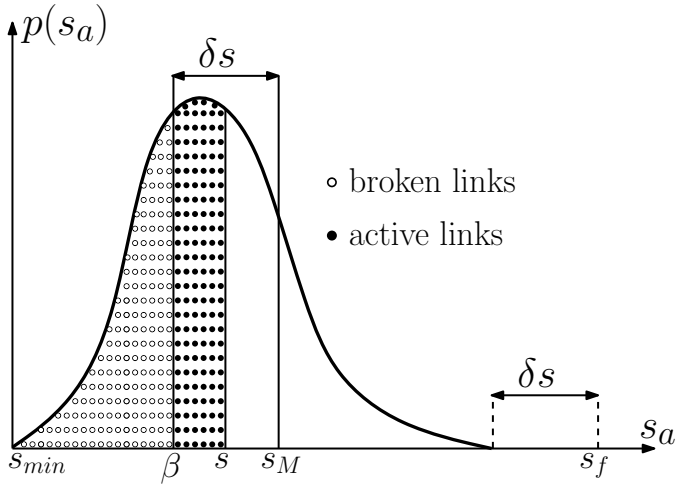

FIGURE 2.4: PDF of the activation threshold.

in the material's loading history, while s_f is the value of $s(\mathbf{F}_1)$ corresponding to the observed failure.

Consistently with the form of hyperelastic potentials in expression (2.8) of Section 2.4.2, a first-invariant-dependent measure of the state of the non-permanent links ③ is retained

$$I_a \leq s(\mathbf{F}_1) = I_{b_1} \leq I_a + \delta I. \tag{2.11}$$

The above choice is supported by a recent analysis conducted by Machado et al. (2010) on existing isotropic models for the Mullins effect, showing that the first invariant of strain is a good measure of stress-softening.

2.6 Global response

Components ①, ② and ③ of the proposed model (Figure 2.1) contribute additively, in terms of internal energy and stress, to the global material response. The total stored energy density U and Cauchy stress $\boldsymbol{\sigma}$ are given by

$$U = U_1 + U_2 + \bar{U}_3, \tag{2.12}$$

$$\boldsymbol{\sigma} = \boldsymbol{\sigma}_1 + \boldsymbol{\sigma}_2 + \bar{\boldsymbol{\sigma}}_3. \tag{2.13}$$

where $\bar{U}_3$ and $\bar{\boldsymbol{\sigma}}_3$ correspond to the total contributions of the active links of type ③, obtained following De Tommasi et al. (2006) by integration over the active range $[\beta, s]$ (see Figure 2.4), with $\beta = \min\{s, \max\{s_{min}, \max\{s, s_M\} - \delta s\}\}$, i.e.

$$\bar{U}_3 = \int_{\beta}^{s} U_3 p(s_a) ds_a, \tag{2.14}$$

$$\bar{\boldsymbol{\sigma}}_3 = \int_{\beta}^{s} \boldsymbol{\sigma}_3 p(s_a) ds_a. \tag{2.15}$$

2.7 Identification of model parameters

A feasible procedure is sought to determine the model parameters from simple uniaxial tension tests. In addition to the unknown probability density function $p(s_a)$ of the activation threshold for the links of type ③, relevant parameters are: η, δs, μ_j and γ_j for $j \in \{1, 2, 3\}$. In isochoric uniaxial tension, the generic deformation gradient $\mathbf{F}_j$ writes

$$\mathbf{F}_j = \begin{bmatrix} \lambda_j & 0 & 0 \\ 0 & \frac{1}{\sqrt{\lambda_j}} & 0 \\ 0 & 0 & \frac{1}{\sqrt{\lambda_j}} \end{bmatrix}, \tag{2.16}$$

where λ_j is the principal stretch in the direction of the applied traction σ_j. Substituting expression (2.16) into equation (2.9) and eliminating the pressure term p_j yields the generic scalar expression for σ_j

$$\sigma_j = 2\mu_j\gamma_j \left(\lambda_j^2 - \frac{1}{\lambda_j}\right) \left(I_{b_j} - 3\right)^{(\gamma_j - 1)}, \tag{2.17}$$

where I_{b_j} and λ_j are in one to one correspondence, since $I_{b_j} = \lambda_j^2 + 2/\lambda_j$ increases monotonically with the stretch $\lambda_j \geq 1$.

2.7.1 Low strain rate response

The material's quasi-static behavior is first examined in order to determine the parameters characterizing the distribution of activable links of type ③. When defor-

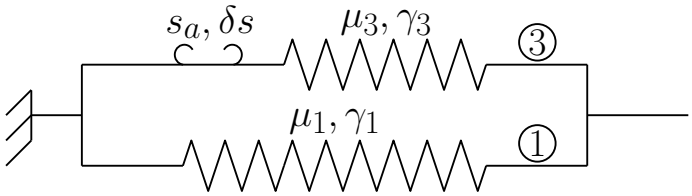

FIGURE 2.5: Reduced model at low strain rate.

mation occurs at a sufficiently low strain rate, the hyper-viscoelastic component ② flows while remaining fully relaxed. As shown in Figure 2.5, the conceptual representation corresponding to this case reduces to branches ① and ③ of the prototypical model.

To simplify notations, let $\lambda = \lambda_1$ and $I(\lambda) = I_{b_1}(\lambda)$. A virgin dumbbell-shaped sample of rubber is loaded and unloaded, at a sufficiently low constant strain rate, up to increasing values of the maximum stretch λ_M corresponding to $I_M = I(\lambda_M)$. This may be done following the increasing triangular strain-history profile shown in Figure 2.11(a) while keeping strain amplitudes globally small. As may be seen on Figure 2.6, the parameter δI defines the global elastic range of the virgin material and may hence be determined from the value λ_M^* of the maximum stretch for which the unloading path differs from the primary loading curve: $\delta I = I_M^* = I(\lambda_M^*)$.

Referring back to Figure 2.4, with $s = I$ and $\beta = \min\{I, \max\{I_{min}, \max\{I, I_M\} - \delta I\}\}$, equations (2.13) and (2.15) can be specialized to uniaxial extension, in the absence of component ② (i.e. $\sigma_2 = 0$), as follows

$$\sigma(\lambda) = \sigma_1(\lambda) + \bar{\sigma}_3(\lambda), \tag{2.18}$$

$$\bar{\sigma}_3(\lambda) = \int_\beta^I \sigma_3 \left(\frac{\lambda(I)}{\lambda(I_a)} \right) p(I_a) dI_a. \tag{2.19}$$

Figure 2.7 illustrates equation (2.18) in relation to the Mullins effect (e.g. Diani et al., 2009; Mullins, 1969), i.e. the softening incurred by a virgin sample of rubber-like material upon deformation. The Cauchy stress σ_3 appears in equation (2.19) as a

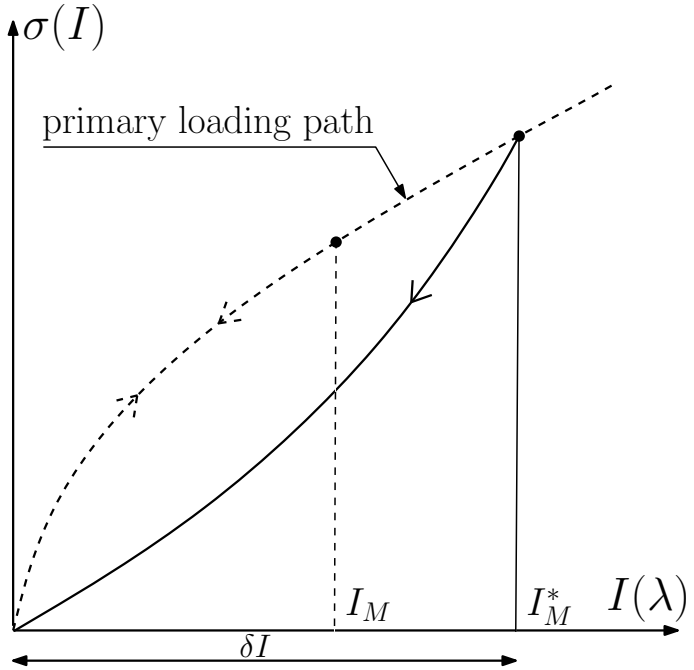

FIGURE 2.6: δI corresponds to the global elastic range of the virgin material.

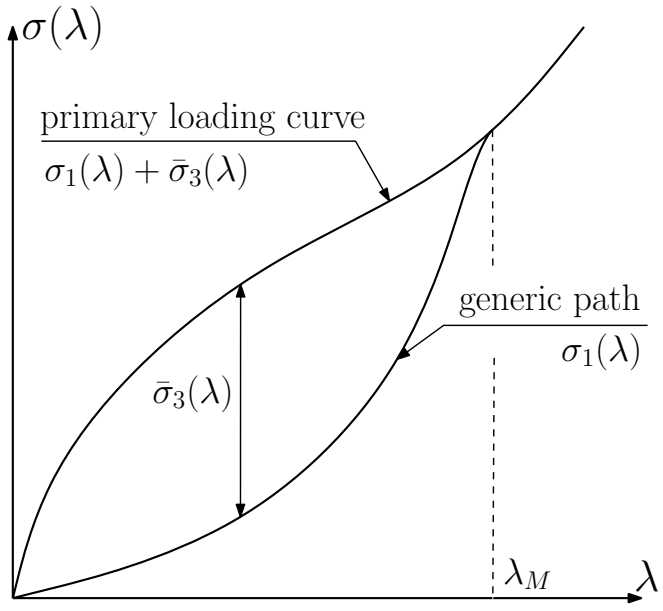

FIGURE 2.7: Illustration of material softening at low strain rate: $\sigma(\lambda) = \sigma_1(\lambda) + \bar{\sigma}_3(\lambda)$.

function of the ratio $\lambda(I)/\lambda(I_a)$ which corresponds to the one-dimensional formulation of the multiplicative decomposition applicable to links of type ③ and described in Figure 2.3. By differentiating equations (2.18) and (2.19) with respect to λ, using Leibniz's rule, it can be shown that the probability density function of the activation threshold can be expressed as

$$p(I_a) = \frac{g\left(\lambda\left(I_a + \delta I\right)\right)}{\sigma_3\left(\frac{\lambda(I_a+\delta I)}{\lambda(I_a)}\right)}, \tag{2.20}$$

where $g(\lambda)$ can be interpolated from measured values of the slope $d\sigma/d\lambda$ at various λ_M along the primary loading curve (L) and the unloading path (U), as illustrated in Figure 2.8

$$g(\lambda_M) = \frac{\lambda_M^2}{(2\lambda_M^3 - 1)}\left(\left.\frac{d\sigma}{d\lambda}\right|_{\lambda_M}^{U} - \left.\frac{d\sigma}{d\lambda}\right|_{\lambda_M}^{L}\right). \tag{2.21}$$

For this purpose, the increasing sawtooth strain-history profile shown in Figure 2.11(b) may be applied at a very low strain rate, to a virgin sample of material, until rupture is reached.

Substituting equation (2.20) into (2.19) and then (2.19) into (2.18), the latter may be written as

$$\int_{I-\delta I}^{I} h\left(\lambda, I_a, \gamma_3\right) dI_a = \sigma(\lambda) - \sigma_1(\lambda), \tag{2.22}$$

where the quantity on the right-hand-side can be deduced from the measured data (see Figure 2.7). The parameter μ_3 simplifies in the expression of $h\left(\lambda, I_a, \gamma_3\right)$, which is given by the ratio

$$\frac{h\left(\lambda, I_a, \gamma_3\right)}{g\left(\lambda\left(I_a + \delta I\right)\right)} = \frac{\sigma_3\left(\frac{\lambda(I)}{\lambda(I_a)}\right)}{\sigma_3\left(\frac{\lambda(I_a+\delta I)}{\lambda(I_a)}\right)}. \tag{2.23}$$

The parameter γ_3 can be obtained from equation (2.22) by prediction error minimization. Once γ_3 is known, equation (2.20) can be normalized such that $\int_0^{I_f-\delta I} p(I_a) dI_a =$

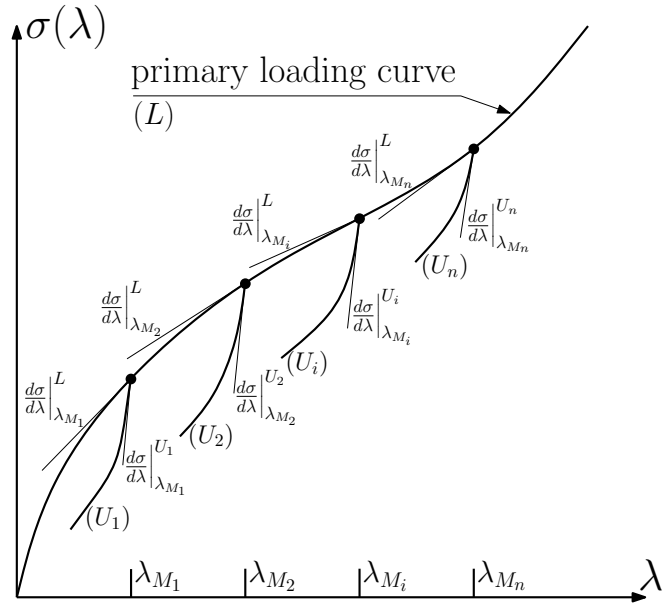

FIGURE 2.8: Determining data points $(\lambda_{M_i}, g(\lambda_{M_i}))$.

1 which yields the parameter μ_3.

It may hence be concluded that all the parameters characterizing the distribution of activable links of type ③, including the probability density function of their activation threshold, can be determined by performing a multistage uniaxial tension test, at low strain rate, on a sample of virgin rubber. It remains to determine the parameters governing the behavior of the links of type ① and ②, which is precisely the goal of the following section.

2.7.2 Repeatable response

In this section, we consider the constitutive behavior of the non-virgin material in a range of deformation such that all remaining non-permanent links of type ③ are kept below their activation threshold. As shown in Figure 2.9 the conceptual representation corresponding to this case reduces to branches ① and ② of the prototypical model.

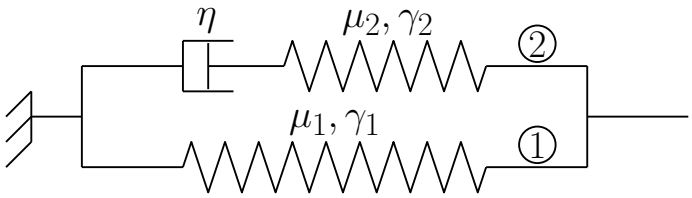

FIGURE 2.9: Reduced model in the repeatable range.

Nonlinear hyper-viscoelastic formulation

With $j \in \{1, 2, v\}$, let $\mathbf{C}_j = \mathbf{F}_j^T \mathbf{F}_j$ and $\mathbf{b}_j = \mathbf{F}_j \mathbf{F}_j^T$ be right and left Cauchy-Green deformation tensors and denote by $\mathbf{E}_j$ and $\mathbf{e}_j$ the corresponding Green and Almansi strain tensors, respectively. Furthermore, let $\mathbf{T}$ and $\mathbf{\Gamma}$ be intermediate measures of the global stress and strain, i.e.

$$\mathbf{T} = \mathbf{F}_v \mathbf{S} \mathbf{F}_v^T = \mathbf{F}_2^{-1} \boldsymbol{\sigma} \mathbf{F}_2^{-T}, \tag{2.24}$$

$$\mathbf{\Gamma} = \mathbf{F}_v^{-T} \mathbf{E}_1 \mathbf{F}_v^{-1} = \mathbf{F}_2^T \mathbf{e}_1 \mathbf{F}_2. \tag{2.25}$$

The tensors $\mathbf{S}$ and $\boldsymbol{\sigma}$ in expression (2.24) correspond to measures of the global stress in the reference and current configurations respectively. Alternatively, $\mathbf{\Gamma}$ may be written as

$$\mathbf{\Gamma} = \frac{1}{2}\left(\mathbf{F}_2^T \mathbf{F}_2 - \mathbf{I}\right) + \frac{1}{2}\left(\mathbf{I} - \mathbf{F}_v^{-T} \mathbf{F}_v^{-1}\right) = \mathbf{E}_2 + \mathbf{e}_v, \tag{2.26}$$

where $\mathbf{E}_2$ and $\mathbf{e}_v$ are seen as intermediate measures of strain associated with the hyperelastic and viscous parts of component ②, respectively. Differentiating (2.26) with respect to time yields the relationship between the corresponding strain rates

$$\dot{\mathbf{\Gamma}} = \dot{\mathbf{E}}_2 + \dot{\mathbf{E}}_v. \tag{2.27}$$

The Lie derivative $\hat{\mathbf{\Gamma}}$ of $\mathbf{\Gamma}$ corresponds to the push-forward of $\dot{\mathbf{E}}_1$ to the intermediate frame, i.e.

$$\hat{\mathbf{\Gamma}} \triangleq \mathbf{F}_v^{-T} \dot{\mathbf{E}}_1 \mathbf{F}_v^{-1} = \dot{\mathbf{\Gamma}} + \mathbf{l}_v^T \mathbf{\Gamma} + \mathbf{\Gamma} \mathbf{l}_v, \tag{2.28}$$

where $\mathbf{l}_v$ is the velocity gradient in the intermediate system of coordinates $\mathbf{x}_v$, i.e.

$$\mathbf{l}_v \triangleq \frac{\partial \mathbf{v}}{\partial \mathbf{x}_v} = \dot{\mathbf{F}}_v \mathbf{F}_v^{-1}. \tag{2.29}$$

Let $\mathcal{D}_{int}$ be the internal power dissipation due to the viscous effects. The second law of thermodynamics may be expressed pointwise, in the reference frame, by means of the Clausius-Planck inequality (e.g. Holzapfel, 2000)

$$\mathcal{D}_{int} = \mathbf{S}\!:\!\dot{\mathbf{E}}_1 - \dot{U} - \mathcal{S}\dot{\Theta} \geq 0, \tag{2.30}$$

where $\mathcal{S}$ is the entropy density, $\dot{\Theta}$ denotes the rate of change in temperature and $\dot{U}$ corresponds to the rate of change in free energy density. Assuming a constant temperature, inequality (2.30) specializes into

$$\mathcal{D}_{int} = \mathbf{S}\!:\!\dot{\mathbf{E}}_1 - \dot{U} \geq 0. \tag{2.31}$$

Expression (2.31) may be pushed forward to the intermediate frame as

$$\mathbf{T}\!:\!\hat{\mathbf{\Gamma}} - \dot{U} \geq 0. \tag{2.32}$$

The total Helmholtz free energy density U is then written as the sum of the energy densities stored in the hyperelastic portions of components ① and ②, each depending on the appropriate measure of strain

$$U = U_1(\mathbf{E}_1) + U_2(\mathbf{E}_2). \tag{2.33}$$

The rates of change of U_1 and U_2 may now be expressed as follows

$$\dot{U}_1 = \frac{\partial U_1}{\partial \mathbf{E}_1}\!:\!\dot{\mathbf{E}}_1, \tag{2.34}$$

$$\dot{U}_2 = \frac{\partial U_2}{\partial \mathbf{E}_2}\!:\!\dot{\mathbf{E}}_2. \tag{2.35}$$

Inverting equation (2.28) for $\dot{\mathbf{E}}_1$ and substituting into equation (2.34) yields the rate of change in $\dot{U}_1$ as

$$\dot{U}_1 = \left(\mathbf{F}_v \frac{\partial U_1}{\partial \mathbf{E}_1} \mathbf{F}_v^T \right) : \hat{\mathbf{\Gamma}}. \tag{2.36}$$

On the other hand, manipulating equations (2.27) and (2.28) it can be shown that $\dot{\mathbf{E}}_2$ satisfies

$$\dot{\mathbf{E}}_2 = \hat{\mathbf{\Gamma}} - \mathbf{d}_v - \mathbf{l}_v^T \mathbf{E}_2 - \mathbf{E}_2 \mathbf{l}_v, \tag{2.37}$$

where $\mathbf{d}_v$ is the rate of deformation of the viscous component in ②

$$\mathbf{d}_v = \frac{1}{2} \left(\mathbf{l}_v + \mathbf{l}_v^T \right) = \dot{\mathbf{E}}_v + \mathbf{l}_v^T \mathbf{e}_v + \mathbf{e}_v \mathbf{l}_v. \tag{2.38}$$

Comparing the right-hand-sides of expressions (2.28) and (2.38) shows that $\mathbf{d}_v$ is the Lie derivative of $\mathbf{e}_v$. Plugging equation (2.38) into (2.37) and then (2.37) into (2.35) yields the rate of change in $\dot{U}_2$ as

$$\dot{U}_2 = \frac{\partial U_2}{\partial \mathbf{E}_2} : \hat{\mathbf{\Gamma}} - \left(\mathbf{C}_2 \frac{\partial U_2}{\partial \mathbf{E}_2} \right) : \mathbf{d}_v, \tag{2.39}$$

where, in the case of an isotropic material, the Mendel stress ($\mathbf{C}_2 \partial U_2 / \partial \mathbf{E}_2$) is symmetric. Defining intermediate measures of partial stress in components ① and ② respectively as

$$\mathbf{T}_1 = \mathbf{F}_v \frac{\partial U_1}{\partial \mathbf{E}_1} \mathbf{F}_v^T \quad \text{and} \quad \mathbf{T}_2 = \frac{\partial U_2}{\partial \mathbf{E}_2}, \tag{2.40}$$

then substituting equation (2.36) and (2.39) into (2.32) yields the following inequality (e.g. Hoo Fatt and Ouyang, 2008; Huber and Tsakmakis, 2000)

$$\mathcal{D}_{int} = \left[\mathbf{T} - (\mathbf{T}_1 + \mathbf{T}_2) \right] : \hat{\mathbf{\Gamma}} + \left[\mathbf{C}_2 \mathbf{T}_2 \right] : \mathbf{d}_v \geq 0, \tag{2.41}$$

where the history of the global deformation gradient $\mathbf{F}_1$, and hence the tensorial quantity $\hat{\mathbf{\Gamma}}$, can be chosen arbitrarily. A standard procedure due to Coleman and Noll (1963); Coleman and Gurtin (1967) is applied to satisfy inequality (2.41):

- In the particular case where the rate of deformation of the viscous component is equal to zero (i.e. $\mathbf{d}_v = \mathbf{0}$), the transformation process is reversible and inequality (2.41) reduces to

$$\mathcal{D}_{int} = [\mathbf{T} - (\mathbf{T}_1 + \mathbf{T}_2)] : \hat{\mathbf{\Gamma}} = 0. \tag{2.42}$$

  Equality (2.42) is satisfied for every choice of $\mathbf{F}_1$ if and only if

$$\mathbf{T} = \mathbf{T}_1 + \mathbf{T}_2 \quad \Longleftrightarrow \quad \boldsymbol{\sigma} = \boldsymbol{\sigma}_1 + \boldsymbol{\sigma}_2. \tag{2.43}$$

- Assuming that local equilibrium (2.43) is satisfied in the general case where $\mathbf{d}_v \neq \mathbf{0}$, expression (2.41) reduces to

$$(\mathbf{C}_2\mathbf{T}_2) : \mathbf{d}_v \geq 0. \tag{2.44}$$

It is noteworthy that inequality (2.44) is independent of the choice of intermediate configuration. For an isotropic material, the "Mandel" stress tensor $\mathbf{C}_2\mathbf{T}_2$ is symmetric. The following evolution law was proposed by Huber and Tsakmakis (2000) as a simple condition that satisfies inequality (2.44)

$$\mathbf{d}_v = \frac{1}{\eta} (\mathbf{C}_2\mathbf{T}_2)^d , \tag{2.45}$$

where the superscript $(.)^d$ denotes a deviatoric component. Using (2.45) and denoting the velocity gradients by $\mathbf{l}_j = \dot{\mathbf{F}}_j \mathbf{F}_j^{-1}$, it can be shown that

$$\dot{\mathbf{b}}_2 = \mathbf{l}_1\mathbf{b}_2 + \mathbf{b}_2\mathbf{l}_1^T - \frac{2}{\eta}\mathbf{b}_2\boldsymbol{\sigma}_2^d. \tag{2.46}$$

Practical subsystem identification (saturation method)

Following a procedure proposed by Hoo Fatt and Ouyang (2008), the parameters μ_1 and γ_1 can be determined first by a nonlinear regression analysis based on equation

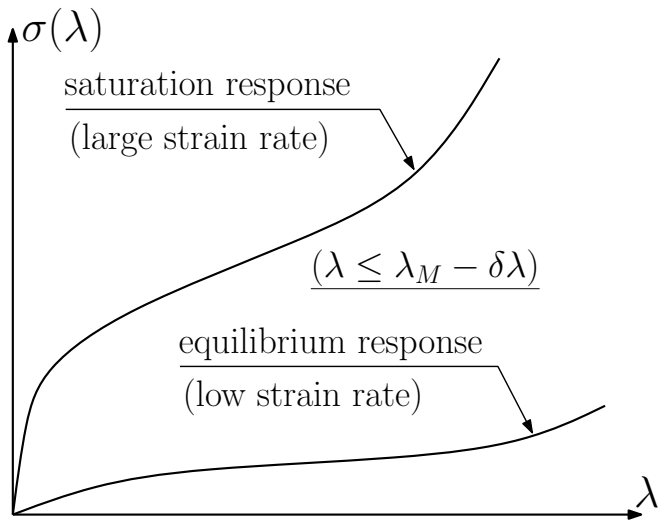

FIGURE 2.10: The material's repeatable response lives between the equilibrium curve and the saturation curve.

(2.17) with $j = 1$. The corresponding equilibrium response σ_1 (see Figure 2.10) is obtained by loading a non-virgin material sample in uniaxial extension at a suitably low constant strain rate (ramp-up) and holding it at increasing values of constant strain (plateau) to allow for relaxation of the overstress σ_2 in component ②. This combined constant strain rate and incremental stress relaxation test is illustrated in Figure 2.11(c). Intervals of constant strain must be adjusted according to the material's relaxation spectrum.

The subsystem in Figure 2.9 may be further identified using monotonic strain-history profiles of (preferably) constant strain rates (see Figure 2.11(d)). Subjecting the sample to a sufficiently high strain rate will induce locking of the viscous component (i.e. $\lambda_v = 0$) and yield the saturation response σ_{sat} (see Figure 2.10) corresponding to $\lambda_1 = \lambda_2 = \lambda$. A nonlinear regression analysis based on equation (2.17) with $\sigma_{sat} = \sigma_1(\lambda) + \sigma_2(\lambda)$ determines the parameters μ_2 and γ_2. The remaining parameter η can be determined at any intermediate elongation rate $\dot{\lambda}_1$ from equation

(2.46) which, in uniaxial tension writes

$$\eta = \frac{2\lambda_1\lambda_2\sigma_2}{3\left(\dot{\lambda}_1\lambda_2 - \lambda_1\dot{\lambda}_2\right)}. \tag{2.47}$$

The viscosity η may show to be practically constant. Conversely, as reported for instance by Hoo Fatt and Ouyang (2008) for Styrene Butadiene, viscosity may be governed by deformation. In the latter case, the dependences on deformation amplitude and rate can be characterized using the state variables I_{b_1} and I_{b_2} respectively: proposed analytical expressions of $\eta\left(I_{b_1}, I_{b_2}\right)$ may be fitted to the observed results using nonlinear regression analysis.

Practical subsystem identification (PEM method)

The methodology described in Section 2.7.2 relies on an ability to achieve sufficiently high (constant) strain rates, in order to provoke saturation of the viscous component. Practically obtainable rates using commercially available servohydraulic test machines are limited. Higher rates in traction can be acheived with specifically-designed testing apparatus like the modified Charpy impact machine described by Hoo Fatt and Ouyang (2008) or the falling weight apparatus proposed by Roland (2006).

In case technical difficulties are encountered in this regard, one alternative approach would be to determine the parameters of components ① and ② simultaneously, by prediction error minimization (PEM) with respect to the repeatable behavior, as observed within the range of achievable strain rates. Indeed, expressions for the overstress σ_2 resulting from equations (2.17) and (2.47) may be equated to obtain a nonlinear ordinary differential equation (ODE) in the elastic component of the stretch $\lambda_2(t)$ in branch ②. For the purpose of numerical computations, a convenient

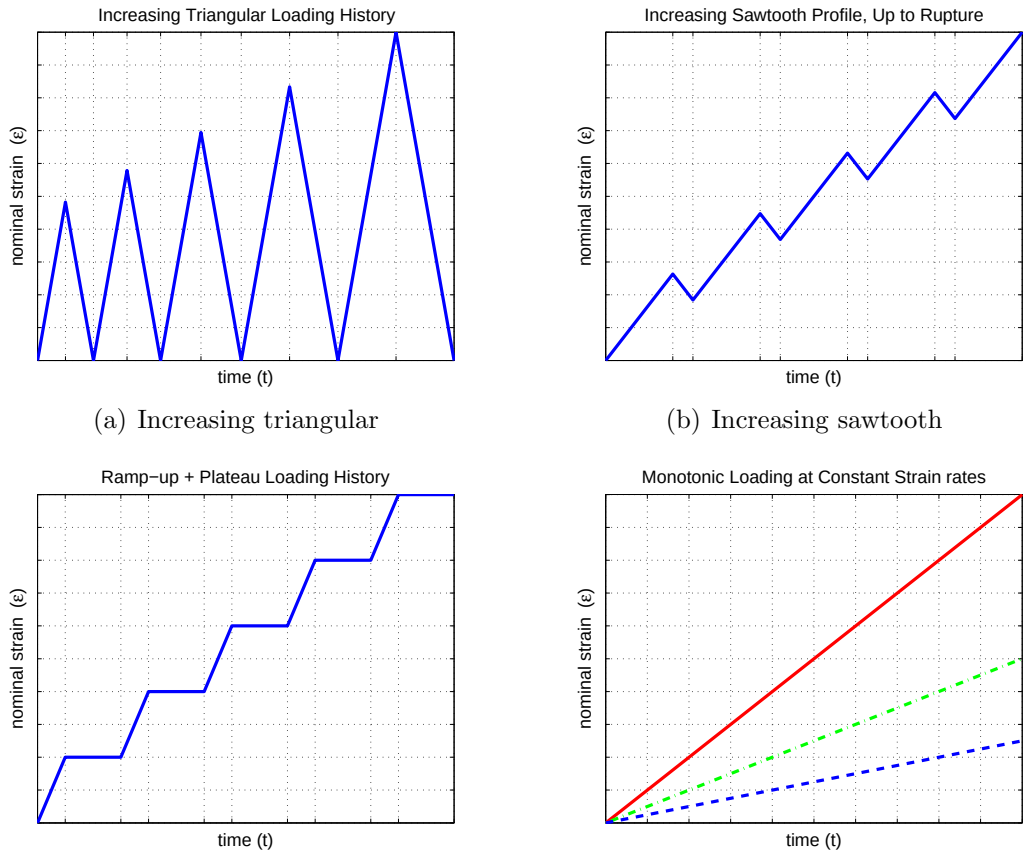

(a) Increasing triangular

(b) Increasing sawtooth

(c) Ramp-up + plateau

(d) Constant strain rates

FIGURE 2.11: Examples of strain-history profiles suitable for material characterization in uniaxial extension.

ODE formulation is obtained in terms of the proxy variable $y = \lambda_1/\lambda_2$, i.e.

$$\frac{dy}{dt} = \frac{2y}{3\eta}\sigma_2\left(\frac{\lambda_1}{y}\right). \tag{2.48}$$

Given a global stretch history $\lambda_1(t) = \lambda(t)$, the aforementioned ODE can be solved for $\lambda_2(t)$ using current iterates for the model's parameters. The predicted history of the total stress $\sigma(t)$ is obtained by adding its two components evaluated using expressions ((2.17) with $j \in \{1, 2\}$) and compared, at each iteration, to the observed response.

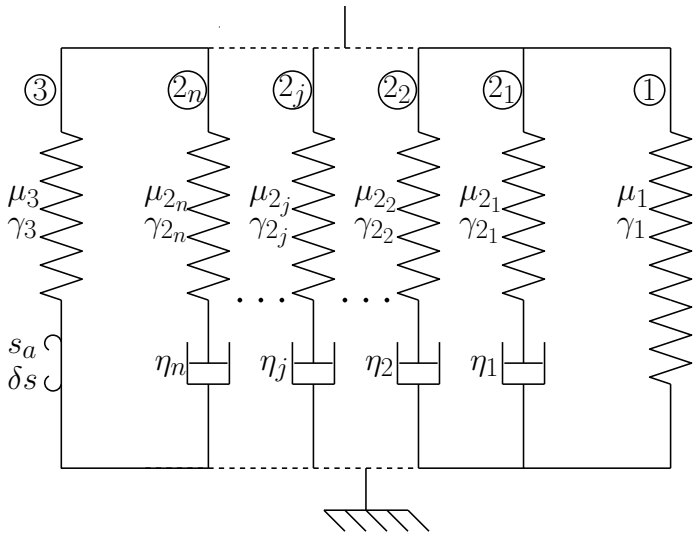

FIGURE 2.12: Generalized model comprising multiple nonlinear hyper-viscoelastic Maxwell elements.

2.8 Generalized model

The prototypical model shown in Figure 2.1 can be generalized further to include a number $n \geq 1$ of nonlinear hyper-viscoelastic Maxwell elements of type ②, as shown in Figure 2.12. The procedure described in Section 2.7.1 for characterizing the low strain rate response remains unchanged. However, for $n > 1$, the saturation method of Section 2.7.2 cannot be applied to identify the repeatable behavior. A generalized version of the alternative method based on prediction error minimization (see Section 2.7.2) may be used instead.

The i^{th} type ② Maxwell element ($1 \leq i \leq n$) is characterized by a viscosity η_i and a free energy density $U_{2,i}$. It is further associated with a proper intermediate configuration $\mathcal{I}_i$ and the corresponding multiplicative decomposition

$$\mathbf{F}_1 = \mathbf{F}_{2,i}\mathbf{F}_{v,i}. \tag{2.49}$$

Following a similar derivation to the one presented in Section 2.7.2, it can be shown

that inequality (2.41) generalizes into a set of n equivalent inequalities of the form

$$\left[\mathbf{T}^i - \left(\mathbf{T}_1^i + \sum_{j=1}^{n} \mathbf{T}_{2,j}^i\right)\right] : \hat{\mathbf{\Gamma}}^i + \sum_{j=1}^{n} \left(\mathbf{C}_{2,j}\mathbf{T}_{2,j}^j\right) : \mathbf{d}_{v,j} \geq 0, \tag{2.50}$$

where the partial stress $\mathbf{T}_{2,j}^i$ in the j^{th} hyperelastic component and the total stress $\mathbf{T}^i$ are expressed in $\mathcal{I}_i$. The quantity $\hat{\mathbf{\Gamma}}^i$ corresponds to the Lie derivative of the i^{th} intermediate measure of global strain and $\mathbf{d}_{v,j}$ denotes the rate of deformation of the j^{th} viscous component, expressed in $\mathcal{I}_j$. Following the Coleman-Noll procedure, expression (2.50) reveals the general additivity of partial stresses, i.e.

$$\mathbf{T}^i = \mathbf{T}_1^i + \sum_{j=1}^{n} \mathbf{T}_{2,j}^i \ (\forall j) \iff \boldsymbol{\sigma} = \boldsymbol{\sigma}_1 + \sum_{j=1}^{n} \boldsymbol{\sigma}_{2,j}, \tag{2.51}$$

as well as a generalized dissipation inequality:

$$\mathcal{D}_{int} = \sum_{j=1}^{n} \left(\mathbf{C}_{2,j}\mathbf{T}_{2,j}^j\right) : \mathbf{d}_{v,j} \geq 0. \tag{2.52}$$

Inequality (2.52) can be satisfied simply, by retaining for the n viscous components, uncoupled evolution laws of the form given by expression (2.45), i.e.

$$\mathbf{d}_{v,j} = \frac{1}{\eta_j}\left(\mathbf{C}_{2,j}\mathbf{T}_{2,j}^j\right)^d. \tag{2.53}$$

Using the laws in (2.53), expressions (2.46), (2.47) and (2.48) can be generalized to the j^{th} component of type ② as follows

$$\dot{\mathbf{b}}_{2,j} = \mathbf{l}_1\mathbf{b}_{2,j} + \mathbf{b}_{2,j}\mathbf{l}_1^T - \frac{2}{\eta_j}\mathbf{b}_{2,j}\boldsymbol{\sigma}_{2,j}^d, \tag{2.54}$$

$$\eta_j = \frac{2\lambda_1\lambda_{2,j}\sigma_{2,j}}{3\left(\dot{\lambda}_1\lambda_{2,j} - \lambda_1\dot{\lambda}_{2,j}\right)}, \tag{2.55}$$

$$\frac{dy_j}{dt} = \frac{2y_j}{3\eta_j}\sigma_{2,j}\left(\frac{\lambda_1}{y_j}\right). \tag{2.56}$$

In a stretch-driven uniaxial extension test, the global stretch history $\lambda_1(t) = \lambda(t)$ is known. Assuming an initial guess for the parameters characterizing component ① and the components of type ②, the n uncoupled ODE's given by expression (2.56) can be solved for the elastic portions $\lambda_{2,i}(t)$ of the stretch in each Maxwell element. The partial stress in each hyperelastic component can be determined from its constitutive equation, i.e. equation (2.17) in the present case. A predicted history of the total stress $\boldsymbol{\sigma}(t)$ is obtained by summation according to expression (2.51). The difference between the predicted response and the observed response can be minimized by iterating on the model's parameters.

2.9 Mullins effect induced anisotropy

2.9.1 A brief overview

Based on considerations of material symmetry, but also on the implicit assumption of a directional network alteration (as opposed to an isotropic one), Horgan et al. (2004) argue that the damage associated with the Mullins effect is inherently anisotropic and briefly discuss a tensorial approach to account for this anisotropy. Experimental data (e.g. Dargazany and Itskov, 2009; Diani et al., 2006; Dorfmann and Pancheri, 2012; Itskov et al., 2006; Machado et al., 2012) confirm that stress softening introduces some anisotropy in the material response. Diani et al. (2006) and Dargazany and Itskov (2009) present micromechanical directional models to handle softening induced anisotropy. The potential of several finite-directional models in reflecting the behavioral anisotropy induced by the Mullins effect in initially isotropic hyperelastic materials is tested by Gillibert et al. (2010), based on the models' initial anisotropy and their ability to replicate the behavior of a full (i.e. infinite-directional) network. Dorfmann and Pancheri (2012) build on the tensorial approach outlined by Horgan et al. (2004) and derive a simple phenomenological model accounting for stress softening and changes in material symmetry. The model applies, in its current form,

to pure homogeneous deformations; however, it may be extended to more general loading conditions by the addition of an evolution law.

2.9.2 Outline of model extension

The formulation characterizing component ③ of the mixed model presented in this chapter can also be extended, in several ways, to handle softening induced anisotropy. A possible directional approach, preserving the form of stored energy density given by equation (2.8), with $j = 3$, as well as the scalar measure of the active range specified in expression (2.11), is outlined hereafter.

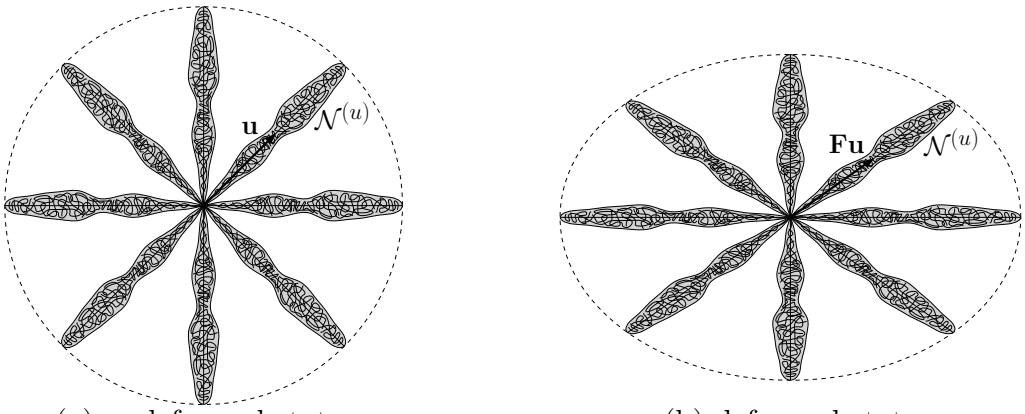

(a) undeformed state (b) deformed state

FIGURE 2.13: Deformation of component ③, seen as a collection of incompressible, elongated, directional networks $\mathcal{N}^{(u)}$.

To this end, component ③ can be considered as a collection of incompressible directional networks, as shown in Figure 2.13. Each network $\mathcal{N}^{(u)}$ has an elongated shape; it is oriented in a given direction of unit vector $\mathbf{u}$ and comprises a very large number of activable/breakable links characterized by a distribution of activation thresholds similar to the one illustrated on Figure 2.4. It is further assumed that, under the global deformation gradient $\mathbf{F} = \mathbf{F}_1$, each directional network $\mathcal{N}^{(u)}$ of component ③ softens isotropically while subjected to a uniaxial deformation char-

acterized by the stretch $\lambda^{(u)}$ resulting from $\mathbf{F}$ in direction $\mathbf{u}$, i.e.

$$\lambda^{(u)} = \sqrt{(\mathbf{Fu}) \,.\, (\mathbf{Fu})} = \sqrt{\mathbf{u}^T \mathbf{C} \mathbf{u}}, \tag{2.57}$$

where $\mathbf{C} = \mathbf{F}^T \mathbf{F}$. Under these conditions, the scalar measure of deformation of network $\mathcal{N}^{(u)}$ is given by the quantity $I^{(u)} = {\lambda^{(u)}}^2 + 2/\lambda^{(u)}$. As is usually the case in directional models, the number of spatial directions $\mathcal{N}^{(u)}$ can be finite or infinite. An infinite-directional formulation is outlined below in analytical form, which can be numerically integrated on the surface of a unit sphere, for instance, using sets of collocation directions and weights determined by Bažant and Oh (1986).

The stored energy density and the principal Cauchy stress in the direction of the current unit vector $\mathbf{Fu}/\lambda^{(u)}$, associated with an active link of network $\mathcal{N}^{(u)}$, are given by

$$U_3^{(u)} = \mu_3 \left(I_3^{(u)} - 3 \right)^{\gamma_3} = \mu_3 \left({\lambda_3^{(u)}}^2 + \frac{2}{\lambda_3^{(u)}} - 3 \right)^{\gamma_3}, \tag{2.58}$$

$$\sigma_3^{(u)} = \lambda_3^{(u)} \frac{dU_3^{(u)}}{d\lambda_3^{(u)}} + p_3^{(u)} = 2 \left({\lambda_3^{(u)}}^2 - \frac{1}{\lambda_3^{(u)}} \right) \frac{dU_3^{(u)}}{dI_3^{(u)}} + p_3^{(u)}, \tag{2.59}$$

where $p_3^{(u)}$ is an undetermined pressure term arising from incompressibility. All active links in a given directional network $\mathcal{N}^{(u)}$ contribute additively, in terms of stored energy density and stress, to the elastic response of the network. The latter is hence found by summation over the active range, i.e.

$$\bar{U}_3^{(u)} = \int_{\beta^{(u)}}^{I_3^{(u)}} U_3^{(u)} p(I_a) dI_a, \tag{2.60}$$

$$\boldsymbol{\sigma}_3^{(u)} = \frac{1}{{\lambda^{(u)}}^2} \int_{\beta^{(u)}}^{I_3^{(u)}} \sigma_3^{(u)} p(I_a) dI_a \, (\mathbf{Fu}) \otimes (\mathbf{Fu}). \tag{2.61}$$

Expressions for the total elastic response of component ③ are finally obtained by

integrating equations (2.60) and (2.61) on the surface of a unit sphere $\mathcal{S}$

$$U_3 = \frac{1}{4\pi}\int_{\mathcal{S}}\left(\int_{\beta^{(u)}}^{I_3^{(u)}} U_3^{(u)} p(I_a) dI_a\right) d\mathcal{S}^{(u)}, \tag{2.62}$$

$$\boldsymbol{\sigma}_3 = 2\mathbf{F}\left[\frac{1}{4\pi}\int_{\mathcal{S}}\left(\int_{\beta^{(u)}}^{I_3^{(u)}}\left(1-\frac{1}{{\lambda_3^{(u)}}^3}\right)\frac{dU_3^{(u)}}{dI_3^{(u)}}\frac{p(I_a)}{\lambda\,(I_a)^2} dI_a\,\mathbf{u}\otimes\mathbf{u}\right) d\mathcal{S}^{(u)}\right]\mathbf{F}^T + p_3\mathbf{I}. \tag{2.63}$$

Assuming a suitable analytical expression for $p(I_a)$ in terms of parameters, the anisotropic stress response of component ③ to a given global deformation history $\mathbf{F}(t)$ can be predicted using equation (2.63). Consequently, the model's parameters can be fitted to experimental data by minimizing the prediction error.

2.10 Example

Referring to Figure 2.1, with a single component of type ②, the following set of numerical parameters is chosen to illustrate some aspects of the isotropic model's behavior in uniaxial extension at different strain rates: $\mu_1 = 1.1$ MPa, $\gamma_1 = 0.8$, $\mu_2 = 3.3$ MPa, $\gamma_2 = 1.1$, $\mu_3 = 19.8$ MPa, $\gamma_3 = 0.7$, $\eta = 0.05$ MPa.s and $\delta I = 5$. The activation threshold I_a of the first invariant of global strain is taken to follow the probability density function of a beta distribution, which is bounded (see e.g. Ang and Tang, 2007), i.e.

$$p(I_a) = \frac{1}{\beta(p,q)}\frac{(I_a - I_{a,min})^{p-1}(I_{a,max} - I_a)^{q-1}}{(I_{a,max} - I_{a,min})^{p+q-1}}, \tag{2.64}$$

where $I_a \in [I_{a,min}, I_{a,max}]$ with $I_{a,min} = 3$ and $I_{a,max} = (I_f - \delta I) = 100$. The standard *beta function* appearing in the denominator of expression (2.64) is given by

$$\beta(p,q) = \int_0^1 x^{p-1}(1-x)^{q-1} dx. \tag{2.65}$$

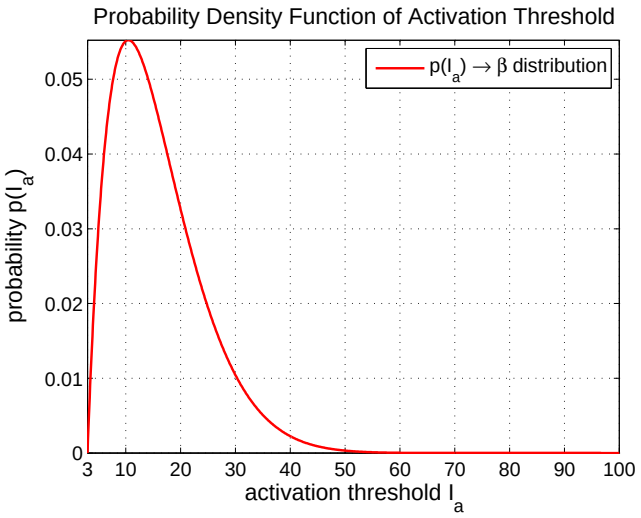

FIGURE 2.14: Assumed probability density function of the activation threshold I_a characterizing the links of type ③: $p\,(I_a)$ follows a β-distribution with $p = 3$, $q = 13$ and $I_a \in [1, 100]$.

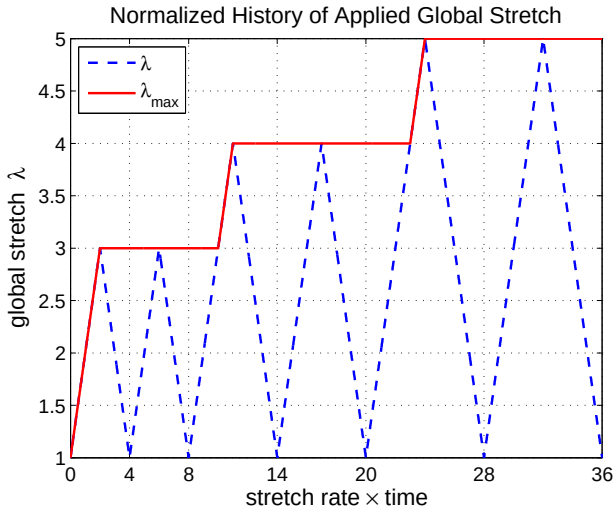

FIGURE 2.15: Virgin models are subjected, in uniaxial extension, to a standardized history of global stretch at different stretch rates: $\dot{\lambda}_1 = 0.1\ \mathrm{s}^{-1}$, $200\ \mathrm{s}^{-1}$ and $600\ \mathrm{s}^{-1}$.

Figure 2.14 shows the probability density function of I_a for $p = 2$ and $q = 13$, which is positively skewed.

The three-component model is subjected, uniaxially, to the normalized history of global stretch defined in Figure 2.15: three sets of two stretch-driven loading cycles are applied to the virgin model, at increasing stretch amplitudes $\lambda_M = 3$, 4 and 5. This virtual experiment is repeated at three different stretch rates $\dot{\lambda}_1 = 0.1$ s^{-1}, 200 s^{-1} and 600 s^{-1}.

The model's response to the lowest stretch rate $\dot{\lambda}_1 = 0.1$ s^{-1} can be seen on the set of plots in Figure 2.16. At this rate, the virtual experiment is performed sufficiently slowly, with respect to the material's internal time-scale, for the viscous subcomponent to flow at nearly the same rate and undertake most of the applied stretch. Consequently, the elastic subcomponent of element ② remains unloaded with $\lambda_2 \approx 0$ and $\sigma_2 \approx 0$. On the other hand, the history of the stress in component ③ is consistent with the deterioration process to which the corresponding links are subjected to. It can be noted for instance that, over each set (i) of two successive loading cycles of same stretch amplitude λ_{M_i}, $\sigma_3(t)$ has a weaker intensity preceding the instant at which the maximum applied stretch λ_{M_i} occurs, and that it follows the same pattern past that point. When subjected to a sufficiently low rate of stretch, the system behaves as the reduced model shown in Figure 2.5 and hence undergoes a pure Mullins effect.

The two sets of plots in Figures 2.17 and 2.18 show the model's behavior at higher stretch rates: $\dot{\lambda}_1 = 200$ s^{-1} and 600 s^{-1} respectively. The responses of components ① and ③ in a stretch-driven experiment are clearly rate-independent. Element ② however, behaves differently: the internal rate of dissipation of its viscous subcomponent being limited, the elastic subcomponent, which responds instantaneously, undertakes larger parts λ_2 of the applied stretch λ_1, at larger stretch rates. Upon unloading, and despite a state of global extension with $\lambda_1 \geq 1$, the delayed viscous response

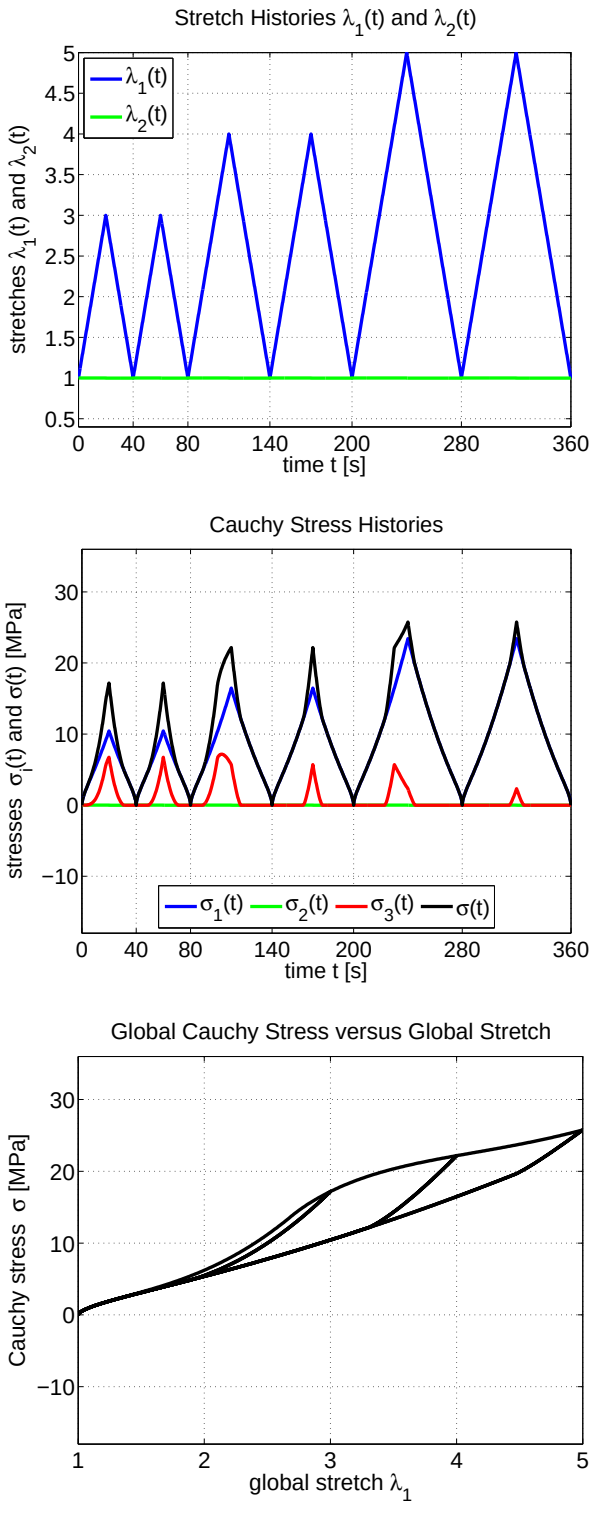

FIGURE 2.16: Model's behavior under the normalized loading, for $\dot{\lambda}_1 = 0.1\ \mathrm{s}^{-1}$.

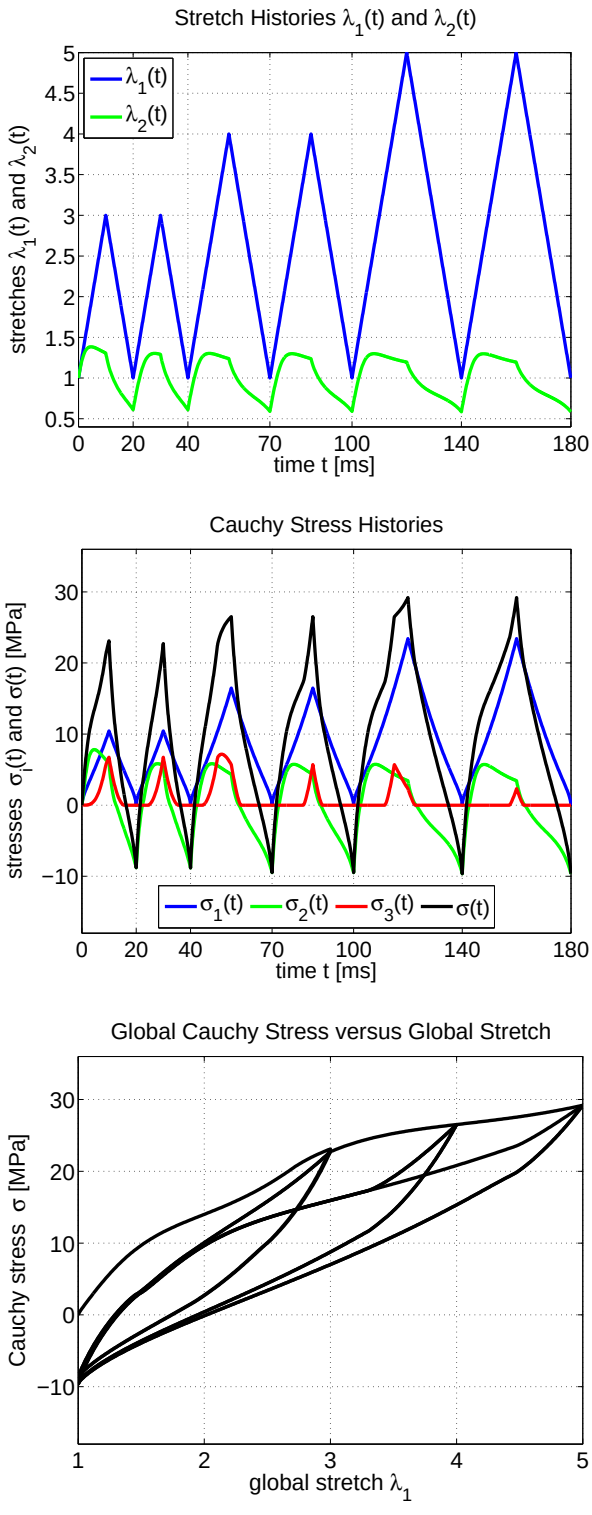

FIGURE 2.17: Model's behavior under the normalized loading, for $\dot{\lambda}_1 = 200\ \mathrm{s}^{-1}$.

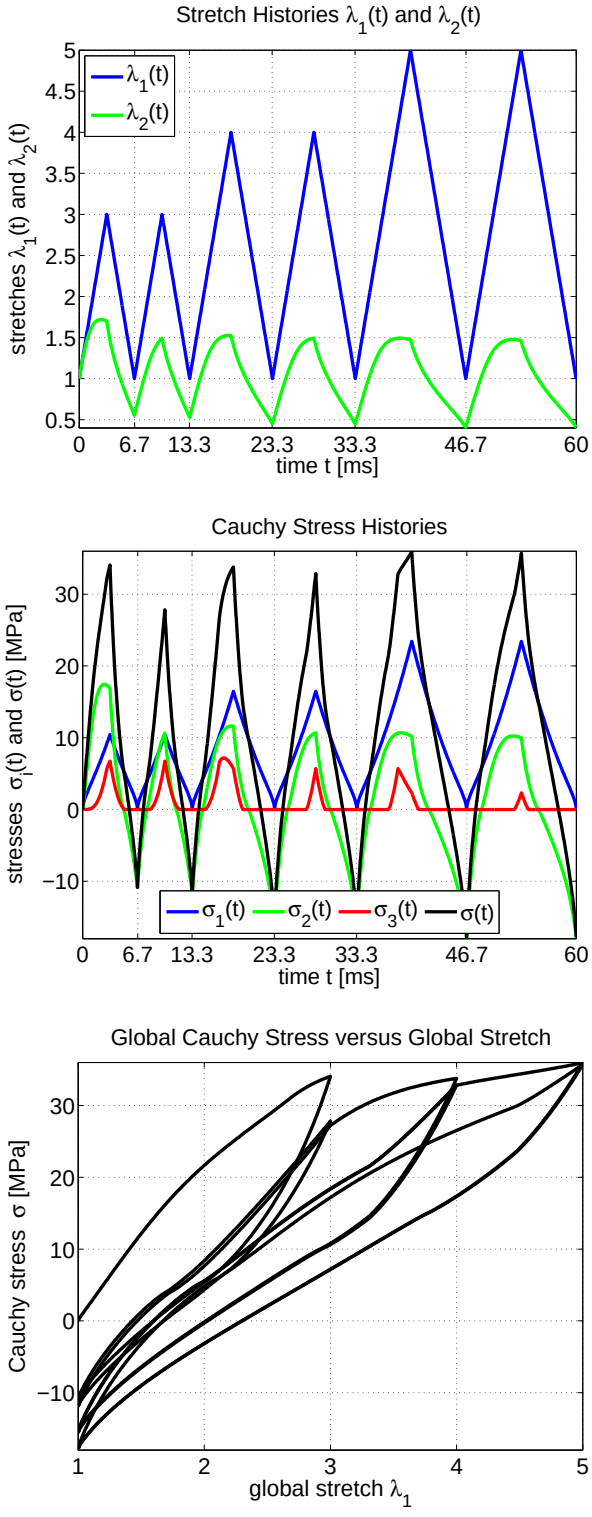

FIGURE 2.18: Model's behavior under the normalized loading, for $\dot{\lambda}_1 = 600\ \mathrm{s}^{-1}$.

results in the compression of component ② with $\lambda_2 \leq 1$ and $\sigma_2 \leq 0$.

Further, it is interesting to note that, at sufficiently high strain rates, the peak in total stress $\sigma(t)$ drops significantly between the first and the second loading cycles. In the present case, this is less apparent in subsequent sets of larger global stretch amplitude. However, the magnitude of such drops can be modulated by changing the stretch rate or introducing time delays between successive loading sets. This phenomenon is clearly a manifestation of the model's viscoelastic behavior and should not be mistaken with stress-softening or damage.

2.11 Summary

A new three-dimensional multi-regime evolution model for rubber-like materials is presented in this chapter. The proposed model is based on a selection of existing components and unifies two major aspects of rubber behavior, in large deformations: nonlinear viscoelasticity and the Mullins effect. The prototypical formulation is further generalized to include multiple nonlinear Maxwell elements accounting for several internal material time-scales. A detailed analysis provides practical means of determining the model's parameters from simple uniaxial extension tests. A numerical example illustrates several aspects of the model's behavior in uniaxial extension, at different stretch rates. A possible directional approach extending the model to handle Mullins effect induced anisotropy is briefly discussed.

3

Simple algorithms for solving steady-state frictional rolling contact problems in two and three dimensions

3.1 Preamble

This chapter presents simple, yet robust and efficient algorithms for solving steady-state, frictional, rolling/sliding contact problems, in two and three dimensions. These are alternatives to powerful, well established, but in particular instances, possibly 'cumbersome' general-purpose numerical techniques, such as finite-element approaches based on constrained optimization. The cores of the solvers rely on very general principles: (i) resolving motional conflicts, and (ii) eliminating unacceptable surface tractions. The proposed algorithms are formulated in the context of small deformations and applied to the cases of a rigid cylinder and a rigid sphere rolling on a linear viscoelastic layer of finite thickness, in two and three dimensions, respectively. The underlying principles are elucidated, relevant mathematical expressions derived and details given about corresponding implementation techniques. The proposed contact algorithms can be extended to more general settings involving a deformable

indenter, material nonlinearities and large deformations.

3.2 Problem setting and conventions

Figure 3.1 shows a round and undeformable object, which may be a cylinder or a sphere. This object is moving to the right in steady state, at a linear speed V_s along direction x, while in contact with a deformable layer on which it may be rolling (at a rotational speed Ω) or sliding, in the presence of surface friction.

Frame $O'x'y'z'$ corresponds to a material coordinate system that is attached to the subbase. However, the (steady-state) contact problem is considered in a moving frame of reference $Oxyz$, traveling along with the object, and in which material time derivatives are expressed such that time becomes an implicit variable

$$\frac{D}{Dt} = -V_s \frac{\partial}{\partial x} \; ; \; \frac{D^2}{Dt^2} = V_s^2 \frac{\partial^2}{\partial x^2}. \tag{3.1}$$

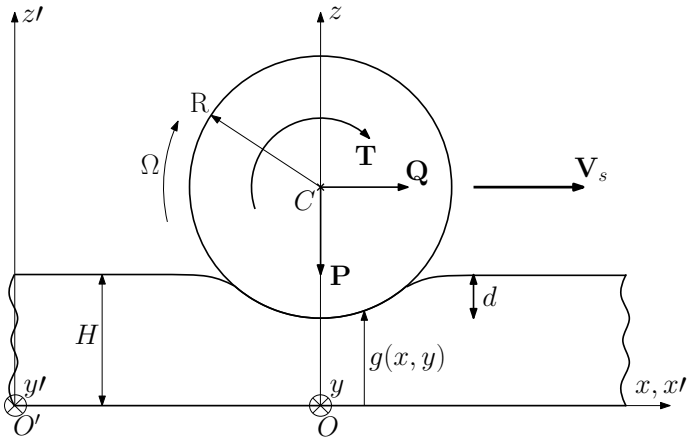

FIGURE 3.1: General model and coordinate systems.

For definiteness and without prejudice to the generality of the foregoing material, we will consider a linear viscoelastic and incompressible foundation of finite thickness H, bounded to a rigid substrate. In a two dimensional setting (the case of a cylinder), plane-strain conditions are applied. It is furthermore assumed that surface friction

follows Coulomb's law, with a constant friction coefficient μ. In the context of linear viscoelasticity, the layer must incur relatively small deformations. Consequently, wherever deemed convenient, relevant physical quantities (e.g. the stress tensor $\boldsymbol{\sigma}$ and the small-strain tensor $\boldsymbol{\epsilon}$) may be expressed in the reference frame or in the current frame, indifferently.

In our general case, the moving object will be subjected to the following external action components, acting in the vertical plane of movement and expressed at its axis C: (i) a driving horizontal force Q acting positively from left to right, (ii) a vertical load P, positive downwards, and (iii) a driving torque T, positive clockwise. The moving object is also subjected to the unknown reaction of the subbase, consisting of vertical and horizontal surface traction fields: $\sigma_z(x, y, H)$, $\tau_{xz}(x, y, H)$ and $\tau_{yz}(x, y, H)$. As demonstrated for instance by Munisamy et al. (1991), shear tractions influence the contact pressure distribution and vice-versa. The main goal behind solving the rolling contact problem is to determine those fully coupled surface tractions, along with the corresponding foundation surface displacement fields (i.e. $u(x, y, H)$, $v(x, y, H)$ and $w(x, y, H)$), as well as the rotational speed Ω and the indentation d. In the absence of friction, the 'frictional' implementations given in this chapter are readily adapted and reduced by eliminating unnecessary equations and solving for the normal contact-stress distribution only, using vertical equilibrium, which excludes the rotational quantities T and Ω that are indeterminate.

In the three dimensional case, the candidate contact surface is discretized as shown in Figure 3.2 with a total number of $N_T = K_x K_y$ nodes. Similar conventions apply in two dimensions. The basic ideas developed in this chapter may be applied to diverse settings and implemented in various numerical contexts, for instance, as part of a finite element or a finite difference model. The contact solving algorithms are presented and discussed in the subsequent sections, assuming that the layer is

modeled by means of a boundary element formulation of the form

$$\mathbf{CF} = \mathbf{D}, \tag{3.2}$$

where $\mathbf{C}$ is a compliance matrix characterizing the mechanical behavior of the discretized candidate contact surface on the layer's upper boundary, $\mathbf{F}$ is a nodal surface force vector and $\mathbf{D}$ is the corresponding nodal surface displacement vector. Suitable methods for building matrix $\mathbf{C}$ are given for instance by Qiu (2006) and Zéhil and Gavin (2013e) (see Chapter 4), in two and three dimensions respectively. Other approaches may be used as well. In the three dimensional case, $\mathbf{F}$ and $\mathbf{D}$ are partitioned into subvectors as follows

$$\mathbf{F} = \left\langle \mathbf{F}_W^T, \mathbf{F}_U^T, \mathbf{F}_V^T \right\rangle^T = \text{ vector of nodal forces,} \tag{3.3}$$

$$\mathbf{D} = \left\langle \mathbf{W}^T, \mathbf{U}^T, \mathbf{V}^T \right\rangle^T = \text{ vector of nodal displacements,} \tag{3.4}$$

each subvector containing nodal components in a given direction. The full compliance matrix $\mathbf{C}$ is of dimensions $(3N_T \times 3N_T)$. Following the Cartesian spatial directions and in accordance with the previous ordering of the nodal subvectors in (3.3) and (3.4), matrix $\mathbf{C}$ may be partitioned into nine $(N_T \times N_T)$ submatrices $\mathbf{C}_{PQ}$ where indices $P, Q \in \{U, V, W\}$. Equation (3.2) may hence be written in the form

$$\begin{bmatrix} \mathbf{C}_{WW} & \mathbf{C}_{WU} & \mathbf{C}_{WV} \\ \mathbf{C}_{UW} & \mathbf{C}_{UU} & \mathbf{C}_{UV} \\ \mathbf{C}_{VW} & \mathbf{C}_{VU} & \mathbf{C}_{VV} \end{bmatrix} \begin{bmatrix} \mathbf{F}_W \\ \mathbf{F}_U \\ \mathbf{F}_V \end{bmatrix} = \begin{bmatrix} \mathbf{W} \\ \mathbf{U} \\ \mathbf{V} \end{bmatrix}. \tag{3.5}$$

As illustrated on Figure 3.2, the nodal force vector components ${F_W}^N$, ${F_U}^N$ and ${F_V}^N$, for $N = 1 \dots N_T$, in the moving Cartesian frame of reference, may be expressed in terms of their spherical counterparts ${F_R}^N$, ${F_\Phi}^N$ and ${F_\Theta}^N$ using the following coordinate transformation

$$\begin{bmatrix} {F_W}^N \\ {F_U}^N \\ {F_V}^N \end{bmatrix} = \begin{bmatrix} \cos(\phi) & \sin(\phi) & 0 \\ -\cos(\theta)\sin(\phi) & \cos(\theta)\cos(\phi) & -\sin(\theta) \\ -\sin(\theta)\sin(\phi) & \sin(\theta)\cos(\phi) & \cos(\theta) \end{bmatrix} \begin{bmatrix} {F_R}^N \\ {F_\Phi}^N \\ {F_\Theta}^N \end{bmatrix}. \tag{3.6}$$

The normal and tangential stress fields corresponding to the spherical nodal force vectors $\mathbf{F}_R$, $\mathbf{F}_\Phi$ and $\mathbf{F}_\Theta$ are designated by $\sigma_r(x, y, H)$, $\tau_{\phi r}(x, y, H)$ and $\tau_{\theta r}(x, y, H)$, respectively.

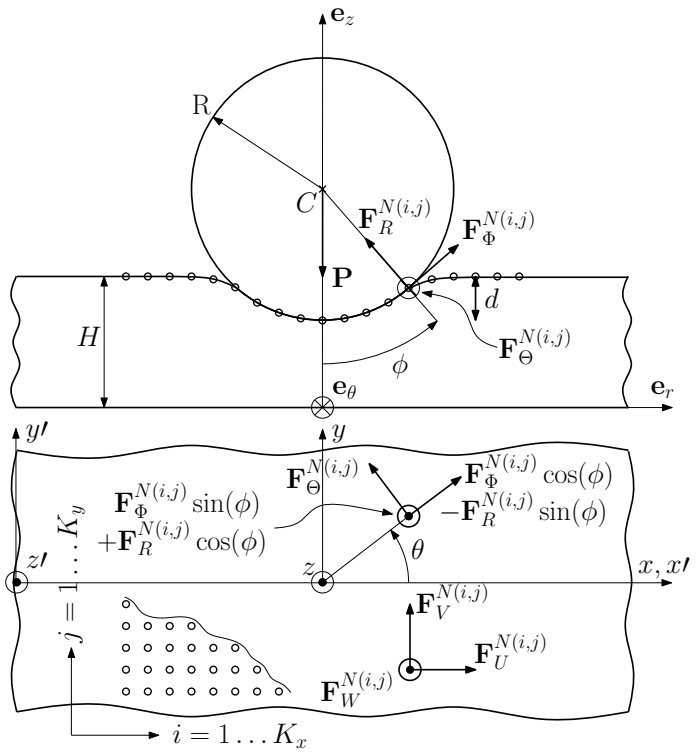

FIGURE 3.2: Discretization and nodal forces in two coordinate systems (a_x and a_y denote the nodal spacing in directions x and y, respectively).

As a consequence of the small-strain assumption resulting from linear viscoelasticity, one may identify *normal* with *vertical* components and *tangent* with *horizontal* components of surface fields. Equivalently, setting $\phi \approx 0$, system (3.6) would reduce to

$$\begin{bmatrix} {F_W}^N \\ {F_U}^N \\ {F_V}^N \end{bmatrix} \approx \begin{bmatrix} 1 & 0 & 0 \\ 0 & \cos(\theta) & -\sin(\theta) \\ 0 & \sin(\theta) & \cos(\theta) \end{bmatrix} \begin{bmatrix} {F_R}^N \\ {F_\Phi}^N \\ {F_\Theta}^N \end{bmatrix}. \tag{3.7}$$

Equation (3.7) is invoked in the following two instances *only*: (i) in the 2D case of Section 3.3, F_R and F_Φ are equated to F_W and F_U in equation (3.8), and (ii) in the 3D

case of Section 3.4, it is assumed that Coulomb's inequality applies to F_W, F_U and F_V instead of F_R, F_Φ and F_Θ in expression (3.38). Conversely, the approximation $\phi \approx 0$ applies to the displacement fields throughout. The following notational conventions are furthermore adopted:

- adding a scalar to an array results in adding that scalar to each of the array's components,
- each component of an array is individually raised at a given power κ when (κ) is displayed between parenthesis.

3.3 2D algorithm for frictional rolling contact

In the 2D problem of a cylinder rolling across a viscoelastic layer, the discretized candidate contact surface is (conceptually) divided into three non-overlapping domains: two free regions denoted by the subscripts 1 and 3, separated by an initially continuous contact area designated by the subscript 2. The nodal position vector $\mathbf{x}$ is hence partitioned into three subvectors, i.e. $\mathbf{x} = \left\langle \mathbf{x}_1^T, \mathbf{x}_2^T, \mathbf{x}_3^T \right\rangle^T$. This is also reflected in the boundary element constitutive equation, written as

$$\begin{bmatrix} \mathbf{C}_{WW,11} & \mathbf{C}_{WW,12} & \mathbf{C}_{WW,13} & \mathbf{C}_{WU,11} & \mathbf{C}_{WU,12} & \mathbf{C}_{WU,13} \\ \mathbf{C}_{WW,21} & \mathbf{C}_{WW,22} & \mathbf{C}_{WW,23} & \mathbf{C}_{WU,21} & \mathbf{C}_{WU,22} & \mathbf{C}_{WU,23} \\ \mathbf{C}_{WW,31} & \mathbf{C}_{WW,32} & \mathbf{C}_{WW,33} & \mathbf{C}_{WU,31} & \mathbf{C}_{WU,32} & \mathbf{C}_{WU,33} \\ \mathbf{C}_{UW,11} & \mathbf{C}_{UW,12} & \mathbf{C}_{UW,13} & \mathbf{C}_{UU,11} & \mathbf{C}_{UU,12} & \mathbf{C}_{UU,13} \\ \mathbf{C}_{UW,21} & \mathbf{C}_{UW,22} & \mathbf{C}_{UW,23} & \mathbf{C}_{UU,21} & \mathbf{C}_{UU,22} & \mathbf{C}_{UU,23} \\ \mathbf{C}_{UW,31} & \mathbf{C}_{UW,32} & \mathbf{C}_{UW,33} & \mathbf{C}_{UU,31} & \mathbf{C}_{UU,32} & \mathbf{C}_{UU,33} \end{bmatrix} \begin{bmatrix} \mathbf{F}_{W,1} \\ \mathbf{F}_{W,2} \\ \mathbf{F}_{W,3} \\ \mathbf{F}_{U,1} \\ \mathbf{F}_{U,2} \\ \mathbf{F}_{U,3} \end{bmatrix} = \begin{bmatrix} \mathbf{W}_1 \\ \mathbf{W}_2 \\ \mathbf{W}_3 \\ \mathbf{U}_1 \\ \mathbf{U}_2 \\ \mathbf{U}_3 \end{bmatrix}, \quad (3.8)$$

where $\mathbf{F}_{W,1}$, $\mathbf{F}_{W,3}$, $\mathbf{F}_{U,1}$ and $\mathbf{F}_{U,3}$ are null vectors. In this two-dimensional case, it is assumed that the constitutive equations of the layer apply in the current configuration, which is a valid assumption under small deformations. Consequently, $\mathbf{F}_R$ and $\mathbf{F}_\Phi$ may be equated to $\mathbf{F}_W$ and $\mathbf{F}_U$ in equation (3.8). One advantage of such a formulation is that it yields directly-exploitable normal and tangential nodal force fields.

3.3.1 2D normal-contact subroutine

For a two-dimensional model in the plane "Oxz", the normal contact boundary conditions may be expressed as

$$H + w(x, H) < g(x) \text{ if } \sigma_r = 0, \tag{3.9}$$

$$H + w(x, H) = g(x) \text{ if } \sigma_r < 0, \tag{3.10}$$

where $g(x)$ corresponds to an analytical expression for the lower surface of the moving rigid body. For for a cylinder of radius R and center C

$$g(x) = z_c - \sqrt{R^2 - x^2}. \tag{3.11}$$

The normal-contact subroutine is based on equation number 2 in system (3.8). It operates in two phases, A and B.

Phase A: given a meshed candidate contact surface and a tangent contact-stress distribution (i.e. $\mathbf{F}_\Phi$ is known), the algorithm initially attempts applying the vertical load P on the smallest allowable area, as determined by the discretization, since rolling objects and the layer have non-conforming surfaces. If, at any given iteration, the current contact area is too small, the foundation material will significantly swell on the sides, thus interfering geometrically with the shape of the moving object. Hence, the currently-free nodes are probed individually for geometrical conflicts using (3.9) and each interfering node is added to the set of contact nodes. Consequently, the contact area grows during phase A while the algorithm is resolving geometrical conflicts.

Phase B: after all geometrical conflicts have been resolved, the current contact area is probed for normal positive tractions. Positive tractions are suppressed by setting free the corresponding nodes, as non-adhesive contact is assumed. Alternatively, an adhesion threshold may be readily set. While iterating in phase B, the contact area mainly shrinks as the algorithm is working on suppressing tensile tractions. If

a geometrical conflict arises while in phase B, it is given priority and resolved by shifting back to phase A, and so on.

At each iteration of both phases A and B, the following linear system, augmented with the penetration d, is solved

$$\begin{bmatrix} \mathbf{C}_{WW,22} & \mathbf{1}_n \\ \left(1-\left(\frac{\mathbf{x}_2}{R}\right)^{(2)}\right)^{(1/2)} & 0 \end{bmatrix} \begin{bmatrix} \mathbf{F}_{R,2} \\ d \end{bmatrix} = \begin{bmatrix} R-\left(R^2-\mathbf{x}_2^{(2)}\right)^{(1/2)} - \mathbf{C}_{WU,22}\mathbf{F}_{\Phi,2} \\ -P-\frac{\mathbf{x}_2^T\mathbf{F}_{\Phi,2}}{R} \end{bmatrix}, \quad (3.12)$$

where n is the number of contact nodes at a given iteration and $\mathbf{1}_n$ corresponds to a column vector with n unit components. The first n equations in system (3.12) reflect the fact that the vertical displacement of the layer across the contact area, i. e. $\mathbf{W}_2$, follows the object's lower profile given by (3.11). The last (additional) equation corresponds to the equilibrium of forces in the vertical direction.

In some practical situations, the penetration d is given directly while the vertical load P is unknown. This case is readily solved by removing the last equation from system (3.12). The global approach remains however unchanged and P is determined by vertical force equilibrium, after the solution has been found.

3.3.2 2D stick-slip subroutine

Given our assumptions pertaining to friction, the tangential contact boundary conditions for a two-dimensional model in plane "Oxz" are given by

$$|\tau_{\phi r}(x,H)| < -\mu\sigma_r(x,H) \text{ if } w_t = 0, \quad (3.13)$$

$$\tau_{\phi r}(x,H) = -\mu\sigma_r(x,H)\,\mathrm{sgn}(w_t) \text{ otherwise}, \quad (3.14)$$

involving the coefficient of solid friction μ for the interface, as well as the differential tangential speed across the contact area, i.e.

$$w_t = V_s\left(1+\frac{\partial u}{\partial x}(x,H)\right) - R\Omega. \quad (3.15)$$

Inequality (3.13) is verified across contact regions that are characterized by the absence of relative movement between touching points, while equality (3.14) is enforced in contact areas that are in relative motion.

The stick-slip subroutine is based on equation number 5 of system (3.8). Given a fixed contact area and a normal stress field, as determined by the normal-contact subroutine (i.e. $\mathbf{F}_{R,2}$ is known), the stick-slip algorithm first assumes that all the contact nodes are in a state of stick-contact. It then solves iteratively for the distribution of tangent contact-stresses (or $\mathbf{F}_{\Phi,2}$) and the rotational speed Ω. Surface shear forces computed from a given solution iterate are compared with the limiting friction at each node. All stick-contact nodes subjected to a nodal shear force exceeding Coulomb's friction are switched to slip-contact nodes at the next iteration.

In practice, at each iteration, the stick-slip algorithm solves a linear system for the unknown tangent nodal forces at the stick-contact nodes $\mathbf{F}_{\Phi,2}(s)$, given the fact that tangent nodal forces at the slipping nodes $\mathbf{F}_{\Phi,2}(\bar{s})$ are defined by the limiting friction. The corresponding set of equations is further augmented with the rotational speed Ω and a displacement of reference u_{ref}, matching the horizontal displacement of the leading edge stick-contact node. The resulting system is written as follows

$$\begin{bmatrix} -\mathbf{C_{UU,22}}(s,s) & -\frac{R}{V_s}\mathbf{q_2} & \mathbf{1}_{nst} \\ \mathbf{1}_{nst}^T & 0 & 0 \\ \mathbf{h} & \frac{aR}{V_s} & 1 \end{bmatrix} \begin{bmatrix} \mathbf{F}_{\Phi,2}(s) \\ \Omega \\ u_{ref} \end{bmatrix} = \begin{bmatrix} \mathbf{q}_1 - \mathbf{q}_2 \\ -\frac{T}{R} - \sum(\mathbf{F}_{\Phi,2}(\bar{s})) \\ a + \delta \end{bmatrix}, \quad (3.16)$$

where

- nst is the number of stick-contact nodes at a given iteration and $\mathbf{1}_{nst}$ corresponds to a column vector with nst unit components,
- the arguments "s" and "$\bar{s}$" stand for extracting from a given array the rows, or columns, corresponding to stick and slip-contact nodes respectively. Alternatively, the argument " : " stands for "all" lines or columns,

- the subscript "ref" refers to the leading edge stick-contact node: i_{ref} corresponds to its index in the subset of contact nodes, A_{ref} corresponds to its global node number and $x_{ref} = \mathbf{x}_2(i_{ref})$ to its position. As previously mentioned, $u_{ref} = \mathbf{U}_2(i_{ref})$ is the horizontal displacement field at that node,
- $\mathbf{q}_1$, $\mathbf{q}_2$, $\mathbf{h}$ and δ are defined for convenience as follows, depending on whether the leading edge contact node has slipped (case A) or not (case B):
  - $\mathbf{q}_1 = \mathbf{C}_{UW,22}(s,:)\mathbf{F}_{R,2} + \mathbf{C}_{UW,22}(s,\bar{s})\mathbf{F}_{\Phi,2}(\bar{s})$,
  - $\mathbf{q}_2 = x_{ref} - \mathbf{x}(s)$,
  - $\mathbf{h} = \begin{cases} -\mathbf{C}_{UU,22}(i_{ref}+1,s) & \text{in case A,} \\ -\mathbf{C}_{UU,32}(1,s) & \text{in case B,} \end{cases}$
  - $\delta = \begin{cases} \mathbf{C}_{UW,22}(i_{ref}+1,:)\mathbf{F}_{R,2} + \mathbf{C}_{UU,22}(i_{ref}+1,\bar{s})\mathbf{F}_{\Phi,2}(\bar{s}) & \text{in case A,} \\ \mathbf{C}_{UU,32}(1,\bar{s})\mathbf{F}_{\Phi,2}(\bar{s}) + \mathbf{C}_{UW,32}(1,:)\mathbf{F}_{R,2} & \text{in case B.} \end{cases}$

The first nst equations in system (3.16) reflect the fact that the horizontal elongational strain $\frac{du}{dx} = \frac{\partial u}{\partial x}(x,H)$ remains constant across all stick-contact zones. This is true because the differential tangent speed $w_t = V_s\left(1+\frac{du}{dx}\right) - R\Omega$ is equal to zero across the sticking interface while V_s and Ω are global constants. The last two equations cover for the the additional unknowns Ω and u_{ref}:

- equation $nst+1$ reflects the fact that the tangent contact-stress distribution equilibrates the driving torque, or equivalently

$$T = -\sum \mathbf{F}_{\Phi,2} R, \tag{3.17}$$

- equation $nst+2$ enforces continuity, as suggested by Qiu (2006), of the horizontal elongational strain on both sides of the leading edge stick-contact node. This is done by means of a finite difference expression

$$\frac{du}{dx}(x_{ref}) = \frac{\mathbf{U}(A_{ref}+1) - u_{ref}}{a}, \tag{3.18}$$

where a is the spacing between nodes. In many practical applications, the driving torque T is related to the horizontal driving force Q. Commonly, only Q is applied at the top of the rolling object, hence generating a torque $T = QR$. In the latter case, system (3.16) becomes

$$\begin{bmatrix} -\mathbf{C}_{UU,22}(s,s) & -\frac{R}{V_s}\mathbf{q}_2 & \mathbf{1}_{nst} \\ \mathbf{q}_3(s) & 0 & 0 \\ \mathbf{h} & \frac{aR}{V_s} & 1 \end{bmatrix} \begin{bmatrix} \mathbf{F}_{\Phi,2}(s) \\ \Omega \\ u_{ref} \end{bmatrix} = \begin{bmatrix} \mathbf{q}_1 - \mathbf{q}_2 \\ -\frac{\mathbf{x}_2^T \mathbf{F}_{R,2}}{R} - \mathbf{q}_3^T(\bar{s})\mathbf{F}_{\Phi,2}(\bar{s}) \\ a + \delta \end{bmatrix},$$

where $\mathbf{q}_3$ is defined for convenience as

$$\mathbf{q}_3 = 1 + \left(1 - \left(\frac{\mathbf{x}_2}{R}\right)^{(2)}\right)^{(\frac{1}{2})}. \tag{3.19}$$

3.3.3 2D combined algorithm

The normal-contact subroutine determines the contact surface and the corresponding normal stress distribution given a tangent stress field on the foundation's surface. Alternatively, the stick-slip subroutine determines the slipping regions of a contact area and the corresponding tangent stress distribution given the normal stress field. These two subroutines are therefore combined in a loop that starts by assuming $\mathbf{F}_\Phi = 0$ and converges towards the actual solution of the frictional rolling contact problem.

If needed, the rolling resistance may be computed, after convergence, according to the expression below

$$R_r = -\frac{\mathbf{x}^T \mathbf{F}_R}{R} + \mathbf{F}_\Phi^T \left(1 - \left(\frac{\mathbf{x}}{R}\right)^{(2)}\right)^{(\frac{1}{2})} + \frac{T\Omega}{V_s}. \tag{3.20}$$

The methodology described in Section 3.3.1 was implemented and tested on a two-dimensional model of a rigid cylinder, rolling in steady-state on an incompressible viscoelastic foundation of finite thickness. It was found to be robust and efficient: full

convergence, based on the relative change in all the outputs, was typically obtained in 5 iterations.

3.4 3D algorithm for frictional rolling contact

Using a similar approach to the one described in Section 3.3, the discretized candidate contact surface, which is now two-dimensional, is conceptually divided into two separate regions: an initially continuous contact area (referred to by "c") surrounded by an external free surface (referred to by "$\bar{c}$"). At any given iteration of the algorithms that are subsequently described, the arguments c and $\bar{c}$ stand for extracting from a given array the lines/columns corresponding to contact nodes and free nodes, respectively. The constitutive equation used for reference is equation (3.5).

In the three-dimensional case, working with Cartesian quantities proves to be more convenient since it avoids composing expressions (3.5) and (3.7) with varying angles ϕ and θ across the contact surface. Results expressed in Cartesian form are furthermore easier to interpret. If normal and tangential stress fields are specifically needed, the Cartesian results can be transformed into spherical form using equation (3.6).

3.4.1 3D normal-contact subroutine

The method presented in Section 3.3.1 is fairly easily extended and adapted to a three dimensional setting. This is done using notations introduced in Section 3.4 along with similar conventions to the ones that were used throughout Section 3.3. The following linear system, augmented with the penetration d, is solved at each iteration of both phases A and B

$$\begin{bmatrix} \mathbf{C}_{WW}(c,c) & \mathbf{1}_n \\ \mathbf{1}_n^T & 0 \end{bmatrix} \begin{bmatrix} \mathbf{F}_W(c) \\ d \end{bmatrix} = \begin{bmatrix} \mathbf{q}_4(c) - \mathbf{C}_{WU}(c,:)\mathbf{F}_U - \mathbf{C}_{WV}(c,:)\mathbf{F}_V \\ -P \end{bmatrix}, \quad (3.21)$$

where, for the purposes of the normal-contact subroutine, $\mathbf{F}_U$ and $\mathbf{F}_V$ are considered as given nodal force fields in directions x and y respectively, while the vertical force field $\mathbf{F}_W(c)$ is equal to $\mathbf{0}$. Vector $\mathbf{q}_4$ is defined for convenience as

$$\mathbf{q}_4 = R - \left(R^2 - \mathbf{x}^{(2)} - \mathbf{y}^{(2)}\right)^{(1/2)}. \tag{3.22}$$

3.4.2 3D stick-slip subroutine

Given a contact surface along with the corresponding nodal vertical force field $\mathbf{F}_W$, the three-dimensional stick-slip subroutine determines the regions where slipping occurs and returns the nodal horizontal force fields $\mathbf{F}_U$ and $\mathbf{F}_V$ as well as the the rotational speed Ω.

The two equations below are first extracted from system (3.5), for stick-contact nodes (s, c), at any given iteration of the stick-slip subroutine

$$\mathbf{C}_{UW}(s,c)\mathbf{F}_W(c) + \mathbf{C}_{UU}(s,c)\mathbf{F}_U(c) + \mathbf{C}_{UV}(s,c)\mathbf{F}_V(c) = \mathbf{U}(s), \tag{3.23}$$

$$\mathbf{C}_{VW}(s,c)\mathbf{F}_W(c) + \mathbf{C}_{VU}(s,c)\mathbf{F}_U(c) + \mathbf{C}_{VV}(s,c)\mathbf{F}_V(c) = \mathbf{V}(s). \tag{3.24}$$

Before the system defined by equations (3.23) and (3.24) can be solved for $\mathbf{F}_U(s)$ and $\mathbf{F}_V(s)$[1], the unknown right-hand-side displacement fields $\mathbf{U}(s)$ and $\mathbf{V}(s)$ must be eliminated. This is subsequently done using the consequences of sticky contact.

In small deformations, using equation (3.1), the horizontal components of the differential speed vector in directions x and y, at contact points, are given by

$$w_{tx} = V_s\left(1 + \frac{\partial u}{\partial x}\right) - R(y)\Omega, \text{ where } R(y) = \sqrt{R^2 - y^2}, \tag{3.25}$$

$$w_{ty} = V_s\left(\frac{\partial v}{\partial x}\right). \tag{3.26}$$

At any stick-contact point, w_{tx} and w_{ty} are equal to zero. Since V_s and Ω are global constants, it follows that $\frac{\partial u}{\partial x}$ and v remain constant along any segment parallel to the

[1] $\mathbf{F}_U(s)$ and $\mathbf{F}_V(s)$ are unknown subvectors of $\mathbf{F}_U(c)$ and $\mathbf{F}_V(c)$, respectively.

x-axis, within the stick-contact area. All components in $\mathbf{U}(s)$ and $\mathbf{V}(s)$ may hence be related to $2 \times K_{st}$ constants, where K_{st} corresponds to the number of nodal rows containing stick-contact nodes. These constants are so far unknown and thus require $2 \times K_{st}$ additional equations which are obtained by enforcing continuity of $\frac{\partial u}{\partial x}$ and v, in direction x, across the leading edge stick-contact nodes.

Referring to Figure 3.2, let $N_{i,j} = N(i,j) = (j-1)K_x + i$ be the global number of a stick-contact node at position $(x,y) = \left((2i - K_x - 1)\frac{a_x}{2}, (2j - K_y - 1)\frac{a_y}{2}\right)$. Also, let $i_{ref}(j)$ designate the x-direction index of the leading edge stick-contact node along the nodal row j. Using a finite difference approach and letting $R_j = R\left((2j - K_y - 1)\,\frac{a_y}{2}\right)$, equations (3.25) and (3.26) lead to

$$\mathbf{U}\left(N_{i,j}\right) = \mathbf{U}\left(N_{i_{ref}(j)+1,j}\right) - \left(i_{ref}(j) + 1 - i\right) a_x \left(R_j \frac{\Omega}{V_s} - 1\right), \tag{3.27}$$

$$\mathbf{V}\left(N_{i,j}\right) = \mathbf{V}\left(N_{i_{ref}(j)+1,j}\right). \tag{3.28}$$

The $2 \times K_{st}$ quantities $\mathbf{U}\left(N_{i_{ref}(j)+1,j}\right)$ and $\mathbf{V}\left(N_{i_{ref}(j)+1,j}\right)$ in equations (3.27) and (3.28) correspond to the horizontal displacements of the nodes that are immediately adjacent to the leading edge contact node in each row. They can be related back to the main unknown fields $\mathbf{F}_U(s)$ and $\mathbf{F}_V(s)$ using system (3.5), which yields

$$\begin{aligned}\mathbf{U}\left(N_{i_{ref}(j)+1,j}\right) = {} & \mathbf{C}_{UW}(N_{i_{ref}(j)+1,j}, c)\mathbf{F}_W(c) + \mathbf{C}_{UU}((N_{i_{ref}(j)+1,j}, c)\mathbf{F}_U(c) \\ & + \mathbf{C}_{UV}(N_{i_{ref}(j)+1,j}, c)\mathbf{F}_V(c),\end{aligned} \tag{3.29}$$

$$\begin{aligned}\mathbf{V}\left(N_{i_{ref}(j)+1,j}\right) = {} & \mathbf{C}_{VW}(N_{i_{ref}(j)+1,j}, c)\mathbf{F}_W(c) + \mathbf{C}_{VU}((N_{i_{ref}(j)+1,j}, c)\mathbf{F}_U(c) \\ & + \mathbf{C}_{VV}(N_{i_{ref}(j)+1,j}, c)\mathbf{F}_V(c).\end{aligned} \tag{3.30}$$

The rotational speed Ω appearing in expression (3.27) is also unknown and thus requires one additional equation provided by the equilibrium of moments about the horizontal axis of the sphere parallel to Oy

$$\mathbf{q}_R^T(s)\mathbf{F}_U(s) = -T - \mathbf{x}^T(c)\mathbf{F}_W(c) - \mathbf{q}_R^T(\bar{s})\mathbf{F}_U(\bar{s}), \tag{3.31}$$

where $\mathbf{q}_R$ is a column vector defined for all contact nodes $M_{i,j} = M(i,j)$ as

$$\mathbf{q}_R(M_{i,j}) = R_j \sqrt{1 - \left(\frac{\mathbf{x}(M_{i,j})}{R_j}\right)^2}. \tag{3.32}$$

On the other hand, systems (3.23) and (3.24) may be rewritten such that each line corresponds to a stick-contact node $N_{i,j}$ as follows

$$\mathbf{C}_{UW}(N_{i,j},c)\mathbf{F}_W(c) + \mathbf{C}_{UW}(N_{i,j},c)\mathbf{F}_U(c) + \mathbf{C}_{UV}(N_{i,j},c)\mathbf{F}_V(c) = \mathbf{U}(N_{i,j}), \tag{3.33}$$

$$\mathbf{C}_{VW}(N_{i,j},c)\mathbf{F}_W(c) + \mathbf{C}_{VU}(N_{i,j},c)\mathbf{F}_U(c) + \mathbf{C}_{VV}(N_{i,j},c)\mathbf{F}_V(c) = \mathbf{V}(N_{i,j}). \tag{3.34}$$

Combining equations (3.27)-(3.34), eliminating $\mathbf{U}(N_{i,j})$ and $\mathbf{V}(N_{i,j})$ and further rearranging the terms results in the final expression of a linear system in $\mathbf{F}_U(s)$, $\mathbf{F}_V(s)$ and Ω, to be solved at each iteration of the 3D stick-slip subroutine

$$\begin{aligned}\mathbf{G}_{UU}(N_{i,j},s)\mathbf{F}_U(s) + \mathbf{G}_{UV}(N_{i,j},s)\mathbf{F}_V(s) + (g_{ij}R_j/V_s)\,\Omega = \ldots \\ g_{ij} - \mathbf{G}_{UW}(N_{i,j},c)\mathbf{F}_W(c) - \mathbf{G}_{UU}(N_{i,j},\bar{s})\mathbf{F}_U(\bar{s}) - \mathbf{G}_{UV}(N_{i,j},\bar{s})\mathbf{F}_V(\bar{s}),\end{aligned} \tag{3.35}$$

$$\begin{aligned}\mathbf{G}_{VU}(N_{i,j},s)\mathbf{F}_U(s) + \mathbf{G}_{VV}(N_{i,j},s)\mathbf{F}_V(s) + 0\times\Omega = \ldots \\ - \mathbf{G}_{VW}(N_{i,j},c)\mathbf{F}_W(c) - \mathbf{G}_{VU}(N_{i,j},\bar{s})\mathbf{F}_U(\bar{s}) - \mathbf{G}_{VV}(N_{i,j},\bar{s})\mathbf{F}_V(\bar{s}),\end{aligned} \tag{3.36}$$

$$\mathbf{q}_R^T(s)\mathbf{F}_U(s) + \mathbf{0}^T(s)\mathbf{F}_V(s) + 0\times\Omega = -T - \mathbf{x}^T(c)\mathbf{F}_W(c) - \mathbf{q}_R^T(\bar{s})\mathbf{F}_U(\bar{s}), \tag{3.37}$$

where the following quantities are defined for convenience:

$$g_{ij} = (i_{ref}(j) + 1 - i)a_x \ , \quad \text{and}$$

$$\mathbf{G}_{AB}(N_{i,j},:) = \mathbf{C}_{AB}(N_{i,j},:) - \mathbf{C}_{AB}(N_{i_{ref}(j)+1,j},:), \text{ for } A,B \in \{U,V,W\}\,.$$

A notable advantage of formulation (3.35)-(3.37) is that it avoids augmenting the system with $2 \times K_{st}$ additional unknown displacements, by analytically eliminating the quantities $\mathbf{U}\left(N_{i_{ref}(j)+1,j}\right)$ and $\mathbf{V}\left(N_{i_{ref}(j)+1,j}\right)$.

In order to avoid unnecessary coordinate transformations, Coulomb's law of friction is applied to F_W, F_U and F_V, instead of F_R, F_Φ and F_Θ, which is a valid approximation under small deformations. After solving system (3.35)-(3.37) for $\mathbf{F}_U(s)$,

$\mathbf{F}_V(s)$ and Ω, the nodal horizontal displacement fields $\mathbf{U}$ and $\mathbf{V}$ are computed by means of system (3.5) and the differential speed components reevaluated at all slipping nodes using equations (3.25) and (3.26). It is then determined whether each currently sticking contact node N should be considered as a slipping node in the following iteration, by checking whether the latest computed friction and relative speed at N have exceeded the corresponding limits, i.e.

$$\left[\mathbf{F}_U^2(N) + \mathbf{F}_V^2(N) > \mu^2 \mathbf{F}_W^2(N)\right] \text{ and } \left[w_{t_x}^2(N) + w_{t_y}^2(N) > w_{th}^2\right], \tag{3.38}$$

where w_{th} is a differential speed threshold, set to a small value. Reciprocally, each currently slipping node M is checked in order to determine whether it should be considered, in the sequel, as a stick-contact node. This is done by comparing the current differential speed at M to the threshold

$$w_{t_x}^2(N) + w_{t_y}^2(N) < w_{th}^2. \tag{3.39}$$

The sets "s" and "$\bar{s}$" of stick/slip nodes are updated accordingly and the limiting friction applied to slipping nodes in the current slipping direction given by w_{tx} and w_{ty}. This includes previously-determined (and still currently) slipping nodes for which the direction of maximum friction is updated such that it matches the latest direction of relative movement.

3.4.3 3D combined algorithm

Following a similar approach to the one described in Section 3.3.3 for the two dimensional case, the normal-contact subroutine and the stick-slip subroutine are combined starting with $\mathbf{F}_U = \mathbf{F}_V = 0$ and converging towards the actual solution of the three-dimensional and frictional rolling contact problem.

After convergence, the rolling resistance may be obtained from the following

general expression

$$R_r = \sum \mathbf{F}_U + \frac{T\Omega}{V_s}. \tag{3.40}$$

The methodology described throughout Section 3.4 was implemented and tested on the three-dimensional model of a rigid sphere, rolling in steady-state on an incompressible viscoelastic foundation of finite thickness. It showed to be robust and efficient: full convergence, based on the relative change in all the outputs, was typically obtained in 7 iterations.

3.5 Examples

In the following two examples, we consider the steady-state rolling with friction of a cylinder (in 2D) and a sphere (in 3D), both of radius $R = 2$ cm at a linear speed $V_s = 5$ cm/s on a viscoelastic layer of thickness $H = 5$ mm and density $\rho = 1000$ kg/m^3. At the contact interface, the coefficient of friction is assumed to be constant and equal to $\mu = 0.2$.

In both cases, the layer's material is modeled by a three-parameter viscoelastic solid whose master curves are given by

$$\begin{aligned} G'(\omega) &= G_0(1+f)\frac{(1+f)+\omega^2\tau^2}{(1+f)^2+\omega^2\tau^2}, \\ G''(\omega) &= G_0(1+f)\frac{f\omega\tau}{(1+f)^2+\omega^2\tau^2}, \end{aligned} \tag{3.41}$$

where $G_o = G'(0) = 3.0$ MPa is the static shear modulus, $\tau = 0.25$ s is the creep time and $f = G'(0)/G'(\infty) - 1 = 1$.

The layer's behavior is described by means of boundary element formulations of the form given by (3.2) where compliance matrices are formed using the methods proposed by Qiu (2006) and Zéhil and Gavin (2013e) (see Chapter 4), in two and three dimensions respectively. Following these references' notations, the spatial periods are

set equal to $L = L_x = L_y = 20$ cm which, at the given speed, allows for sufficient creep recovery of the foundation layer between two successive arrivals of moving objects and therefore enforces aperiodicity. Spacings between nodes are set equal to $a = a_x = a_y = 0.25$ mm. With these choices of L and a, retaining 2000 terms in the series yields stable matrices of sufficient accuracy (see table 1 in Zéhil and Gavin (2013e), or Table 4.1 in Chapter 4).

3.5.1 Rigid cylinder on a viscoelastic foundation in 2D

In this first example, a cylinder is rolling under the influence of a distributed horizontal load Q (per unit length) applied along its upper generatrix (i.e. accompanied by a driving torque $T = QR$). A concomitant distributed vertical load $P = 20$ kN/m is applied along the cylinder's axis. The corresponding mean vertical pressure is of 2.58 MPa, which is about the same as for the sphere in Section 3.5.2. The two-dimensional rolling contact problem is solved following the guidelines presented in Section 3.3 and some of the main results are reported below.

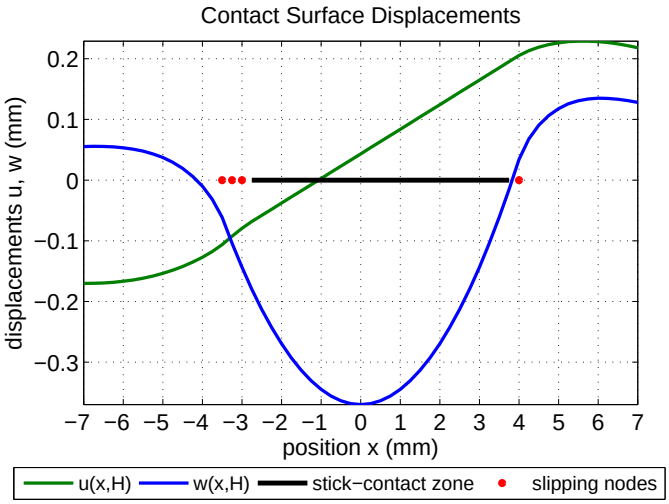

FIGURE 3.3: Foundation surface displacements.

Surface displacements are plotted in Figure 3.3 along with a horizontal line indicator showing the stick-contact area and the slipping regions, as determined by

the 2D stick-slip subroutine. Given the current geometry, loading, speed, interface and foundation characteristics as well as the discretization, slipping occurs at the leading edge of the contact surface (1 node) and to a greater extent, at its trailing edge (counting 3 nodes). It may be noted that, due to viscoelasticity, the deformation fields are asymmetrical. Indeed, the contact surface extends further to the front (i.e. in the direction of movement) as the foundation material looses contact with the cylinder at a higher ordinate than it does at the trailing edge. As implemented in the last equation of system (3.16), the horizontal displacement $u(x, H)$ keeps a constant slope across the stick-contact region, which, according to (3.15), reflects the absence of relative movement between touching points. It is also noteworthy that $u(x, H)$ takes a steeper slope in the slipping region at the back of the cylinder, which indicates that in that region, given (3.1) and (3.15), the cylinder is slipping forwards relative to the foundation and hence is, consistently with what appears on Figure 3.4, applying to it the maximum contact shear in the positive direction.

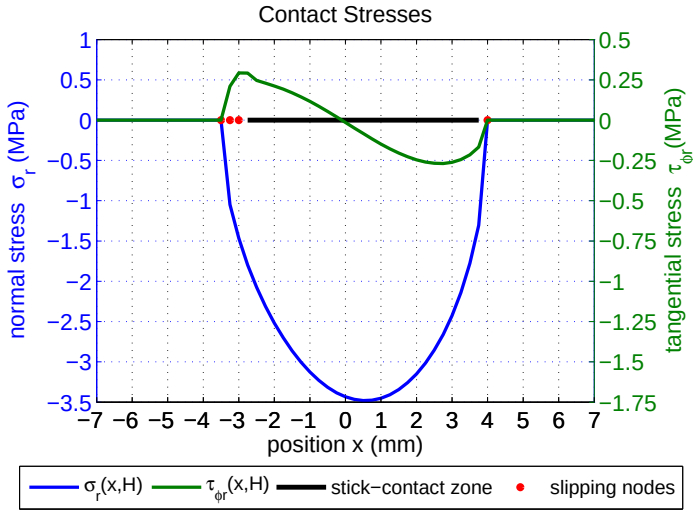

FIGURE 3.4: Surface contact stress fields.

The contact stress fields are given in Figure 3.4 along with the same contact nature indicator. The normal stress distribution is clearly asymmetrical, giving rise

to a viscoelastic rolling resistance. In the slip-contact zone, at the back of the rolling cylinder, the tangential stress field follows the shape of the normal stress field, scaled by $-\mu$. It may also be noted that the negative area between the curve $\tau(x, H)$ and the horizontal axis at the front, is slightly larger than the positive one located at the back. Hence as expected, the shear stress distribution generates a moment about the cylinder's axis balancing the driving torque $T = QR$.

3.5.2 Rigid sphere on a viscoelastic foundation in 3D

A horizontal point load Q is now applied at the top of a sphere, pushing it forward in direction x. The sphere is assumed to be rolling in steady state, without spinning about its vertical axis z. As in Section 3.5.1 a driving torque $T = QR$ about the center of the sphere is accounted for. A concomitant point load $P = 150$ N is applied vertically at the center. Load P was chosen such that the mean vertical pressure on the foundation (which is of 2.56 MPa) be approximately the same as for the cylinder in Section 3.5.1.

The corresponding three-dimensional rolling contact problem is solved according to the principles exposed in Section 3.4. Some of the main results are presented hereafter.

Figure 3.5 reveals two different regions, in terms of contact nature, across the contact interface. Slipping occurs over a crescent-shaped region at the back of the sphere while its remaining contact surface sticks to the subbase. Referring to its dimension in the direction of movement, the slip-contact zone appears to be thicker on the sides than it is in the central part of the contact interface. This observation may be explained by the greater vertical pressure acting in the middle (see Figures 3.6), which increases the slipping threshold in that region.

Figure 3.6 shows a contour plot of the vertical stress field over the contact area. Minor irregularities in the outline are due to the rectangular mesh following a curved

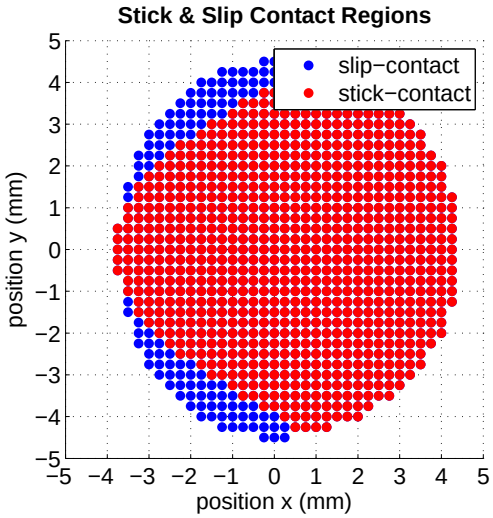

FIGURE 3.5: Stick and slip-contact regions.

path. The asymmetrical shape of $\sigma_z(x, y, z = H)$ is comparable to the one presented for $\sigma_z(x, H)$ in Figure 3.4 in the case of a rolling cylinder. It mainly results from the time-dependent behavior of the foundation strip and opposes a viscoelastic resistance to the rolling of the sphere. Simplified approaches to estimating the 3D rolling resistance on a sphere, based on the observed similarities between 2D and 3D solutions, are presented in Chapter 7 (Zéhil and Gavin, 2013d).

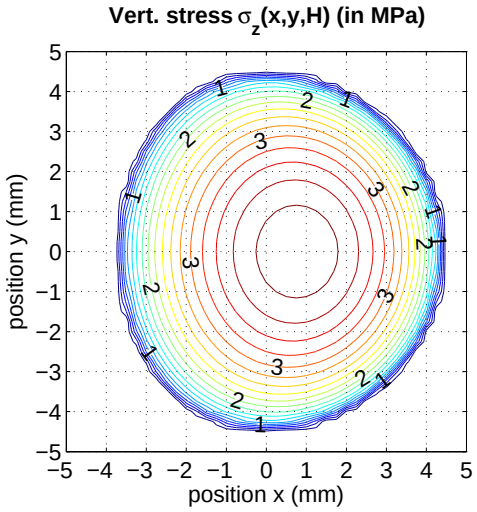

FIGURE 3.6: Contour plot of $\sigma_z(x, y, H)$.

A contour plot of the horizontal stress field in the direction of movement (i.e. direction x), across the contact surface, is given in Figure 3.7. The corresponding surface plot may be seen on Figure 3.8. It has marked similarities with the tangent contact stress field $\tau_{xz}(x, H)$ presented in Figure 3.4 for the 2D cylinder. Indeed, performing a vertical cut parallel to the x-axis on the central part of Figure 3.8 would yield a very similar shape to the one obtained in the two-dimensional case.

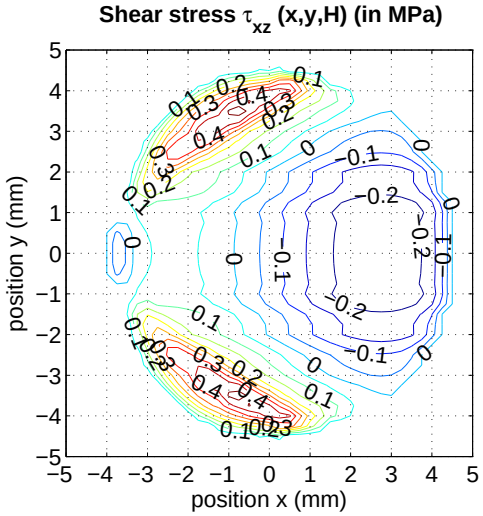

FIGURE 3.7: Contour plot of $\tau_{xz}(x, y, H)$.

While it is rolling clockwise, the sphere rubs against the foundation pushing it backwards in the front part of the stick-contact zone, which explains the negative sign of τ_{xz} on the corresponding region of the plots. In contrast, the sphere slides forward on the lateral slip-contact areas at the back, hence shearing the subbase in the direction of movement and yielding a positive sign of τ_{xz}. These features are further described by the quiver plot given in Figure 3.14. The latter also reveals that the divergence of the horizontal stress field is equal to zero in the vicinity of the point defined by $(x, y) = (-1, 0)$. Furthermore, the vertical and longitudinal contact stress distributions satisfy the moment equilibrium condition given by equation (3.37), which also involves the applied torque $T = QR$. As a consequence, the rolling

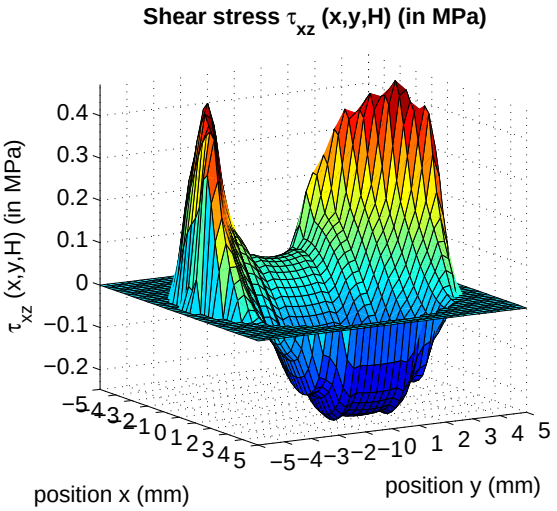

FIGURE 3.8: Surface plot of $\tau_{xz}(x, y, H)$.

resistance may be computed according to expression (3.40) yielding a value of 3.07 N, in the present case.

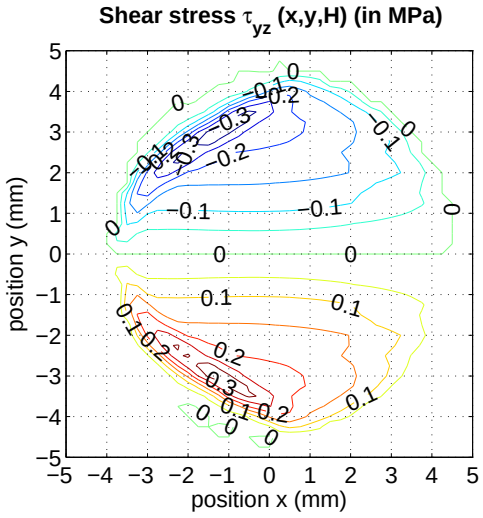

FIGURE 3.9: Contour plot of $\tau_{yz}(x, y, H)$.

Figure 3.9 shows a contour plot of the transverse contact stress distribution. The field $\tau_{yz}(x, y, H)$ is antisymmetric with respect to the x-axis (i.e. odd in y). The corresponding resultant force is therefore equal to zero, which corresponds to an equilibrium condition that was not specifically enforced but is naturally satisfied by

the algorithm. The sign of τ_{yz} reveals that, through surface interaction, the subbase is being transversally maintained as it moves away from the x-axis. This is consistent with information found on the quiver plot (Figure 3.14) as well as on the plot of the lateral displacement field (Figure 3.13). The maximum transverse projection of the horizontal stress, which is slightly above 0.4 MPa, is reached within the lateral slipping regions, near the interface with the stick-contact zone.

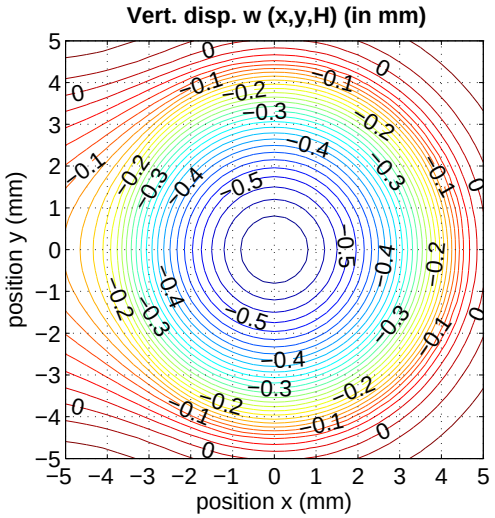

FIGURE 3.10: Contour plot of $w(x, y, H)$.

The vertical displacement field is shown in Figures 3.10. It is asymmetrical, consistent with the vertical pressure field and may be compared to its two-dimensional counterpart given in Figure 3.3. The contour lines of $w(x, y, z)$ are closer to each other at the front of the contact surface where the layer touches the cylinder about 0.1 mm higher than it does at its trailing edge. Indeed, from Figure 3.5, the leading edge stick-contact nodes are positioned at $x = 4.25$ mm, while the trailing edge slip-contact nodes are located at $x = -3.75$ mm. The corresponding contour lines on Figure 3.10 are $w = -0.12$ mm and $w = -0.22$ mm, respectively.

In this example, the foundation strip is made of an incompressible material. Consequently, the integral of $w(x, y, H)$ over a rectangular area of dimensions $L_x \times L_y$

centered at $(x, y) = (0, 0)$ should be equal to zero. This fact is however difficult to verify numerically since doing so would require discretizing the entire domain, which in this case, is much larger than the contact area. As a consolation, it may be noted that the level lines of w indicate a positive vertical displacement near the edges of the discretized surface.

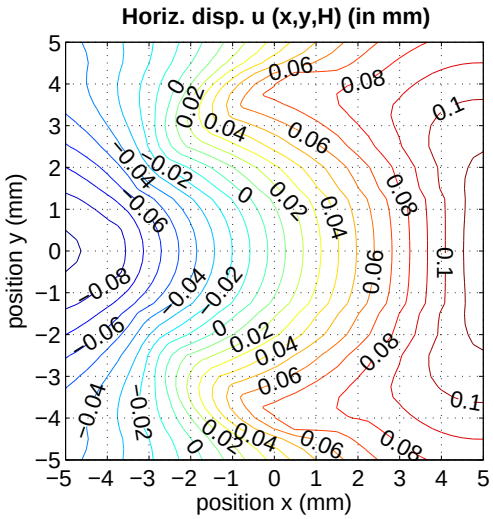

FIGURE 3.11: Contour plot of $u(x, y, H)$.

A contour plot of the horizontal displacement field $u(x, y, H)$, in the direction of movement, is given in Figure 3.11 across the entire candidate contact surface. Striking similarities of $u(x, y, H)$ may be noticed with its two dimensional counterpart $u(x, H)$ presented in Figure 3.3 for the 2D cylinder. Indeed, it has a constant slope across each segment of constant ordinate (i.e. constant y) in the stick-contact zone, which may be seen directly on the surface plot in Figure 3.12, or alternatively by noticing the constant spacing between contour lines in the same region of the contour plot. Referring to equations (3.1) and (3.25), the constant slope of $u(x, y, H)$ in the stick-contact zone reflects the fact that w_{t_x} is equal to zero. Furthermore, the distance between consecutive level lines of $u(x, y, H)$, measured parallel to the x-axis, becomes clearly smaller in the lateral parts of the slipping region, which indicates

that the sphere is slipping forwards relatively to the surface and hence applying to it a positive (limiting) shear stress. This is illustrated further by the quiver plot of the horizontal shear stress applied to the layer's surface, presented in Figure 3.14, where it may also be seen that slipping occurs backwards in the thin central part of the slip-contact zone, which is consistent with an increased spacing between level lines on Figure 3.11 in that same region.

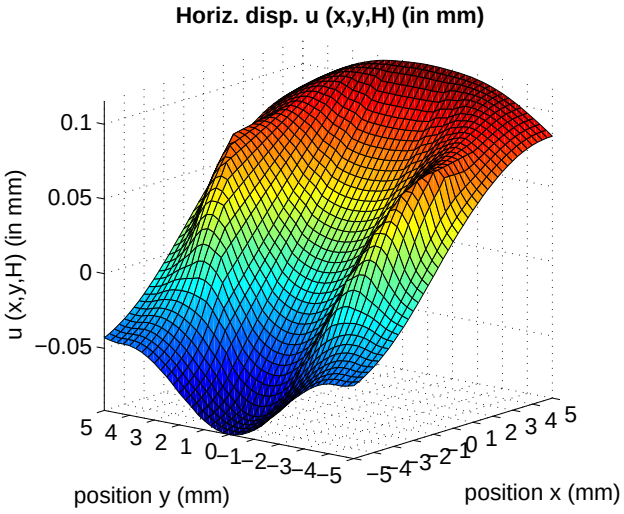

FIGURE 3.12: Surface plot of $u(x, y, H)$.

Figure 3.13 shows the contour lines of the lateral displacement field. As expected, the level lines of $v(x, y, H)$ are parallel to the x-axis in the sticking region which, referring to (3.26), confirms that v is constant across segments of constant ordinate within the stick-contact zone where w_{t_y} is equal to zero.

The sign of v on Figure 3.13 indicates that, as a result of vertical pressure, the sphere pushes the subbase laterally, away from its path as it is moving forward. Conversely, according to the quiver plot on Figure 3.14, the sphere exerts surface frictions on the foundation that are oriented inwards (i.e. towards the central line of movement). As a result of these opposite actions, the lateral displacement field increases linearly with the distance from the centerline as revealed by the constant

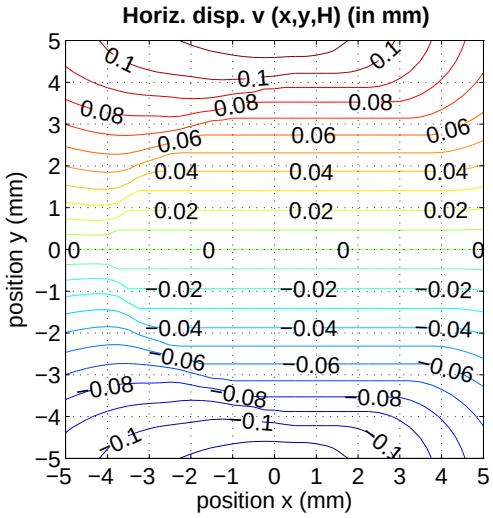

FIGURE 3.13: Contour plot of $v(x, y, H)$.

spacing, in the stick-contact zone, between level lines of v, on Figure 3.13. In the slipping region, as well as in the vicinity of the contact area, surface interactions fade which causes the foundation to move further away as revealed by a closer spacing between contour lines of v. At a larger distance from the x-axis, the sphere's influence decreases and the lateral displacement field behaves accordingly.

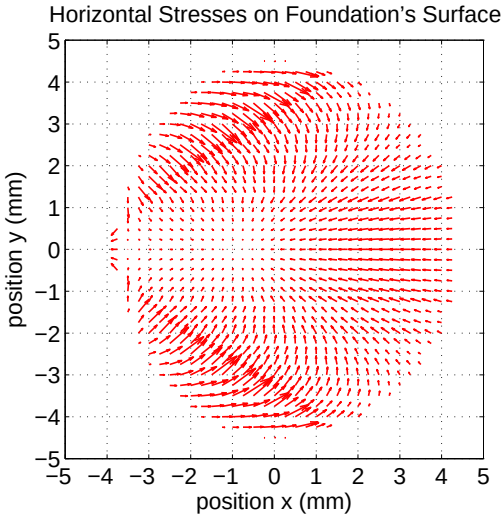

FIGURE 3.14: Horizontal stresses on foundation's surface (quiver plot).

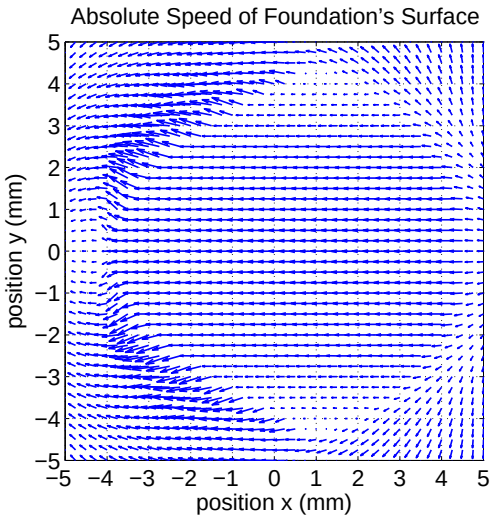

FIGURE 3.15: Absolute speed of foundation's surface (quiver plot).

A quiver plot of the absolute velocity field across the foundation's surface is given in Figure 3.15. Consistently with all previous observations, it may be seen that, under the influence of the incoming sphere and as a result of continuum mechanics, the layer moves laterally away from the x-axis before it is actually reached by the sphere. Once it becomes part of the stick-contact area, the subbase is maintained by surface friction. It is swept under the sphere and travels backwards in a straight line. In the slip-contact regions, the frictional limit is exceeded and the layer's surface moves away from the x-axis under the influence of unbalanced volume forces. Behind the sphere, the foundation's surface starts recovering its original configuration. Comparing local inclinations of the velocity field, between regions that are located in front and at the back of the moving sphere, one can tell that recovery occurs at a slower rate than the one at which deformation takes place. Beyond the local disturbances of the velocity field, which may be associated with wake effects in fluids, and are due to friction, this observation is further explained by the time-dependent behavior of the foundation material. The rates at which displacements occur depend on the relaxation spectrum of the viscoelastic layer. In the present case whereby a simple three-parameter model

is used, with f set equal to 1, the creep time is twice as large as the relaxation time.

3.6 Summary

Simple algorithms for solving steady-state frictional rolling contact problems in two and three dimensions were presented in this chapter. These algorithms constitute appealing alternatives to fully comprehensive contact solving strategies involving more complex implementations. In contrast with other 'simplified' theories based on very limiting assumptions, the cores of our contact algorithms only rely on general principles: (i) the "normal-contact" subroutine determines the (possibly discontinuous) contact surface by resolving geometrical conflicts and eliminating unacceptable surface tractions as they arise, and (ii) the "stick-slip" subroutine determines the (possibly discontinuous) regions of same tangential contact-nature by eliminating differential motions in the sticking regions and enforcing frictional limitations in the slipping regions. The proposed algorithms are formulated in the context of small deformations and applied to the cases of a rigid cylinder and a rigid sphere rolling on a linear viscoelastic layer of finite thickness, in two and three dimensions, respectively. These formulations pose no limitations regarding the layer's thickness or the viscoelastic model and are easily adapted to handle deformable indenters by solving for stresses and strains on two candidate contact surfaces simultaneously. The proposed contact algorithms can also be extended to problems including material nonlinearities, provided that the linear systems (3.12) and (3.16) in 2D, or (3.21) and (3.35)-(3.37) in 3D, are replaced by their nonlinear counterparts and handled using a suitable iterative solving scheme, embedded in the contact subroutines. Furthermore, the small-strain assumption can be dropped and the method extended to handle finite deformations by accounting for the horizontal displacements of the nodes while checking for geometrical conflicts. In order to illustrate the functioning of the proposed algorithms and demonstrate their capabilities, two application exam-

ples were treated. Results from the examples were presented, discussed and related to a certain extent. The algorithms showed to be robust and efficient at solving the two and three-dimensional rolling contact problems on which they were tried. It is noteworthy that full solutions to three-dimensional problems are undeniably rich and constitute an important contribution to understanding their underlying physics.

4

Three-dimensional boundary element formulation of an incompressible viscoelastic layer of finite thickness applied to the rolling resistance of a rigid sphere

4.1 Preamble

A three-dimensional boundary element formulation of an incompressible viscoelastic layer of finite thickness is proposed, in a moving frame of reference. The formulation is based on two-dimensional Fourier series expansions of relevant mechanical fields in the continuum of the layer. The linear viscoelastic material is characterized, in the most general way, by its frequency-domain master curves. The presented methodology results in a compliance matrix for the layer's upper boundary, which includes the effects of steady-state motion and can be used in any contact problem-solving strategy. The proposed formulation is used, in combination with a contact solver, to build a full three-dimensional model for the steady-state rolling/sliding resistance incurred by a rigid sphere on the layer. Energy losses include viscoelastic damping and surface friction. The model is tested and its results are found to be

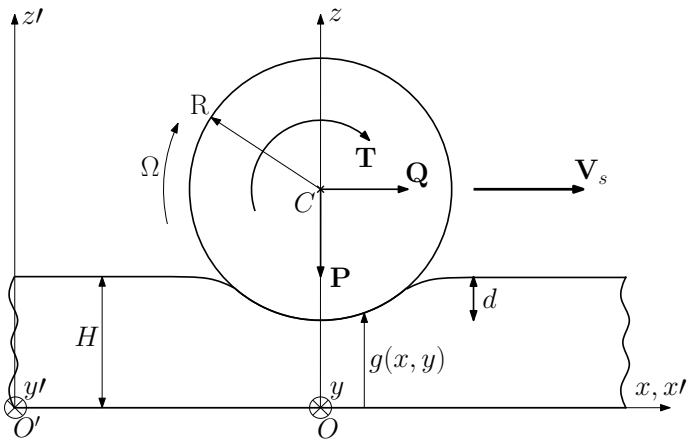

FIGURE 4.1: General model and coordinate systems.

consistent with existing solutions in limiting cases. An example is explored and the corresponding results are used to illustrate the influence of different parameters on the rolling resistance. General aspects of previously-described dependences are confirmed.

4.2 Defining rolling resistance

Figure 4.1 shows a round rigid object (cylinder or sphere of center C and radius R) rolling in steady-state conditions, on a viscoelastic layer of finite thickness H. The object moves in direction x at a constant linear velocity V_s while rotating about its axis at a rotational speed Ω. It is subjected to a vertical load P (positive downwards), a driving horizontal force Q (positive in the direction of increasing x) and a driving torque T (positive clockwise). The indentation d corresponds to the maximum penetration of the rolling object below the surface of the unloaded layer.

Because the contact surface takes the form of the rigid object, tangential shear stresses are circumferential and normal stresses are radial, with respect to a polar coordinate system centered at point C. However, contact stresses can be re-expressed in the Cartesian coordinate system $Oxyz$ as well.

For the purposes of this work, rolling resistance is defined as a conceptual horizontal resisting force R_r, expressed as a positive quantity. If it were to be applied at the axis of the moving object, the rolling resistance would dissipate energy at a rate that is equivalent to the power dissipation actually incurred by the system. Rolling resistance R_r is related to Q and T by

$$R_r = Q + \frac{T\Omega}{V_s}. \tag{4.1}$$

In equation (4.1), R_r is the rolling resistance corresponding to the total dissipated power. It is considered here that, in the absence of surface friction, rolling resistance is entirely due to viscous dissipations in the bulk. In such cases, the value of a driving torque is indeterminate, as it can not be equilibrated, and rolling resistance is equal to the sum of the horizontal projection of the radial contact forces. Because of the asymmetry of these forces, the rolling resistance is non-zero.

In the presence of friction, the interfacial shear stresses are not zero and a driving torque T can be balanced by either taking the moment of the tangential contact forces about the roller axis, or taking moments of the vertical and horizontal components of the contact forces about the same axis. Surface frictions influence rolling resistance in two ways: (i) directly, by means of their resisting work localized in the slipping regions of the contact surface, and (ii) indirectly, as demonstrated by Munisamy et al. (1991), by modifying the (frictionless) contact pressure distribution, which further impacts the global energy balance. The contribution of slipping friction to rolling resistance may be evaluated as follows

$$R_r^F = \frac{1}{V_s} \int_{A_c} \mathbf{w}_t . \boldsymbol{\tau}_t dA, \tag{4.2}$$

where A_c stands for the contact area, $\mathbf{w}_t$ is the local tangent differential speed between the sphere and the foundation layer and $\boldsymbol{\tau}_t$ corresponds to the tangent stress

field across the contact interface. In the presence of friction, the rolling resistance attributed to the viscoelastic behavior of the layer, is obtained by subtraction

$$R_r^V = R_r - R_r^F. \tag{4.3}$$

A common case is when the horizontal driving force Q is applied at the top of the moving object, thus generating a dependent torque $T = QR$. Substituting into expression (4.1) yields

$$R_r = Q(1 + \frac{R\Omega}{V_s}). \tag{4.4}$$

4.3 Governing equations

Following the development of Qiu (2006), the viscoelastic layer of thickness H is assumed to be incompressible, sustains small deformations and behaves linearly. As shown in Figure 4.1, $Oxyz$ corresponds to a moving coordinate system traveling with the sphere, while $O'x'y'z'$ remains at rest. Both coordinate systems are related according to

$$x = x' - V_s t, \qquad y = y', \qquad \text{and} \qquad z = z'. \tag{4.5}$$

Also, in the traveling coordinate system, material derivatives are expressed such that time becomes an implicit variable

$$\frac{D}{Dt} = -V_s \frac{\partial}{\partial x} \qquad ; \qquad \frac{D^2}{Dt^2} = V_s^2 \frac{\partial^2}{\partial x^2}. \tag{4.6}$$

The equilibrium equations for the elastomer in $O'x'y'z'$ are given, in tensorial form, by

$$\rho \frac{D^2\mathbf{u}}{Dt^2} = \mathbf{div}'(\mathbf{s}) - \mathbf{grad}'(p), \tag{4.7}$$

where $\mathbf{u} =< u, v, w >^T$ is the displacement field, ρ stands for the material's density, p is the pressure and $\mathbf{s}$ denotes the stress deviator. Equation (4.7) may be expressed

in $Oxyz$ using (4.6) and hence becomes

$$\rho V_s^2 \frac{\partial^2 \mathbf{u}}{\partial x^2} = \mathbf{div}(\mathbf{s}) - \mathbf{grad}(p). \tag{4.8}$$

The constitutive behavior of the incompressible viscoelastic material may be described using the following general integral equations (e.g. Flügge, 1975; Lakes, 2009)

$$\mathbf{s}(t) = 2 \int_{-\infty}^{t} G(t-s) \frac{d\boldsymbol{\epsilon}(s)}{ds} ds, \tag{4.9}$$

where $G(t)$ is the shear relaxation modulus of an isotropic elastomer and $\boldsymbol{\epsilon}$ corresponds to the small-stain tensor. Due to incompressibility, $\text{trace}(\boldsymbol{\epsilon}) = 0$.

4.4 Boundary conditions

It is assumed that the foundation strip is fully adherent to its rigid subbase, which implies boundary conditions on the displacements at $z = 0$

$$\mathbf{u}(x, y, z = 0) = 0, \quad \forall (x, y). \tag{4.10}$$

Upper boundary conditions for the elastomer are determined by the contact problem occurring at the interface between the moving object and the foundation. The normal contact boundary conditions are expressed as

$$H + w(x, y, z = H) < g(x, y) \quad \text{if} \quad \sigma_z = 0, \tag{4.11}$$

$$H + w(x, y, z = H) = g(x, y) \quad \text{if} \quad \sigma_z < 0, \tag{4.12}$$

where, designating by z_c the coordinate of point C on the z-axis (see Figure 4.1), $g(x, y)$ corresponds to an analytical expression for the lower surface of the moving object, i.e. for a sphere

$$g(x, y) = z_c - \sqrt{R^2 - x^2 - y^2}. \tag{4.13}$$

In small deformations, using equation (4.6), the horizontal components of the differential speed in directions x and y are given by

$$w_{tx} = V_s \left(1 + \frac{\partial u}{\partial x}\right) - R(y)\Omega, \text{ where } R(y) = \sqrt{R^2 - y^2}, \tag{4.14}$$

$$w_{ty} = V_s \left(\frac{\partial v}{\partial x}\right). \tag{4.15}$$

The tangential contact boundary conditions involve the coefficient of sliding friction μ for the interface, as well as the components w_{tx} and w_{ty} of the differential speed, across the contact area

$$\tau_{xz}^2(H) + \tau_{yz}^2(H) < \mu^2 \sigma_z^2(H) \qquad \text{if} \quad w_{t_x}^2 + w_{t_y}^2 = 0, \tag{4.16}$$

$$\tau_{xz}^2(H) + \tau_{yz}^2(H) = \mu^2 \sigma_z^2(H) \qquad \text{otherwise.} \tag{4.17}$$

Inequality (4.16) applies in stick-contact conditions (i.e. in the case of an absence of relative movement between touching points) while equality (4.17) prevails at contact points where slipping occurs. In the latter case, following Coulomb's law of friction, the orientation of the limiting tangential contact stress must be consistent with the direction of relative movement. This additional slip-contact condition may be expressed by the constraint

$$\tau_{xz} w_{ty} - \tau_{yz} w_{tx} = 0. \tag{4.18}$$

Because the present three-dimensional case is treated using two-variable Fourier series, the following periodic boundary conditions are introduced, in both horizontal directions x and y for all the physical quantities ψ involved in the problem

$$\psi(x, y, z) = \psi(x + L_x, y, z), \quad \forall (x, y), \tag{4.19}$$

$$\psi(x, y, z) = \psi(x, y + L_y, z), \quad \forall (x, y). \tag{4.20}$$

Geometrically non-periodic configurations may be handled as well by prescribing values of the spatial periods L_x and L_y that are much larger than the dimensions of the contact surface.

4.5 Two-variable Fourier series

The steady state solution may be expressed using complex exponential Fourier series in the two variables x and y. Letting $f(x, y, z)$ be a generic physical quantity of the problem with $f \in \{\ u,\ v,\ w,\ \epsilon_x,\ \epsilon_y,\ \epsilon_z,\ \gamma_{xy},\ \gamma_{xz},\ \gamma_{yz},\ p,\ s_x,\ s_y,\ s_z,\ \tau_{xy},\ \tau_{xz},\ \tau_{yz},\ \sigma_z\ \}$, its complex Fourier series expansion is written as

$$f(x, y, z) = \sum_{m,n=-\infty}^{+\infty} f_{mn}(z) e^{i\frac{2\pi m}{L_x}x} e^{i\frac{2\pi n}{L_y}y}, \tag{4.21}$$

where corresponding Fourier coefficients are defined by

$$f_{mn}(z) = \frac{1}{L_x L_y} \int_{y=0}^{L_y} \int_{x=0}^{L_x} f(x, y, z) e^{-i\frac{2\pi m}{L_x}x} e^{-i\frac{2\pi n}{L_y}y} dxdy. \tag{4.22}$$

Since $f(x, y)$ is real, $f_{m,-n} = \bar{f}_{-m,n}$ and $f_{-m,-n} = \bar{f}_{m,n}$, which reduces computational costs.

4.6 General solutions to Fourier coefficients

Substituting material coordinates for moving reference coordinates (i.e. $x = x' - V_s t$, $y = y'$ and $z = z'$) in expression (4.21) we may write

$$f(x', y', z', t) = \sum_{m,n=-\infty}^{+\infty} c_{mn}(x', y', z') e^{-i\frac{2\pi m}{L_x}V_s t}, \tag{4.23}$$

$$c_{mn}(x', y', z') = f_{mn}(z') e^{i\frac{2\pi m}{L_x}x'} e^{i\frac{2\pi n}{L_y}y'}, \tag{4.24}$$

and thus interpret that the material particles of the foundation (x', y', z') are subjected to an infinite sum of harmonic excitations to which, using the principle of superposition, the fundamental theory of viscoelasticity applies separately. Angular frequencies of individual harmonic movements are given by

$$\omega_m = -\frac{2\pi m}{L_x} V_s. \tag{4.25}$$

Identifying the generic quantity $f(x', y', z', t)$ with each component of stress ($\mathbf{s}$) and strain ($\boldsymbol{\epsilon}$) deviators, then applying the fundamental theory of viscoelasticity to each harmonic, while using the orthogonality property of complex exponentials, leads to the following relation between Fourier coefficient tensors

$$\mathbf{s}_{mn}(z) = 2G_m^* \boldsymbol{\epsilon}_{mn}(z), \tag{4.26}$$

where $G_m^* = G'(\omega_m) + iG''(\omega_m)$ is the dynamic shear modulus, $G'(\omega_m)$ and $G''(\omega_m)$ corresponding to the storage and loss moduli, respectively. The following shorthand parameters will be used in the sequel

$$\begin{aligned} &\nu_x = 2\pi m/L_x \ ; \ \nu_y = 2\pi n/L_y, \\ &\beta_x = (4\nu_x^2 + \nu_y^2)G_m^* - \rho V_s^2 \nu_x^2, \\ &\beta_y = (\nu_x^2 + 4\nu_y^2)G_m^* - \rho V_s^2 \nu_x^2, \\ &\beta_{xy} = 3\nu_x \nu_y G_m^*. \end{aligned} \tag{4.27}$$

Small strain complex Fourier coefficients are related to their deformation counterparts differentiating (4.21)

$$\epsilon_{x,mn}(z) = i\nu_x u_{mn}(z), \tag{4.28}$$

$$\epsilon_{y,mn}(z) = i\nu_y v_{mn}(z), \tag{4.29}$$

$$\epsilon_{z,mn}(z) = \dot{w}_{mn}(z), \tag{4.30}$$

$$\gamma_{xy,mn}(z) = i\nu_x v_{mn}(z) + i\nu_y u_{mn}(z), \tag{4.31}$$

$$\gamma_{xz,mn}(z) = i\nu_x w_{mn}(z) + \dot{u}_{mn}(z), \tag{4.32}$$

$$\gamma_{yz,mn}(z) = i\nu_y w_{mn}(z) + \dot{v}_{mn}(z). \tag{4.33}$$

where the up dot denotes the derivative with respect to z. Equilibrium equations are transformed into linear ordinary differential equations relating stresses to displacements, in terms of their respective Fourier coefficients, by plugging the generic

Fourier expansion (4.21) into expression (4.8) and further using the orthogonality property of complex exponentials

$$-\rho V_s^2 \nu_x^2 u_{mn} = i\nu_x s_{x,mn} + i\nu_y \tau_{xy,mn} + \dot{\tau}_{xz,mn} - i\nu_x p_{mn}, \tag{4.34}$$

$$-\rho V_s^2 \nu_x^2 v_{mn} = i\nu_x \tau_{xy,mn} + i\nu_y s_{y,mn} + \dot{\tau}_{yz,mn} - i\nu_y p_{mn}, \tag{4.35}$$

$$-\rho V_s^2 \nu_x^2 w_{mn} = i\nu_x \tau_{xz,mn} + i\nu_y \tau_{yz,mn} + \dot{s}_{z,mn} - \dot{p}_{mn}. \tag{4.36}$$

Additional ODE's are obtained by substituting (4.28-4.33) into (4.26) in order to eliminate the strains

$$s_{x,mn} = 2i\nu_x G_m^* u_{mn}, \tag{4.37}$$

$$s_{y,mn} = 2i\nu_y G_m^* v_{mn}, \tag{4.38}$$

$$s_{z,mn} = 2G_m^* \dot{w}_{mn}, \tag{4.39}$$

$$\tau_{xy,mn} = iG_m^*(\nu_y u_{mn} + \nu_x v_{mn}), \tag{4.40}$$

$$\tau_{xz,mn} = G_m^*(\dot{u}_{mn} + i\nu_x w_{mn}), \tag{4.41}$$

$$\tau_{yz,mn} = G_m^*(\dot{v}_{mn} + i\nu_y w_{mn}). \tag{4.42}$$

A reduced number of six state variables is retained. The chosen state variables are ordered and stored in a complex-valued state vector $\mathbf{q}_{mn}(z)$, as follows

$$\mathbf{q}_{mn} = \langle w_{mn}, u_{mn}, v_{mn}, \sigma_{z,mn}, \tau_{xz,mn}, \tau_{yz,mn} \rangle^T. \tag{4.43}$$

Equations (4.34)-(4.42) are rearranged such that only the chosen state variables remain. The following system of linear ODE's is finally obtained

$$\dot{\mathbf{q}}_{mn} = \mathbf{A}_{mn}\mathbf{q}_{mn}, \tag{4.44}$$

where the complex valued matrix $\mathbf{A}_{mn}$ is given by

$$\mathbf{A}_{mn} = \begin{bmatrix} 0 & -i\nu_x & -i\nu_y & 0 & 0 & 0 \\ -i\nu_x & 0 & 0 & 0 & G_m^{*^{-1}} & 0 \\ -i\nu_y & 0 & 0 & 0 & 0 & G_m^{*^{-1}} \\ -\rho V_s^2 \nu_x^2 & 0 & 0 & 0 & -i\nu_x & -i\nu_y \\ 0 & \beta_x & \beta_{xy} & -i\nu_x & 0 & 0 \\ 0 & \beta_{xy} & \beta_y & -i\nu_y & 0 & 0 \end{bmatrix}. \tag{4.45}$$

The general solution to system (4.44) has the following form

$$\mathbf{q}_{mn}(z) = \mathbf{T}_{mn}(z)\mathbf{q}_{mn}(0) \text{ for } (0 \leq z \leq H), \tag{4.46}$$

where $\mathbf{T}_{mn}(z) = \exp(\mathbf{A}_{mn}z)$ is the complex matrix exponential of $\mathbf{A}_{mn}z$, which may be readily computed using mathematical software handling complex numbers. Alternatively, the following real valued system of double size may be solved

$$\begin{bmatrix} Re(\dot{\mathbf{q}}_{mn}) \\ -Im(\dot{\mathbf{q}}_{mn}) \end{bmatrix} = \begin{bmatrix} Re(\mathbf{A}_{mn}) & -Im(\mathbf{A}_{mn}) \\ Im(\mathbf{A}_{mn}) & Re(\mathbf{A}_{mn}) \end{bmatrix} \begin{bmatrix} Re(\mathbf{q}_{mn}) \\ -Im(\mathbf{q}_{mn}) \end{bmatrix}, \tag{4.47}$$

where $Re()$ and $Im()$ correspond, respectively, to the real and imaginary parts of a given quantity.

Displacement boundary conditions (i.e. $u_{mn}(0)$, $v_{mn}(0)$, $w_{mn}(0)$) are known at the bottom of the foundation strip while the boundary conditions on stresses (i.e. $\sigma_{z,mn}(H)$, $\tau_{xz,mn}(H)$, $\tau_{yz,mn}(H)$) result from the surface tractions applied on the contact surface. This two-point boundary value problem is solved by dividing the vector of unknowns $\mathbf{q}_{mn}$ into two subvectors:

$$\mathbf{q}_{mn}(z) = \left\langle \mathbf{d}_{mn}^T(z), \mathbf{f}_{mn}^T(z) \right\rangle^T, \tag{4.48}$$

where

$$\mathbf{d}_{mn}(z) = \langle w_{mn}(z), u_{mn}(z), v_{mn}(z) \rangle^T,$$

$$\mathbf{f}_{mn}(z) = \langle \sigma_{z,mn}(z), \tau_{xz,mn}(z), \tau_{yz,mn}(z) \rangle^T,$$

and writing solution (4.46) in the form

$$\begin{bmatrix} \mathbf{d}_{mn}(z) \\ \mathbf{f}_{mn}(z) \end{bmatrix} = \begin{bmatrix} \mathbf{T}_{mn,11}(z) & \mathbf{T}_{mn,12}(z) \\ \mathbf{T}_{mn,21}(z) & \mathbf{T}_{mn,22}(z) \end{bmatrix} \times \begin{bmatrix} \mathbf{d}_{mn}(0) \\ \mathbf{f}_{mn}(0) \end{bmatrix}. \tag{4.49}$$

Since $\mathbf{d}_{mn}(0) = \mathbf{0}$, rearranging expression (4.49) results in equation (4.50) relating the Fourier coefficients of displacements and stresses at $z = H$

$$\mathbf{d}_{mn}(H) = \mathbf{T}_{mn,12}(H)\mathbf{T}_{mn,22}^{-1}(H)\mathbf{f}_{mn}(H), \tag{4.50}$$

which opens the way to developing a boundary element formulation reflecting the foundation's behavior.

4.7 Boundary element formulation

Let K_x and K_y be the number of nodes discretizing the candidate contact surface, in directions x and y respectively, as illustrated in figure (4.2). The total number of nodes is hence $N_T = K_x K_y$. The boundary element compliance matrix $\mathbf{C}$ is defined by the constitutive equation

$$\begin{bmatrix} \mathbf{C}_{WW} & \mathbf{C}_{WU} & \mathbf{C}_{WV} \\ \mathbf{C}_{UW} & \mathbf{C}_{UU} & \mathbf{C}_{UV} \\ \mathbf{C}_{VW} & \mathbf{C}_{VU} & \mathbf{C}_{VV} \end{bmatrix} \times \begin{bmatrix} \mathbf{F}_W \\ \mathbf{F}_U \\ \mathbf{F}_V \end{bmatrix} = \begin{bmatrix} \mathbf{W} \\ \mathbf{U} \\ \mathbf{V} \end{bmatrix}, \tag{4.51}$$

where $\mathbf{F} = \left\langle \mathbf{F}_W^T, \mathbf{F}_U^T, \mathbf{F}_V^T \right\rangle^T$ and $\mathbf{D} = \left\langle \mathbf{W}^T, \mathbf{U}^T, \mathbf{V}^T \right\rangle^T$ correspond to the nodal displacement vector and the nodal force vector respectively, each subvector containing nodal components in a given direction. Nodal forces, applied at a given node N, are further associated with the corresponding surface traction using formulas that are similar to the one given below in the normal direction

$$\sigma_z^N(x, y, H) = \begin{cases} \frac{F_W^N}{a_x a_y}, & \text{if } \begin{cases} x^N - \frac{a_x}{2} \leq x \leq x^N + \frac{a_x}{2} \\ y^N - \frac{a_y}{2} \leq y \leq y^N + \frac{a_y}{2} \end{cases} \\ 0, & \text{otherwise.} \end{cases} \tag{4.52}$$

4.8 Building the compliance matrix

Entry $\mathbf{C}_{PQ}(M, N)$ of the compliance matrix $\mathbf{C}$ matches with the displacement in the direction corresponding to index "$P \in \{U, V, W\}$", at node M, when a unit force is applied at node N, in the direction corresponding to index "$Q \in \{U, V, W\}$". Hence in theory, the entries of matrix $\mathbf{C}$ may be obtained by applying unit forces, separately in each direction x, y and z and at each node, while determining the corresponding nodal displacements over the entire grid.

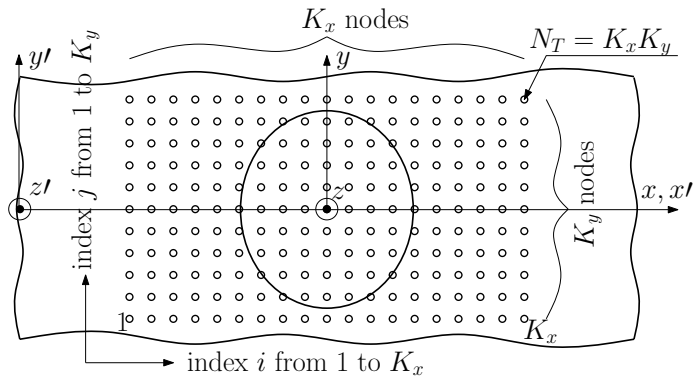

FIGURE 4.2: Discretization of the candidate contact surface.

The computational cost of building compliance matrices increases quadratically with the number of discretization nodes and the truncation order. However, the cost can be reduced: in practice, provided that the spacings a_x and a_y between the nodes are uniform, in each of directions x and y, one may take advantage of configurational similarities such that less than six well-chosen columns of $\mathbf{C}$ need to be formed explicitly, by adding Fourier terms. Furthermore, depending on each problem's particular assumptions, mainly assumptions pertaining to friction along with the types of results that are specifically needed, building the entire compliance matrix may not be necessary. For instance, in applications where friction may be neglected one can set $\mathbf{F}_U = \mathbf{F}_V = \mathbf{0}$. Hence, provided that the horizontal displacements are not explicitly sought, only $1/9^{th}$ of the compliance matrix needs to be formed as (4.51) reduces to

$$\mathbf{C}_{WW}\mathbf{F}_W = \mathbf{W}. \tag{4.53}$$

Further details are given below on building relevant parts of the compliance matrix in a frictionless setting where only vertical unit forces need to be applied to appropriate nodes. Other parts of the compliance matrix may be obtained by following a very similar approach in the horizontal directions.

Letting i (from 1 to K_x) and j (from 1 to K_y) be the nodal indexes in directions of increasing x and y respectively, as shown in figure (4.2), a global node numbering

may be obtained through the expression $N = (j-1)K_x + i$. With this numbering convention, unit vertical forces need only be applied to nodes number 1 and K_x. Indeed, if node couples (M_1, N_1) and (M_2, N_2) have the same relative position, i.e. $(x_2^M - x_2^N) = (x_1^M - x_1^N)$ and $(y_2^M - y_2^N) = \pm(y_1^M - y_1^N)$, the vertical displacement of M_1 due to a vertical point load applied at N_1 will be the same as the displacement of M_2 when the load is applied at N_2. Note however that, due to motion along the x-axis, Oy is not an axis of symmetry. Hence, all other entries in matrices $\mathbf{C}_{WW}$, $\mathbf{C}_{UW}$ and $\mathbf{C}_{VW}$ can be deduced from columns 1 and K_x and therefore need not be formed by explicitly computing and adding Fourier terms. Similar considerations also apply to other submatrices of $\mathbf{C}$ in the case of frictional contact in 3D.

Implementing such configurational similarities in practice, drastically reduces the computational cost of building 3D compliance matrices as well as their storage space: both are divided by $N_T/2$. For instance, in the frictional example given in Section 4.11, the candidate contact surface is discretized using $N_T = 41 \times 41 = 1681$ nodes, in which case, the computational cost of forming compliance matrices is roughly divided by 840. It takes for instance approximately 18 minutes (instead of days) using an Intel® Core™ i7 M620 CPU with 4 MB of cache memory and a clock speed of 2.66 GHz to compute a full 3D compliance matrix including $N_{t_x} = N_{t_y} = 500$ Fourier terms. Applying the same reasoning in two dimensions based on $N_T = 80$ nodes, the method presented by Qiu (2006) is rendered roughly 40 times more efficient.

By means of expression (4.52), a unit vertical force applied at a candidate contact node N is associated with the following normal traction

$$\sigma_z^N(x, y, H) = \begin{cases} \frac{1}{a_x a_y}, & \text{if } \begin{cases} x^N - \frac{a_x}{2} \leq x \leq x^N + \frac{a_x}{2} \\ y^N - \frac{a_y}{2} \leq y \leq y^N + \frac{a_y}{2} \end{cases} \\ 0, & \text{otherwise.} \end{cases} \tag{4.54}$$

The corresponding complex Fourier coefficients are obtained for relevant combination

cases of m and n, using expression (4.22) in the following form

$$\sigma_{z,mn}(z) = \frac{1}{L_x L_y} \int_{y=0}^{L_y} \int_{x=0}^{L_x} \sigma_z(x,y,z) e^{-i\frac{2\pi m}{L_x}x} e^{-i\frac{2\pi n}{L_y}y} dxdy, \tag{4.55}$$

with the result given by

$$\sigma_{z,mn}^N(H) = \frac{\sin(\frac{\pi m a_x}{L_x})}{\pi m a_x} \frac{\sin(\frac{\pi n a_y}{L_y})}{\pi n a_y} e^{-i2\pi(\frac{m}{L_x}x^N + \frac{n}{L_y}y^N)}, \tag{4.56}$$

for $m \neq 0$ and $n \neq 0$. The remaining cases are

$$\sigma_{z,0n}^N(H) = \frac{e^{-i\frac{2\pi n}{L_y}y^N}}{\pi n L_x a_y} \sin(\frac{\pi n a_y}{L_y}) \text{ for } m = 0 \text{ and } n \neq 0, \tag{4.57}$$

$$\sigma_{z,m0}^N(H) = \frac{e^{-i\frac{2\pi m}{L_x}x^N}}{\pi m L_y a_x} \sin(\frac{\pi m a_x}{L_x}) \text{ for } m \neq 0 \text{ and } n = 0, \tag{4.58}$$

$$\sigma_{z,00}^N(H) = \frac{1}{L_x L_y} \text{ for } m = 0 \text{ and } n = 0. \tag{4.59}$$

It is now possible to determine Fourier coefficients for the displacements using expression (4.50). We hence write

$$\mathbf{f}_{mn}(H) = \left\langle \sigma_{z,mn}^N(H), 0, 0 \right\rangle^T, \tag{4.60}$$

$$\mathbf{d}_{mn}^N(H) = \left\langle w_{mn}^N(H), u_{mn}^N(z), v_{mn}^N(z) \right\rangle^T = \mathbf{T}_{mn,12}(H)\mathbf{T}_{mn,22}^{-1}(H)\mathbf{f}_{mn}^N(H). \tag{4.61}$$

Corresponding Fourier terms are finally assembled into the entries of the relevant compliance submatrix. In this case

$$\mathbf{C}_{WW}(M,N) = \sum_{m,n=-\infty}^{+\infty} w_{mn}^N(H) e^{i\frac{2\pi m}{L_x}x^M} e^{i\frac{2\pi n}{L_y}y^M}. \tag{4.62}$$

4.9 Solving the rolling contact problem

At this point both physical entities have been modeled, i.e. described in mathematical terms. The behavior of the viscoelastic layer, in the moving frame of reference,

is comprehensively depicted by the boundary element formulation given by equation (4.51) while the hard rolling object is fully described by its lower geometrical profile (4.13).

Solving the rolling contact problem mainly involves the implementation of normal and tangential contact boundary conditions as given by sets of equations (4.11)-(4.12) and (4.16)-(4.18), respectively. As performed by Qiu (2006) in a two-dimensional context, while implementing the tangential boundary conditions, specific constraints are imposed on the stick-contact nodes such that the absence of relative motion is satisfied in regions of sticky contact. Because V_s and Ω are global constants, it can be derived from (4.14) and (4.15) that $\frac{\partial u}{\partial x}(x, y, H)$ and $v(x, y, H)$ remain both constant across stick-contact zones, in each plane of constant y. Continuity of these fields, in direction x, is imposed across leading edge stick-contact nodes.

Nonlinear constraints resulting from contact problems are usually difficult to model. They may be enforced using FEM schemes as detailed, for instance, in Oden and Lin (1986) or Zienkiewicz and Taylor (2005). Alternatively, Zéhil and Gavin (2013c) (see Chapter 3) describe a relatively simple solving strategy for frictional rolling contact problems in two and three dimensions. The latter is used in its 3D version for the purposes of this work in order to determine the problem unknowns: (i) the vertical forces acting on all contact nodes, (ii) the horizontal forces acting on stick-contact nodes, (iii) the vertical displacements of the free nodes, (iv) the horizontal displacements of all the nodes, (v) the indentation d and (vi) the rotational speed Ω. Rolling resistance (4.1) may finally be computed according to the following expression

$$R_r = \sum \mathbf{F}_U + \frac{T\Omega}{V_s}. \tag{4.63}$$

In the example of Section 4.11, rolling resistance results *with* and *without* surface friction are compared. The results *without* friction were obtained using a reduced ver-

sion of the contact solver, based on equation (4.53) derived by setting $F_U = F_V = 0$ (see Section 4.8), and on vertical equilibrium. In such cases, the rotational quantities T and Ω are indeterminate and the rolling resistance writes $\bar{R}_r = -\mathbf{x}^T\mathbf{F}_W/R$, where $\mathbf{x}$ is the nodal vector of x-coordinates.

4.10 Verification examples

In the present section, the three-dimensional model is tested in elastic and stationary conditions. The results are compared with those given by Jaffar (2008) and Jaffar (1997) for thick and thin foundation layers respectively.

4.10.1 Thick foundation

The stationary contact of a rigid sphere with an elastic layer of finite thickness H was examined by Jaffar (2008) in frictionless conditions. It was found that, for a relatively thick foundation strip in comparison with the contact radius r_c (i.e. $\gamma = r/r_c \leq 0.9$) the contact pressure distribution followed the form given by Hertz, i.e.

$$\sigma_z(r) = \frac{3P}{2\pi r_c^2}\sqrt{1-\left(\frac{r}{r_c}\right)^2}, \tag{4.64}$$

while the contact radius was given by the following expression

$$r_c = \left[\frac{PRD(1-\nu)}{8\pi G}\right]^{\frac{1}{3}}, \tag{4.65}$$

where G and ν are the shear modulus and Poisson's ratio respectively and D is defined as follows

$$D = 3\pi + 8\gamma^3\left(b_1 + \frac{2}{5}b_2\gamma^2\right), \tag{4.66}$$

with coefficients b_m expressed (for $m = 1, 2$) as

$$b_m = \left(-\frac{1}{4}\right)^m \int_0^\infty (1 - L(\omega))\,\omega^{2m} d\omega. \tag{4.67}$$

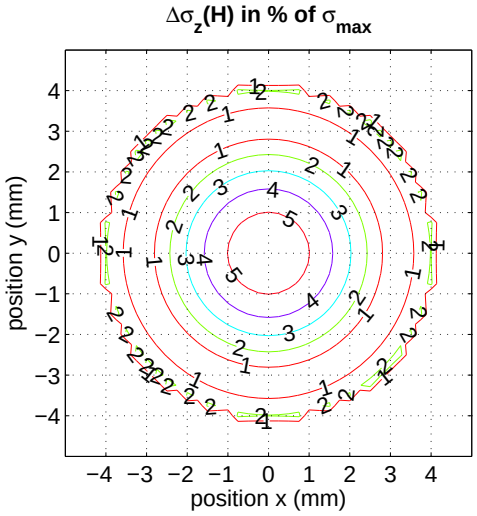

FIGURE 4.3: Relative difference between model and asymptotic pressure fields for $H = 5$mm.

For a foundation bonded to its substrate $L(w)$ is given by

$$L(\omega) = \frac{2\kappa \sinh(2\omega) - 4\omega}{2\kappa \cosh(2\omega) + 4\omega^2 + \kappa^2 + 1}, \text{ with } \kappa = 3 - 4\nu. \tag{4.68}$$

In order to simulate conditions by which the above estimates apply, we consider the case of a rigid sphere of radius $R = 2$ cm in stationary ($V_s = 0$ m/s) and frictionless ($\mu = 0$) contact with an elastic layer ($G'(\omega) = G_0 = 3.0$ MPa ; $G''(\omega) = 0$ MPa) of thickness $H = 5$ mm. A vertical load of $P = 100$ N is applied to the sphere. The periodic lengths are set to $L_x = L_y = 20$ cm and the nodal spacings are taken equal to $a_x = a_y = 0.25$ mm. The truncation orders are set to $N_{t_x} = N_{t_y} = 2000$.

The contact radius resulting from the 3D model is of 4.5 ± 0.125 mm, which is compatible with the one given by solving (4.65) and (4.66) i.e. 4.56 mm. Figure 4.3 shows a contour plot of the difference between pressure fields, which does not exceed $\approx 5\%$ of the maximum pressure at the center σ_{max}. Given the current precision settings on the 3D model and the fact that (4.66) corresponds to a truncated quantity, the comparison is quite satisfactory. Note that minor irregularities in the vicinity

of the outer contour arise from the fact that the rectangular grid cannot perfectly match the circular shape of the contact area while both pressure profiles are rapidly changing: referring to equation (4.64), it can be shown that $|d\sigma_z(r)/dr| \to \infty$ as $r \to r_c$.

4.10.2 Thin foundation

Jaffar (1997) provides an asymptotic solution to the stationary contact problem of a rigid sphere with a thin elastic and incompressible foundation at the distinguished limit $\epsilon = r_c/H \to 0$. In this case, the contact pressure takes the following form

$$\sigma_z(r) = \frac{3P}{\pi r_c^2}\left(1 - \left(\frac{r}{r_c}\right)^2\right)^2, \tag{4.69}$$

while the contact radius r_c may be expressed as

$$r_c = \left[\frac{48PRH^3}{\pi G(1+\nu)}\right]^{\frac{1}{6}}. \tag{4.70}$$

Taking the same parameters as in 4.10.1, the foundation's thickness is reduced to $H = 0.1$ mm and the sphere's radius increased to $R = 80$ m so that a relatively large contact radius can be obtained. A vertical load of $P = 10$ N is applied to the sphere.

The contact radius resulting from the 3D model is of 3.75 ± 0.125 mm, which is compatible with the solution given by (4.70) i.e. 3.7 mm. The contour plot in Figure 4.4 shows that the difference between pressure fields remains below $\approx 5\%$ of σ_{max}. The comparison is satisfactory given the finite precision of the 3D model and the fact that (4.69) corresponds to an asymptotic solution.

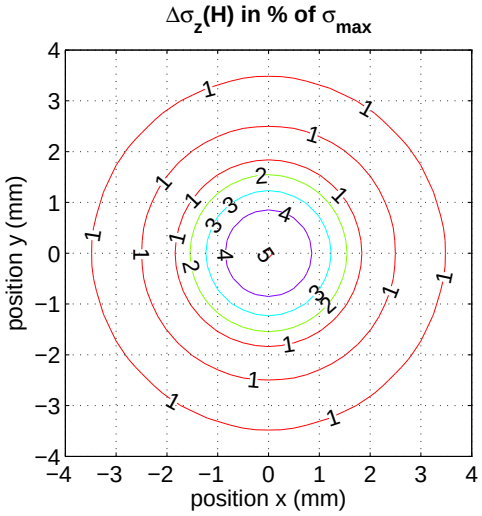

FIGURE 4.4: Relative difference between model and asymptotic pressure fields for $H = 0.1$mm.

4.11 Example of rolling with friction

4.11.1 Default parameters

Referring to equation (4.4) in Section 4.2, let us consider a rigid sphere of radius $R = 2$ cm driven by a horizontal force Q applied at the top. A concomitant vertical load of $P = 150$ N is applied at the center. The sphere is rolling with friction ($\mu = 0.2$), in steady state, at a linear speed $V_s = 0.05$ m/s on a viscoelastic layer of thickness $H = 5$ mm and density $\rho = 1000$ kg/m^3.

For illustrative purposes the foundation's material is modeled by a three parameter viscoelastic solid (see Figure 4.5) whose master curves are given by

$$\begin{aligned} G'(\omega) &= G_0(1+f)\frac{(1+f)+\omega^2\tau^2}{(1+f)^2+\omega^2\tau^2}, \\ G''(\omega) &= G_0(1+f)\frac{f\omega\tau}{(1+f)^2+\omega^2\tau^2}. \end{aligned} \tag{4.71}$$

where $G_o = G'(0) = (G_1G_2)/(G_1+G_2) = 3.0$ MPa is the static shear modulus, $\tau = \eta/G_2 = 0.25$ s is the creep time and $f = G_1/G_2 = 1$.

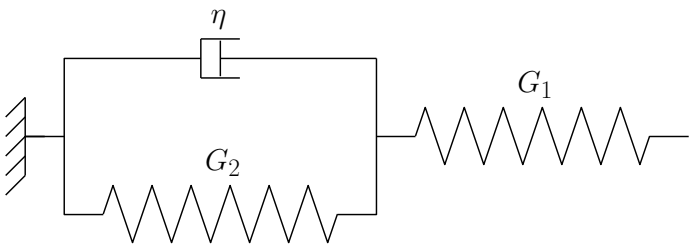

FIGURE 4.5: Three-parameter viscoelastic solid.

The spatial periods are set to $L_x = L_y = 20$ cm which, up to a speed of about 50 cm/s, is large enough to allow for sufficient (i.e. more than 80%) creep recovery of the foundation layer between two successive sphere arrivals. Based on the convergence results of Table 4.1, nodal spacings are set equal to $a_x = a_y = 0.25$ mm and truncation orders of $N_{t_x} = N_{t_y} = 2000$ are retained for the main calculations. Figures that require building multiple compliance matrices are drawn using $N_{t_x} = N_{t_y} = 500$, which is sufficient for plotting purposes.

In following subsections, two cases are compared: (i) a *frictional* case corresponding to the rolling speed V_s, the vertical load P and the driving torque $T = QR$, and (ii) a *frictionless* case characterized by the same rolling speed V_s and vertical load P. For illustration purposes, some of the parameters introduced in this subsection will be changed in the following ones, depending on the topic requirements.

4.11.2 General results

Figure 4.6 shows a contour plot of the vertical stress field $\sigma_z(x, y, z = H)$ over the contact area. The observed dissymmetry is mainly due to the viscoelastic behavior of the foundation layer and is responsible for the viscoelastic rolling resistance.

The rolling resistance is computed according to equations (4.2)-(4.4) which in this case yield a total rolling resistance of $R_r = 3.07$ N, from which less than 0.05 N originate from slipping friction.

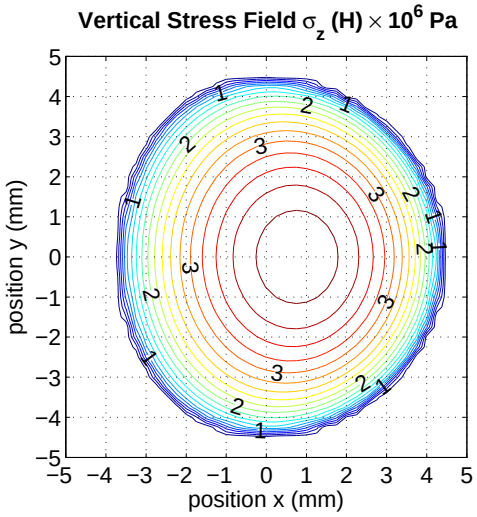

FIGURE 4.6: General results of the 3D model: vertical stress field $\sigma_z(x, y, H)$.

Table 4.1: Effects of nodal spacing and truncation order on convergence.

a (mm)	Truncation order N_t (Number of Terms)					
	500	1000	1500	2000	2500	3000
1.00	3.1129	3.1131	3.1135	3.1133	3.1135	3.1135
0.50	3.0138	3.0130	3.0130	3.0130	3.0130	3.0131
0.30	3.0212	3.0208	3.0206	3.0207	3.0206	3.0207
0.25	3.0259	3.0255	3.0257	3.0257	3.0257	3.0257
0.20	3.0252	3.0251	3.0255	3.0256	3.0255	3.0254
0.15	N/A	3.0258	3.0257	3.0257	3.0257	3.0257

4.11.3 Convergence table

In order to verify convergence, the rolling resistance was evaluated in frictionless conditions using the same nodal spacing in both directions (i.e. $a = a_x = a_y$) varying from 0.15 to 1 mm and the same truncation order in both spatial frequencies (i.e. $N_t = N_{t_x} = N_{t_y}$) ranging from 500 to 3000 terms. The resulting values are reproduced in Table 4.1 and fall within 3.4% of each other. It may furthermore be noted that, when the node spacing is less than or equal to 0.30 mm, the results are well within 0.2%, which is suitable for most engineering applications.

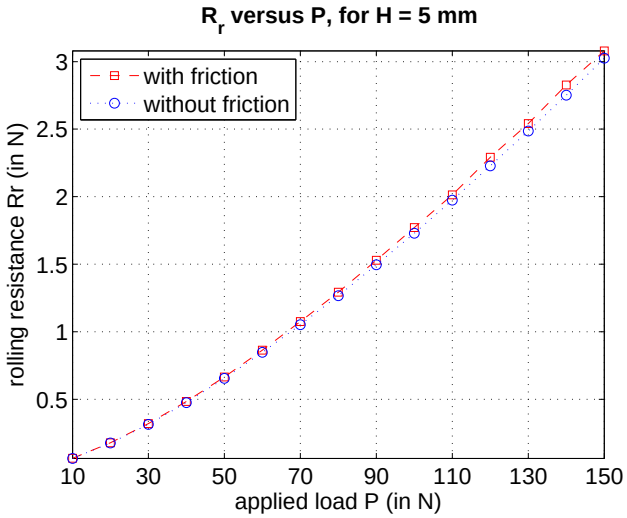

FIGURE 4.7: Influence of the vertical load on rolling resistance, for $H = 5$ mm.

Table 4.2: Power fitting coefficients for $R_r(P)$ - 95% confidence intervals (r^2 is the square of the multiple correlation coefficient).

	$H = 5$ mm ($r^2 = 0.9999$)		$H = 30$ mm ($r^2 = 1$)	
	Lower bound	Upper bound	Lower bound	Upper bound
a_p	2.701×10^{-3}	3.056×10^{-3}	2.554×10^{-3}	2.701×10^{-3}
b_p	1.381	1.407	1.510	1.521

4.11.4 Influence of the vertical load

Variations of the rolling resistance with respect to the vertical load, for $H = 5$ mm and $H = 30$ mm, are plotted on Figures 4.7 and 4.8 respectively. Both cases, with and without friction, are considered. The resulting curves are concave upwards and are very similar in shape to the example given by Qiu (2006) corresponding to a two-dimensional model of a rigid cylinder rolling on a viscoelastic foundation.

The rolling resistance increases monotonically with the applied load. Curves from Figures 4.7 and 4.8 may be closely fitted using a power law of the form $R_r = a_p P^{b_p}$. In the cases including friction, the 95% confidence intervals on coefficients a_p and b_p are given in Table 4.2.

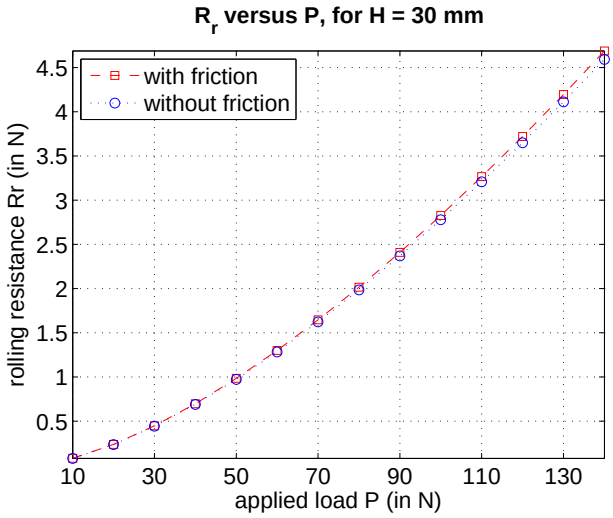

FIGURE 4.8: Influence of the vertical load on rolling resistance, for $H = 30$ mm.

Table 4.3: Exponential fitting coefficients for $R_r(H)$, 95% confidence intervals.

	$P = 50$ N ($r^2 = 0.9999$)		$P = 125$ N ($r^2 = 1$)	
	Lower bound	Upper bound	Lower bound	Upper bound
a_e	0.9306	0.9403	3.738	3.768
b_e	1.555	1.954	1.706	2
c_e	-0.8799	-0.8555	-3.704	-3.662
d_e	-233	-223.2	-198.6	-193.8

4.11.5 Influence of the foundation's thickness

Variations of the rolling resistance with respect to the foundation's thickness, for $P = 50$ N and $P = 125$ N are plotted on Figures 4.9 and 4.10 respectively. Both cases, with and without friction, are also considered. As expected, the resulting curves are concave downwards and converge asymptotically towards a limiting case corresponding to a viscoelastic "half-space", at the given speed.

The rolling resistance is a monotonically increasing function of the layer thickness. Curves from Figures 4.9 and 4.10 may be closely fitted using an exponential law of the form $R_r = a_e \exp^{b_e P} + c_e \exp^{d_e P}$. In the case including friction, the 95% confidence

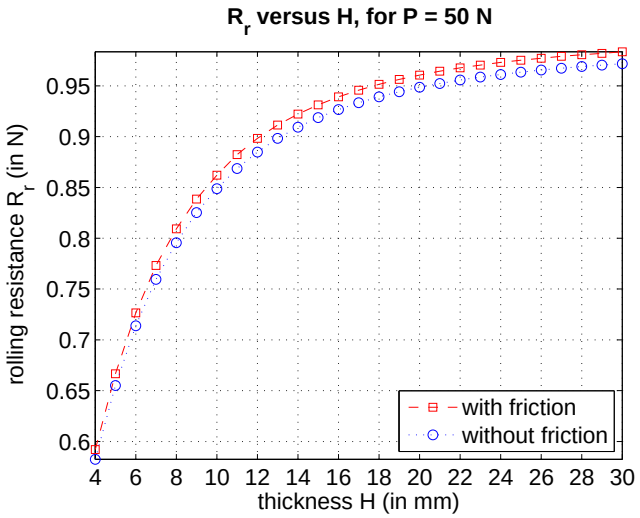

FIGURE 4.9: Influence of foundation thickness on rolling resistance, for $P = 50$ N.

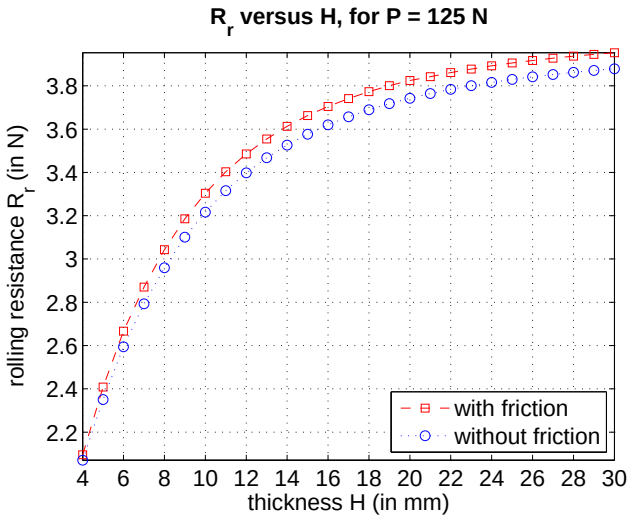

FIGURE 4.10: Influence of foundation thickness on rolling resistance, for $P = 125$ N.

intervals on coefficients a_e, b_e, c_e and d_e are given in Table 4.3.

4.11.6 Influence of friction

In Section 4.11.2 we mentioned that the rolling resistance due to friction was small in comparison with the one resulting from viscoelasticity. Two curves for $R_r(P)$, with and without friction, were compared on each of Figures 4.7 and 4.8 for $H = 5$ mm and $H = 30$ mm respectively. The influence of friction was also highlighted by comparing two curves for $R_r(H)$ on each of Figures 4.9 and 4.10, for $P = 50$ N and $P = 125$ N respectively [1]. It may be noted that, for values of P up to 150 N (corresponding to a mean vertical pressure of 2.56 MPa), the contribution of friction remains below 1.55%, which suggests that it may be neglected for many engineering applications.

Friction losses vary with the different parameters but remain relatively small. For instance, the dependence upon the foundation's thickness of their percentage contribution to rolling resistance, is illustrated in Figures 4.11 and 4.12 for $P = 50$ N and $P = 125$ N respectively. Data points present minor discontinuities due to the spatial discretization of slipping, which is a continuous process across the contact area. Indeed, in the model, changes in contact nature can only occur over surface elements of area $a_x \times a_y$. Considering the limited influence of friction on the rolling resistance, fitting the available data points was deemed more cost efficient than refining the mesh. In both cases of vertical loading, it can be seen that the contribution of friction to the total rolling resistance reaches a maximum for layer thickness between 6 and 8 mm.

[1] $P = 50$ and 125 N correspond to mean vertical pressures of 1.64 and 2.35 MPa respectively

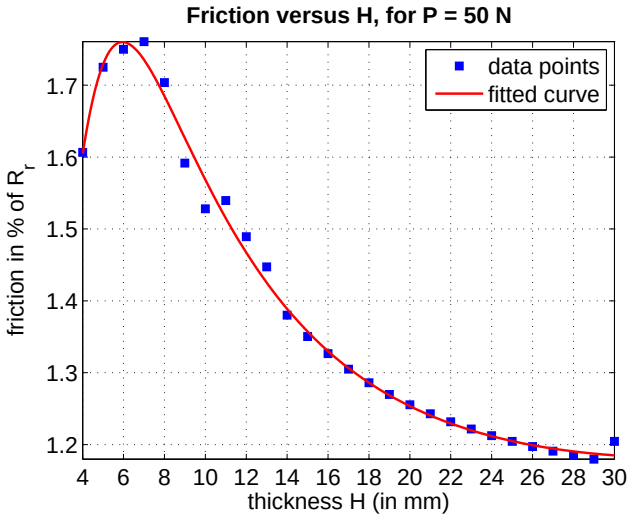

FIGURE 4.11: Percentage contribution of friction to rolling resistance, for $P = 50$ N.

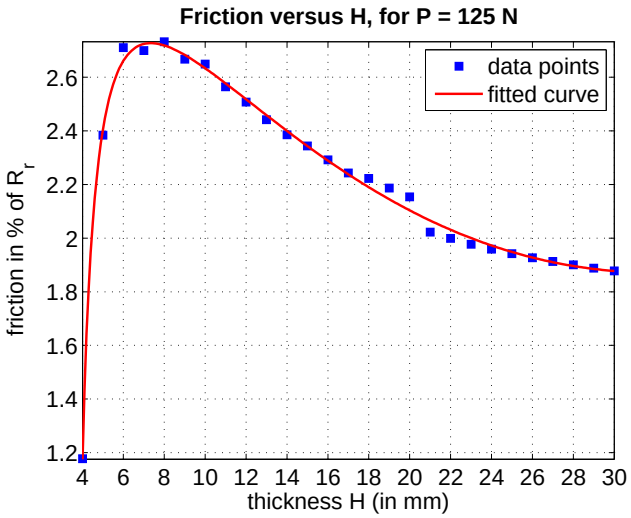

FIGURE 4.12: Percentage contribution of friction to rolling resistance, for $P = 125$ N.

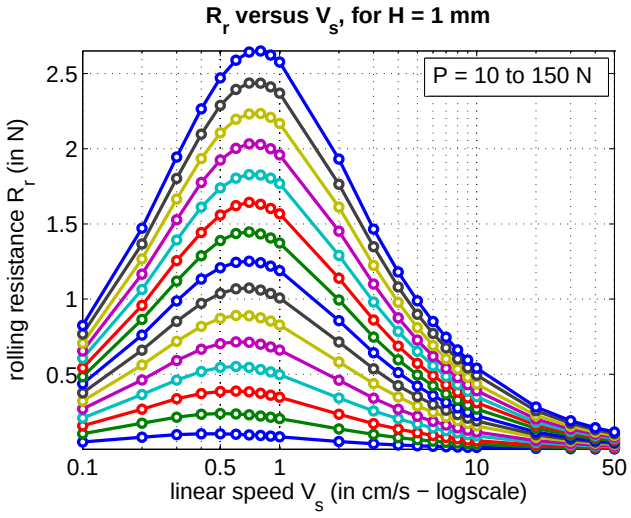

FIGURE 4.13: Influence of speed on rolling resistance, for $H = 1$ mm.

4.11.7 Influence of speed

The dependence of rolling resistance upon linear speed is perhaps the most important in that it more directly reflects the time dependent behavior of the viscoelastic foundation. Using various approximations, its main features were commendably approached for instance by May et al. (1959) and Pöschel et al. (1999) in the case of a hard cylinder and more recently by Persson (2010) for both rigid cylinders and spheres on a viscoelastic foundation. Plots of $R_r(V_s)$ are shown in Figures 4.13 and 4.14, for different values of the vertical load ($10 \leq P \leq 150$ N) and two layer thicknesses ($H = 1$,and 30 mm).

Referring to the three-parameter model drawn in Figure 4.5, viscoelastic energy dissipation only occurs in the dashpot. Besides, the material's internal clocks are defined by its creep time τ and its relaxation time $\tau_r = \tau/(1+f)$ which, in the case of our example, are of the same order of magnitude and therefore constitute a single time scale. According to this time scale, when the sphere is moving slowly (stationary limit), the dashpot flows and the layer behaves like an elastic spring of stiffness G_o. Conversely, when the sphere rolls rapidly, the dashpot locks and the foundation

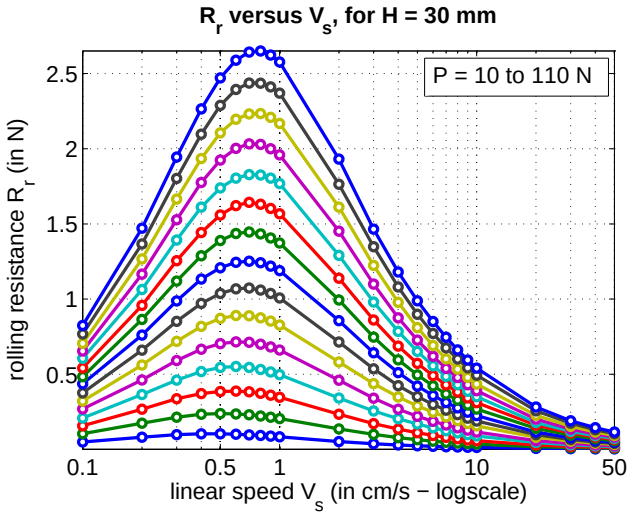

FIGURE 4.14: Influence of speed on rolling resistance, for $H = 30$ mm.

behaves also elastically, with stiffness E_1. Hence at low and high speeds, viscoelastic energy losses are expected to be small. The dashpot dissipates more energy at intermediate motion velocities, yielding a maximum rolling resistance depending on the problem's parameters, in particular the foundation's relaxation spectrum.

4.12 Summary

A three-dimensional boundary element formulation of an incompressible, linear viscoelastic layer of finite thickness was proposed, in a frame of reference moving at constant speed. The constitutive behavior of the layer's material is characterized, in the frequency domain, using general master-curves, which allows any linear viscoelastic model, including fully empirical material models. The presented developments resulted in the formation of a compliance matrix characterizing the mechanical behavior of the layer's upper boundary and including the effects of steady-state motion. Such representation eliminates the need to model the entire layer and avoids any related artefacts on the lateral boundaries. As opposed to certain existing approaches, the proposed formulation does not rely on the elastic half-space approximation and

poses no limitations regarding how thin the layer can be. The stresses and strains resulting from the boundary's interaction with its environment are propagated into the layer's continuum 'exactly', according to linear viscoelasticity. The proposed formulation can be used as a component in various settings, such as problems involving deformable indenters, multilayered contact or bifurcation and standing-wave phenomena. Taking advantage of configurational similarities and symmetry, the full computational cost and storage space of compliance matrices were divided by $N_T/2$. Furthermore, it is noteworthy that, for a given rolling/sliding speed, the compliance matrix of a viscoelastic layer needs to be built once and can be stored for multiple use. For instance, varying parameters such as the intensity of the applied loads, the coefficient of surface friction, the adhesion threshold, the shape or the dimensions of the indenter does not require re-forming the compliance matrix of the layer. The proposed formulation is hence suitable for efficiently generating sequences of high fidelity solution results for various quantities of interest, such as rolling resistance. In this chapter, it was implemented, in combination with a contact solver, to build a full three-dimensional model for the resistance incurred by a rigid sphere rolling or sliding on the layer. Energy losses include viscoelastic damping and surface friction. Responses from the model in limiting cases were found to be consistent with existing solutions. In order to illustrate some of the model's capabilities, an example was treated in which the foundation is described by a three-parameter viscoelastic solid and friction is assumed to follow Coulomb's law. Results from the example were used to illustrate the influence of vertical loading, foundation thickness, friction and speed on the rolling resistance. Some general aspects of previously-described dependences based on two-dimensional models in plane strain for rolling cylinders or simplified approaches for spheres were confirmed. In particular, the contribution of surface friction to the total rolling resistance was found to be limited. Energy losses increase unboundedly with vertical loading on which the dependency is fitted well by power

laws. Rolling resistance also increases with foundation thickness but tends asymptotically towards a limiting case corresponding to a viscoelastic "half-space" solution. Alternatively, frictional losses were found to first increase then decrease with foundation thickness. Finally, starting from rest, viscoelastic dissipation grows with the rate of motion reaching a maximum that depends on the problem's parameters, then decays to become negligible at high speed.

5

Two and three-dimensional boundary element formulations of compressible isotropic, transversely isotropic and orthotropic viscoelastic layers of arbitrary thickness, applied to the rolling resistance of rigid cylinders and spheres

5.1 Preamble

A three-dimensional boundary element formulation of an *incompressible* viscoelastic layer of arbitrary thickness was proposed in Chapter 4 (Zéhil and Gavin, 2013e). This formulation was applied, in combination with appropriate rolling/sliding contact algorithms, presented in Chapter 3 (Zéhil and Gavin, 2013c), to determine the resistance incurred by a rigid sphere rolling, in steady-state, on such a layer. New two-dimensional and three-dimensional boundary element formulations of *compressible* viscoelastic layers of arbitrary thickness are presented in this chapter. The formulations are derived in increasing order of complexity for: (i) compressible isotropic layers, (ii) transversely isotropic layers, and (iii) fully orthotropic layers. It is further shown that existing 2D and 3D models for *incompressible* isotropic layers may be

regarded as particular instances of case (i). The proposed formulations are based on Fourier series and support any linear viscoelastic material model characterized by general frequency-domain master-curves. These approaches result in a compliance matrix for the layer's upper boundary, which includes the effects of steady-state motion. This characterization may be used as a component in various problem settings to generate sequences of high fidelity solutions for varying parameters. The proposed modeling techniques are applied, in combination with appropriate contact solvers, to the rolling resistance of rigid cylinders and spheres on compressible isotropic, transversely isotropic and orthotropic layers. The latter case reveals that the dissipated power varies with the direction of motion, which suggests new ways of optimizing the level of damping in various engineering applications of very high impact. Interesting lateral viscoelastic effects resulting from material asymmetry are unveiled. These phenomena could be harnessed to achieve smooth and 'invisible' guides across three-dimensional viscoelastic surfaces, and hence suggest new ways of controlling trajectories, with a broad range of potential applications.

5.2 Common setting

The different cases considered in this work share a common setting, which is illustrated in Figure 5.1: a mechanical load is translated at constant speed V_s, in direction x, on a viscoelastic layer of arbitrary thickness H, attached to a rigid backing. The load is periodic in directions x and y, with periods L_x and L_y, respectively. The coordinate system $Ox'y'z'$ is fixed while $Oxyz$ moves with the load.

5.3 A brief review of 3D linear viscoelasticity

Linear elasticity corresponds to a time-independent behavioral material model characterized by the constitutive equation below, also known as Hook's law, written in

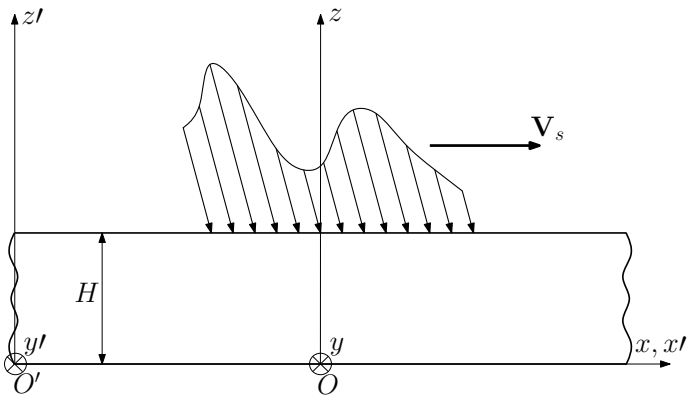

FIGURE 5.1: General model and coordinate systems.

indicial notation as

$$\sigma_{ij} = C_{ijkl}\epsilon_{kl}, \tag{5.1}$$

where σ_{ij}, ϵ_{ij} and C_{ijkl} are components of the second order stress tensor, the small-strain tensor, and the fourth order elasticity tensor, respectively.

Alternatively, linear viscoelasticity is characterized by the dependence of the elasticity tensor on time. The state of stress in a linear viscoelastic material, subjected to a strain history of the form $\epsilon_{kl}(t) = \bar{\epsilon}_{kl}\mathcal{H}(t)$, where $\bar{\epsilon}_{kl}$ are constant strain components and $\mathcal{H}(.)$ designates the Heaviside unit step function, is given by

$$\sigma_{ij}(t) = C_{ijkl}(t)\,\bar{\epsilon}_{kl}, \quad t \geq 0. \tag{5.2}$$

The linear viscoelastic response to a more general strain history (on $t \geq 0$) can be deduced, using the principle of superposition, by convolution of (5.2), in the form of a hereditary integral (e.g. Flügge, 1975; Lakes, 2009), i.e.

$$\sigma_{ij}(t) = \int_0^t C_{ijkl}(t-\tau)\frac{d\epsilon_{kl}}{d\tau}d\tau. \tag{5.3}$$

Taking the Fourier transform of (5.3), frequency-domain linear viscoelasticity is characterized under cyclic loading by

$$\hat{\sigma}_{ij}(\omega) = C^*_{ijkl}(\omega)\,\hat{\epsilon}_{kl}(\omega), \tag{5.4}$$

where the circumflex refers to complex-valued functions of the angular frequency ω, and $C^*_{ijkl}(\omega) = i\omega\hat{C}_{ijkl}(\omega)$, with $i^2 = -1$, are complex elastic moduli. Equation (5.4) can also be written, using the Voigt notation, in the following form

$$\hat{\boldsymbol{\sigma}}(\omega) = \mathbf{C}^*(\omega)\,\hat{\boldsymbol{\epsilon}}(\omega), \tag{5.5}$$

where $\hat{\boldsymbol{\sigma}}(\omega) = \langle \hat{\sigma}_{11}, \hat{\sigma}_{22}, \hat{\sigma}_{33}, \hat{\sigma}_{23}, \hat{\sigma}_{13}, \hat{\sigma}_{12} \rangle^T$, $\hat{\boldsymbol{\epsilon}}(\omega) = \langle \hat{\epsilon}_{11}, \hat{\epsilon}_{22}, \hat{\epsilon}_{33}, \hat{\gamma}_{23}, \hat{\gamma}_{13}, \hat{\gamma}_{12} \rangle^T$ with $\hat{\gamma}_{kl} = 2\hat{\epsilon}_{kl}$, and $\mathbf{C}^*(\omega)$ is a 6×6 complex-valued elasticity matrix. In particular, orthogonally isotropic materials are characterized by nine independent elastic moduli (e.g. Boresi and Schmidt, 2003; Lekhnitskiĭ, 1963; Rand et al., 2005; Sadd, 2009; Slawinski, 2010), which may be selected among the ones populating the *symmetric* elasticity matrix below, written in the principal axes of orthotropy

$$\mathbf{C}^*(\omega) = \begin{bmatrix} \frac{E_1^*}{\Delta^*}(1-\nu_{23}^*\nu_{32}^*) & \frac{E_1^*}{\Delta^*}(\nu_{21}^*+\nu_{23}^*\nu_{31}^*) & \frac{E_1^*}{\Delta^*}(\nu_{31}^*+\nu_{32}^*\nu_{21}^*) & 0 & 0 & 0 \\ \frac{E_2^*}{\Delta^*}(\nu_{12}^*+\nu_{13}^*\nu_{32}^*) & \frac{E_2^*}{\Delta^*}(1-\nu_{13}^*\nu_{31}^*) & \frac{E_2^*}{\Delta^*}(\nu_{32}^*+\nu_{31}^*\nu_{12}^*) & 0 & 0 & 0 \\ \frac{E_3^*}{\Delta^*}(\nu_{13}^*+\nu_{12}^*\nu_{23}^*) & \frac{E_3^*}{\Delta^*}(\nu_{23}^*+\nu_{21}^*\nu_{13}^*) & \frac{E_3^*}{\Delta^*}(1-\nu_{21}^*\nu_{12}^*) & 0 & 0 & 0 \\ 0 & 0 & 0 & G_{23}^* & 0 & 0 \\ 0 & 0 & 0 & 0 & G_{13}^* & 0 \\ 0 & 0 & 0 & 0 & 0 & G_{12}^* \end{bmatrix}, \tag{5.6}$$

where E_i^* is Young's modulus along the i-axis, ν_{ij} refers to Poisson's ratio corresponding to a contraction along the j-axis upon extension in direction i, and G_{ij} is the complex shear modulus in the ij-plane. The shorthand parameter $\Delta^*(\omega)$ is defined as

$$\Delta^*(\omega) = 1 - \nu_{12}^*\nu_{21}^* - \nu_{13}^*\nu_{31}^* - \nu_{23}^*\nu_{32}^* - \nu_{12}^*\nu_{23}^*\nu_{31}^* - \nu_{13}^*\nu_{32}^*\nu_{21}^*. \tag{5.7}$$

A transversely isotropic material whose properties are symmetric about the 3-axis is characterized by five independent elastic moduli, such that $\mathbf{C}^*(\omega)$ is a *symmetric*

matrix of the form

$$\mathbf{C}^{*}(\omega)=\begin{bmatrix} \frac{1-\nu_{LT}^{*}\nu_{TL}^{*}}{E_{L}^{*}E_{T}^{*}\Gamma^{*}} & \frac{\nu_{T}^{*}+\nu_{LT}^{*}\nu_{TL}^{*}}{E_{L}^{*}E_{T}^{*}\Gamma^{*}} & \frac{\nu_{LT}^{*}\left(1+\nu_{T}^{*}\right)}{E_{L}^{*}E_{T}^{*}\Gamma^{*}} & 0 & 0 & 0 \\ \frac{\nu_{T}^{*}+\nu_{LT}^{*}\nu_{TL}^{*}}{E_{L}^{*}E_{T}^{*}\Gamma^{*}} & \frac{1-\nu_{LT}^{*}\nu_{TL}^{*}}{E_{L}^{*}E_{T}^{*}\Gamma^{*}} & \frac{\nu_{LT}^{*}\left(1+\nu_{T}^{*}\right)}{E_{L}^{*}E_{T}^{*}\Gamma^{*}} & 0 & 0 & 0 \\ \frac{\nu_{TL}^{*}\left(1+\nu_{T}^{*}\right)}{{E_{T}^{*}}^{2}\Gamma^{*}} & \frac{\nu_{TL}^{*}\left(1+\nu_{T}^{*}\right)}{{E_{T}^{*}}^{2}\Gamma^{*}} & \frac{1-{\nu_{T}^{*}}^{2}}{{E_{T}^{*}}^{2}\Gamma^{*}} & 0 & 0 & 0 \\ 0 & 0 & 0 & G_{LT}^{*} & 0 & 0 \\ 0 & 0 & 0 & 0 & G_{LT}^{*} & 0 \\ 0 & 0 & 0 & 0 & 0 & \frac{E_{T}^{*}}{2\left(1+\nu_{T}^{*}\right)} \end{bmatrix}, \tag{5.8}$$

where the subscripts T and L refer to the "transverse" plane of isotropy (i.e. the 12-plane) and the "longitudinal" axis of symmetry (i.e. the 3-axis), respectively. The shorthand parameter $\Gamma^{*}(\omega)$ is defined as

$$\Gamma^{*}(\omega)=\frac{\left(1+\nu_{T}^{*}\right)\left(1-\nu_{T}^{*}-2\nu_{TL}^{*}\nu_{LT}^{*}\right)}{{E_{T}^{*}}^{2}E_{L}^{*}}. \tag{5.9}$$

In the isotropic case, C_{ijkl}^{*} are given in terms of two complex-valued Lamé functions $\mu^{*}(\omega)=i\omega\hat{\mu}(\omega)$ and $\lambda^{*}(\omega)=i\omega\hat{\lambda}(\omega)$, as

$$C_{ijkl}^{*}(\omega)=\left(\delta_{ik}\delta_{jl}+\delta_{il}\delta_{jk}\right)\mu^{*}(\omega)+\delta_{ij}\delta_{kl}\lambda^{*}(\omega). \tag{5.10}$$

Alternatively, traditional "engineering" quantities, such as the complex Young's modulus $E^{*}(\omega)$ and Poisson's ratio $\nu^{*}(\omega)$, may be substituted to Lamé's functions in (5.10), with

$$\mu^{*}(\omega)=\frac{E^{*}(\omega)}{2\left(1+\nu^{*}(\omega)\right)}, \tag{5.11}$$

$$\lambda^{*}(\omega)=\frac{E^{*}(\omega)\,\nu^{*}(\omega)}{\left(1+\nu^{*}(\omega)\right)\left(1-2\nu^{*}(\omega)\right)}. \tag{5.12}$$

When (5.10) applies, the constitutive relation in (5.4) can be split into isochoric and volumetric parts, involving the complex shear modulus $G^{*}(\omega)=\mu^{*}(\omega)$, and the complex bulk modulus $K^{*}(\omega)=(2/3)\,\mu^{*}(\omega)+\lambda^{*}(\omega)$, respectively, i.e.

$$\hat{\sigma'}_{ij}(\omega)=2G^{*}(\omega)\,\hat{\epsilon'}_{ij}(\omega), \tag{5.13}$$

$$\hat{\sigma}_o(\omega) = K^*(\omega)\,\phi(\omega), \tag{5.14}$$

where primed quantities correspond to deviator components, $\phi(\omega) = \hat{\epsilon}_{kk}(\omega)$ and $\hat{\sigma}_o(\omega) = \hat{\sigma}_{kk}(\omega)/3$. Expressions (5.13) and (5.14) are typically used in experimental setups to effectively determine $G^*(\omega)$ and $K^*(\omega)$ in a wide frequency range (e.g. Pritz, 2000). These are related to the engineering moduli by

$$E^*(\omega) = \frac{9K^*(\omega)\,G^*(\omega)}{3K^*(\omega) + G^*(\omega)}, \tag{5.15}$$

$$\nu^*(\omega) = \frac{1}{2}\left(\frac{3K^*(\omega) - 2G^*(\omega)}{3K^*(\omega) + G^*(\omega)}\right). \tag{5.16}$$

5.4 Three-dimensional isotropic formulation

A three-dimensional boundary element formulation for an *incompressible* layer of finite thickness was proposed in Chapter 4 (Zéhil and Gavin, 2013e). The derivation presented here follows somewhat similar steps, adapted to the context of a *compressible* layer. Designating by $\mathbf{u} =< u, v, w >^T$ the displacement vector field, and by $\mathbf{f}$ any general field in the continuum of the layer, specific boundary conditions for the layer, of spatial periods L_x and L_y, in directions x and y respectively, can be expressed as

$$\mathbf{u}(x, y, z = 0) = \mathbf{0}, \quad \forall (x, y), \tag{5.17}$$

$$\mathbf{f}(x + pL_x, y + qL_y, z) = \mathbf{f}(x, y, z), \quad \begin{cases} \forall (x, y) \in \mathbb{R}^2, \\ \forall z \in [0, H], \text{ and} \\ \forall (p, q) \in \mathbb{Z}^2. \end{cases} \tag{5.18}$$

Coordinate sytems $Oxyz$ and $O'x'y'z'$ are related by $x = x' - V_s t$, $y = y'$ and $z = z'$. Consequently, material time-derivatives write

$$\frac{d}{dt} = -V_s \frac{\partial}{\partial x} \quad \text{and} \quad \frac{d^2}{dt^2} = V_s^2 \frac{\partial^2}{\partial x^2}. \tag{5.19}$$

Let ρ be the material's density. In the absence of volume forces, equilibrium equations in the continuum of the layer are expressed in $Oxyz$, by means of (5.19) using tensor notation as

$$\rho V_s^2 \frac{\partial^2 \mathbf{u}}{\partial x^2} = \mathbf{div}(\boldsymbol{\sigma}). \tag{5.20}$$

Individual components of all fields are expanded into Fourier series in the spatial variables x and y. The expansions are subsequently written in terms of x', y' and t. This is shown below on a generic scalar quantity $f(x, y, z)$ of the problem

$$f(x, y, z) = \sum_{m,n=-\infty}^{+\infty} f_{mn}(z) e^{i\nu_x x} e^{i\nu_y y} = \sum_{m,n=-\infty}^{+\infty} f_{mn}(z) e^{i\nu_x x'} e^{i\nu_x y'} e^{i\omega_m t}, \tag{5.21}$$

where $\nu_x = 2\pi m/L_x$, $\nu_y = 2\pi n/L_y$ and $\omega_m = -2\pi m V_s/L_x$. Corresponding Fourier coefficients are given by

$$f_{mn}(z) = \frac{1}{L_x L_y} \int_{y=0}^{L_y} \int_{x=0}^{L_x} f(x, y, z) e^{-i\nu_x x} e^{-i\nu_y y} dx dy. \tag{5.22}$$

Substituting expansion (5.21) into the hereditary integral in (5.3) for $\sigma_{ij}(t)$ and $\epsilon_{kl}(\tau)$, then integrating over spatial periods while using the orthogonality property of complex exponentials yields a behavioral formulation in terms of Fourier coefficients, i.e.

$$\sigma_{ij_{mn}}(z) = C^*_{ijkl_m} \epsilon_{kl_{mn}}(z), \tag{5.23}$$

where $C^*_{ijkl_m} = C^*_{ijkl}(\omega_m)$, with no summation implied on indices m and n. Transcribed into Voigt's notation, equation (5.23) becomes

$$\boldsymbol{\sigma}_{mn}(z) = \mathbf{C}^*_m \boldsymbol{\epsilon}_{mn}(z), \tag{5.24}$$

where

$$\boldsymbol{\sigma}_{mn}(z) = \langle \sigma_{11_{mn}}, \sigma_{22_{mn}}, \sigma_{33_{mn}}, \sigma_{23_{mn}}, \sigma_{13_{mn}}, \sigma_{12_{mn}} \rangle^T, \tag{5.25}$$

$$\boldsymbol{\epsilon}_{mn}(z) = \langle \epsilon_{11_{mn}}, \epsilon_{22_{mn}}, \epsilon_{33_{mn}}, \gamma_{23_{mn}}, \gamma_{13_{mn}}, \gamma_{12_{mn}} \rangle^T , \tag{5.26}$$

with $\gamma_{kl_{mn}} = 2\epsilon_{kl_{mn}}$, and $\mathbf{C}_m^* = \mathbf{C}^*(\omega_m)$. Expressions (5.23) and (5.24) may be compared to their (single-variable) Fourier transform counterparts given in (5.4) and (5.5), respectively. For brevity, explicit references to the dependence of Fourier coefficients on the spatial variable z will be omitted in the following. In the isotropic case, substituting expressions (5.15) and (5.16) into (5.10) then (5.10) into (5.23), yields

$$\sigma_{ij_{mn}} = \frac{E_m^*}{1+\nu_m^*} \left(\epsilon_{ij_{mn}} + \frac{\nu_m^*}{1-2\nu_m^*} \epsilon_{kk_{mn}} \delta_{ij} \right). \tag{5.27}$$

Expansion (5.21) can also be plugged into the equilibrium equations in (5.20), which, following a procedure similar to the one described above, yields a system of linear ordinary differential equations (ODE's) relating stress and displacement Fourier coefficients

$$-\rho V_s^2 \nu_x^2 u_{mn} = i\nu_x \sigma_{xx_{mn}} + i\nu_y \tau_{xy_{mn}} + \dot{\tau}_{xz_{mn}}, \tag{5.28}$$

$$-\rho V_s^2 \nu_x^2 v_{mn} = i\nu_x \tau_{xy_{mn}} + i\nu_y \sigma_{yy_{mn}} + \dot{\tau}_{yz_{mn}}, \tag{5.29}$$

$$-\rho V_s^2 \nu_x^2 w_{mn} = i\nu_x \tau_{xz_{mn}} + i\nu_y \tau_{yz_{mn}} + \dot{\sigma}_{zz_{mn}}. \tag{5.30}$$

Further, differentiating expression (5.21) for the displacements (u, v, w) with respect to the spatial variables (x, y, z) and eliminating strain coefficients $\epsilon_{ij_{mn}}$ in (5.27) results in additional ODE's relating Fourier coefficients of displacements and stresses

$$\sigma_{xx_{mn}} = \frac{E_m^*}{(1+\nu_m^*)(1-2\nu_m^*)} \left[(1-\nu_m^*) i\nu_x u_{mn} + \nu_m^* (i\nu_y v_{mn} + \dot{w}_{mn}) \right], \tag{5.31}$$

$$\sigma_{yy_{mn}} = \frac{E_m^*}{(1+\nu_m^*)(1-2\nu_m^*)} \left[(1-\nu_m^*) i\nu_y v_{mn} + \nu_m^* (i\nu_x u_{mn} + \dot{w}_{mn}) \right], \tag{5.32}$$

$$\sigma_{zz_{mn}} = \frac{E_m^*}{(1+\nu_m^*)(1-2\nu_m^*)} \left[(1-\nu_m^*) \dot{w}_{mn} + \nu_m^* (i\nu_x u_{mn} + i\nu_y v_{mn}) \right], \tag{5.33}$$

$$\tau_{xy_{mn}} = \frac{E_m^*}{2(1+\nu_m^*)} (i\nu_y u_{mn} + i\nu_x v_{mn}), \tag{5.34}$$

$$\tau_{xz_{mn}} = \frac{E_m^*}{2\left(1+\nu_m^*\right)}\left(i\nu_x w_{mn} + \dot{u}_{mn}\right), \tag{5.35}$$

$$\tau_{yz_{mn}} = \frac{E_m^*}{2\left(1+\nu_m^*\right)}\left(i\nu_y w_{mn} + \dot{v}_{mn}\right), \tag{5.36}$$

where the up dot denotes the derivative with respect to z. For a given couple of Fourier indices (m,n), a complex-valued state vector $\mathbf{q}_{mn}(z)$ is defined, as follows

$$\mathbf{q}_{mn}(z) = \left\langle \mathbf{d}_{mn}^T(z), \mathbf{f}_{mn}^T(z) \right\rangle^T, \tag{5.37}$$

where

$$\mathbf{d}_{mn}(z) = \left\langle w_{mn}(z), u_{mn}(z), v_{mn}(z) \right\rangle^T, \tag{5.38}$$

$$\mathbf{f}_{mn}(z) = \left\langle \sigma_{zz_{mn}}(z), \tau_{xz_{mn}}(z), \tau_{yz_{mn}}(z) \right\rangle^T. \tag{5.39}$$

Eliminating the remaining quantities from equations (5.28)-(5.36) results in a reduced system of linear ODE's of the form

$$\dot{\mathbf{q}}_{mn}(z) = \mathbf{A}_{mn}\mathbf{q}_{mn}(z) \tag{5.40}$$

where the 6×6 complex-valued matrix $\mathbf{A}_{mn}$ is given by

$$\mathbf{A}_{mn} = \begin{bmatrix} 0 & -i\xi^*\nu_x & -i\xi^*\nu_y & \zeta^* & 0 & 0 \\ -i\nu_x & 0 & 0 & 0 & {G_m^*}^{-1} & 0 \\ -i\nu_y & 0 & 0 & 0 & 0 & {G_m^*}^{-1} \\ -\rho V_s^2\nu_x^2 & 0 & 0 & 0 & -i\nu_x & -i\nu_y \\ 0 & \beta_x^* & \beta_{xy}^* & -i\xi^*\nu_x & 0 & 0 \\ 0 & \beta_{xy}^* & \beta_y^* & -i\xi^*\nu_y & 0 & 0 \end{bmatrix}. \tag{5.41}$$

Shorthand parameters appearing in (5.41) are defined below

$$\beta_x^* = \frac{E_m^*}{2\left(1+\nu_m^*\right)}\left(\frac{2\nu_x^2}{1-\nu_m^*} + \nu_y^2\right) - \rho V_s^2\nu_x^2, \tag{5.42}$$

$$\beta_y^* = \frac{E_m^*}{2\left(1+\nu_m^*\right)}\left(\frac{2\nu_y^2}{1-\nu_m^*} + \nu_x^2\right) - \rho V_s^2\nu_x^2, \tag{5.43}$$

$$\beta_{xy}^* = \frac{E_m^*\nu_x\nu_y}{2\left(1-\nu_m^*\right)}, \quad G_m^* = \frac{E_m^*}{2\left(1+\nu_m^*\right)}, \tag{5.44}$$

$$\zeta^* = \frac{(1+\nu_m^*)(1-2\nu_m^*)}{E_m^*(1-\nu_m^*)} \quad \text{and} \quad \xi^* = \frac{\nu_m^*}{1-\nu_m^*}. \tag{5.45}$$

The remaining steps correspond to an inverse Fourier analysis, i.e. to the formation of a compliance matrix $\mathbf{C}$ fully characterizing the mechanical behavior of the layer's upper boundary, in the physical space. These steps, are identical to those described in Chapter 4 (Zéhil and Gavin, 2013e), in the context of an incompressible layer. Briefly, the solution to system (5.40) is written in the following form

$$\begin{bmatrix} \mathbf{d}_{mn}(z) \\ \mathbf{f}_{mn}(z) \end{bmatrix} = \begin{bmatrix} \mathbf{T}_{mn,11}(z) & \mathbf{T}_{mn,12}(z) \\ \mathbf{T}_{mn,21}(z) & \mathbf{T}_{mn,22}(z) \end{bmatrix} \times \begin{bmatrix} \mathbf{d}_{mn}(0) \\ \mathbf{f}_{mn}(0) \end{bmatrix}, \tag{5.46}$$

where $\mathbf{T}_{mn}(z) = \exp(\mathbf{A}_{mn}z)$ is the complex matrix exponential of $\mathbf{A}_{mn}z$. Accounting for the boundary conditions on displacements at the bottom of the layer, i.e. $\mathbf{d}_{mn}(0) = \mathbf{0}$, Fourier coefficients of displacements and stresses at $z = H$ can be related explicitly

$$\mathbf{d}_{mn}(H) = \mathbf{T}_{mn,12}(H)\mathbf{T}_{mn,22}^{-1}(H)\mathbf{f}_{mn}(H). \tag{5.47}$$

The upper boundary of the layer is discretized into nodes with nodal spacings a_x and a_y in directions x and y respectively. The nodal displacement vector $\mathbf{D} = \left\langle \mathbf{W}^T, \mathbf{U}^T, \mathbf{V}^T \right\rangle^T$ is related to the nodal force vector $\mathbf{F} = \left\langle \mathbf{F_W}^\mathbf{T}, \mathbf{F_U}^\mathbf{T}, \mathbf{F_V}^\mathbf{T} \right\rangle^\mathbf{T}$ through a boundary-element compliance matrix $\mathbf{C}$ as

$$\begin{bmatrix} \mathbf{C}_{WW} & \mathbf{C}_{WU} & \mathbf{C}_{WV} \\ \mathbf{C}_{UW} & \mathbf{C}_{UU} & \mathbf{C}_{UV} \\ \mathbf{C}_{VW} & \mathbf{C}_{VU} & \mathbf{C}_{VV} \end{bmatrix} \begin{bmatrix} \mathbf{F}_W \\ \mathbf{F}_U \\ \mathbf{F}_V \end{bmatrix} = \begin{bmatrix} \mathbf{W} \\ \mathbf{U} \\ \mathbf{V} \end{bmatrix}, \tag{5.48}$$

where the indices U, V and W refer to the spatial directions x, y and z respectively. Each entry $C_{PQ}(M,N)$ of matrix $\mathbf{C}$ is determined by applying a unit point load F_Q^N in direction $Q \in \{U,V,W\}$ at node N and, using equation (5.47), computing the Fourier series expansion of the resulting displacement in direction $P \in \{U,V,W\}$ at node M, from the series expansion of the surface stress $\sigma_Q^N(x,y,H)$ associated with

the applied load, i.e.

$$\sigma_Q^N(x,y,H) = \begin{cases} \frac{F_Q^N}{a_x a_y}, & \text{if } \begin{cases} x^N - \frac{a_x}{2} \leq x \leq x^N + \frac{a_x}{2} \\ y^N - \frac{a_y}{2} \leq y \leq y^N + \frac{a_y}{2} \end{cases} \\ 0, & \text{otherwise.} \end{cases} \tag{5.49}$$

The generic surface stress distribution given by (5.49) corresponds to a two - dimensional periodic rectangle function of widths a_x and a_y, and spatial periods L_x and L_y, in directions x and y respectively.

Entries of the compliance matrix corresponding to two pairs of nodes (M_1,N_1) and (M_2,N_2) are equal if M_1 and M_2 are in the same relative position with respect to N_1 and N_2, respectively. Similar considerations apply (with attention to signs) when the two pairs of nodes are symmetrical with respect to the vertical plane containing the direction of motion, which is also a plane of material symmetry. Hence in practice, taking advantage of configurational similarities and symmetry, as described in further detail in Chapter 4 (Zéhil and Gavin, 2013e), unit point loads need only be applied at one extremity of the leading edge, and the trailing edge, of the candidate contact surface.

5.5 Three-dimensional transversely isotropic formulation

It is here assumed that the properties of the layer are symmetric about the z-axis only. The layer is hence transversely isotropic in the xy-plane. Following similar steps as the ones described in Section 5.4, equations (5.31)-(5.36) are re-written as

$$\sigma_{xx_{mn}} = C^*_{11_m} i\nu_x u_{mn} + C^*_{12_m} i\nu_y v_{mn} + C^*_{13_m} \dot{w}_{mn}, \tag{5.50}$$

$$\sigma_{yy_{mn}} = C^*_{12_m} i\nu_x u_{mn} + C^*_{11_m} i\nu_y v_{mn} + C^*_{13_m} \dot{w}_{mn}, \tag{5.51}$$

$$\sigma_{zz_{mn}} = C^*_{13_m} i\nu_x u_{mn} + C^*_{13_m} i\nu_y v_{mn} + C^*_{33_m} \dot{w}_{mn}, \tag{5.52}$$

$$\tau_{xy_{mn}} = \left(C^*_{11_m} - C^*_{12_m}\right)\left(i\nu_y u_{mn} + i\nu_x v_{mn}\right)/2, \tag{5.53}$$

$$\tau_{xz_{mn}} = C^*_{44_m}\left(i\nu_x w_{mn} + \dot{u}_{mn}\right), \tag{5.54}$$

$$\tau_{yz_{mn}} = C^*_{44_m}\left(i\nu_y w_{mn} + \dot{v}_{mn}\right), \tag{5.55}$$

where $C^*_{ij_m} = C^*_{ij}\left(\omega_m\right)$ are given in expression (5.8). Eliminating non-state variables from equations (5.28)-(5.30) and (5.50)-(5.55), yields a similar expression of matrix $\mathbf{A}_{mn}$ as in (5.41), where the shorthand parameters in (5.42)-(5.45) become

$$\beta^*_x = \frac{E^*_{T_m}}{1-\nu^{*2}_{T_m}}\nu_x^2 + \frac{E^*_{T_m}}{2\left(1+\nu^*_{T_m}\right)}\nu_y^2 - \rho V_s^2\nu_x^2, \tag{5.56}$$

$$\beta^*_y = \frac{E^*_{T_m}}{1-\nu^{*2}_{T_m}}\nu_y^2 + \frac{E^*_{T_m}}{2\left(1+\nu^*_{T_m}\right)}\nu_x^2 - \rho V_s^2\nu_x^2, \tag{5.57}$$

$$\beta^*_{xy} = \frac{E^*_{T_m}\nu_x\nu_y}{2\left(1-\nu^*_{T_m}\right)},\ \ G^*_m = G^*_{LT_m}, \tag{5.58}$$

$$\zeta^* = \frac{1-\nu^*_{T_m}-2\nu^*_{TL_m}\nu^*_{LT_m}}{E^*_{L_m}\left(1-\nu^*_{T_m}\right)} \quad \text{and} \quad \xi^* = \frac{E^*_{T_m}}{E^*_{L_m}}\frac{\nu^*_{LT_m}}{1-\nu^*_{T_m}}. \tag{5.59}$$

5.6 Three-dimensional orthotropic formulation

Generalizing further, we consider here an orthogonally anisotropic layer. The principal directions of orthotropy are designated by the numbers 1, 2 and 3, with the 3-axis oriented in the vertical direction z. A spatially periodic load, in directions x and y, is applied to the upper boundary of the layer, as depicted in Figure 5.2. The load moves at a constant speed V_s in direction x, which is at an angle θ from the 1-axis, in the horizontal plane.

The constitutive relation in (5.24), whose matrix of elastic moduli $\mathbf{C}^*_m = \mathbf{C}^*\left(\omega_m\right)$ in coordinate system $OX_1X_2X_3$ is given by (5.6), can be expressed in coordinate system $Oxyz$. The transformed matrix of elastic moduli $\bar{\mathbf{C}}^*_m$ is of the form

$$\bar{\mathbf{C}}^*\left(\omega_m\right) = \begin{bmatrix} \bar{C}^*_{11_m} & \bar{C}^*_{12_m} & \bar{C}^*_{13_m} & 0 & 0 & \bar{C}^*_{16_m} \\ \bar{C}^*_{12_m} & \bar{C}^*_{22_m} & \bar{C}^*_{23_m} & 0 & 0 & \bar{C}^*_{26_m} \\ \bar{C}^*_{13_m} & \bar{C}^*_{23_m} & \bar{C}^*_{33_m} & 0 & 0 & \bar{C}^*_{36_m} \\ 0 & 0 & 0 & \bar{C}^*_{44_m} & \bar{C}^*_{45_m} & 0 \\ 0 & 0 & 0 & \bar{C}^*_{45_m} & \bar{C}^*_{55_m} & 0 \\ \bar{C}^*_{16_m} & \bar{C}^*_{26_m} & \bar{C}^*_{36_m} & 0 & 0 & \bar{C}^*_{66_m} \end{bmatrix}. \tag{5.60}$$

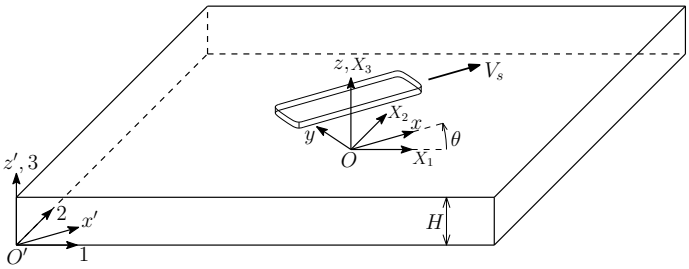

FIGURE 5.2: Spatially periodic load moving at constant speed V_s, in direction x, on the upper boundary of an orthotropic layer. Directions 1, 2 and 3 correspond to the principal directions of orthotropy.

Detailed expressions of the transformed moduli $\bar{C}^*_{ij_m}$, in terms of the principal elastic moduli $C^*_{ij_m}$ and the angle θ defining the direction of movement are derived according to fourth order contravariant tensor transformation rules (e.g. Fung and Tong, 2001). These expressions are given below

$$\bar{C}^*_{11_m} = C^*_{11_m} + \left(C^*_{11_m} + C^*_{22_m} - 2C^*_{12_m} - 4C^*_{66_m}\right)\sin^4(\theta) + 2\left(C^*_{12_m} - C^*_{11_m} + 2C^*_{66_m}\right)\sin^2(\theta), \tag{5.61}$$

$$\bar{C}^*_{22_m} = C^*_{22_m} + \left(C^*_{11_m} + C^*_{22_m} - 2C^*_{12_m} - 4C^*_{66_m}\right)\sin^4(\theta) + 2\left(C^*_{12_m} - C^*_{22_m} + 2C^*_{66_m}\right)\sin^2(\theta), \tag{5.62}$$

$$\bar{C}^*_{33_m} = C^*_{33_m}, \tag{5.63}$$

$$\bar{C}^*_{44_m} = C^*_{44_m}\cos^2(\theta) + C^*_{55_m}\sin^2(\theta), \tag{5.64}$$

$$\bar{C}^*_{55_m} = C^*_{55_m}\cos^2(\theta) + C^*_{44_m}\sin^2(\theta), \tag{5.65}$$

$$\bar{C}^*_{66_m} = C^*_{66_m} + \left(C^*_{11_m} + C^*_{22_m} - 2C^*_{12_m} - 4C^*_{66_m}\right)\sin^2(2\theta)/4, \tag{5.66}$$

$$\bar{C}^*_{12_m} = C^*_{12_m} + \left(C^*_{11_m} + C^*_{22_m} - 2C^*_{12_m} - 4C^*_{66_m}\right)\sin^2(2\theta)/4, \tag{5.67}$$

$$\bar{C}^*_{13_m} = C^*_{13_m}\cos^2(\theta) + C^*_{23_m}\sin^2(\theta), \tag{5.68}$$

$$\bar{C}^*_{23_m} = C^*_{23_m}\cos^2(\theta) + C^*_{13_m}\sin^2(\theta), \tag{5.69}$$

$$\bar{C}^*_{16_m} = \left(C^*_{22_m} - C^*_{11_m}\right)\sin(2\theta)/4 - \left(C^*_{11_m} + C^*_{22_m} - 2C^*_{12_m} - 4C^*_{66_m}\right)\sin(4\theta)/8, \tag{5.70}$$

$$\bar{C}^*_{26_m} = \left(C^*_{22_m} - C^*_{11_m}\right)\sin(2\theta)/4 + \left(C^*_{11_m} + C^*_{22_m} - 2C^*_{12_m} - 4C^*_{66_m}\right)\sin(4\theta)/8, \tag{5.71}$$

$$\bar{C}^*_{36_m} = \left(C^*_{23_m} - C^*_{13_m}\right)\sin(2\theta)/2, \tag{5.72}$$

$$\bar{C}^*_{45_m} = \left(C^*_{44_m} - C^*_{55_m}\right)\sin(2\theta)/2. \tag{5.73}$$

Following an approach similar to that described in Section 5.5, equations (5.50)-(5.55) are re-derived in the form

$$\sigma_{xx_{mn}} = i\left(\bar{C}^*_{11_m}\nu_x + \bar{C}^*_{16_m}\nu_y\right)u_{mn} + i\left(\bar{C}^*_{12_m}\nu_y + \bar{C}^*_{16_m}\nu_x\right)v_{mn} + \bar{C}^*_{13_m}\dot{w}_{mn}, \tag{5.74}$$

$$\sigma_{yy_{mn}} = i\left(\bar{C}^*_{12_m}\nu_x + \bar{C}^*_{26_m}\nu_y\right)u_{mn} + i\left(\bar{C}^*_{22_m}\nu_y + \bar{C}^*_{26_m}\nu_x\right)v_{mn} + \bar{C}^*_{23_m}\dot{w}_{mn}, \tag{5.75}$$

$$\sigma_{zz_{mn}} = i\left(\bar{C}^*_{13_m}\nu_x + \bar{C}^*_{36_m}\nu_y\right)u_{mn} + i\left(\bar{C}^*_{23_m}\nu_y + \bar{C}^*_{36_m}\nu_x\right)v_{mn} + \bar{C}^*_{33_m}\dot{w}_{mn}, \tag{5.76}$$

$$\tau_{xy_{mn}} = i\left(\bar{C}^*_{16_m}\nu_x + \bar{C}^*_{66_m}\nu_y\right)u_{mn} + i\left(\bar{C}^*_{26_m}\nu_y + \bar{C}^*_{66_m}\nu_x\right)v_{mn} + \bar{C}^*_{36_m}\dot{w}_{mn}, \tag{5.77}$$

$$\tau_{xz_{mn}} = \bar{C}^*_{55_m}\dot{u}_{mn} + \bar{C}^*_{45_m}\dot{v}_{mn} + i\left(\bar{C}^*_{45_m}\nu_y + \bar{C}^*_{55_m}\nu_x\right)w_{mn}, \tag{5.78}$$

$$\tau_{yz_{mn}} = \bar{C}^*_{45_m}\dot{u}_{mn} + \bar{C}^*_{44_m}\dot{v}_{mn} + i\left(\bar{C}^*_{44_m}\nu_y + \bar{C}^*_{45_m}\nu_x\right)w_{mn}. \tag{5.79}$$

Referring back to system (5.40), eliminating non-state variables from equations (5.28)-(5.30) and (5.74)-(5.79) results in the following expression of the state matrix $\mathbf{A}_{mn}$

$$\mathbf{A}_{mn} = \begin{bmatrix} 0 & -i\xi^*_x & -i\xi^*_y & \zeta^* & 0 & 0 \\ -i\nu_x & 0 & 0 & 0 & \Gamma^*_1 & \Gamma^*_3 \\ -i\nu_y & 0 & 0 & 0 & \Gamma^*_3 & \Gamma^*_2 \\ -\rho V_s^2\nu_x^2 & 0 & 0 & 0 & -i\nu_x & -i\nu_y \\ 0 & \beta^*_x & \beta^*_{xy} & -i\xi^*_x & 0 & 0 \\ 0 & \beta^*_{xy} & \beta^*_y & -i\xi^*_y & 0 & 0 \end{bmatrix}. \tag{5.80}$$

Shorthand parameters appearing in (5.41) are defined below

$$\Gamma^*_1 = \frac{\bar{C}^*_{44_m}}{\bar{C}^*_{44_m}\bar{C}^*_{55_m} - \bar{C}^{*2}_{45_m}}, \tag{5.81}$$

$$\Gamma^*_2 = \frac{\bar{C}^*_{55_m}}{\bar{C}^*_{44_m}\bar{C}^*_{55_m} - \bar{C}^{*2}_{45_m}}, \tag{5.82}$$

$$\Gamma_3^* = -\frac{\bar{C}^*_{45_m}}{\bar{C}^*_{44_m}\bar{C}^*_{55_m} - \bar{C}^{*2}_{45_m}}, \tag{5.83}$$

$$\beta_x^* = \left(\bar{C}^*_{11_m} - \frac{\bar{C}^{*2}_{13_m}}{\bar{C}^*_{33_m}}\right)\nu_x^2 + \left(\bar{C}^*_{66_m} - \frac{\bar{C}^{*2}_{36_m}}{\bar{C}^*_{33_m}}\right)\nu_y^2 + 2\left(\bar{C}^*_{16_m} - \frac{\bar{C}^*_{13_m}\bar{C}^*_{36_m}}{\bar{C}^*_{33_m}}\right)\nu_x\nu_y - \rho V_s^2\nu_x^2, \tag{5.84}$$

$$\beta_y^* = \left(\bar{C}^*_{66_m} - \frac{\bar{C}^{*2}_{36_m}}{\bar{C}^*_{33_m}}\right)\nu_x^2 + \left(\bar{C}^*_{22_m} - \frac{\bar{C}^{*2}_{23_m}}{\bar{C}^*_{33_m}}\right)\nu_y^2 + 2\left(\bar{C}^*_{26_m} - \frac{\bar{C}^*_{23_m}\bar{C}^*_{36_m}}{\bar{C}^*_{33_m}}\right)\nu_x\nu_y - \rho V_s^2\nu_x^2, \tag{5.85}$$

$$\beta_{xy}^* = \left(\bar{C}^*_{16_m} - \frac{\bar{C}^*_{13_m}\bar{C}^*_{36_m}}{\bar{C}^*_{33_m}}\right)\nu_x^2 + \left(\bar{C}^*_{26_m} - \frac{\bar{C}^*_{23_m}\bar{C}^*_{36_m}}{\bar{C}^*_{33_m}}\right)\nu_y^2 + \left(\bar{C}^*_{12_m} + \bar{C}^*_{66_m} - \frac{\bar{C}^{*2}_{36_m} + \bar{C}^*_{13_m}\bar{C}^*_{23_m}}{\bar{C}^*_{33_m}}\right)\nu_x\nu_y, \tag{5.86}$$

$$\xi_x^* = \frac{\bar{C}^*_{13_m}\nu_x + \bar{C}^*_{36_m}\nu_y}{\bar{C}^*_{33_m}}, \tag{5.87}$$

$$\xi_y^* = \frac{\bar{C}^*_{36_m}\nu_x + \bar{C}^*_{23_m}\nu_y}{\bar{C}^*_{33_m}}, \tag{5.88}$$

$$\zeta^* = \bar{C}^{*-1}_{33_m}. \tag{5.89}$$

In the case of an orthotropic layer, the vertical plane containing the direction of motion is generally not a plane of material symmetry, as opposed to the case of isotropic and transversely isotopic layers. Consequently, when forming the compliance matrix of an orthotropic layer, unit point loads must be applied at both extremities of the leading edge, and the trailing edge, of the candidate contact surface.

5.7 Isotropic formulation in plain strain

A two-dimensional boundary-element formulation for the layer in plane strain can be deduced from the three-dimensional formulation presented in Section 5.4, by eliminating all dependences on the spatial variable y, which corresponds to dropping the subscript n, and by setting out-of-plane deformation and strain coefficients to zero, i.e.

$$v_m = 0, \quad \epsilon_{yy_m} = 0, \quad \gamma_{xy_m} = 0, \quad \text{and} \quad \gamma_{yz_m} = 0. \tag{5.90}$$

The behavioral law in (5.27) hence implies

$$\tau_{xy_m} = 0, \quad \tau_{yz_m} = 0, \quad \text{and} \quad \sigma_{yy_m} = \lambda_m^* \left(\epsilon_{xx_m} + \epsilon_{zz_m}\right). \tag{5.91}$$

In light of (5.90) and (5.91), equilibrium equations (5.28)-(5.30) specialize into

$$-\rho V_s^2 \nu_x^2 u_m = i\nu_x \sigma_{xx_m} + \dot{\tau}_{xz_m}, \tag{5.92}$$

$$-\rho V_s^2 \nu_x^2 w_m = i\nu_x \tau_{xz_m} + \dot{\sigma}_{zz_m}, \tag{5.93}$$

Constitutive equations (5.31)-(5.36) also reduce to three relevant expressions, i.e.

$$\sigma_{xx_m} = \frac{E_m^*}{\left(1+\nu_m^*\right)\left(1-2\nu_m^*\right)} \left[\left(1-\nu_m^*\right) i\nu_x u_m + \nu_m^* \dot{w}_m\right], \tag{5.94}$$

$$\sigma_{zz_m} = \frac{E_m^*}{\left(1+\nu_m^*\right)\left(1-2\nu_m^*\right)} \left[\left(1-\nu_m^*\right) \dot{w}_m + \nu_m^* i\nu_x u_m\right], \tag{5.95}$$

$$\tau_{xz_m} = \sigma_{xz_m} = \frac{E_m^*}{2\left(1+\nu_m^*\right)} \left(i\nu_x w_{mn} + \dot{u}_{mn}\right). \tag{5.96}$$

The complex-valued state vector $\mathbf{q}_{mn}(z)$ defined in (5.37) becomes

$$\mathbf{q}_m(z) = \left\langle w_m(z), u_m(z), \sigma_{zz_m}(z), \tau_{xz_m}(z)\right\rangle^T. \tag{5.97}$$

Eliminating the remaining quantities from equations (5.92)-(5.96) results in a reduced and specialized version of equation (5.40), i.e.

$$\dot{\mathbf{q}}_m\left(z\right) = \mathbf{A}_m \mathbf{q}_m\left(z\right) \tag{5.98}$$

where $\mathbf{A}_{mn}$ is a complex-valued 4×4 matrix given by

$$\mathbf{A}_m = \begin{bmatrix} 0 & -i\xi^*\nu_x & \zeta^* & 0 \\ -i\nu_x & 0 & 0 & G_m^{*\,-1} \\ -\rho V_s^2 \nu_x^2 & 0 & 0 & -i\nu_x \\ 0 & \beta^* & -i\xi^*\nu_x & 0 \end{bmatrix}, \tag{5.99}$$

with ζ^* and ξ^* given by (5.45), and a new shorthand parameter β^* defined as

$$\beta^* = \left(\frac{E_m^*}{1 - \nu_m^{*\,2}} - \rho V_s^2 \right) \nu_x^2. \tag{5.100}$$

5.8 Transversely isotropic formulation in plain strain

A transversely isotropic formulation in plain strain can also be deduced from its three-dimensional counterpart derived in Section 5.5. Following a similar approach to that presented in Section 5.7, all dependences on the spatial variable y are eliminated by dropping the subscript n; the out-of-plane deformation and strain coefficients are set to zero, according to expression (5.90), which also yields equations (5.92)-(5.93). The constitutive equations in (5.50)-(5.55) reduce to the three relevant expressions below

$$\sigma_{xx_m} = C_{11_m}^* i\nu_x u_m + C_{13_m}^* \dot{w}_m, \tag{5.101}$$

$$\sigma_{zz_m} = C_{13_m}^* i\nu_x u_m + C_{33_m}^* \dot{w}_m, \tag{5.102}$$

$$\tau_{xz_m} = C_{44_m}^* \left(i\nu_x w_m + \dot{u}_m \right). \tag{5.103}$$

Defining the state vector as in (5.97), then combining equations (5.92)-(5.93) and (5.101)-(5.103), while eliminating all non-state variables, produces a similar formulation as in (5.99), where ζ^* and ξ^* are given by (5.59), $G_{LT_m}^*$ replaces G_m^*, and β^* is redefined as

$$\beta^* = \left(\frac{E_{T_m}^*}{1 - \nu_{T_m}^{*\,2}} - \rho V_s^2 \right) \nu_x^2. \tag{5.104}$$

5.9 Consistency checks

5.9.1 Linking the compressible and incompressible isotropic formulations

The full 3D *compressible* formulation derived in Section 5.4 is checked against the *incompressible* formulation presented in Chapter 4 (Zéhil and Gavin, 2013e). Setting Poisson's ratio $\nu^*(\omega)$ to the real and constant value of 1/2, the shorthand parameters defined in (5.42)-(5.45) become

$$\beta_x^* = G_m^* \left(4\nu_x^2 + \nu_y^2\right) - \rho V_s^2 \nu_x^2, \tag{5.105}$$

$$\beta_y^* = G_m^* \left(4\nu_y^2 + \nu_x^2\right) - \rho V_s^2 \nu_x^2, \tag{5.106}$$

$$\beta_{xy}^* = 3G_m^* \nu_x \nu_y, \tag{5.107}$$

$$\zeta^* = 0 \quad \text{and} \quad \xi^* = 1. \tag{5.108}$$

Substituting equations (5.105)-(5.108) into equation (5.41) and comparing to expressions (4.27) and (4.45) in Chapter 4 ((27) and (45) in Zéhil and Gavin, 2013e) reveals that the the two formulations match analytically for $\nu^*(\omega) = 1/2$. Consequently, the incompressible formulations proposed by Qiu (2006) and Zéhil and Gavin (2013e) may be regarded as particular cases of the more general formulations presented in Sections 5.4 and 5.7 of this work.

5.9.2 Linking the compressible orthotropic, transversely isotropic and isotropic formulations

It can be easily verified that the orthotropic formulation given by equations (5.6) and (5.80)-(5.89) matches the transversely isotropic formulation in equations (5.8), (5.41) and (5.56)-(5.59) when $E_1^* = E_2^* = E_T^*$, $\nu_{31}^* = \nu_{32}^* = \nu_{LT}^*$, $G_{13}^* = G_{23}^* = G_{LT}^*$, and $G_{12}^* = E_T^* / \left(2\left(1 + \nu_T^*\right)\right)$. It is noteworthy that, in this case, all combinations of $C_{ij_m}^*$ terms enclosed within parenthesis in equations (5.61)-(5.73) and multiplying functions of the variable θ vanish. Hence as expected, the polar anisotropic formulation is rendered independent of the direction of motion.

The parameters defined by expressions (5.56)-(5.59) also match those defined in equations (5.42)-(5.45) when $\nu^*_{LT_m} = \nu^*_{T_m} = \nu^*_m$, $E^*_{L_m} = E^*_{T_m} = E^*_m$ and $G^*_{LT_m} = E^*_m/\left(2\left(1+\nu^*_m\right)\right) = G^*_m$. The transversely isotropic formulation specializes into the isotropic formulations in this case.

5.10 Application examples to rolling resistance

In the following numerical examples, we consider a viscoelastic layer of thickness $H = 1$ mm and density $\rho = 1000$ kg/m^3. For simplicity, and without prejudice to the generality of the proposed formulations, which can accommodate any relaxation spectrum to each of the model's parameters, it is further assumed that Poisson's ratios are constant and that any frequency-dependent dynamic (longitudinal or shear) modulus $\mathcal{P}\left(\omega\right)$ follows the standard linear solid model defined by the following master-curves

$$\begin{aligned}\mathcal{P}'\left(\omega\right) &= \mathcal{P}_0(1+f_\mathcal{P})\frac{(1+f_\mathcal{P})+\omega^2\tau_\mathcal{P}^2}{(1+f_\mathcal{P})^2+\omega^2\tau_\mathcal{P}^2},\\ \mathcal{P}''\left(\omega\right) &= \mathcal{P}_0(1+f_\mathcal{P})\frac{f_\mathcal{P}\omega\tau}{(1+f_\mathcal{P})^2+\omega^2\tau_\mathcal{P}^2},\end{aligned} \tag{5.109}$$

where $\mathcal{P}_0 = \mathcal{P}'\left(0\right)$ is the static modulus, $\tau_\mathcal{P}$ s is the creep time and

$$f_\mathcal{P} = \mathcal{P}'\left(0\right)/\mathcal{P}'\left(\infty\right) - 1 = 1. \tag{5.110}$$

The viscoelastic resistances incurred by a rigid cylinder and a rigid sphere rolling in steady-state on the layer are sought, in two and three-dimensional settings respectively.

In the two-dimensional setting, we consider a rigid cylinder of radius $R = 2$ cm rolling on the layer at a constant speed V_s while subjected to a vertical load per unit length P. A constant coefficient of surface friction $\mu = 0.2$ is retained between the rolling cylinder and the layer's upper boundary. The cylinder is driven by a constant

force per unit length Q_x, applied tangentially to its upper generatrix in the direction of motion, i.e. towards the positive side of the x-axis. The described setting is taken to be spatially periodic, of period $L_x = 0.2$ m, in direction x.

The three-dimensional setting corresponds to that of a hard sphere of radius $R = 2$ cm, subjected to a vertical load P, and rolled on the layer by a driving force Q_x applied at its center, in the direction of positive x. Spatial periodicity is assumed in directions x and y with spatial periods $L_x = L_y = 0.2$ m. Given that the contribution of surface friction to rolling resistance is marginal (e.g. Greenwood and Tabor, 1958; Qiu, 2006; Tabor, 1955; Zéhil and Gavin, 2013e) (see Chapter 4), μ is set to zero to reduce three-dimensional computational costs.

In each of the following examples, the candidate contact surface on the layer's upper boundary is discretized into nodes and a compliance matrix $\mathbf{C}$ is built based on the formulations outlined in sections 5.4 through 5.8. Rolling resistance is then evaluated based on the solution to the rolling contact problem between: (i) the layer's upper boundary, which is fully characterized by $\mathbf{C}$, and (ii) the rigid rolling object. Almost any contact solving strategy may be used to this aim. The contact algorithms described in Chapter 3 (Zéhil and Gavin, 2013c) were retained for this work.

To optimize further the computational costs related to the three-dimensional models, appropriate nodal spacings and truncation orders are sought such to yield a satisfactory level of convergence. To this aim, rolling resistance is evaluated, in the conditions of Section 5.10.3, using a nodal spacing $a = a_x = a_y$ varying from 0.15 mm to 1 mm and a truncation order $N_t = N_{t_x} = N_{t_y}$ ranging from 100 to 1500 terms. The resulting values are reproduced in Table 5.1 and found to fall within 9% of each other. It is furthermore noted that, when the spacing between nodes is less than or equal to 0.75 mm, the results are well within 0.75%, which is suitable for most engineering applications. Table 5.1 furthermore reveals that the truncation order

Table 5.1: Effects of nodal spacing and truncation order on the convergence of 3D models.

a	Truncation order N_t [Number of Terms]					
[mm]	100	200	500	750	1000	1500
1.00	1.2406	1.1777	1.2025	1.2024	1.1992	1.2012
0.75	N/A	1.2867	1.2837	1.2856	1.2846	1.2849
0.50	N/A	1.2882	1.2906	1.2896	1.2900	1.2900
0.30	N/A	N/A	1.2906	1.2894	1.2905	1.2910
0.25	N/A	N/A	1.2914	1.2910	1.2911	1.2912
0.20	N/A	N/A	1.2925	1.2923	1.2920	1.2923
0.15	N/A	N/A	N/A	1.2927	1.2930	1.2931

has less impact on the accuracy of the solution than the nodal spacing. However, when the spatial mesh is refined, the surface stress distribution given by the generic expression in (5.49) takes a larger 'bandwidth.' Consequently, the number of terms in the Fourier series must be increased to prevent oscillations in the compliance matrix that would otherwise render the rolling contact problem impossible to solve ("N/A" entries in Table 5.1). Based on these observations, a nodal spacing of $a_x = a_y = 0.50$ mm and a truncation order of $N_{t_x} = N_{t_y} = 200$ terms are retained for the purposes of the following examples.

5.10.1 Compressible isotropic layer in 2D and 3D

Rolling cylinder in 2D

In this first two-dimensional example, the viscoelastic layer is taken to be compressible and isotropic with a static Young modulus $E_0 = 9$ MPa and a creep time $\tau_{E_0} = 0.25$ s. A linear speed $V_s = 5$ cm/s is retained for the rolling cylinder subjected to a vertical load $P = 5$ kN/m. The frequency-independent parameter ν of the layer is varied between -1 and 0.5 to illustrate the incidence of Poisson's ratio on the dynamic indentation and the rolling resistance.

The cylinder's penetration into the viscoelastic layer and the rolling resistance it is subjected to, including a marginal contribution from surface friction, are plotted

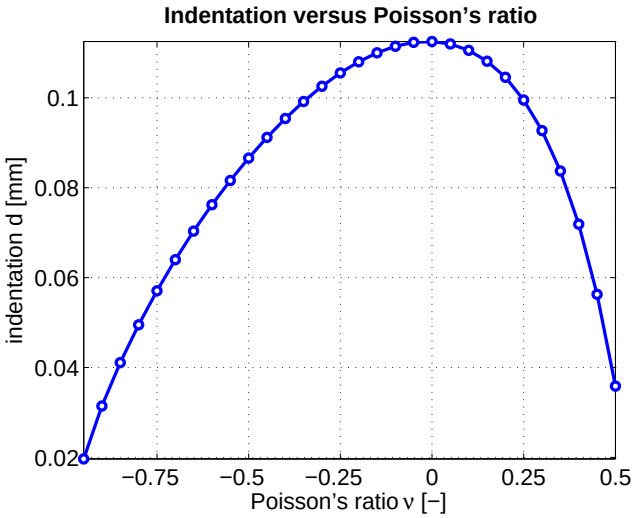

FIGURE 5.3: Rigid cylinder on a compressible isotropic viscoelastic layer (2D model in plane strain): variations of the indentation d with Poisson's ratio ν.

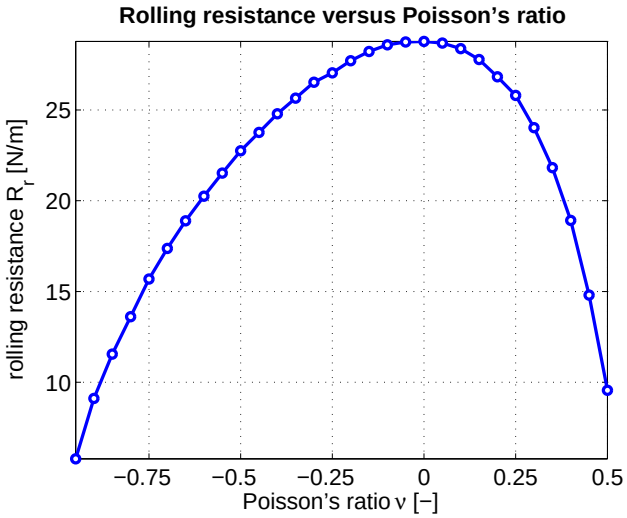

FIGURE 5.4: Rigid cylinder on a compressible isotropic viscoelastic layer (2D model in plane strain): variations of the rolling resistance R_r with Poisson's ratio ν.

in Figures 5.3 and 5.4 respectively, against Poisson's ratio. It is noteworthy that the relationship between indentation and rolling resistance is roughly linear in this case.

Rolling sphere in 3D

The compressible isotropic viscoelastic layer described in Section 5.10.1 is now modeled in three-dimensions. The sphere is rolled on the layer at the same speed as the cylinder, i.e. at $V_s = 5$ cm/s, while subjected to a vertical load $P = 100$ N. The average contact pressure corresponding to P is roughly the same as for the cylinder in Section 5.10.1.

The sphere's penetration into the viscoelastic layer and the rolling resistance it is subjected to are plotted in Figures 5.5 and 5.6 respectively, against Poisson's ratio. The corresponding curves are qualitatively similar to the curves shown in Figures 5.3 and 5.4 for the cylinder. Both quantities are maximized by a Poisson ratio that is close to zero, as predicted by the approximate equations reproduced in (1.1)-(1.3) for spheres. As noted in Section 5.10.1 for cylinders, the dependence of rolling resistance on the sphere's penetration into the layer, for the current range of

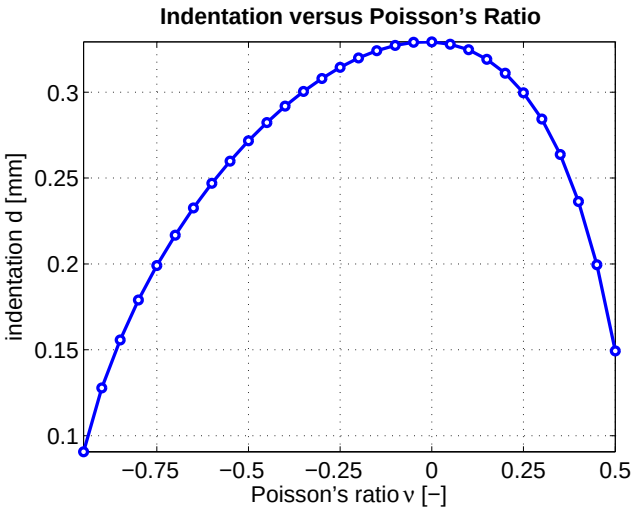

FIGURE 5.5: Rigid sphere on a compressible isotropic viscoelastic layer (3D model): variations of the indentation d with Poisson's ratio ν.

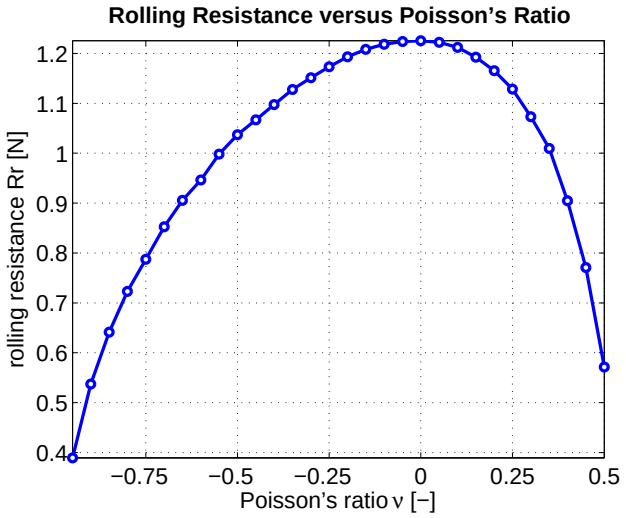

FIGURE 5.6: Rigid sphere on a compressible isotropic viscoelastic layer (3D model): variations of the rolling resistance R_r with Poisson's ratio ν.

parameters, appears to be linear.

5.10.2 Transversely isotropic layer in 2D

The rolling of a hard cylinder on a transversely isotropic viscoelastic layer is considered here and analyzed in plane strain. The material model is further characterized by the following values of its parameters: $E_{L_0} = 4$ MPa, $E_{T_0} = 9$ MPa, $G_{LT_0} = 3$ MPa, $\nu_T = 0.45$ and $\nu_{LT} = 0$. All creep times are taken equal to 0.25 s.

The penetration of the rolling cylinder into the layer and the rolling resistance it incurs are plotted in Figures 5.7 and 5.8 respectively, against the rolling speed V_s ranging from 0.1 cm/s to 50 cm/s. Starting at 500 N, the applied load P is increased by steps of 500 N, up to 5 kN. The shapes of the curves are typical of viscoelastic models: the indentation decreases with increasing speed between two asymptotes, as the layer's stiffness does; alternatively, hysteretic dissipations tend to zero as the time to cover a distance equal to a dimension of reference, such as the radius of the rolling object, becomes very small, or very large, as compared to the material's internal time scales. A peak in rolling resistance is hence reached at an intermediate velocity

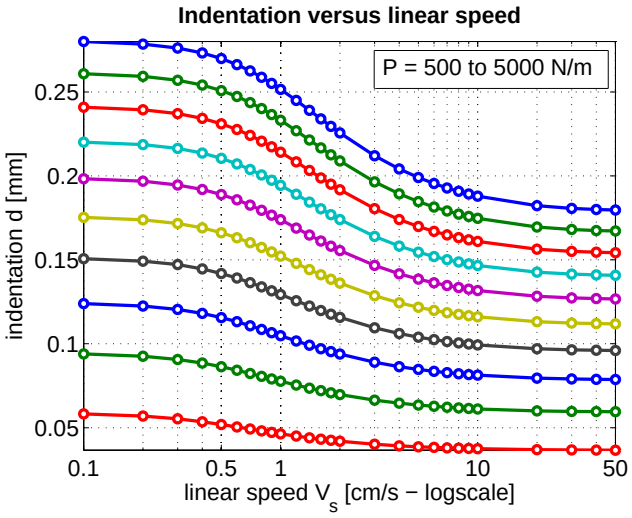

FIGURE 5.7: Rigid cylinder on a transversely isotropic viscoelastic layer (2D model in plane strain): variations of the indentation d with the rolling speed V_s. The curves correspond to different load levels between 500 N and 5 kN, in steps of 500 N. Indentation and rolling resistance increase with the applied load.

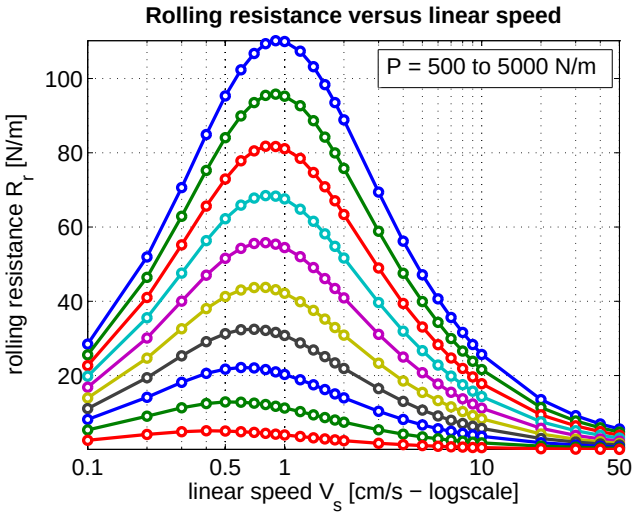

FIGURE 5.8: Rigid cylinder on a transversely isotropic viscoelastic layer (2D model in plane strain): variations of the rolling resistance R_r with the rolling speed V_s. The curves correspond to different load levels between 500 N and 5 kN, in steps of 500 N. Indentation and rolling resistance increase with the applied load.

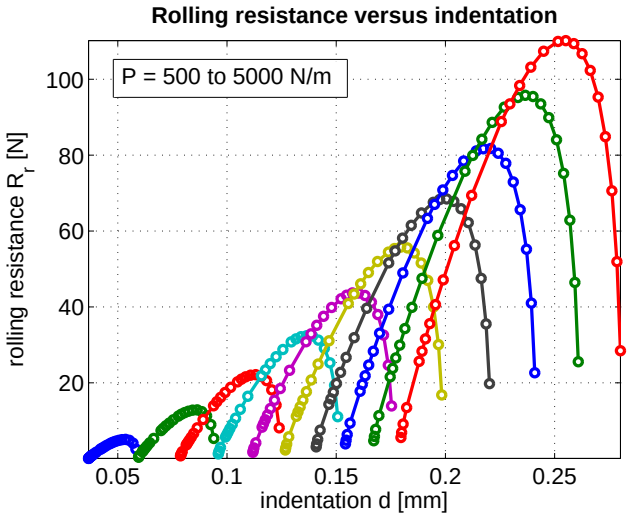

FIGURE 5.9: Rigid cylinder on a transversely isotropic viscoelastic layer (2D model in plane strain): variations of rolling resistance with indentation for different values of the applied load. The curves correspond to different load levels between 500 N and 5 kN, in steps of 500 N. Indentation and rolling resistance increase with the applied load.

depending on the parameters of the problem, including the relaxation spectrum of the layer.

In Figure 5.9, rolling resistance values from Figure 5.8 are plotted against the corresponding indentations taken from Figure 5.7, which produces one curve for each value of the load P. Referring to Figure 5.7, the end of each curve in Figure 5.9 with the higher rolling resistance and indentation corresponds to the lower rolling speed of 0.1 cm/s. A roughly quadratic dependence of rolling resistance on indentation is revealed in this case.

5.10.3 Orthotropic layer in 3D

The rolling of a hard sphere on an orthotropic layer is considered in this example. The viscoelastic material model of the layer is further characterized by the static moduli, creep times and frequency-independent Poisson ratios given in Table 5.2.

The x-axis, corresponding to the direction of motion, is defined by its angle θ from

Table 5.2: Static moduli, creep times and Poisson ratios characterizing the orthotropic viscoelastic layer.

Index i	1	2	3
E_{i_0} [MPa]	9.00	6.00	4.00
τ_{E_i} [s]	2.00	0.05	0.25
Indices i / j	1 / 2	1 / 3	2 / 3
G_{ij_0} [MPa]	3.00	3.00	3.00
$\tau_{G_{ij}}$ [s]	0.25	2.00	0.05
ν_{ij} [-]	0.20	0.00	0.50

the the first axis of orthotropy in the plane of the layer, as depicted in Figure 5.2. The viscoelastic resistance incurred by the rolling sphere is plotted in Figure 5.10 against the angle θ, varying between 0 and 90 degrees, for $P = 100$ N and $V_s = 0.1$ and 5 cm/s. Given the choice of parameters in Table 5.2, the dependence of rolling resistance on the direction of motion varies with the rolling speed. For instance, at $V_s = 5$ cm/s, minimum (resp. maximum) rolling resistance occurs when the direction of motion is at an angle of roughly 40 (resp. 90) degrees from the 1-axis. Alternatively, at $V_s = 0.1$ cm/s, maximum and minimum rolling resistances occur when θ equals 45 and 90 degrees, respectively.

Rolling resistance results as usual from the asymmetry of the normal contact stress distribution, induced by viscoelasticity, in the longitudinal direction. However, in contrast with all previous cases, when the direction of motion is at a nonzero angle from the principal axes of orthotropy, the mechanical response of the layer is different on each side of the vertical plane containing the x-axis, which results in a lateral asymmetry of contact generating an additional resultant acting on the sphere in direction y. Hence, an equal and opposite lateral force Q_y must be applied to the center of the sphere, in addition to Q_x, to maintain steady-state motion along a straight path. The variations of Q_y with the direction of motion, for $P = 100$ N and $V_s = 0.1$ and 5 cm/s, are shown in Figure 5.11. Q_y reaches a peak at an angle θ

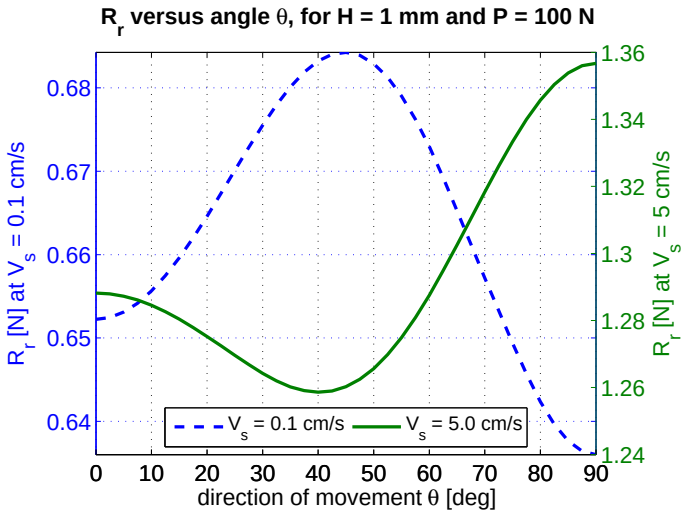

FIGURE 5.10: Rigid sphere on an orthotropic viscoelastic layer (3D model): variations of the rolling resistance R_r with the direction of motion θ.

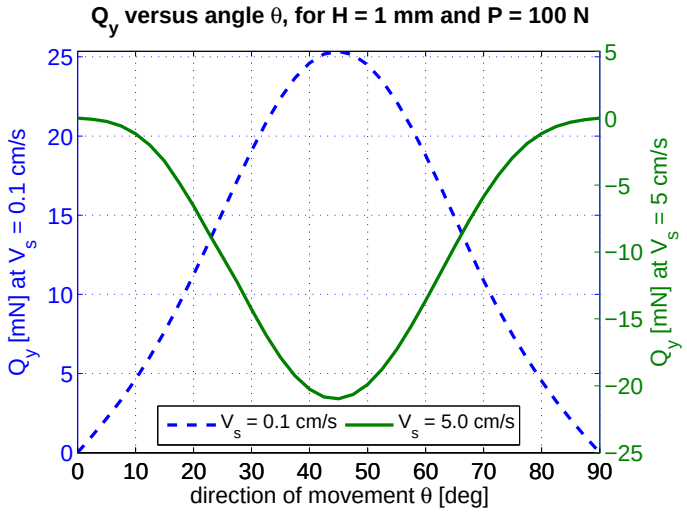

FIGURE 5.11: Rigid sphere on an orthotropic viscoelastic layer (3D model): variations of the lateral guiding force Q_y with the direction of motion θ.

depending on the rate of motion and drops to zero, as expected, along the principal axes of orthotropy. It is interesting to note that the sign of Q_y depends on the rolling speed. For instance, at $V_s = 0.1$ cm/s, the sphere tends to deviate to the right in the absence of lateral support, whereas at $V_s = 5$ cm/s, it tends to deviate to the left.

The variations of rolling resistance R_r and of the lateral supporting force Q_y with the rolling speed V_s, ranging from 0.01 cm/s to 50 cm/s, are shown in Figures 5.12 and 5.13 respectively, for the direction of motion defined by $\theta = 40$ deg. Each curve corresponds to a fixed value of the applied load P, which is increased by steps of 10 N, starting at 10 N and up to a 100 N. The dependence of rolling resistance on the rate of motion is of the usual kind, briefly described for instance in Section 5.10.2. It is again interesting to note that Q_y tends to zero at low and high speeds which confirms its viscoelastic nature. Furthermore, in relation with what was previously noted in Figure 5.11 regarding the sign of Q_y, Figure 5.13 reveals the existence of an intermediate speed at which Q_y also vanishes.

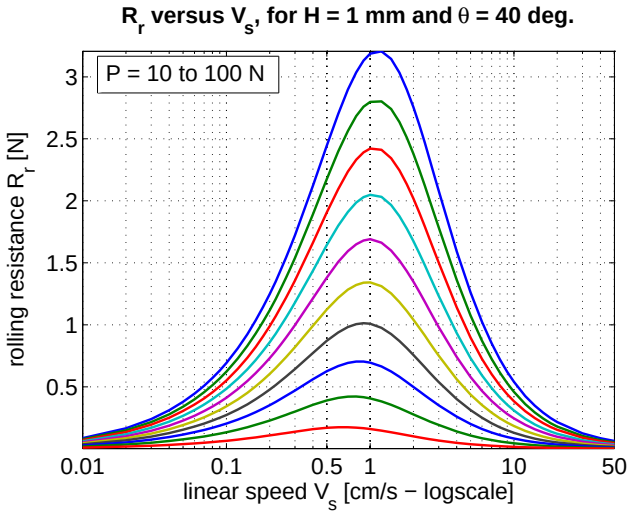

FIGURE 5.12: Rigid sphere on an orthotropic viscoelastic layer (3D model): variations of the rolling resistance R_r with the rolling speed V_s. The curves correspond to different load levels between 10 N and 100 N, in steps of 10 N. Rolling resistance and lateral force increase in magnitude with the applied load.

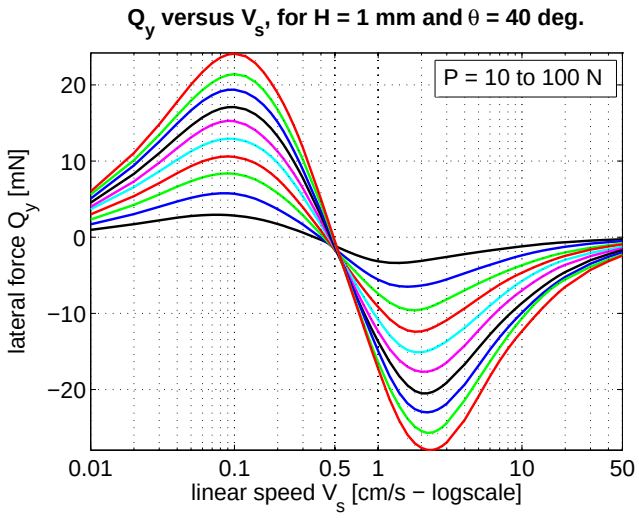

FIGURE 5.13: Rigid sphere on an orthotropic viscoelastic layer (3D model): variations of the lateral guiding force Q_y with the rolling speed V_s. The curves correspond to different load levels between 10 N and 100 N, in steps of 10 N. Rolling resistance and lateral force increase in magnitude with the applied load.

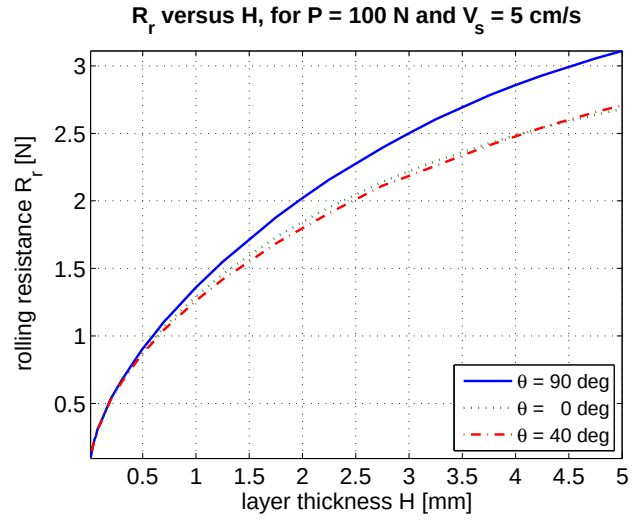

FIGURE 5.14: Rigid sphere on an orthotropic viscoelastic layer (3D model): variations of the rolling resistance R_r with the layer's thickness H.

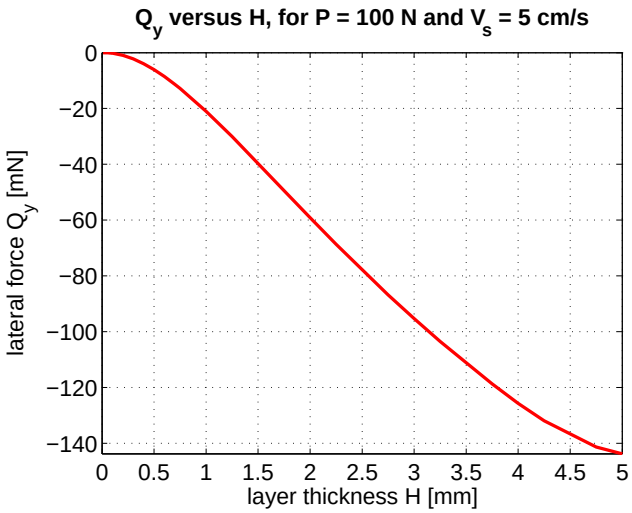

FIGURE 5.15: Rigid sphere on an orthotropic viscoelastic layer (3D model): variations of the lateral guiding force Q_y with the layer's thickness H.

The influence of layer thickness (H) on the rolling resistance incurred by the sphere (R_r) and on the lateral supporting force (Q_y) are shown in Figures 5.14 and 5.15 respectively, for the directions of motion defined by $\theta = 0$ deg., $\theta = 40$ deg. and $\theta = 90$ deg. The trivial cases corresponding to $Q_y(H, \theta) = 0 \ \forall H$ for $\theta = 0$ deg. and $\theta = 90$ deg. are hidden in Figure 5.15. As in the case of an incompressible and isotropic foundation (e.g. Qiu, 2006; Zéhil and Gavin, 2013e) (see Chapter 4), the resistance to rolling increases with layer thickness and tends progressively towards a horizontal asymptote corresponding to the limiting case of an orthotropic viscoelastic "half-space". The magnitude of Q_y is also an increasing function of H. Its change of curvature is consistent with the existence of a limiting case as H tends to infinity. The dependence of both quantities (R_r and Q_y) on layer thickness can be fitted, for instance, by rational functions with negative poles. These expressions should be further characterized by a numerator that vanishes as H tends to zero and by a denominator of the same degree as the numerator, such that the fitted function tends asymptotically to the "half-space" solution as H becomes large.

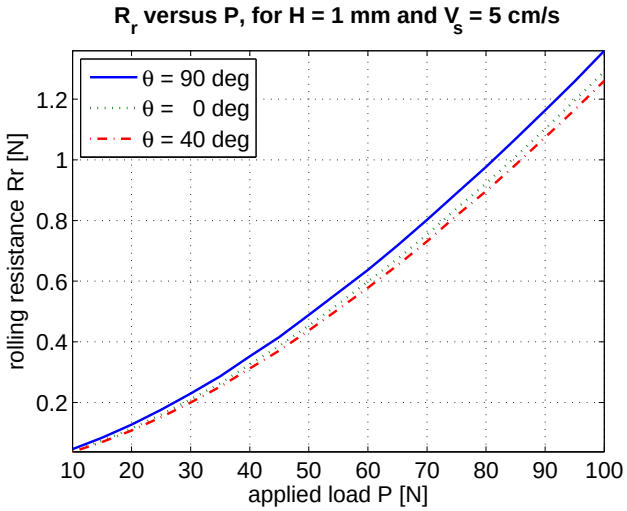

FIGURE 5.16: Rigid sphere on an orthotropic viscoelastic layer (3D model): variations of the rolling resistance R_r with the applied load P.

Rolling resistance (R_r) and lateral force (Q_y) are plotted in Figures 5.16 and 5.17 respectively, against the applied load P, ranging from 10 to 100 N, for $H = 1$ mm, $V_s = 5$ cm/s and for the directions of motion corresponding to $\theta = 0$ deg., $\theta = 40$ deg. and $\theta = 90$ deg. The trivial cases given by $Q_y(P, \theta) = 0 \; \forall P$ for $\theta = 0$ deg. and $\theta = 90$ deg. are hidden from Figure 5.17. The resistance to motion and the magnitude of the lateral force increase with the vertical load supported by the rolling sphere, which is in agreement with the information displayed in Figures 5.12 and 5.13. The dependence of Q_y on P appears to be quasi-linear. Alternatively, the relationship between R_r and P is well fitted by power laws of the form $R_r(P) = a_p P^{b_p}$. The coefficient b_p falls between 0.49 and 0.55 for the curves plotted in Figure 5.16. It is furthermore noteworthy that, in accordance with the results shown earlier in Figure 5.10, the dashed curve and the dotted curve in Figure 5.14 remain below the solid curve corresponding to the direction of maximum dissipation.

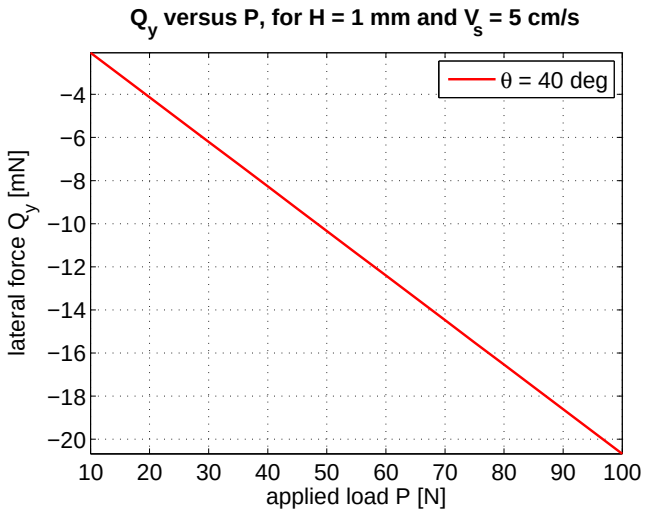

FIGURE 5.17: Rigid sphere on an orthotropic viscoelastic layer (3D model): variations of the lateral guiding force Q_y with the applied load P.

5.11 Summary

New two-dimensional and three-dimensional boundary element formulations of *compressible* viscoelastic layers of arbitrary thickness were presented in this work, in a moving frame of reference. These formulations were derived in increasing order of complexity for: (i) compressible isotropic layers, (ii) transversely isotropic layers, and (iii) fully orthotropic layers. The proposed modeling techniques include, extend and complement existing 2D (Qiu, 2006) and 3D (Zéhil and Gavin, 2013e) formulations for *incompressible* layers (see Chapter 4) and are hence characterized by similar (and further improved) strengths, such as: (i) the ability to accommodate any orthotropic linear viscoelastic model comprising as many internal time scales as necessary for each of the nine complex frequency-dependent model parameters, (ii) versatility in that the formulations can be used as components in various problem settings such as steady-state rolling or sliding contact problems involving soft or rigid indenters, and other layers, (iii) accuracy compared to other existing approaches relying on the elastic half-space approximation (e.g. Kalker, 1979; Vollebregt, 2012) in propagating

viscoelastic surface effects to the layer's continuum, and posing limitations on how thin the layer can be, (iv) computational efficiency resulting from the fact that a compliance matrix for the layer's upper boundary needs to be formed once and can be used to generate sequences of high fidelity results for varying problem parameters, (v) the avoidance of certain types of numerical difficulties associated with finite elements, which are best described by Hughes (2000), such as element locking. Consistency checks were performed, at the analytical level, to verify the mathematical equivalence between formulations in limiting cases and on overlapping parts of their application domains. In 2D and 3D application examples, the proposed formulations were applied, in combination with appropriate contact solvers, presented in Chapter 3 (Zéhil and Gavin, 2013c), to illustrate the influence of several parameters on the resistance to motion incurred by rigid cylinders and spheres rolling on compressible isotropic, transversely isotropic and orthotropic layers. In particular, the latter case revealed the existence, at each given speed, of specific directions of motion along which maximum and minimum dissipation occur. This observation may have broader impacts of notable significance, such as on the design and proper orientation of new anisotropic metamaterials, possibly including auxetic components, to optimize the level of damping according to the needs of a given application. For instance, in the strive to achieve more resilient and sustainable infrastructures, higher levels of damping may be sought, in preferential directions, for better earthquake mitigation. Alternatively, low rolling resistance conveyor belts could be produced to reduce industrial power consumption. Similarly, low rolling resistance vehicle tires and road pavements could be designed to limit energy losses and further improve road transport efficiency and vehicle handling. A transverse asymmetry in contact stresses was also noted when the motion takes place at a nonzero angle from the principal axes of orthotropy. In the absence of lateral support, the contact resultant tends to deviate the moving object from its initial course. This observation implies that smooth and

'invisible' guides can be achieved across three-dimensional viscoelastic surfaces by suitable modification of their mechanical properties. Potential fields of impact include vehicle handling, the control of rainwater runoff, the modification of boundary layers in fluid dynamics (with applications to vehicle, watercraft, submarine, aircraft, rocket sled and missile technologies) and the selection of moving components based on speed. The new modeling tools presented in this work stand, as a contribution, to achieving such global goals.

6

Rolling resistance of a rigid sphere with viscoelastic coatings

6.1 Preamble

The problem of a viscoelastic object rolling (or sliding) across a rigid surface raises more difficulties than that of a rigid indenter moving in contact with a viscoelastic plane. Our modeling of the former, which is significantly more complicated, relies on the assumption of a relatively small contact surface in order to decouple equilibrium equations in the frequency domain. These and other complexities described in this chapter may explain why previous work on this topic is so sparse. A boundary element model for the multi-layered viscoelastic coating of a rigid sphere is developed and an adapted rolling contact solving strategy is proposed. These are applied to the rolling resistance of a coated sphere. The model is verified by comparison to dynamic finite element simulations. The dependencies of rolling resistance on problem parameters are then explored.

6.2 Background

In the following, we briefly review four studies that focus on the rolling resistance incurred by a *solid* viscoelastic sphere on a rigid plane, mostly, in narrow ranges of the parameters.

Brilliantov and Pöschel (1998) propose an approximate closed-form expression for the friction coefficient of a solid viscoelastic sphere of radius R rolling on a hard plane, in quasi-static conditions and under small deformations. The authors assume that the characteristic time of the motion, defined as the ratio of the sphere's deformation $d = R - H$ (H being the distance between the center of the deformed sphere and the contact surface) to its rolling velocity V_s, is much larger than the material's internal time scales τ_k. In agreement with this regime of motion and with the small strain assumption $d/R \ll 1$, inertial forces are neglected and the vertical displacement field is approximated by the corresponding result of the stationary contact problem, as given by Hertz (1881). The behavioral characterization of the viscoelastic material is limited to two viscous parameters, or equivalently, to a single relaxation time for each of the shear modulus and the bulk modulus. In fact, the stress field is written as the sum of an elastic part $\boldsymbol{\sigma}_e$, and a viscous part $\boldsymbol{\sigma}_v$, which corresponds to the Kelvin-Voigt model, characterized by a constant storage modulus, and by a loss modulus increasing linearly with frequency. This choice is consistent with the other assumptions retained by the authors in the sense that the linearization of any frequency-domain viscoelastic master-curves about zero frequency, corresponds to a Kelvin-Voigt model. This fact is readily inferred, for instance, from their equations (6.75a) and (6.75b). It is assumed that the elastic part of the contact stress field is almost unaffected by the (slow) motion, and that it remains roughly symmetrical. Its contribution to the resisting torque T_r is hence neglected, in comparison to that of the viscous stress field. The authors show that, within the framework of the

proposed theory, the resisting torque scales linearly with the vertical load applied to the rolling sphere P, with its radius R, its angular speed Ω, and therefore with its velocity $V_s \approx R\Omega$. The proposed expression is however flawed due to an error in a coordinate system transformation, as recently determined by Zheng et al. (2011).

A few years later, Yung and Xu (2003) argue that, in most practical cases, the material's internal rates of dissipation cannot be considered much smaller than the characteristic time of motion, and therefore conclude that more accurate expressions are needed for the rolling resistance of viscoelastic spheres, which take into account the "influence of relaxation". To this aim, the authors 'relax' the assumption $d/V_s \gg \tau_k$, attempting to reveal the nonlinear dependence of rolling resistance on velocity, at moderately higher rates of motion. They however stipulate, for simplicity, that the fields in the continuum of the sphere, at a given cycle, are not influenced by the preceding cycles, which is equivalent to maintaining the limiting condition that $\Omega\tau_k \ll 1$. It is interesting to note that the latter constraint is satisfied implicitly under the assumptions retained earlier by Brilliantov and Pöschel (1998), i.e. $\Omega\tau_k \ll d/R \ll 1$. In contrast, Yung and Xu (2003)'s assumptions that $\Omega\tau_k \ll 1$ and that $d/R \ll 1$ are unconnected, which expands the applicability domain of their theory to the nonlinear regime, by increasing the upper bound on Ω. In deriving a nonlinear relation for rolling resistance, the authors make several other simplifying assumptions, some of which are quite limiting, and somewhat inconsistent with their stated goal, such as retaining one Kelvin-Voigt element to model the material's behavior. Indeed, this material model is characterized by a single rate of internal dissipation and is known to better reflect creep than relaxation. Other approximations include: (i) introducing the viscous behavior vertically and pointwise (ii) neglecting inertial effects under the quasi-static approximation, (iii) retaining the same contact radius r_c and deformation d as the stationary Hertzian solution, (iv) assuming a sinusoidal stress distribution across the contact surface, calibrated to yield the same

maximum contact pressure as that of the stationary solution, (v) evaluating an 'average' density of dissipated energy at one point of 'average' position with 'average' values of the fields, and (vi) evaluating the total dissipation by integration over a "deformed volume" $2\pi R r_c d$ of ring-like cross section defined by the contact path $2\pi R$, the 'average' contact width r_c, and the deformation d. The resulting analytical expression for rolling resistance is quite cumbersome. A numerical example reveals that, according to the proposed theory, rolling friction first increases, then decreases, with increasing velocity. However, given the constitutive model retained, and in the absence of inertial effects, the physical mechanisms causing the rolling friction to decrease with increasing speed is rather unclear.

Xu et al. (2007) present an experimental apparatus that measures the steady-state coefficient of rolling friction $T_r/(PR)$ of a squash ball on a conveyor belt, at moderate velocities. The setup was designed to fill an identified gap in the availability of accessible methods to perform rolling resistance experiments involving deformable spheres. It was later used in a classroom for teaching purposes. The different sources of power dissipation contributing to rolling resistance cannot be clearly distinguished using the proposed device. Indeed, energy losses occur not only in the bulk of the sphere, but also to some extent in the bulk of the deformable conveyor belt, and at the contact interface in case of slipping friction as well. Nevertheless, the experimental results presented by the authors, for the combined losses, confirm the linear dependence of the coefficient of rolling friction on the translational velocity V_s, at moderate rates of motion.

More recently, Zheng et al. (2011) implement, using the commercial software ABAQUS, a finite element (FE) model for the steady-state rolling resistance of a solid viscoelastic sphere on a rigid plane, under the quasi-static approximation. The material's behavior is characterized as in the work of Brilliantov and Pöschel (1998), with the additional assumption that the viscous parameter associated with the bulk

modulus is equal to zero, which in fact corresponds to the three-dimensional formulation of the material behavior retained by Yung and Xu (2003). The FE model's implementation is focused on the regime where $\Omega\tau_k \ll 1$, which corresponds to the elastic part of the contact stress field being much larger than the viscous part, but also to small values of rolling resistance. To avoid that the resisting torque be affected by numerical errors on $\boldsymbol{\sigma}_e$, the authors override the finite element software to compute the resisting torque from $\boldsymbol{\sigma}_v$ only, hence neglecting the contribution of $\boldsymbol{\sigma}_e$. The numerical model is exploited in the conditions corresponding to $\Omega\tau_k \ll d/R$ and to $d/R \ll 1$. In this regime, the coefficient of rolling friction, defined as $T_r/(PR)$, is found to be almost independent from the vertical load P applied to the sphere, and to vary linearly with the rolling speed Ω. The authors also derive an analytical expression for rolling friction, based on the assumptions retained by Brilliantov and Pöschel (1998), which matches the results of their numerical model fairly well.

It is interesting to note that, in the papers discussed above, either (i) a simplified formulation is retained which does not involve a rolling contact problem, or (ii) a more sophisticated numerical approach is adopted, but the resolution of contact is carried out by means of a commercially available tool, with minimal discussion.

To date, no work has ever addressed the modeling (and the solving) of the resistance incurred by a rigid sphere, covered with a viscoelastic coating, rolling or sliding, on a rigid plane. In this chapter, we present a novel three-dimensional boundary-element formulation that fully characterizes the mechanical behavior of the external boundary of a multi-layered viscoelastic coating attached to a hard rotating spherical core. A brief comparison between the semi-analytical model proposed here and the previous relevant works addressing the rolling friction of solid viscoelastic spheres is presented in Table 6.1. The proposed formulation incorporates both, the viscoelastic, and the inertial effects of the steady-state rolling motion of the sphere, including the Coriolis effect. Linear viscoelastic materials are characterized

Table 6.1: Comparison between the semi-analytical model proposed in this work and previous relevant works addressing the rolling resistance of *solid* viscoelastic spheres: principal model characteristics and main assumptions retained.

	Relevant models: Author (Year)				
Principal model characteristics and main assumptions retained	Brilliantov and Pöschel (1998)	Yung and Xu (2003)	Zheng et al. (2011)	Zheng et al. (2011)	Zéhil and Gavin (2013b)
Type of the proposed model	Analytical	Analytical	Analytical	Numerical (FE)	Semi-Analytical
Viscoelastic material description retained	Kelvin-Voigt	Kelvin-Voigt	Kelvin-Voigt	Kelvin-Voigt	General
Are inertial effects accounted for?	No	No	No	No	Yes
Is the Coriolis effect accounted for?	No	No	No	No	Yes
Does the model support surface frictions?	No	No	No	No	Yes
Can the model handle coated spheres?	No	No	No	No	Yes
Does the model support multiple layers?	No	No	No	No	Yes
Is a contact solving strategy proposed?	No	No	No	FE (ABAQUS)	Yes
Are stationary contact fields retained?	Yes	Yes	Yes	Partially	No
Is the contribution of $\boldsymbol{\sigma}_e$ to T_r neglected?	Yes	Yes	Yes	Yes	No
Does the model rely on the assumption: $\Omega\tau_k \ll d/R$?	Yes	Yes	Yes	Yes	No
Does the model rely on the assumption: $d/R \ll 1$?	Yes	Yes	Yes	Yes	Partially
Does the model rely on the assumption: $\Omega\tau_k \ll 1$?	Yes	Yes	Yes	Yes	No

by frequency-domain master-curves. This choice of material description is the most general in that it accommodates broad-spectrum Prony series with as many internal time-scales as practically needed, as well as fully experimental results from dynamic mechanical analyses, resonant ultrasound spectroscopies, or broadband viscoelastic spectroscopies (e.g. Eakasit et al., 2009; Lakes, 2004, 2009; Lee et al., 2000; Menard, 2008). The proposed formulation takes advantage of the periodicity of all fields in the continuum. It is based on Fourier-domain expressions of local equilibrium equations, constitutive equations and boundary conditions. It relates two-dimensional Fourier series expansions of surface displacements and stresses, which results in the formation of a compliance matrix for the outer boundary of the deformable coating, discretized into nodes. Taking advantage of configurational similarities and symmetry, the computational cost of building compliance matrices is reduced significantly. The proposed formulation may be leveraged in important aspects of the modeling of several types of problems, pertaining to different fields, in various settings and at multiple scales, such as mechanical interactions between nano-particles and/or biological organisms, bone articulations, granular materials, round-shaped components in industrial machineries, in transport vehicles of all kinds, in satellites, in robots, and in risk mitigation devices such as seismic isolation platforms. Furthermore, in the constant improvement process of discrete element models (DEM), which are often used to study the flow of granular materials, such as earth materials in traditional extruders, or plastic pellets in micro-injection moulding machines (e.g Yung et al., 2007), aspects of the proposed formulation may be called upon to account for the viscoelastic rolling friction between particles. An extension of the three-dimensional rolling contact solving strategy proposed in Chapter 3 (Zéhil and Gavin, 2013c), to the case of a deformable sphere rolling/sliding on rigid plane, is also presented in this chapter. The boundary element model of the coated sphere and the rolling contact algorithm are combined to evaluate the resistance to motion. A detailed applica-

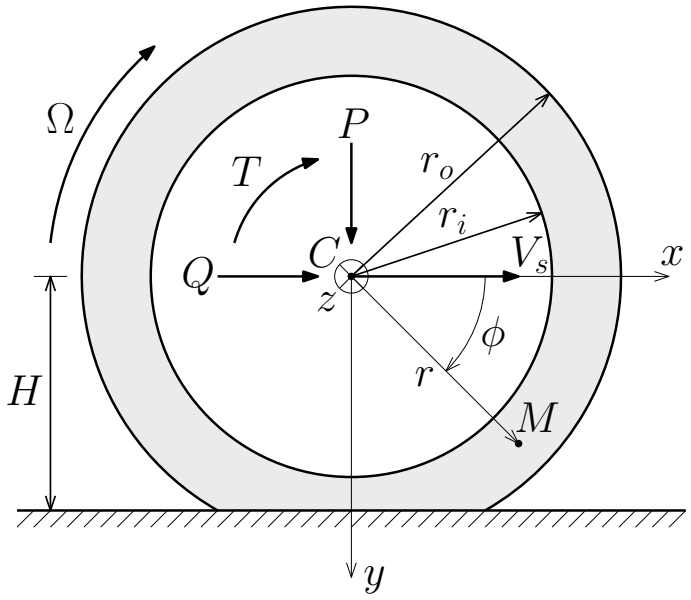

FIGURE 6.1: General model of a coated sphere and its coordinate systems.

tion example includes a verification of convergence and illustrates the dependence of rolling friction on the applied load, the thickness of the coating, and the rolling speed.

6.3 Problem setting

Figure 6.1 shows a hard spherical core, of radius r_i, coated with a layer of viscoelastic material of uniform thickness $h = r_o - r_i$, which is perfectly bonded to the core. The sphere is considered to be rolling on a rigid plane, in the x-direction, at a constant angular speed Ω. In our most general case, the rolling object is subjected to: (i) a vertical load P acting downwards, (ii) a driving horizontal force Q acting in the direction of motion, and (iii) a driving torque T, acting clockwise. The external actions P, Q and T are applied at point C, at the center of the rolling sphere. The absolute linear velocity of point C is designated by V_s. Due to the deformation of the coating, the distance H between point C and the rigid plane is smaller than the outer radius of the sphere, i.e. $H \leq r_o$.

The moving rectangular coordinate system $Cxyz$ follows point C, without rotating. Let $Cr\phi\theta$ be the spherical coordinate system to which $Cxyz$ is related, according to the set of equations below:

$$\begin{aligned} x &= r\cos(\phi)\sin(\theta), \\ y &= r\sin(\phi)\sin(\theta), \\ z &= rcos(\theta). \end{aligned} \tag{6.1}$$

The spherical coordinates r, ϕ and θ can be related to their primed counterparts, rotating with the sphere, by a simple transformation involving the time variable t, i.e.

$$\begin{aligned} r &= r', \\ \phi &= \phi' + \Omega t, \\ \theta &= \theta'. \end{aligned} \tag{6.2}$$

Because the state of motion is steady, any generic field $f(r, \phi, \theta)$ in the continuum of the coating does not depend explicitly on time. Furthermore, equations (6.2) lead to a spatial expression of the n^{th}-order derivative of $f(r, \phi, \theta)$ with respect to time

$$\frac{d^n f}{dt^n} = \Omega^n \frac{\partial f}{\partial \phi}. \tag{6.3}$$

6.4 Governing equations

Let u_r, u_ϕ and u_θ be the components of the displacement field in $Cr\phi\theta$, along the unit vectors $\mathbf{e}_r$, $\mathbf{e}_\phi$ and $\mathbf{e}_\theta$ respectively. The position vector of a (displaced) point $M(r, \phi, \theta)$ in the continuum writes

$$\mathbf{x}(r, \phi, \theta) = (r + u_r)\,\mathbf{e}_r + u_\phi \mathbf{e}_\phi + u_\theta \mathbf{e}_\theta. \tag{6.4}$$

The velocity and acceleration fields are obtained by differentiating equation (6.4) with respect to time, according to expression (6.3), which yields

$$\mathbf{v}(r, \phi, \theta) = \Omega\left(u_{r,\phi} - u_\phi \sin(\theta)\right)\mathbf{e}_r \ldots$$

$$+ \Omega \left(u_{\phi,\phi} + (r + u_r) \sin(\theta) + u_\theta \cos(\theta) \right) \mathbf{e}_\phi \ldots \tag{6.5}$$
$$+ \Omega \left(u_{\theta,\phi} - u_\phi \cos(\theta) \right) \mathbf{e}_\theta,$$

$$\begin{aligned} \mathbf{a}(r,\phi,\theta) = {} & \Omega^2 \left(u_{r,\phi\phi} - 2u_{\phi,\phi} \sin(\theta) - (r + u_r) \sin(\theta)^2 - u_\theta \sin(\theta) \cos(\theta) \right) \mathbf{e}_r \ldots \\ & + \Omega^2 \left(u_{\phi,\phi\phi} - u_\phi + 2u_{r,\phi} \sin(\theta) + 2u_{\theta,\phi} \cos(\theta) \right) \mathbf{e}_\phi \ldots \\ & + \Omega^2 \left(u_{\theta,\phi\phi} - 2u_{\phi,\phi} \cos(\theta) - (r + u_r) \sin(\theta) \cos(\theta) - u_\theta \cos(\theta)^2 \right) \mathbf{e}_\theta. \end{aligned} \tag{6.6}$$

The local equilibrium equations in the continuum of the layer write

$$\mathbf{div}(\boldsymbol{\sigma}) = \rho \mathbf{a} \tag{6.7}$$

where $\boldsymbol{\sigma}$ is the stress tensor and ρ is the density of the viscoelastic material. Plugging equation (6.6) into (6.7) and expressing (6.7) in spherical coordinates yields

$$\sigma_{rr,r} + \frac{1}{r}\sigma_{r\theta,\theta} + \frac{1}{r\sin(\theta)}\sigma_{r\phi,\phi} + \frac{1}{r}\left(2\sigma_{rr} - \sigma_{\theta\theta} - \sigma_{\phi\phi} + \sigma_{r\theta}\cot(\theta)\right) = \ldots$$
$$\rho\Omega^2 \left(u_{r,\phi\phi} - 2u_{\phi,\phi} \sin(\theta) - (r + u_r) \sin(\theta)^2 - u_\theta \sin(\theta) \cos(\theta) \right) \tag{6.8a}$$

$$\sigma_{r\phi,r} + \frac{1}{r}\sigma_{\theta\phi,\theta} + \frac{1}{r\sin(\theta)}\sigma_{\phi\phi,\phi} + \frac{1}{r}\left(2\sigma_{\theta\phi}\cot(\theta) + 3\sigma_{r\phi}\right) = \ldots$$
$$\rho\Omega^2 \left(u_{\phi,\phi\phi} - u_\phi + 2u_{r,\phi} \sin(\theta) + 2u_{\theta,\phi} \cos(\theta) \right) \tag{6.8b}$$

$$\sigma_{r\theta,r} + \frac{1}{r}\sigma_{\theta\theta,\theta} + \frac{1}{r\sin(\theta)}\sigma_{\theta\phi,\phi} + \frac{1}{r}\left(\left(\sigma_{\theta\theta} - \sigma_{\phi\phi}\right)\cot(\theta) + 3\sigma_{r\theta}\right) = \ldots$$
$$\rho\Omega^2 \left(u_{\theta,\phi\phi} - 2u_{\phi,\phi} \cos(\theta) - (r + u_r) \sin(\theta) \cos(\theta) - u_\theta \cos(\theta)^2 \right) \tag{6.8c}$$

It is interesting to note that the term $\rho\Omega^2 r \sin(\theta)^2$ appearing in equation (6.8a), which is maximum in the xy-plane and decreases laterally, corresponds to the Coriolis effect due to the rotation of the sphere about the z-axis. The components of the strain tensor $\boldsymbol{\epsilon}$ are expressed, in spherical coordinates, in terms of the displacements as follows

$$\epsilon_{rr} = u_{r,r}, \tag{6.9a}$$

$$\epsilon_{\phi\phi} = \frac{1}{r\sin(\theta)}\left(u_{\phi,\phi} + u_r\sin(\theta) + u_\theta\cos(\theta)\right), \tag{6.9b}$$

$$\epsilon_{\theta\theta} = \frac{1}{r}\left(u_{\theta,\theta} + u_r\right), \tag{6.9c}$$

$$\epsilon_{r\phi} = \frac{1}{2}\left(\frac{1}{r\sin(\theta)}u_{r,\phi} + u_{\phi,r} - \frac{1}{r}u_\phi\right), \tag{6.9d}$$

$$\epsilon_{r\theta} = \frac{1}{2}\left(\frac{1}{r}u_{r,\theta} + u_{\theta,r} - \frac{1}{r}u_\theta\right), \tag{6.9e}$$

$$\epsilon_{\phi\theta} = \frac{1}{2r}\left(\frac{1}{\sin(\theta)}u_{\theta,\phi} + u_{\phi,\theta} - u_\phi\cot(\theta)\right). \tag{6.9f}$$

Let $\lambda(t)$ and $\mu(t)$ be the time dependent Lamé parameters characterizing the viscoelastic behavior of the layer's material. Assuming that stresses and strains are equal to zero for all negative values of the time variable t, the constitutive equations of linear isotropic viscoelasticity can be written, using indicial tensor notation, as (Flügge, 1975; Lakes, 2009; Tschoegl, 1989)

$$\sigma_{ij}(t) = \int_{-\infty}^{\infty} 2\mu(t-\tau)\frac{\partial\epsilon_{ij}}{\partial\tau}d\tau + \delta_{ij}\int_{-\infty}^{\infty}\lambda(t-\tau)\frac{\partial\epsilon_{kk}}{\partial\tau}d\tau. \tag{6.10}$$

6.5 Boundary conditions

The normal contact boundary conditions express the absence of overclosure between the outer boundaries of the two contacting entities, in a direction perpendicular to the rigid plane. Furthermore, across the actual contact surface, which is characterized by a positive pressure field, the lower portion of the coated sphere follows the shape of the rigid plane on which it rests, i.e.

$$H - \mathbf{x}(r_o,\phi,\theta).\mathbf{e}_y \geq 0, \quad \text{if } \sigma_y(r_o,\phi,\theta) = 0, \tag{6.11a}$$

$$H - \mathbf{x}(r_o,\phi,\theta).\mathbf{e}_y = 0, \quad \text{if } \sigma_y(r_o,\phi,\theta) < 0, \tag{6.11b}$$

where $\mathbf{e}_y$ is the unit vector pointing in the y-direction and σ_y corresponds to the normal traction field across the candidate contact surface.

The relative velocities w_{t_x} and w_{t_z} of the coated sphere with respect to the rigid plane, tangent to the contact interface in directions x and z, respectively, are given by

$$w_{t_x}(r_o,\phi,\theta) = V_s + \mathbf{v}(r_o,\phi,\theta).\mathbf{e}_x, \tag{6.12a}$$

$$w_{t_z}(r_o,\phi,\theta) = \mathbf{v}(r_o,\phi,\theta).\mathbf{e}_z. \tag{6.12b}$$

These differential speeds are equal to zero in regions of stick-contact where no slipping occurs. The tangential contact boundary conditions express Coulomb's law of surface friction (Coulomb, 1821)

$$\tau_{yx}(r_o,\phi,\theta)^2 + \tau_{yz}(r_o,\phi,\theta)^2 < \mu^2\sigma_y(r_o,\phi,\theta)^2, \quad \text{if } w_{t_x}^2 + w_{t_z}^2 = 0, \tag{6.13a}$$

$$\tau_{yx}(r_o,\phi,\theta)^2 + \tau_{yz}(r_o,\phi,\theta)^2 = \mu^2\sigma_y(r_o,\phi,\theta)^2, \quad \text{otherwise}, \tag{6.13b}$$

where τ_{ij} is the shear stress acting in the j-direction on a plane normal to the i-direction, and μ is Coulomb's friction coefficient.

6.6 Two-variable Fourier series

Due to the point symmetry of the coated sphere and to the fact that the rolling takes places in steady-state, and in a constant direction, any generic field $\hat{f}(r,\phi,\theta)$ in the continuum of the coating can be extended into a periodic function $f(r,\phi,\theta)$ of period 2π in both spatial variables ϕ, and θ (see appendix A.3). A two variable Fourier series expansion of f writes

$$f(r,\phi,\theta) = \sum_{m,n=-\infty}^{\infty} f_{mn}(r)\, e^{im\phi} e^{in\theta}, \tag{6.14}$$

where the Fourier coefficients $f_{mn}(r)$ are given by

$$f_{mn}(r) = \frac{1}{(2\pi)^2}\int_{-\pi}^{\pi}\int_{-\pi}^{\pi} f(r,\phi,\theta)\, e^{-im\phi} e^{-in\theta} d\theta d\phi. \tag{6.15}$$

Equations (6.14) and (6.15) are applied to the stresses, displacements and strains in the viscoelastic coating.

6.7 Geometric approximation

We wish to follow a typical procedure (Qiu, 2006, 2009; Zéhil and Gavin, 2013e, 2014c, e.g.) (see Chapters 4 and 6) in transforming the sets of governing equations (6.8), (6.9) and (6.10) to the domain of Fourier coefficients by: (i) plugging expression (6.14) for the stresses, displacements and strains in the equations being transformed, (ii) multiplying by $\exp(-i(p\phi+q\theta))$ where p and q are integers, and (iii) integrating over one period (i.e. 2π) in the spatial variables ϕ and θ, to take advantage of the orthogonality property of complex exponentials. However, the dependence of certain coefficients in (6.8) and (6.9) on the spatial variable θ complicates this task significantly. The simplest terms, such as $\sin(\theta)$ and $\cos(\theta)$ introduce a coupling between Fourier series coefficients of neighboring order in m and n. To show this fact, we consider, for simplicity, the following equation involving two fields $f(r,\phi,\theta)$ and $g(r,\phi,\theta)$

$$f(r,\phi,\theta) - \sin(\theta)\, g(r,\phi,\theta) = 0. \tag{6.16}$$

Applying the aforementioned transformation procedure to equation (6.16) yields

$$f_{pq}(r) - \sum_{n=-\infty}^{\infty} g_{pn}(r)\, \frac{1}{2\pi} \int_{-\pi}^{\pi} \sin(\theta)\, e^{in\theta} e^{-iq\theta} d\theta = \dots$$

$$f_{pq}(r) + \frac{i}{2}\left(g_{p(q-1)}(r) - g_{p(q+1)}(r)\right) = 0. \tag{6.17}$$

Hence, equation (6.16) in the spatial domain transforms into an equation (i.e. (6.17)) relating the Fourier coefficient f_{mn} of field $f(r,\phi,\theta)$ to the Fourier coefficients $g_{m(n-1)}$ and $g_{m(n+1)}$ of field $g(r,\phi,\theta)$, which are of different order. Other terms such as $1/\sin(\theta)$ and $\cot(\theta)$ lead to non-converging integrals. We consider, for instance, the following integral in $\cot(\theta)$, which arises when the transformation procedure is applied to equations (6.8b), (6.8c) or (6.9f)

$$\frac{1}{2\pi} \int_{-\pi}^{\pi} \cot(\theta)\, e^{i(n-q)\theta} d\theta. \tag{6.18}$$

Expression (6.18) does not correspond to a finite quantity. Nevertheless, provided that the fields generated by the Coriolis effect are small in comparison witch those due to contact (see equation (6.8a)), the function $\cot(\theta)$ may be restricted as follows

$$\overline{\cot}(\theta) = \begin{cases} \cot(\theta), & \text{if } \theta \in \left[\frac{\pi}{2} - \beta, \frac{\pi}{2} + \beta\right], \\ 0, & \text{otherwise,} \end{cases} \tag{6.19}$$

where the dihedral angle 2β is taken sufficiently large so that all fields are negligible outside of the interval $[\pi/2 - \beta, \pi/2 + \beta]$. With these assumptions, expression (6.18) becomes

$$\frac{1}{2\pi}\int_{-\pi}^{\pi} \overline{\cot}(\theta)\, e^{i(n-q)\theta} d\theta = \frac{1}{2\pi}\int_{\pi/2-\beta}^{\pi/2+\beta} \cot(\theta)\, e^{i(n-q)\theta} d\theta, \tag{6.20}$$

which is convergent. Unfortunately, it turns out that the Fourier series expansion of expression (6.19) has an infinite number of terms. Thus, despite the restriction proposed in (6.19), terms such as $\cot(\theta)$ generate a coupling between Fourier series coefficients of different order in m and n, involving an infinite number of terms.

To move forward with the proposed approach, it is convenient to assume, as is often the case in practice (see Section 1.2.3), that the characteristic dimension of the contact surface is small compared to that of the rolling sphere, i.e. $r_c/R \ll 1$, or equivalently $d/R \ll 1$. Under this condition, the angular coordinate θ can be approximated by $\pi/2$ across the contact surface, which simplifies the sets of equations (6.8) and (6.9) significantly, so as to eliminate the coupling between Fourier coefficients of different orders. The equilibrium equations in (6.8) reduce to

$$\sigma_{rr,r} + \frac{1}{r}\sigma_{r\theta,\theta} + \frac{1}{r}\sigma_{r\phi,\phi} + \frac{1}{r}\left(2\sigma_{rr} - \sigma_{\theta\theta} - \sigma_{\phi\phi}\right) = \rho\Omega^2\left(u_{r,\phi\phi} - 2u_{\phi,\phi} - (r + u_r)\right), \tag{6.21a}$$

$$\sigma_{r\phi,r} + \frac{1}{r}\sigma_{\theta\phi,\theta} + \frac{1}{r}\sigma_{\phi\phi,\phi} + \frac{3}{r}\sigma_{r\phi} = \rho\Omega^2\left(u_{\phi,\phi\phi} - u_\phi + 2u_{r,\phi}\right), \tag{6.21b}$$

$$\sigma_{r\theta,r} + \frac{1}{r}\sigma_{\theta\theta,\theta} + \frac{1}{r}\sigma_{\theta\phi,\phi} + \frac{3}{r}\sigma_{r\theta} = \rho\Omega^2 u_{\theta,\phi\phi}, \tag{6.21c}$$

and the strain equations in (6.9) simplify to

$$\epsilon_{rr} = u_{r,r}, \tag{6.22a}$$

$$\epsilon_{\phi\phi} = \frac{1}{r}\left(u_{\phi,\phi} + u_r\right), \tag{6.22b}$$

$$\epsilon_{\theta\theta} = \frac{1}{r}\left(u_{\theta,\theta} + u_r\right), \tag{6.22c}$$

$$\epsilon_{r\phi} = \frac{1}{2}\left(\frac{1}{r}u_{r,\phi} + u_{\phi,r} - \frac{1}{r}u_\phi\right), \tag{6.22d}$$

$$\epsilon_{r\theta} = \frac{1}{2}\left(\frac{1}{r}u_{r,\theta} + u_{\theta,r} - \frac{1}{r}u_\theta\right), \tag{6.22e}$$

$$\epsilon_{\phi\theta} = \frac{1}{2r}\left(u_{\theta,\phi} + u_{\phi,\theta}\right). \tag{6.22f}$$

6.8 General solution to Fourier coefficients

Both sets of equations (6.21) and (6.22) can be expressed in terms of Fourier coefficients by substituting relevant fields by their Fourier series expansions (i.e equation (6.14)) and using the orthogonality property of complex exponentials. In the domain of Fourier coefficients, the equilibrium equations write

$$\dot{\sigma}_{rr_{mn}} + \frac{2}{r}\sigma_{rr_{mn}} - \frac{1}{r}\sigma_{\phi\phi_{mn}} - \frac{1}{r}\sigma_{\theta\theta_{mn}} + \frac{im}{r}\sigma_{r\phi_{mn}} + \frac{in}{r}\sigma_{r\theta_{mn}} + \ldots$$
$$\rho\Omega^2\left(\left(1+m^2\right)u_{r_{mn}} + 2imu_{\phi_{mn}} + r\right) = 0, \tag{6.23a}$$

$$\dot{\sigma}_{r\phi_{mn}} + \frac{im}{r}\sigma_{\phi\phi_{mn}} + \frac{in}{r}\sigma_{\theta\phi_{mn}} + \frac{3}{r}\sigma_{r\phi_{mn}} + \ldots$$
$$\rho\Omega^2\left(\left(1+m^2\right)u_{\phi_{mn}} - 2imu_{r_{mn}}\right) = 0, \tag{6.23b}$$

$$\dot{\sigma}_{r\theta_{mn}} + \frac{in}{r}\sigma_{\theta\theta_{mn}} + \frac{im}{r}\sigma_{\theta\phi_{mn}} + \frac{3}{r}\sigma_{r\theta_{mn}} + \rho\Omega^2 m^2 u_{\theta_{mn}} = 0, \tag{6.23c}$$

where the upper dot ($\dot{}$) denotes differentiation with respect to the spatial variable r. The strain equations in (6.22) are transformed into the Fourier domain, similarly, which yields

$$\epsilon_{rr_{mn}} = \dot{u}_{r_{mn}}, \tag{6.24a}$$

$$\epsilon_{\phi\phi_{mn}} = \frac{1}{r}\left(imu_{\phi_{mn}} + u_{r_{mn}}\right), \tag{6.24b}$$

$$\epsilon_{\theta\theta_{mn}} = \frac{1}{r}\left(inu_{\theta_{mn}} + u_{r_{mn}}\right), \tag{6.24c}$$

$$\epsilon_{r\phi_{mn}} = \frac{1}{2}\left(\frac{1}{r}imu_{r_{mn}} + \dot{u}_{\phi_{mn}} - \frac{1}{r}u_{\phi_{mn}}\right), \tag{6.24d}$$

$$\epsilon_{r\theta_{mn}} = \frac{1}{2}\left(\frac{1}{r}inu_{r_{mn}} + \dot{u}_{\theta_{mn}} - \frac{1}{r}u_{\theta_{mn}}\right), \tag{6.24e}$$

$$\epsilon_{\phi\theta_{mn}} = \frac{1}{2r}\left(imu_{\theta_{mn}} + inu_{\phi_{mn}}\right). \tag{6.24f}$$

The constitutive equations are handled as follows: Fourier series expansions (6.14) of stresses and strains are plugged into equation (6.10) and all terms in the latter are shifted to the left-hand-side

$$\sum_{m,n=-\infty}^{\infty} \sigma_{ij_{mn}}(r)\, e^{im\phi}e^{in\theta} - \int_{-\infty}^{\infty} 2\mu(t-\tau)\frac{\partial}{\partial\tau}\left(\sum_{m,n=-\infty}^{\infty} \epsilon_{ij_{mn}}(r)\, e^{im\phi}e^{in\theta}\right)d\tau \ldots$$

$$- \delta_{ij}\int_{-\infty}^{\infty} \lambda(t-\tau)\frac{\partial}{\partial\tau}\left(\sum_{m,n=-\infty}^{\infty} \epsilon_{kk_{mn}}(r)\, e^{im\phi}e^{in\theta}\right)d\tau = 0. \tag{6.25}$$

Equation (6.2) is then used to reveal the time variable explicitly

$$\sum_{m,n=-\infty}^{\infty} \sigma_{ij_{mn}}(r)\, e^{im\phi'}e^{in\theta'}e^{im\Omega t} \ldots$$

$$- \int_{-\infty}^{\infty} 2\mu(t-\tau)\frac{\partial}{\partial\tau}\left(\sum_{m,n=-\infty}^{\infty} \epsilon_{ij_{mn}}(r)\, e^{im\phi'}e^{in\theta'}e^{im\Omega\tau}\right)d\tau \ldots$$

$$- \delta_{ij}\int_{-\infty}^{\infty} \lambda(t-\tau)\frac{\partial}{\partial\tau}\left(\sum_{m,n=-\infty}^{\infty} \epsilon_{kk_{mn}}(r)\, e^{im\phi'}e^{in\theta'}e^{im\Omega\tau}\right)d\tau = 0. \tag{6.26}$$

Partial differentiation with respect to time is performed and terms are rearranged under the same summation sign so that complex exponentials in ϕ' and θ' are factored

out

$$\sum_{m,n=-\infty}^{\infty}\Bigg[\sigma_{ij_{mn}}(r)\,e^{im\Omega t}-im\Omega\int_{-\infty}^{\infty}2\mu\,(t-\tau)\,e^{im\Omega\tau}d\tau\epsilon_{ij_{mn}}(r)\ldots$$

$$-\delta_{ij}im\Omega\int_{-\infty}^{\infty}\lambda\,(t-\tau)\,e^{im\Omega\tau}d\tau\epsilon_{kk_{mn}}(r)\Bigg]e^{im\phi'}e^{in\theta'}=0, \tag{6.27}$$

after which the orthogonality of complex exponentials is invoked to eliminate the summation sign

$$\sigma_{ij_{mn}}(r)\,e^{im\Omega t}-im\Omega\int_{-\infty}^{\infty}2\mu\,(t-\tau)\,e^{im\Omega\tau}d\tau\epsilon_{ij_{mn}}(r)\ldots$$

$$-\delta_{ij}im\Omega\int_{-\infty}^{\infty}\lambda\,(t-\tau)\,e^{im\Omega\tau}d\tau\epsilon_{kk_{mn}}(r)=0. \tag{6.28}$$

The change of variable $\xi=t-\tau$ is then introduced, and the complex exponential in the variable t is factored out

$$\Bigg[\sigma_{ij_{mn}}(r)-im\Omega\int_{-\infty}^{\infty}2\mu\,(\xi)\,e^{-im\Omega\xi}d\xi\epsilon_{ij_{mn}}(r)\ldots$$

$$-\delta_{ij}im\Omega\int_{-\infty}^{\infty}\lambda\,(\xi)\,e^{-im\Omega\xi}d\xi\epsilon_{kk_{mn}}(r)\Bigg]e^{im\Omega t}=0. \tag{6.29}$$

The above being true for all times t, it may be concluded that

$$\sigma_{ij_{mn}}(r)=2\mu^*_m\epsilon_{ij_{mn}}(r)+\lambda^*_m\epsilon_{kk_{mn}}(r)\,\delta_{ij}, \tag{6.30}$$

where $\omega_m=m\Omega$, $\mu^*_m=\mu^*(\omega_m)=i\omega_m\hat{\mu}(\omega_m)$, $\lambda^*_m=\lambda^*(\omega_m)=i\omega_m\hat{\lambda}(\omega_m)$, $\hat{\mu}(\omega_m)$ and $\hat{\lambda}(\omega_m)$ being the Fourier transforms of $\mu(t)$ and $\lambda(t)$, respectively.

After all governing equations have been transformed into the domain of Fourier coefficients, a set of six state variables is retained. These variables are arrange is a state vector $\mathbf{q}_{mn}$ as indicated below

$$\mathbf{q}_{mn}(r)=\langle\mathbf{d}_{mn}(r),\mathbf{f}_{mn}(r)\rangle^T, \tag{6.31}$$

where

$$\mathbf{d}_{mn}(r) = \langle u_{r_{mn}}(r), u_{\phi_{mn}}(r), u_{\theta_{mn}}(r) \rangle^T, \tag{6.32a}$$

$$\mathbf{f}_{mn}(r) = \langle \sigma_{rr_{mn}}(r), \sigma_{r\phi_{mn}}(r), \sigma_{r\theta_{mn}}(r) \rangle^T. \tag{6.32b}$$

Combining equations (6.23), (6.24) and (6.30), and eliminating non-state quantities yields the following system of ordinary differential equations in the state variables

$$\dot{u}_{r_{mn}} = -\mathcal{S}^*_{2_{mn}}(r)\left(2u_{r_{mn}} + imu_{\phi_{mn}} + inu_{\theta_{mn}}\right) + \mathcal{S}^*_{1_{mn}}\sigma_{rr_{mn}}, \tag{6.33a}$$

$$\dot{u}_{\phi_{mn}} = -\frac{im}{r}u_{r_{mn}} + \frac{1}{r}u_{\phi_{mn}} + \frac{1}{\mu^*_m}\sigma_{r\phi_{mn}}, \tag{6.33b}$$

$$\dot{u}_{\theta_{mn}} = -\frac{in}{r}u_{r_{mn}} + \frac{1}{r}u_{\theta_{mn}} + \frac{1}{\mu^*_m}\sigma_{r\theta_{mn}}, \tag{6.33c}$$

$$\begin{aligned}\dot{\sigma}_{rr_{mn}} =& \mathcal{S}_{6_{mn}}(r)u_{r_{mn}} + \mathcal{S}^*_{7_{mn}}(r)u_{\phi_{mn}} + 2in\mathcal{S}^*_{4_{mn}}(r)u_{\theta_{mn}} \ldots \\ & - 4\mathcal{S}^*_{3_{mn}}(r)\sigma_{rr_{mn}} - \frac{im}{r}\sigma_{r\phi_{mn}} - \frac{in}{r}\sigma_{r\theta_{mn}} - \rho\Omega^2 r\delta_{m0}\delta_{n0},\end{aligned} \tag{6.33d}$$

$$\begin{aligned}\dot{\sigma}_{r\phi_{mn}} =& -\mathcal{S}^*_{7_{mn}}(r)u_{r_{mn}} + \mathcal{S}^*_{8_{mn}}(r)u_{\phi_{mn}} + mn\mathcal{S}^*_{4_{mn}}(r)u_{\theta_{mn}} \ldots \\ & - im\mathcal{S}^*_{2_{mn}}(r)\sigma_{rr_{mn}} - \frac{3}{r}\sigma_{r\phi_{mn}},\end{aligned} \tag{6.33e}$$

$$\begin{aligned}\dot{\sigma}_{r\theta_{mn}} =& -2in\mathcal{S}^*_{4_{mn}}(r)u_{r_{mn}} + mn\mathcal{S}^*_{4_{mn}}(r)u_{\phi_{mn}} + \mathcal{S}^*_{9_{mn}}(r)u_{\theta_{mn}} \ldots \\ & - in\mathcal{S}^*_{2_{mn}}(r)\sigma_{rr_{mn}} - \frac{3}{r}\sigma_{r\theta_{mn}},\end{aligned} \tag{6.33f}$$

where $S^*_{1_{mn}}$, $S^*_{2_{mn}}$, …, $S^*_{9_{mn}}$ are shorthand parameters defined below

$$\mathcal{S}^*_{1_{mn}} = 1/\left(\lambda^*_m + 2\mu^*_m\right), \tag{6.34a}$$

$$\mathcal{S}^*_{2_{mn}}(r) = \lambda^*_m\mathcal{S}^*_{1_m}/r, \tag{6.34b}$$

$$\mathcal{S}^*_{3_{mn}}(r) = \mu^*_m\mathcal{S}^*_{1_m}/r, \tag{6.34c}$$

$$\mathcal{S}^*_{4_{mn}}(r) = \left(3\lambda^*_m + 2\mu^*_m\right)\mathcal{S}^*_{3_m}(r)/r, \tag{6.34d}$$

$$\mathcal{S}^*_{5_{mn}}(r) = \left(\lambda^*_m + \mu^*_m\right)\mathcal{S}^*_{3_m}(r)/r, \tag{6.34e}$$

$$\mathcal{S}^*_{6_{mn}}(r) = 4\mathcal{S}^*_{4_m}(r) - \rho\Omega^2\left(1 + m^2\right), \tag{6.34f}$$

$$\mathcal{S}^*_{7_{mn}}(r) = 2im\left(\mathcal{S}^*_{4_m}(r) - \rho\Omega^2\right), \tag{6.34g}$$

$$\mathcal{S}^*_{8_{mn}}(r) = 4m^2\mathcal{S}^*_{5_m}(r) + n^2\mu^*_m/r^2 - \rho\Omega^2\left(1+m^2\right), \tag{6.34h}$$

$$\mathcal{S}^*_{9_{mn}}(r) = 4n^2\mathcal{S}^*_{5_m}(r) + m^2\mu^*_m/r^2 - \rho\Omega^2 m^2. \tag{6.34i}$$

By analogy to forced time-varying systems in linear system theory (e.g. Lygeros and Ramponi, 2010), equations (6.33) can be written in the form

$$\dot{\mathbf{q}}_{mn}(r) = \mathbf{A}_{mn}(r)\,\mathbf{q}_{mn}(r) + \mathbf{b}_{mn}(r) \tag{6.35}$$

where the 6×6 complex-valued matrix $\mathbf{A}_{mn}(r)$ is given by

$$\mathbf{A}_{mn}(r) = \begin{bmatrix} -2\mathcal{S}^*_{2_{mn}}(r) & -im\mathcal{S}^*_{2_{mn}}(r) & -in\mathcal{S}^*_{2_{mn}}(r) & \mathcal{S}^*_{1_{mn}} & 0 & 0 \\ -im/r & 1/r & 0 & 0 & 1/\mu^*_m & 0 \\ -in/r & 0 & 1/r & 0 & 0 & 1/\mu^*_m \\ \mathcal{S}^*_{6_{mn}}(r) & \mathcal{S}^*_{7_{mn}}(r) & 2in\mathcal{S}^*_{4_{mn}}(r) & -4\mathcal{S}^*_{3_{mn}}(r) & -im/r & -in/r \\ -\mathcal{S}^*_{7_{mn}}(r) & \mathcal{S}^*_{8_{mn}}(r) & mn\mathcal{S}^*_{4_{mn}}(r) & -im\mathcal{S}^*_{2_{mn}}(r) & -3/r & 0 \\ -2in\mathcal{S}^*_{4_{mn}}(r) & mn\mathcal{S}^*_{4_{mn}}(r) & \mathcal{S}^*_{9_{mn}}(r) & -in\mathcal{S}^*_{2_{mn}}(r) & 0 & -3/r \end{bmatrix}, \tag{6.36}$$

and the 'forcing' term $\mathbf{b}_{mn}(r)$, resulting from the Coriolis effect, writes

$$\mathbf{b}_{mn}(r) = \left\langle 0,0,0,-\rho\Omega^2 r\delta_{m0}\delta_{n0},0,0\right\rangle^T. \tag{6.37}$$

The solution to system (6.35) is of the form

$$\mathbf{q}_{mn}(r) = \mathbf{T}_{mn}(r,r_i)\,\mathbf{q}_{mn}(r_i) + \mathbf{J}_{mn}(r,r_i), \tag{6.38}$$

where $\mathbf{J}_{mn}(r,r_i)$ is given by

$$\mathbf{J}_{mn}(r,r_i) = \int_{r_i}^{r} \mathbf{T}_{mn}(r,s)\,\mathbf{b}_{mn}(s)\,ds, \tag{6.39}$$

and $\mathbf{T}_{mn}(r,r_i)$ corresponds to the state-transition matrix. Equation 6.38 can be written in the form

$$\begin{bmatrix} \mathbf{d}_{mn}(r) \\ \mathbf{f}_{mn}(r) \end{bmatrix} = \begin{bmatrix} \mathbf{T}_{mn,11}(r,r_i) & \mathbf{T}_{mn,12}(r,r_i) \\ \mathbf{T}_{mn,21}(r,r_i) & \mathbf{T}_{mn,22}(r,r_i) \end{bmatrix} \times \begin{bmatrix} \mathbf{d}_{mn}(r_i) \\ \mathbf{f}_{mn}(r_i) \end{bmatrix} + \begin{bmatrix} \mathbf{J}_{mn}(r,r_i)(1:3) \\ \mathbf{J}_{mn}(r,r_i)(4:6) \end{bmatrix}, \tag{6.40}$$

where $\mathbf{J}_{mn}(r, r_i)(p:q)$ denotes the subvector of $\mathbf{J}_{mn}(r, r_i)$ comprising its components p through q. Incorporating the boundary conditions at $r = r_i$, i.e. $\mathbf{d}_{mn}(r_i) = \mathbf{0}$, Fourier coefficients of displacements and stresses at r are related explicitly

$$\mathbf{d}_{mn}(r) = \mathbf{T}_{mn,12}(r, r_i)\mathbf{T}^{-1}_{mn,22}(r, r_i)\left(\mathbf{f}_{mn}(r) - \mathbf{J}_{mn}(r, r_i)(4:6)\right) + \mathbf{J}_{mn}(r, r_i)(1:3). \quad (6.41)$$

The evaluation of $\mathbf{T}_{mn}(r, r_i)$ can be carried out numerically, to the desired degree of accuracy, using the block-pulse technique proposed by Rammohan Rao and Ganapathy (1979). As a more efficient and straightforward alternative, the integration domain $[r_i, r]$ is divided into n_r sub-intervals of equal size $\Delta r = (r_o - r)/n_r$, and the state-transition matrix $\mathbf{T}_{mn}(r, r_i)$ is written as

$$\mathbf{T}_{mn}(r, r_i) = \prod_{k=1}^{n_r} \mathbf{e}^{\Delta r \mathbf{A}_k}, \quad (6.42)$$

where $\mathbf{A}_k = \mathbf{A}_{mn}(r_i + (k - \alpha)\Delta r)$, with α chosen in $[0, 1]$. Evaluating expression (6.39) requires numerical integration, which is computationally expensive. Fortunately, in the present case, a single evaluation is necessary since $\mathbf{b}_{mn} \neq \mathbf{0}$, and hence $\mathbf{J}_{mn}(r, r_i) \neq \mathbf{0}$, for $m = n = 0$, only.

6.9 Case of multiple layers

Solution (6.38) is readily adapted to the case of a hard sphere coated with multiple (k) layers of different thickness and material characteristics. Contacting layers are bonded to one another, the first being attached to the hard core. This case is illustrated in Figure 6.2. Using an upper index to denote layer numbering, the continuity of displacements and stresses across the interface between layers $j-1$ and j writes

$$\mathbf{q}^{(j-1)}_{mn}(r_{(j-1)j}) = \mathbf{q}^{(j)}_{mn}(r_{(j-1)j}). \quad (6.43)$$

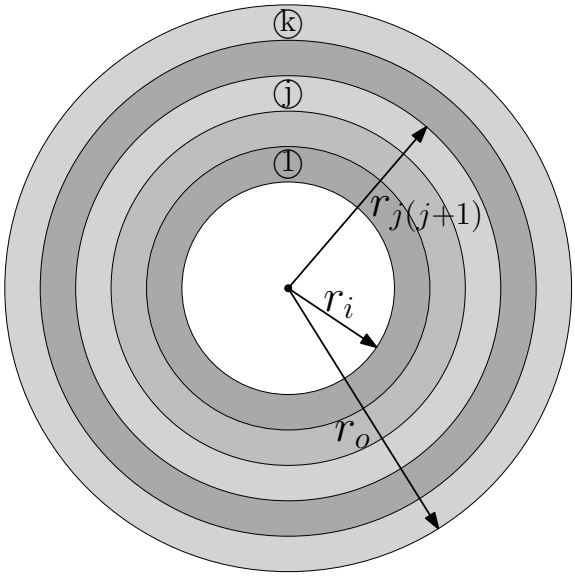

FIGURE 6.2: Rigid sphere coated with multiple viscoelastic layers.

By combining equations (6.38) and (6.43) for layers 1 through k, it can be shown that $\mathbf{q}^k_{mn}(r_o)$ is given by

$$\mathbf{q}^k_{mn}(r_o) = \left(\prod_{j=1}^{k} \mathbf{T}^{(j)}_{mn}\right) \mathbf{q}^1_{mn}(r_i) + \sum_{j=1}^{k-1} \left(\prod_{i=j+1}^{k} \mathbf{T}^{(i)}_{mn}\right) \mathbf{J}^j_{mn}\left(r_{j(j+1)}\right) + \mathbf{J}^k_{mn}(r_o) \quad (6.44)$$

where $\mathbf{T}^{(j)}_{mn} = \mathbf{T}^{(j)}_{mn}\left(r_{j(j+1)}, r_{(j-1)j}\right)$.

6.10 Boundary element formulation

The candidate contact surface on the outer boundary of the viscoelastic coating is discretized into $N_T = K_\phi K_\theta$ nodes, as illustrated in Figures 6.3(a) and 6.3(b), with angular spacings between nodes $\Delta\phi$ and $\Delta\theta$. A global number $A = i + (j-1)K_\phi$ is assigned to each node.

The nodal displacement vector $\mathbf{D}_s = \left\langle \mathbf{D}^T_R, \mathbf{D}^T_\Phi, \mathbf{D}^T_\Theta \right\rangle^T$ is related to the nodal force vector $\mathbf{F}_s = \left\langle \mathbf{F_R}^T, \mathbf{F_\Phi}^T, \mathbf{F_\Theta}^T \right\rangle^T$ through a boundary-element compliance matrix $\mathbf{C}_s$

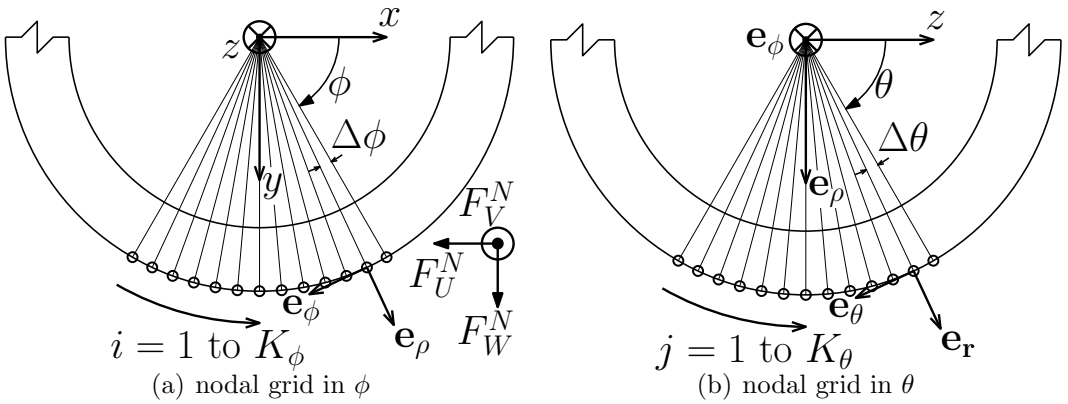

(a) nodal grid in ϕ (b) nodal grid in θ

FIGURE 6.3: Discretization of the candidate contact surface.

according to

$$\begin{bmatrix} \mathbf{C}_{RR} & \mathbf{C}_{R\Phi} & \mathbf{C}_{R\Theta} \\ \mathbf{C}_{\Phi R} & \mathbf{C}_{\Phi\Phi} & \mathbf{C}_{\Phi\Theta} \\ \mathbf{C}_{\Theta R} & \mathbf{C}_{\Theta\Phi} & \mathbf{C}_{\Theta\Theta} \end{bmatrix} \begin{bmatrix} \mathbf{F}_R \\ \mathbf{F}_\Phi \\ \mathbf{F}_\Theta \end{bmatrix} + d_R^{(c)} \begin{bmatrix} \mathbf{1} \\ \mathbf{0} \\ \mathbf{0} \end{bmatrix} = \begin{bmatrix} \mathbf{D}_R \\ \mathbf{D}_\Phi \\ \mathbf{D}_\Theta \end{bmatrix}, \tag{6.45}$$

where the subscript "s" refers to the system of spherical coordinates attached to point C, indices R, Φ and Θ refer to the spatial coordinates of the same name, and $d_R^{(c)}$ is the (uniform) radial displacement due to the Coriolis effect, i.e. retaining the first row of (6.41), with $m = n = 0$

$$d_R^{(c)} = \mathbf{J}_{00}\,(r, r_i)\,(1) - \mathbf{T}_{00,12}(r, r_i)(1, :)\mathbf{T}_{00,22}^{-1}(r, r_i)\mathbf{J}_{00}\,(r, r_i)\,(4:6). \tag{6.46}$$

6.11 Building the compliance matrix

Each entry $C_{PQ}(M, N)$ of matrix $\mathbf{C}_s$ corresponds to the displacement of node M in direction $P \in \{R, \Phi, \Theta\}$ under the influence of a unit point load F_Q^N applied at node N, in direction $Q \in \{R, \Phi, \Theta\}$. Based on this interpretation, matrix $\mathbf{C}_s$ is formed in three conceptual steps:

1. a 2π-periodic rectangular distribution of surface stresses $\sigma_Q^N(r_o, \phi, \theta)$ is associ-

ated with F_Q^N

$$\sigma_Q^N(r_o,\phi,\theta) = \begin{cases} \frac{F_Q^N}{r_o^2\sin(\theta)\Delta\phi\Delta\theta}, & \text{if } \begin{cases} \phi^N - \frac{\Delta\phi}{2} \le \phi \le \phi^N + \frac{\Delta\phi}{2} \\ \theta^N - \frac{\Delta\theta}{2} \le \theta \le \theta^N + \frac{\Delta\theta}{2} \end{cases} \\ 0, & \text{otherwise.} \end{cases}, \quad (6.47)$$

2. the Fourier series coefficients of the surface stress field given by (6.47) are computed from their analytical expression below

$$\sigma_{Q_{mn}}^N(r) = \frac{F_Q^N}{(2\pi r_o)^2}\,\mathrm{sinc}\left(m\frac{\Delta\phi}{2}\right)e^{-im\phi^N}\frac{1}{\Delta\theta}\int_{\theta^N-\frac{\Delta\theta}{2}}^{\theta^N+\frac{\Delta\theta}{2}}\frac{1}{\sin(\theta)}e^{-in\theta^N}d\theta, \quad (6.48)$$

3. the Fourier series coefficients of the displacements at point M are deduced from (6.48) using equation (6.41).

6.12 Solving the rolling contact problem

Because the contact interface is flat and lies in the rigid plane supporting the rolling sphere, the solution to the rolling contact problem is better addressed in a rectangular system of coordinates. To this end, alternative nodal force and displacement vectors are defined by

$$\mathbf{F}_s^N = \mathbf{Q}^N\mathbf{F}_r^N \quad \text{and} \quad \mathbf{D}_s^N = \mathbf{Q}^N\mathbf{D}_r^N, \quad (6.49)$$

where

$$\mathbf{F}_s^N = \left\langle F_R^N, F_\Phi^N, F_\Theta^N \right\rangle^T,$$

$$\mathbf{D}_s^N = \left\langle D_R^N, D_\Phi^N, D_\Theta^N \right\rangle^T,$$

$$\mathbf{F}_r^N = \left\langle F_W^N, F_U^N, F_V^N \right\rangle^T,$$

$$\mathbf{D}_r^N = \left\langle D_W^N, D_U^N, D_V^N \right\rangle^T,$$

the subscripts "r" and "s" refer to rectangular and spherical coordinates, respectively, the superscript "N" corresponds to the node number, and the nodal transformation

matrix $\mathbf{Q}^N$ is given by

$$\mathbf{Q}^N = \begin{bmatrix} \sin(\theta^N)sin(\phi^N) & -\sin(\theta^N)cos(\phi^N) & -cos(\theta^N) \\ \cos(\phi^N) & sin(\phi^N) & 0 \\ \cos(\theta^N)sin(\phi^N) & -\cos(\theta^N)cos(\phi^N) & \sin(\theta^N) \end{bmatrix}. \tag{6.50}$$

The nodal force components F_W^N, F_U^N and F_V^N in the rectangular system of coordinates are counted positively when acting on the external boundary of the sphere's coating as shown in Figure 6.3(a). The nodal expressions in (6.49) can be assembled into global transformation equations, i.e.

$$\mathbf{F}_s = \mathbf{Q}\mathbf{F}_r \quad \text{and} \quad \mathbf{D}_s = \mathbf{Q}\mathbf{D}_r, \tag{6.51}$$

where $\mathbf{Q}$ is a $3N_T \times 3N_T$ unitary global transformation matrix. Matrix $\mathbf{Q}$ comprises nine $N_T \times N_T$ purely diagonal blocs, i.e.

$$\mathbf{Q} = \begin{bmatrix} \mathbf{Q}_{RW} & \mathbf{Q}_{RU} & \mathbf{Q}_{RV} \\ \mathbf{Q}_{\Phi W} & \mathbf{Q}_{\Phi U} & \mathbf{0} \\ \mathbf{Q}_{\Theta W} & \mathbf{Q}_{\Theta U} & \mathbf{Q}_{\Theta V} \end{bmatrix}. \tag{6.52}$$

The diagonals of the blocs shown in (6.52) are given by

$$\text{diag}\left(\mathbf{Q}_{RW}\right) = \left\langle +\sin(\theta^1)\sin(\phi^1),\ \ldots\ , +\sin(\theta^{N_T})\sin(\phi^{N_T})\right\rangle, \tag{6.53a}$$

$$\text{diag}\left(\mathbf{Q}_{RU}\right) = \left\langle -\sin(\theta^1)\cos(\phi^1),\ \ldots\ , -\sin(\theta^{N_T})\cos(\phi^{N_T})\right\rangle, \tag{6.53b}$$

$$\text{diag}\left(\mathbf{Q}_{RV}\right) = \left\langle -\cos(\theta^1),\ \ldots\ , -\cos(\theta^{N_T})\right\rangle, \tag{6.53c}$$

$$\text{diag}\left(\mathbf{Q}_{\Phi W}\right) = \left\langle +\cos(\phi^1),\ \ldots\ , +\cos(\phi^{N_T})\right\rangle, \tag{6.53d}$$

$$\text{diag}\left(\mathbf{Q}_{\Phi U}\right) = \left\langle +\sin(\phi^1),\ \ldots\ , +\sin(\phi^{N_T})\right\rangle, \tag{6.53e}$$

$$\text{diag}\left(\mathbf{Q}_{\Theta W}\right) = \left\langle +\cos(\theta^1)\sin(\phi^1),\ \ldots\ , +\cos(\theta^{N_T})\sin(\phi^{N_T})\right\rangle, \tag{6.53f}$$

$$\text{diag}\left(\mathbf{Q}_{\Theta U}\right) = \left\langle -\cos(\theta^1)\cos(\phi^1),\ \ldots\ , -\cos(\theta^{N_T})\cos(\phi^{N_T})\right\rangle, \tag{6.53g}$$

$$\text{diag}\left(\mathbf{Q}_{\Theta V}\right) = \left\langle +\sin(\theta^1),\ \ldots\ , +\sin(\theta^{N_T})\right\rangle. \tag{6.53h}$$

The boundary element formulation of the viscoelastic coating is expressed in rectangular coordinates by combining equations (6.45) and (6.51), which yields

$$\mathbf{C}_r\mathbf{F}_r + \mathbf{D}_r^{(c)} = \mathbf{D}_r, \tag{6.54}$$

where $\mathbf{D}_r^{(c)} = \langle \mathrm{diag}\,(\mathbf{Q}_{RW})\,, \mathrm{diag}\,(\mathbf{Q}_{RU})\,, \mathrm{diag}\,(\mathbf{Q}_{RV})\rangle^T$ is the vector of nodal displacements due to the Coriolis effect, and $\mathbf{C}_r = \mathbf{Q}^T\mathbf{C}_s\mathbf{Q}$ is the compliance matrix, in rectangular coordinates. It is helpful to write equation (6.54) in more explicit form as

$$\begin{bmatrix} \mathbf{C}_{WW} & \mathbf{C}_{WU} & \mathbf{C}_{WV} \\ \mathbf{C}_{UW} & \mathbf{C}_{UU} & \mathbf{C}_{UV} \\ \mathbf{C}_{VW} & \mathbf{C}_{VU} & \mathbf{C}_{VV} \end{bmatrix} \begin{bmatrix} \mathbf{F}_W \\ \mathbf{F}_U \\ \mathbf{F}_V \end{bmatrix} + d_R^{(c)} \begin{bmatrix} \mathrm{diag}\,(\mathbf{Q}_{RW}) \\ \mathrm{diag}\,(\mathbf{Q}_{RU}) \\ \mathrm{diag}\,(\mathbf{Q}_{RV}) \end{bmatrix} = \begin{bmatrix} \mathbf{D}_W \\ \mathbf{D}_U \\ \mathbf{D}_V \end{bmatrix}. \tag{6.55}$$

The rolling contact problem may be solved, for instance, by extending the contact algorithms proposed in Chapter 3 (Zéhil and Gavin, 2013c) to the case of a deformable object rolling on a rigid plane. Equation (6.55) reduces, for the vertical behavior, to

$$\mathbf{C}_{WW}\mathbf{F}_W + \mathbf{C}_{WU}\mathbf{F}_U + \mathbf{C}_{WV}\mathbf{F}_V + d_R^{(c)}\,\mathrm{diag}\,(\mathbf{Q}_{RW}) = \mathbf{D}_W. \tag{6.56}$$

In the following, a scalar function applied to an array (arrays are typed in bold) operates on each of the array's elements. Likewise, the product of two arrays of the same size is meant as an element-by-element multiplication. Also, the addition of a scalar to an array corresponds to adding the scalar to each element of the array. The characters "c" and "$\overline{c}$", used as arguments of a given array, stand for extracting from this array the rows/columns corresponding to contact nodes and free nodes respectively. Alternatively, the argument ":" stands for "all" rows or columns. Finally, the symbol $\mathbf{1}$ designates a column vector whose size follows naturally from the context, and whose components are all equal to unity.

It is here assumed, as will be substantiated below, that the horizontal nodal force fields $\mathbf{F}_U$ and $\mathbf{F}_V$ are given. The vertical nodal forces at the free nodes are also

known, i.e. $\mathbf{F}_W(\bar{c}) = \mathbf{0}$. The restriction of system (6.56) to the contact nodes must therefore be solved for the unknown contact forces $\mathbf{F}_W(c)$, i.e.

$$\mathbf{C}_{WW}(c,c)\mathbf{F}_W(c) + \mathbf{C}_{WU}(c,:)\mathbf{F}_U + \mathbf{C}_{WV}(c,:)\mathbf{F}_V + d_R^{(c)}\,\mathrm{diag}\left(\mathbf{Q}_{RW}\right)(c) = \mathbf{D}_W(c). \tag{6.57}$$

To this end, vertical nodal displacements across the contact surface $\mathbf{D}_W(c)$ may be expressed, according to the normal boundary condition (6.11b), in terms of the additional unknown H (see Figure 6.1) as

$$\mathbf{D}_W(c) \approx H - r_o \sin\left(\boldsymbol{\theta}(c)\right)\sin\left(\boldsymbol{\phi}(c)\right), \tag{6.58}$$

which requires one additional equation provided by the vertical equilibrium of the sphere, i.e.

$$\mathbf{1}^T\mathbf{F}_W(c) + P = 0. \tag{6.59}$$

Equations (6.57) and (6.59) are then combined into an augmented system in the unknowns $\mathbf{F}_W(c)$ and H

$$\begin{bmatrix} \mathbf{C}_{WW}(c,c) & -\mathbf{1} \\ \mathbf{1}^T & 0 \end{bmatrix} \begin{bmatrix} \mathbf{F}_W(c) \\ H \end{bmatrix} = - \begin{bmatrix} \mathbf{q} \\ P \end{bmatrix}, \tag{6.60}$$

where the shorthand vector $\mathbf{q}$ is given by

$$\mathbf{q} = r_o \sin\left(\boldsymbol{\theta}(c)\right)\sin\left(\boldsymbol{\phi}(c)\right) + d_R^{(c)}\,\mathrm{diag}\left(\mathbf{Q}_{RW}\right)(c) + \mathbf{C}_{WU}(c,:)\mathbf{F}_U + \mathbf{C}_{WV}(c,:)\mathbf{F}_V. \tag{6.61}$$

It is convenient to assume, as later justified in Sections 6.14 and 6.15.3, that surface friction is negligible, in which case $\mathbf{F}_U = \mathbf{F}_V = \mathbf{0}$. Under these conditions, a "normal-contact" algorithm is readily set up, as descried in Chapter 3 (Zéhil and Gavin, 2013c), to solve system (6.60) while iterating on the subset of contact nodes to satisfy the normal boundary conditions (6.11), i.e. to achieve negative tractions across the contact area and eliminate the overclosures characterized by the inequality

$$\mathbf{D}_W(c) + r_o \sin\left(\boldsymbol{\theta}(c)\right)\sin\left(\boldsymbol{\phi}(c)\right) - H \geq 0. \tag{6.62}$$

6.13 Aspects of computational efficiency

In this section, we briefly discuss a few aspects of computational efficiency in the implementation of the proposed modeling and solving strategies:

- According to the transformation equation $\mathbf{C}_r = \mathbf{Q}^T \mathbf{C}_s \mathbf{Q}$, forming $\mathbf{C}_{WW}$, which, in the absence of surface friction, is the only part of $\mathbf{C}_r$ needed for the solution of the rolling contact problem (6.60), requires building the full compliance matrix $\mathbf{C}_s$ in spherical coordinates, as well as the full transformation matrix $\mathbf{Q}$. A cheaper alternative, from a computational aspect, would be to take advantage of the fact that, under small strains, the reference configuration and the deformed configuration are very close to each other, which renders the constitutive equations formulated in one configuration applicable in the other, i.e. practically $\mathbf{C}_{WW} \approx \mathbf{C}_{RR}$. Both approaches were implemented and yielded comparable results: for instance, with the parameters retained in Section 6.15, relative differences in the resisting torque of less than 3% were observed, up to 12% strains.

- In building parts of the compliance matrix $\mathbf{C}_s$ of a spherical viscoelastic layer rolling about the horizontal z-axis, advantage can be taken from configurational similarities and symmetry, but to a lesser extent than in the case discussed in Chapters 4, 5 and 7 (Zéhil and Gavin, 2013e,d) of a plane layer punched by a moving indenter. In the present case (see Figure 6.3), due to symmetry in the transverse direction, only nodes located in, and on one side of, the xy-plane need be considered. Furthermore, two pairs of nodes located on the same nodal rows (constant j and θ) and in the same relative position with respect to each other in the ϕ-coordinate will behave in the same way. Consequently, unit point loads need be applied at only the first ($i = 1$) and last ($i = K_\phi$) node of a

nodal row. By implementing these changes, the computational cost of building a full compliance matrix is reduced from the order of N_T^2 to the order of $N_T^{3/2}$.

- To avoid numerical integration in computing the Fourier series coefficients of the surface stress field from their general expression in (6.48), the term $\sin(\theta)$ in the integrand may be approximated by 1 across the candidate contact surface, in which case equation (6.48) simplifies to

$$\sigma^N_{Q_{mn}}(r) \approx \frac{F^N_Q}{(2\pi r_o)^2} \operatorname{sinc}\left(m\frac{\Delta\phi}{2}\right) \operatorname{sinc}\left(n\frac{\Delta\theta}{2}\right) e^{-i\left(m\phi^N + n\theta^N\right)}. \tag{6.63}$$

  The difference between expressions (6.48) and (6.63) was tested under the assumptions retained in this work, and it was found to be numerically small. For instance, with the parameters retained in Section 6.15, the relative change in rolling resistance is well within 0.1%.

6.14 Considerations related to surface friction

It is interesting to note that, in the absence of surface friction, a deformable viscoelastic solid does not incur any resistance when sliding in steady-state, without rolling, on a rigid plane. This is due to the absence of any dynamics in the viscoelastic continuum, the deformation field being independent of time. Referring back to Figure 6.1 for the coated sphere, it is also noteworthy that, in the absence of surface friction, the resultant of the (normal) contact stress field acts in the vertical direction, because the contact surface is flat, and horizontal. As a consequence, the horizontal driving force Q cannot be balanced. We hence gather that, without surface friction, the linear velocity V_s of point C as well as the driving force Q are undetermined, and therefore irrelevant. The frictionless problem is therefore restricted to the coated sphere spinning under the influence of the driving torque T, which is balanced by

an equal and opposite resisting torque T_r generated by the horizontal offset of the normal contact force, $-P$.

In the presence of surface friction, two additional phenomena contribute to increasing, or decreasing, the resistance incurred by the rolling sphere:

1. the field of contact shear stresses influences the normal contact stress distribution, which modifies the offset of its vertical resultant. Analytical and numerical studies suggest that this influence is, in many cases, limited. It is expected to be increasingly so, inasmuch as (i) the coefficient of surface friction is small, (ii) the deformable material is less compressible, and (iii) the characteristic dimension of the contact surface is small as compared to the thickness of the coating (e.g. Bogy, 1968; Kuznetsov, 1978; Scheibert et al., 2009),

2. slipping occurs in regions of the contact surface where the contact shear stress reaches Coulomb's limit. Thus, further dissipation arises from the work of shear stresses in the slipping regions. However, because parts of the interface remain in a state of stick-contact, the differential velocities in the slipping regions are due to local deformation dynamics only, and are hence of limited magnitude. It follows that, in most cases of partial slipping, the contribution of slipping friction to rolling resistance will also be limited, as noted for instance by Greenwood and Tabor (1958); Qiu (2006); Tabor (1955); Zéhil and Gavin (2013e) (see Chapter 4).

It is worth mentioning that, if generalized slipping occurs across the entire contact surface, as opposed to the case of partial slipping, the differential velocities are mostly governed by indeterminate global kinematics, i.e. Ω and V_s, which results in rolling resistance being arbitrarily large. However, this 'extreme' case is not of direct interest to us.

In the following, the characters "s" and "$\bar{s}$", used as arguments, stand for extracting from a given array the rows/columns corresponding to stick-contact nodes and slipping nodes, respectively. The solution to the frictional rolling contact problem, at a given angular speed Ω, involves determining, in addition to the nodal normal force vector $\mathbf{F}_W(c)$ and the distance H, the nodal tangential force vectors $\mathbf{F}_U(s)$ and $\mathbf{F}_V(s)$ across the regions of stick-contact, and the unknown linear speed V_s. The solution process may conceptually be 'decoupled' into

1. a "normal-contact" subroutine, similar to that described in Section 6.12, solving for $\mathbf{F}_W(c)$ and H, given $\mathbf{F}_U$ and $\mathbf{F}_V$, as provided by the "stick-slip" subroutine (see below), and

2. a "stick-slip" subroutine, solving for $\mathbf{F}_U(s)$, $\mathbf{F}_V(s)$ and V_s, given $\mathbf{F}_W(c)$, as provided by the "normal-contact" subroutine.

These two algorithms are combined in an iterative solving scheme starting from $\mathbf{F}_U = \mathbf{F}_V = \mathbf{0}$, as an initial guess, and converging to the fully coupled solution of the rolling contact problem. The present section briefly outlines the structure of the "stick-slip" subroutine. The latter is based on the restriction of equations (6.55) to stick-contact nodes $N_{i,j}$, expressed as

$$\begin{aligned}\mathbf{C}_{UU}(N_{i,j},s)\mathbf{F}_U(s) + \mathbf{C}_{UV}(N_{i,j},s)\mathbf{F}_V(s) = \mathbf{D}_U(N_{i,j}) - \mathbf{C}_{UW}(N_{i,j},c)\mathbf{F}_W(c)\ldots \\ - \mathbf{C}_{UU}(N_{i,j},\bar{s})\mathbf{F}_U(\bar{s}) - \mathbf{C}_{UV}(N_{i,j},\bar{s})\mathbf{F}_V(\bar{s}) - d_R^{(c)}\,\mathrm{diag}\,(\mathbf{Q}_{RU})\,(N_{i,j})\,, \qquad (6.64a)\end{aligned}$$

$$\begin{aligned}\mathbf{C}_{VU}(N_{i,j},s)\mathbf{F}_U(s) + \mathbf{C}_{VV}(N_{i,j},s)\mathbf{F}_V(s) = \mathbf{D}_V(N_{i,j}) - \mathbf{C}_{VW}(N_{i,j},c)\mathbf{F}_W(c)\ldots \\ - \mathbf{C}_{VU}(N_{i,j},\bar{s})\mathbf{F}_U(\bar{s}) - \mathbf{C}_{VV}(N_{i,j},\bar{s})\mathbf{F}_V(\bar{s}) - d_R^{(c)}\,\mathrm{diag}\,(\mathbf{Q}_{RV})\,(N_{i,j})\,, \qquad (6.64b)\end{aligned}$$

where it is assumed that $\mathbf{F}_W(c)$ is known, and that $\mathbf{F}_U(\bar{s})$ and $\mathbf{F}_V(\bar{s})$ follow Coulomb's law of surface friction. Before system (6.64) can be solved for $\mathbf{F}_U(s)$ and $\mathbf{F}_V(s)$, expressions for the horizontal displacements $\mathbf{D}_U(N_{i,j})$ and $\mathbf{D}_V(N_{i,j})$, appearing on

the right-hand-sides of equations (6.64a) and (6.64b), are determined from equations (6.12). The conditions $w_{t_x} = 0$ and $w_{t_z} = 0$ in regions of stick contact write

$$u_{x,\phi} = r_o \sin(\theta)\sin(\phi) - \frac{V_s}{\Omega} - \cos(\phi)^2 u_y + \sin(\phi)\cos(\phi) u_x \approx r_o - \frac{V_s}{\Omega}, \quad (6.65a)$$

$$u_{z,\phi} = 0. \quad (6.65b)$$

Using a finite difference approach, $\mathbf{D}_U(N_{i,j})$ and $\mathbf{D}_V(N_{i,j})$ are related, through equations (6.65), to $\mathbf{D}_U(N_{i_{ref}(j)+1,j})$ and $\mathbf{D}_V(N_{i_{ref}(j)+1,j})$, where the index "$i_{ref}(j)$" refers to the leading edge stick contact node on nodal row j

$$\mathbf{D}_U(N_{i,j}) = \mathbf{D}_U\left(N_{i_{ref}(j)+1,j}\right) + \left(\frac{V_s}{\Omega} - r_o\right)(i_{ref}(j) + 1 - i)\,\Delta\phi, \quad (6.66a)$$

$$\mathbf{D}_V(N_{i,j}) = \mathbf{D}_V\left(N_{i_{ref}(j)+1,j}\right). \quad (6.66b)$$

Because the $N_{i_{ref}(j)+1,j}$ correspond to slipping nodes, or to free nodes, the additional unknowns $\mathbf{D}_U\left(N_{i_{ref}(j)+1,j}\right)$ and $\mathbf{D}_V\left(N_{i_{ref}(j)+1,j}\right)$ can be associated with as many additional equations taken from system (6.55)

$$\mathbf{D}_U\left(N_{i_{ref}(j)+1,j}\right) = \mathbf{C}_{UW}(N_{i_{ref}(j)+1,j}, c)\mathbf{F}_W(c) + \mathbf{C}_{\mathbf{UU}}((N_{i_{ref}(j)+1,j}, c)\mathbf{F}_U(c)\ldots$$
$$+ \mathbf{C}_{UV}(N_{i_{ref}(j)+1,j}, c)\mathbf{F}_V(c) + d_R^{(c)}\,\mathrm{diag}\left(\mathbf{Q}_{RU}\right)\left(N_{i_{ref}(j)+1,j}\right), \quad (6.67a)$$

$$\mathbf{D}_V\left(N_{i_{ref}(j)+1,j}\right) = \mathbf{C}_{VW}(N_{i_{ref}(j)+1,j}, c)\mathbf{F}_W(c) + \mathbf{C}_{VU}((N_{i_{ref}(j)+1,j}, c)\mathbf{F}_U(c)\ldots$$
$$+ \mathbf{C}_{VV}(N_{i_{ref}(j)+1,j}, c)\mathbf{F}_V(c) + d_R^{(c)}\,\mathrm{diag}\left(\mathbf{Q}_{RV}\right)\left(N_{i_{ref}(j)+1,j}\right). \quad (6.67b)$$

The unknown velocity V_s appearing in expression (6.66a) requires one additional equation provided by balancing the torque about the z-axis

$$\mathbf{1}^T\mathbf{F}_U(s) + \mathbf{0}^T\mathbf{F}_V(s) + 0.V_s = -\frac{T}{H}\ldots$$
$$- \frac{r_o}{H}\left[\sin(\boldsymbol{\theta}(c))\cos(\boldsymbol{\theta}(c))\right]^T\mathbf{F}_W(c) - \mathbf{1}^T\mathbf{F}_U(\bar{s}). \quad (6.68)$$

Combining equations (6.64) to (6.68) leads to a system of equations in the unknowns $\mathbf{F}_U(s)$, $\mathbf{F}_V(s)$ and V_s

$$\mathbf{G}_{UU}(N_{i,j}, s)\mathbf{F}_U(s) + \mathbf{G}_{UV}(N_{i,j}, s)\mathbf{F}_V(s) - (g_{ij}/\Omega)\,V_s = -r_o g_{ij}\ldots$$

$$- \mathbf{G}_{UW}(N_{i,j},c)\mathbf{F}_W(c) - \mathbf{G}_{UU}(N_{i,j},\bar{s})\mathbf{F}_U(\bar{s}) - \mathbf{G}_{UV}(N_{i,j},\bar{s})\mathbf{F}_V(\bar{s}) \ldots$$

$$- d_R^{(c)} \left(\mathrm{diag}\left(\mathbf{Q}_{RU}\right)\left(N_{i,j}\right) - \mathrm{diag}\left(\mathbf{Q}_{RU}\right)\left(N_{i_{ref}(j)+1,j}\right)\right) \tag{6.69a}$$

$$\mathbf{G}_{VU}(N_{i,j},s)\mathbf{F}_U(s) + \mathbf{G}_{VV}(N_{i,j},s)\mathbf{F}_V(s) + 0 \times V_s = \ldots$$

$$- \mathbf{G}_{VW}(N_{i,j},c)\mathbf{F}_W(c) - \mathbf{G}_{VU}(N_{i,j},\bar{s})\mathbf{F}_U(\bar{s}) - \mathbf{G}_{VV}(N_{i,j},\bar{s})\mathbf{F}_V(\bar{s}) \ldots$$

$$- d_R^{(c)} \left(\mathrm{diag}\left(\mathbf{Q}_{RV}\right)\left(N_{i,j}\right) - \mathrm{diag}\left(\mathbf{Q}_{RV}\right)\left(N_{i_{ref}(j)+1,j}\right)\right) \tag{6.69b}$$

$$H\mathbf{1}^T(s)\mathbf{F}_U(s) + \mathbf{0}^T(s)\mathbf{F}_V(s) + 0 \times V_s = -T \ldots$$

$$- r_o \left[\sin\left(\boldsymbol{\theta}(c)\right)\sin\left(\boldsymbol{\phi}(c)\right)\right]^T \mathbf{F}_W(c) - H\mathbf{1}^T(\bar{s})\mathbf{F}_U(\bar{s}) \tag{6.69c}$$

where the following quantities are defined for convenience:

$$g_{ij} = (i_{ref}(j) + 1 - i)\Delta\phi \ , \ \text{ and}$$

$$\mathbf{G}_{AB}(N_{i,j},:) = \mathbf{C}_{AB}(N_{i,j},:) - \mathbf{C}_{AB}(N_{i_{ref}(j)+1,j},:) \ \text{ for } A,B \in \{U,V,W\} \, .$$

As descried in further detail in Chapter 3 (Zéhil and Gavin, 2013c), a "stick-slip" algorithm may be implemented, in combination with the "normal-contact" algorithm described in section (6.12), to solve system (6.69) while iterating on the subset of stick-contact nodes to satisfy the tangential boundary conditions given by (6.13).

6.15 Verification and application example

We consider the case of a hard sphere of radius $r_i = 20$ mm, coated with an incompressible viscoelastic layer of thickness $h = r_o - r_i = 1$ mm, and density $\rho = 1000$ kg/m^3, rolling in steady-state, without surface friction, on a rigid plane, at an angular speed $\Omega = 2.5$ rad/s. A vertical load $P = 100$ N is applied to the rolling sphere. The constitutive behavior of the viscoelastic coating is characterized by a single relaxation time $\tau = 0.125$ s. The short-term and long-term shear moduli are taken equal to $G_o = 6$ MPa and $G_\infty = 3$ MPa, respectively. We have chosen to present the simple case of a Standard Viscoelastic Solid, as is common practice in the relevant literature (e.g. Carbone and Putignano, 2013; Hunter, 1961; Persson,

2010; Qiu, 2006, 2009; Zéhil and Gavin, 2013e,c,d), for purposes of illustration and comparison. In fact, any linear viscoelastic solid would present the similar global trends of behavior, for instance, such as illustrated in Figures 6.13 and 6.14. We are interested in determining the viscoelastic rolling resistance incurred by the sphere, as we vary some of the parameters specified above.

6.15.1 Verification of convergence

To optimize the computational costs related to building the boundary-element compliance matrices for the coating, an appropriate level of mesh refinement and a suitable truncation order are sought, based on convergence. To this aim, the resisting torque T_r is evaluated, in the conditions specified above, using an angular spacing between nodes $\Delta = \Delta\phi = \Delta\theta$ varying from $\pi/50$ rad to $\pi/400$ rad, and a truncation order $N_t = N_{t_\phi} = N_{t_\theta}$ ranging from 250 to 1500 terms. In evaluating expression (6.42) the integration domain $[r_i, r_o]$ is divided into $n_r = 50$ sub-intervals of equal amplitude. The resulting values of T_r are reproduced in Table 6.2 and found to fall within 10% of each other. It is furthermore noted that, when the angular spacing between nodes is less than or equal to $\pi/250$ rad, the results are well within 0.6%, which corresponds to a satisfactory level of convergence. Table 6.2 confirms, as previously noted in Chapters 4 and 5 (Zéhil and Gavin, 2013e, 2014c), that the spatial mesh refinement has more impact on convergence than the truncation order. The "N/A" entries in this table correspond to cases where the number of Fourier terms retained in the series is insufficient to cover the 'bandwidth' taken by expression (6.48), or (6.63), at the specified level of refinement of the spatial mesh. Based on these observations, a nodal spacing of $\Delta\phi = \Delta\theta = \pi/250$ rad and a truncation order of $N_{t_\phi} = N_{t_\theta} = 500$ terms are retained for the purposes of this application example.

The relative error on the resisting torque T_r, evaluated with respect to the best available estimate of 11.44 mN.m, is plotted against the number of sub-intervals n_r in

Table 6.2: Resisting torque T_r [mN.m]. Influence of spatial mesh refinement and truncation order on convergence.

Δ	Truncation order N_t [Number of Terms]					
[rad]	250	500	750	1000	1250	1500
$\pi/50$	10.50	10.36	10.43	10.46	10.44	10.43
$\pi/75$	11.42	11.47	11.50	11.44	11.43	11.42
$\pi/100$	11.22	11.01	11.01	11.03	11.01	11.01
$\pi/150$	11.09	11.10	11.11	11.10	11.11	11.10
$\pi/200$	11.33	11.31	11.32	11.32	11.31	11.32
$\pi/250$	11.41	11.38	11.39	11.40	11.40	11.39
$\pi/300$	N/A	11.42	11.41	11.42	11.43	11.42
$\pi/350$	N/A	11.45	11.44	11.45	11.44	11.45
$\pi/400$	N/A	11.45	11.44	11.44	11.44	11.44

Figure 6.4, for $\Delta = \pi/250$ rad and $N_t = 500$ Fourier terms. The error is well within $3.10^{-3}\%$ for $n_r \geq 10$. The value of $n_r = 50$, retained in this example, is therefore deemed sufficient.

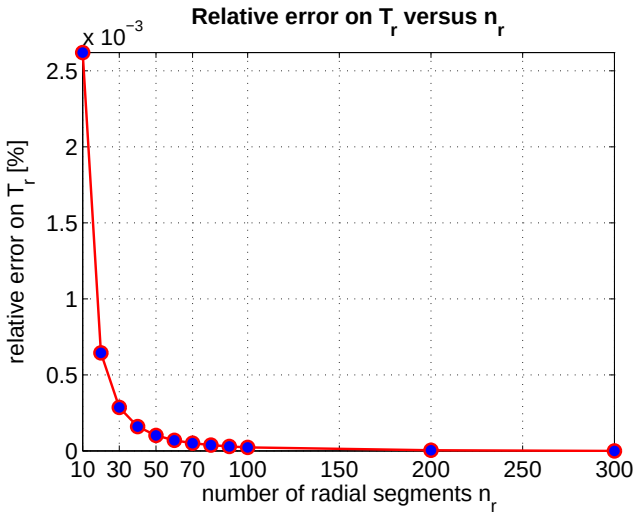

FIGURE 6.4: Influence of radial mesh fineness on convergence.

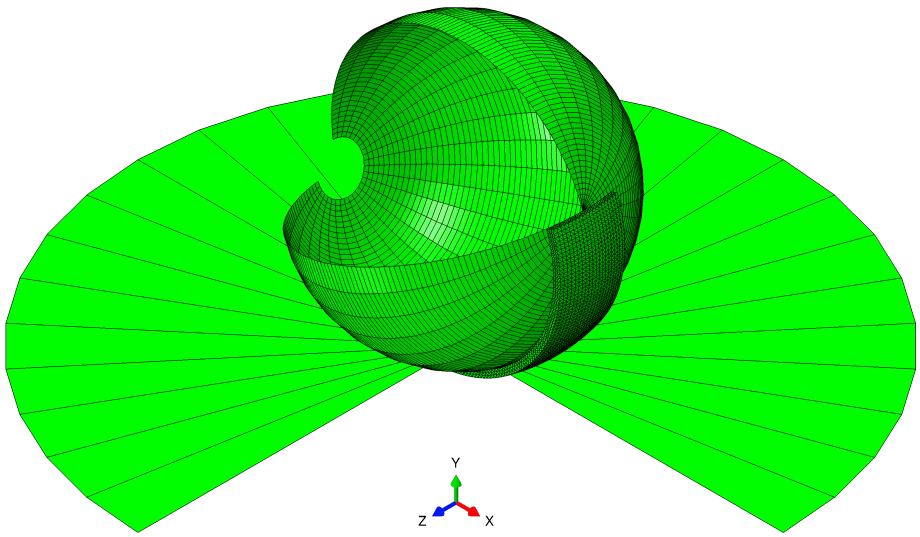

FIGURE 6.5: Finite element model under ABAQUS: rigid sphere coated with a viscoelastic strip, rolling on a rigid plane.

6.15.2 Verification of results

To verify that the steady-state model presented in this chapter yields accurate results, a three-dimensional finite element model of the same physical system is implemented under ABAQUS and rolling contact simulations are run, in implicit dynamic analyses, at prescribed angular velocities, until a steady-state rolling resistance is reached. To limit the computational cost of the temporal finite element simulations, the modeling of the viscoelastic coating is limited to a strip, rigidly tied to the sphere, as illustrated in Figure 6.5. The width of the strip is chosen so as to contain the largest area of influence of the contact interactions, characterized by stresses and strains in the continuum of the coating of the same order of magnitude as the contact fields.[1] Due to material incompressibility, a hybrid formulation is used to avoid volumetric locking (e.g. Hughes, 2000): the strip is discretized using 10-node quadratic tetrahedra, with constant pressure. The mesh parameter (element size) is

[1] For verification purposes, a finite element simulation is run at a rolling speed of $\Omega = 0.3$ rad/s, which corresponds roughly to the deepest penetration, with a strip of double the retained width. The difference in rolling resistance is found to be less than 0.1%.

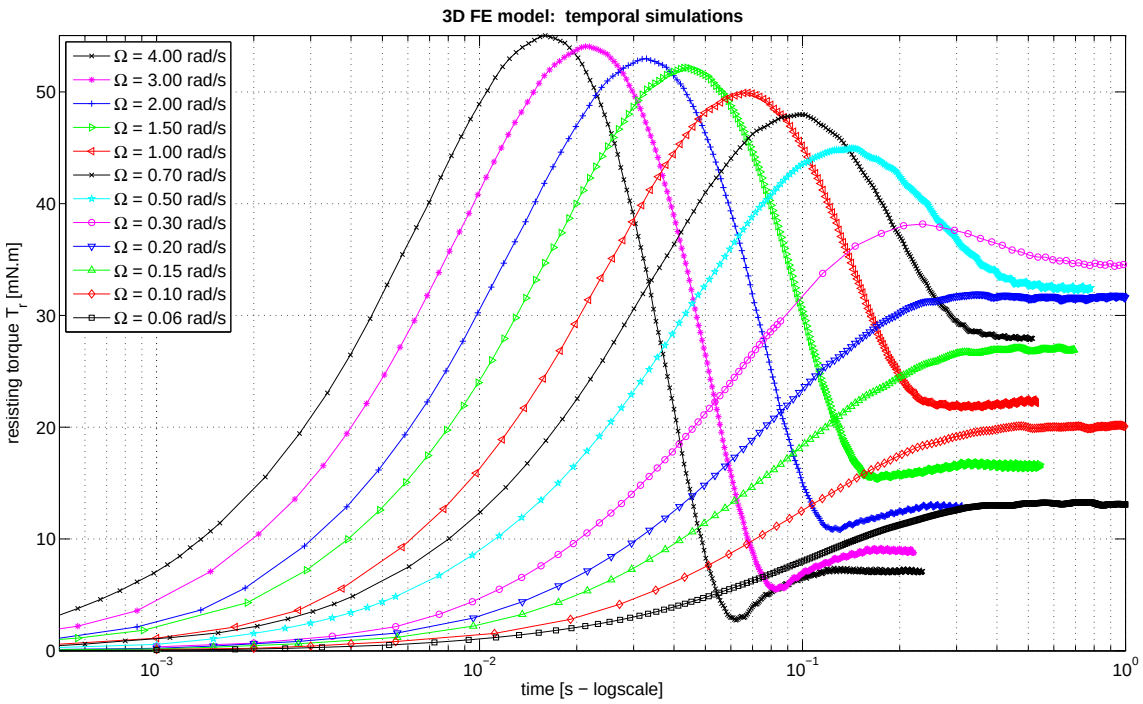

FIGURE 6.6: Finite element simulations at prescribed rolling speeds, without surface friction: time-history of the resisting torque.

set to approximately one third of the layer's thickness. Inertial forces and geometric nonlinearities are accounted for in the solution scheme (e.g. Zienkiewicz and Taylor, 2005), and surface-to-surface normal contact is implemented using the "hard" contact pressure-overclosure relationship.

Figure 6.6 shows the time-history of the resisting torque T_r for several simulations run at different angular speeds Ω, ranging between 0.5 rad/s and 4.0 rad/s. In each simulation, the prescribed rolling speed is applied instantaneously, as a boundary condition on the rigid sphere. Shorter integration time-steps are used at larger velocities. The simulations are interrupted once a stead-state in rolling contact is reached.

The steady-state rolling resistance is then evaluated using the three-dimensional boundary element formulation and the contact solving strategy proposed in this

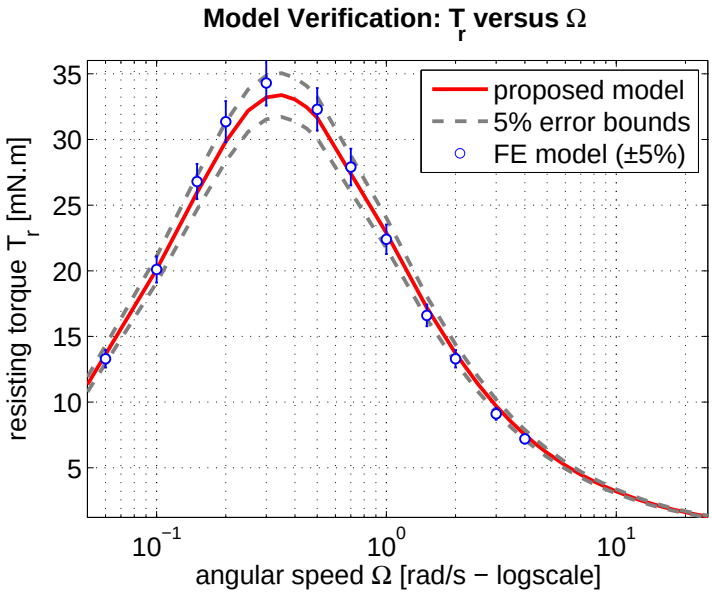

FIGURE 6.7: Model verification: rolling resistance results are in good agreement with finite element simulations.

chapter, for angular velocities ranging from 0.05 rad/s to 25 rad/s. Steady-state results from both the proposed model and the finite element model are compared in Figure 6.7 which shows that they are in very good agreement. Indeed, despite the various sources of uncertainty in the predictions of both models, such as approximations in geometry, numerical errors related to both spatial and temporal discretizations, truncation errors, and the uncertainty associated with the detection of a steady-state in the finite element simulation, all the numerical values are well within 5% of each other.

6.15.3 Influence of surface friction

Surface friction of the Coulomb type is added to the finite element model described in Section 6.15.2. Several simulations are performed at the same prescribed angular speed $\Omega = 0.2$ rad/s, but with different values of the coefficient of surface friction μ in the interval $[0, 2]$. The time-histories of the resisting torque T_r are plotted, for each

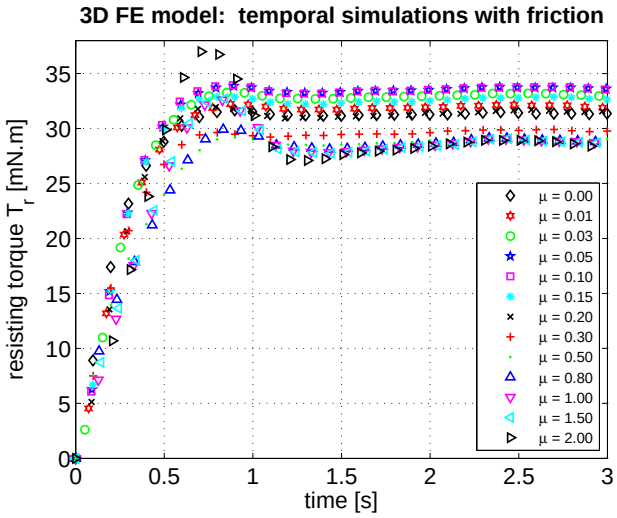

FIGURE 6.8: Frictional finite element simulations, performed at a constant angular speed $\Omega = 0.2$ rad/s, prescribed instantaneously at $t = 0$ s, for different values of the coefficient of surface friction μ, varying between 0 and 2. To improve the clarity of the plot, only 5% of the time integration points are shown. The overshoot is an increasing function of μ.

value of μ, in Figure 6.8. It may be noted that the difference (overshoot) between the peak value of T_r during the transient and its final value in steady-state increases with μ.

Numerical errors originating from the finite element model generate a moderate waviness in the time histories of T_r, even in steady-state. The resulting uncertainty is accounted for by computing a mean steady-state value of $T_r(\mu)$ and a standard deviation $S_{T_r}(\mu)$ from the samples of data corresponding to $t \geq 2$ seconds. These finite element results are plotted against μ in Figure 6.9. Qualitatively, from the pattern taken by the data points, which reveals a left boundary layer of width $\epsilon_\mu \approx 0.1$ (see e.g. Logan, 2006), it is clear that the behavior of $T_r(\mu)$ is driven by two competing mechanisms, each dominant in a given range of the parameter μ:

1. For relatively small values of the friction coefficient, i.e. $\mu \leq \epsilon_\mu$, the maximum contact shear stresses are small. Their influence on the normal contact stress

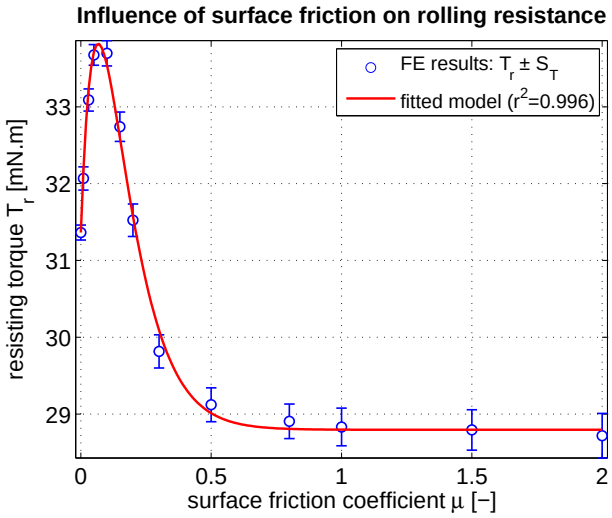

FIGURE 6.9: Influence of the coefficient of surface friction μ on steady-state values of the resisting torque T_r. The behavior of $T_r(\mu)$ is characterized by a left boundary layer of width $\epsilon_\mu \approx 0.1$. Slipping friction is dominant in the inner domain ($\mu \leq \epsilon_\mu$). The influence of contact shear stresses on the offset of the vertical resultant is dominant in the outer domain ($\mu > \epsilon_\mu$).

field, and on the viscoelastic rolling friction, is therefore negligible. On the other hand, because the slipping thresholds are low, slipping occurs on large portions of the contact surface, which results in energy losses from surface friction that are relatively significant. The overall frictional resistance to rolling is hence larger than the purely viscoelastic resistance, computed without friction,

2. for relatively large values of the friction coefficient, i.e. $\mu > \epsilon_\mu$, the slipping thresholds are large and most of the contact surface sticks to the plane. The contribution of slipping friction to rolling resistance is therefore negligible. On the other hand, because contact shear stresses are relatively large, their influence on the distribution of normal contact stresses, which reduces the offset of the vertical resultant $-P$, is significant. The overall frictional resistance to motion therefore decreases in comparison to that computed in the absence of surface friction.

This brief discussion on the governing mechanisms of rolling resistance is interesting. However, from a quantitative point of view, the influence of μ on T_r is limited. Indeed, as can be seen in Figure 6.9, all computed values of the resisting torque are roughly within 15% of each other. Furthermore, if the localized peak in $T_r(\mu)$ corresponding to the narrow left boundary-layer is disregarded, rolling resistance decreases no more than 8.5% with added surface friction. The dependence of T_r on μ may be fitted in four steps:

1. an 'inner' model $T_{r,i}(\mu)$ operating on the scaled variable μ/ϵ_μ is chosen to apply inside of the left boundary layer, i.e. for small values of the independent variable μ. An exponential model is retained in this case

$$T_{r,i}(\mu) = a_i \left(1 + b_i \left(1 - e^{-\frac{(\mu/\epsilon_\mu)}{c_i}}\right)\right), \tag{6.70}$$

   where a_i, b_i and c_i are parameters of the inner model. The first parameter a_i is in fact fixed, since $a_i = T_r(\mu = 0)$.

2. an 'outer' model $T_{r,o}(\mu)$ is chosen to apply outside of the left boundary layer, i.e. for larger values of μ. A model of the exponential form, with parameters a_o, b_o and c_o, is retained as well

$$T_{r,o}(\mu) = a_o \left(1 + b_o e^{-\frac{\mu}{c_o}}\right). \tag{6.71}$$

3. the limit of the inner model is matched to the limit of the outer model at the intermediate scale characterized by the variable $\eta = \mu/\sqrt{\epsilon_\mu}$. This is done as follows

$$\delta = \lim_{\epsilon_\mu \to 0} T_{r,i}\left(\sqrt{\epsilon_\mu}\eta\right) = \lim_{\epsilon_\mu \to 0} T_{r,o}\left(\sqrt{\epsilon_\mu}\eta\right) \quad \Rightarrow \quad a_i(1 + b_i) = a_o(1 + b_o). \tag{6.72}$$

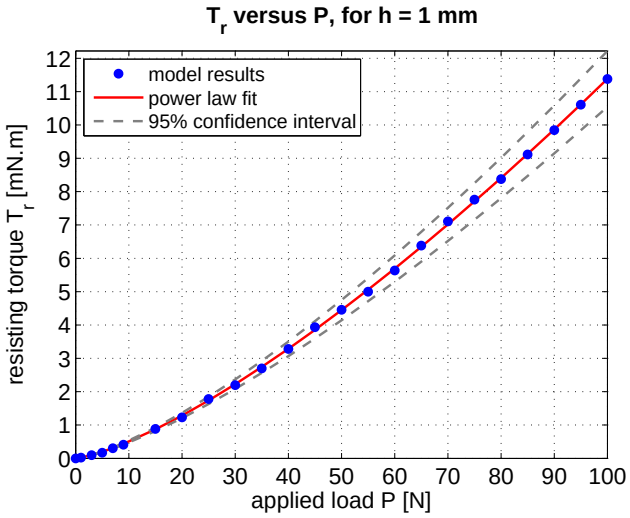

FIGURE 6.10: Influence of the applied load on the resisting torque, for $h = 1$ mm.

Table 6.3: Fitting coefficients for $T_r(P)$ [N.m] corresponding to 95% confidence intervals (r is the multiple correlation coefficient).

	$H = 1$ mm	$H = 5$ mm
r^2	≈ 1	≈ 1
$a_{p,max}$	5.037×10^{-5}	2.321×10^{-5}
$a_{p,min}$	4.766×10^{-5}	2.097×10^{-5}
$b_{p,max}$	1.430	1.368
$b_{p,min}$	1.418	1.344

4. a uniformly valid model $T_{r,u}(\mu)$ is obtained by adding the inner model to the outer model and subtracting their common intermediate-scale limit δ

$$T_{r,u}(\mu) = T_{r,i}(\mu) + T_{r,o}(\mu) - \delta. \tag{6.73}$$

The model $T_{r,u}$, which has four independent parameters a_o, b_o, c_o, and c_i, is fitted to the finite element results, as shown in Figure 6.9.

6.15.4 Influence of the applied load

To date, there are no closed-form expressions for the rolling resistance of a viscoelastic sphere on rigid plane that reflects the nonlinear dependence on the load P. As an

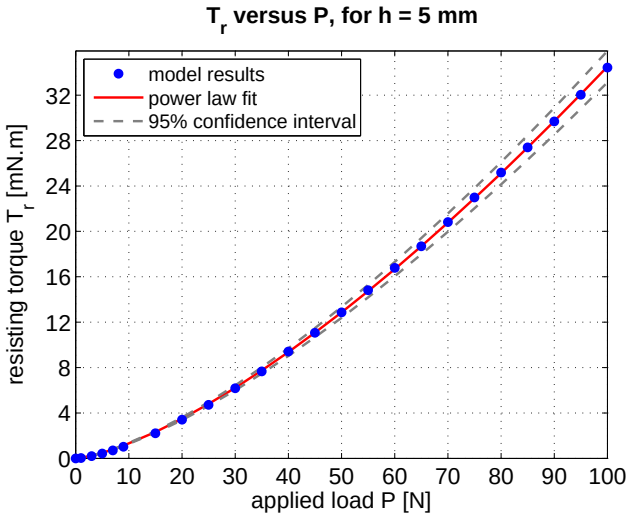

FIGURE 6.11: Influence of the applied load on the resisting torque, for $h = 5$ mm.

alternative, we consider for guidance, an approximate closed-form expression for the rolling resistance incurred by a rigid sphere rolling on a viscoelastic half-space, as derived by Greenwood and Tabor (1958) who integrated, under the small strain assumption, the horizontal projection of the stationary normal stress distribution, as given by Hertz (1881), over the front half of the contact disk. The resisting torque corresponding to this formulation may be written as follows

$$T_r \approx \left(\frac{3^4 \left(1 - \nu\right) R P^4}{2^{15} G} \right)^{\frac{1}{3}}, \tag{6.74}$$

where G is the shear modulus and ν corresponds to Poisson's ratio. Expression (6.74) does not reflect the dependence of rolling resistance on velocity. However, according to (6.74), T_r depends on P raised at the power 4/3. It is interesting to know whether the more accurate rolling resistance estimates given by the model proposed in this work show the same dependence on P. To this aim, the resisting torque T_r is plotted, in the context of our example, against the vertical load P, which ranges between 10 N and 100 N, in Figures 6.10 and 6.11, for $h = 1$ mm and $h = 5$ mm, respectively. Rolling resistance clearly increases with the applied load, and it does so unboundadly.

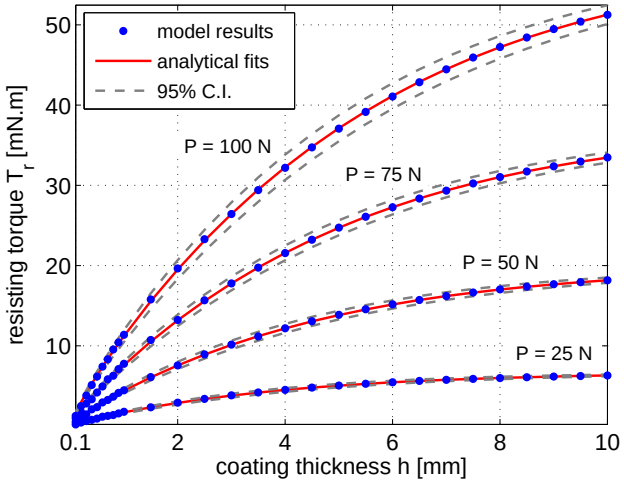

FIGURE 6.12: Influence of layer thickness on the resisting torque, at fixed $r_o = 21$ mm, for $P = 25$ N, 50 N, 75 N, and 100 N.

As can be seen on Figures 6.10 and 6.11, the dependence of T_r on P is well fitted by power laws of the form $T_r(P) = a_p P^{b_p}$ (solid lines). The dashed lines correspond to 95% confidence intervals on the fits. The parameter bounds corresponding to the same level of confidence are given in Table 6.3. It can be observed that the values taken by the parameter b_p are close, but not equal, to the value of 4/3 given by expression (6.74). In fact, b_p appears to be larger than 4/3 and to decrease with increasing h, i.e. as the coating becomes thicker and the systems tends towards a *solid* viscoelastic sphere.

6.15.5 Influence of coating thickness

The resisting torque T_r is plotted in figure 6.12 against coating thickness in the range $0.1 \leq h \leq 10$ mm, at fixed $r_o = 21$ mm, for $P = 25$ N, 50 N, 75 N, and 100 N. The dependence of rolling resistance on h is comparable, from a qualitative point of view, to that incurred by a hard cylinder (e.g Qiu, 2006) or by a hard sphere (e.g Zéhil and Gavin, 2013e) (see Chapter 4) rolling on a viscoelastic layer attached to a plane rigid subbase: the resisting toque increases with h and tends towards a limiting value

Table 6.4: Fitting coefficients for $T_r(h)$ [N.m] corresponding to 95% confidence intervals (r is the multiple correlation coefficient).

	$P = 25$ N	$P = 50$ N	$P = 75$ N	$P = 100$ N
r^2	0.9999	0.9999	0.9999	0.9999
$a_{h,max}$	0.677×10^{-2}	2.018×10^{-2}	3.811×10^{-2}	5.972×10^{-2}
$a_{h,min}$	0.670×10^{-2}	1.997×10^{-2}	3.770×10^{-2}	5.895×10^{-2}
$b_{h,max}$	78.446	71.332	67.310	64.205
$b_{h,min}$	69.702	64.898	61.842	58.431
$c_{h,max}$	0.827	0.835	0.840	0.842
$c_{h,min}$	0.809	0.821	0.827	0.828

which, in the present case, corresponds to that incurred by a *solid* viscoelastic sphere rolling on a rigid plane. This dependence is well fitted by three-parameter composite sigmoidal-power-law functions of the form $T_r(h) = a_h \tanh\left(b_h h^{c_h}\right)$, which correspond to the solid lines in Figure 6.12. The dashed lines reflect the 95% confidence intervals on the fits. The 95% confidence intervals on the fitted parameters are given in Table 6.4.

6.15.6 Influence of rolling speed

The influence of rolling speed on the resisting torque is shown in Figures 6.13 and 6.14 for a coating thickness of $h = 1$ mm and $h = 5$ mm, respectively. The different curves plotted on these figures correspond to equally spaced values of the applied load P, ranging from 10 N to 100 N. To understand the dependence of rolling resistance on velocity, it is useful to recall that the frequency-dependent viscoelastic master-curves of a linear viscoelastic material can be written in the form of a Prony series, i.e.

$$G'(\omega) = G_o\left(g_\infty + \sum_{k=1}^{n} \frac{g_k \omega^2 \tau_k^2}{1+\omega^2\tau_k^2}\right) \qquad \text{(storage modulus)}, \tag{6.75a}$$

$$G''(\omega) = G_o \sum_{k=1}^{n} \frac{g_k \omega \tau_k}{1+\omega^2\tau_k^2} \qquad \text{(loss modulus)}, \tag{6.75b}$$

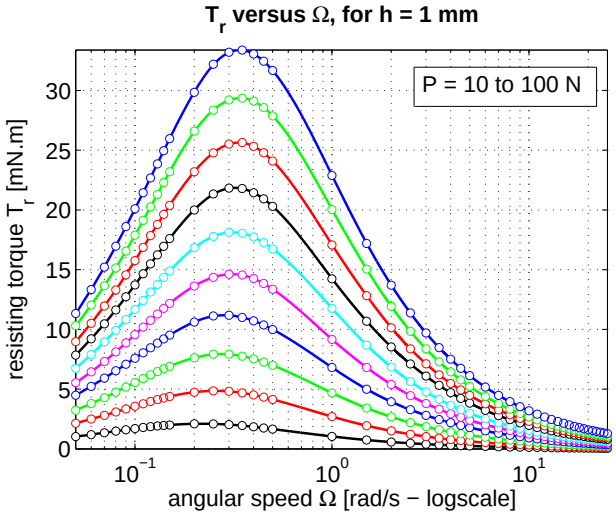

FIGURE 6.13: Influence of rolling speed on the resisting torque, for $h = 1$ mm. The curves correspond to different load levels between 10 N and 100 N, in steps of 10 N. Rolling resistance and lateral force increase in magnitude with the applied load.

where ω is the angular frequency, the material parameters τ_k correspond to internal relaxation times, and the associated weights g_k satisfy

$$g_\infty + \sum_{k=1}^{n} g_k = 1. \tag{6.76}$$

The loss modulus $G''(\omega)$ reflects the amount of dissipated energy at a given frequency ω. In relation to the material's distribution of internal time-scales, when the rolling occurs at a relatively low speed, the forcing frequencies tend to zero, and so does the loss modulus. Alternatively, at a relatively large rolling velocity, the forcing frequencies tend to infinity and $G''(\omega)$ also vanishes. The loss modulus reaches a peak at an intermediate rolling speed, which depends on the material's parameters. The material parameters retained in this example were stated at the beginning of Section 6.15. These correspond to $G_o = 6$ MPa, $n = 1$, $g_\infty = g_1 = 0.5$, and $\tau_1 = 0.125$ s.

It is here assumed that the sphere's coating does not heat significantly because

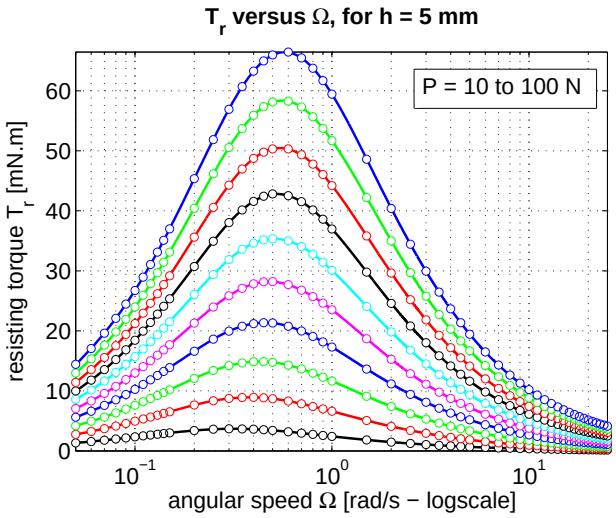

FIGURE 6.14: Influence of rolling speed on the resisting torque, for $h = 5$ mm. The curves correspond to different load levels between 10 N and 100 N, in steps of 10 N. Rolling resistance and lateral force increase in magnitude with the applied load.

of the motion. In general, this is justified under certain assumptions, such as: (i) small activation energy, (ii) small loss factor, (iii) small deformations, (iv) limited slipping and/or surface friction at the contact interface, (v) moderate velocity, (vi) coating of limited thickness, (vii) low specific heat capacity, and (viii) favorable conditions of heat dissipation, so as to limit the accumulation of thermal energy in the coating. It is interesting to note that rolling resistance is usually governed by material properties in a limited range of relevant frequencies, depending on the rolling speed. At higher velocities, this range is shifted towards higher frequencies, thus partially compensating the shift incurred by frequency-domain master-curves due to a moderate increase in temperature.

6.15.7 Influence of inertial effects

A simple dimensional analysis reveals that inertial effects can be related by the following dimensionless group, of which rolling resistance is a function:

$$\Pi = \frac{\rho \Omega^2 r_i^2}{G_o}. \tag{6.77}$$

By analogy to a single degree-of-freedom oscillator, the dimensionless group Π may be interpreted as the square of the ratio of a 'forcing' frequency Ω (i.e. the rolling speed) to a 'natural' frequency Ω_n given by

$$\Omega_n = \sqrt{\frac{G_o}{\rho r_i^2}}. \tag{6.78}$$

The influence of inertial effects on the resisting torque, and on the plane's penetration into the sphere's coating, are illustrated in Figure 6.15, which shows a sharp increase in penetration, and in rolling resistance, as Ω approaches Ω_n. The numerical value taken by Π in the example treated in this section is of the order of 10^{-7},

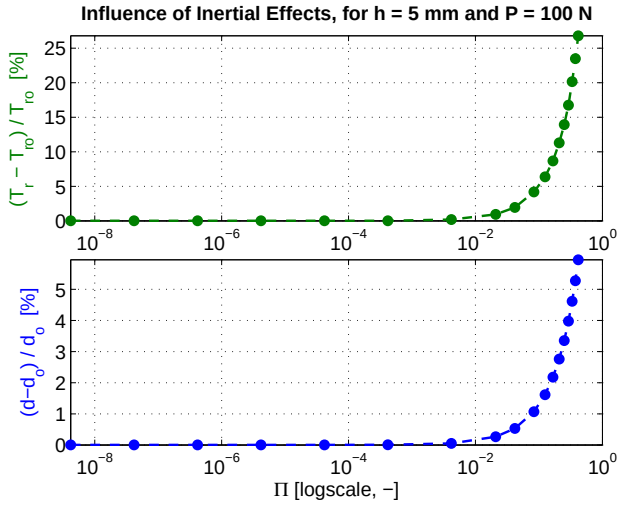

FIGURE 6.15: Influence of inertial effects on the resisting torque T_r, and on the penetration $d = r_o - H$, for $h = 5$ mm, and $P = 100$ N. The quantities T_{ro} and d_o corresponding to zero density ($\rho = 0$) are taken as reference.

which is very small compared to 1. At moderate velocities, with typical material properties, and unless the rolling object is exceptionally large, Π is small, and the influence of inertial effects is rather limited. Getting Π closer to 1 by increasing the density, with all other quantities remaining equal would be of course unrealistic. This is especially true as material stiffness usually increases with density. However, one can imagine applications where Π would approach the value of 1, for instance, due to high velocities, such in transportation, industry, and defense.

6.16 Summary

A full three-dimensional boundary element formulation of a multi-layered viscoelastic coating covering a hard spherical core rotating in steady-state is presented in this chapter. This formulation accommodates an arbitrary number of layers, each layer being of arbitrary thickness. It incorporates the viscoelastic and inertial effects of steady-state motion, including the Coriolis effect. Linear viscoelastic materials are characterized, in the most general way, by their frequency-domain master-curves, which enables the implementation of as many rates of internal dissipation as necessary to model their actual behavior. The proposed formulation relates two-dimensional Fourier series expansions of surface displacements and stresses. Based on these relations, a compliance matrix is constructed, in the spatial domain, by discretizing the outer boundary of the deformable coating into nodes. The computational cost of building such a compliance matrix is optimized, based on configurational similarities and symmetry.

This numerical model, which fully characterizes the mechanical behavior of the coating's outer boundary, can be used in diverse problem settings, at various scales, and in different fields, such as modeling important aspects in the behavior of interacting nano-particles, biological organisms, particles, grains or pellets in granular materials, bones in articulations, spherical components in industrial machines,

transport vehicles, satellites and robots, or in risk mitigation devices such as rolling isolation platforms.

In this work, the proposed formulation was applied, in combination with a rolling contact solving strategy, to evaluate the resistance to motion incurred by a hard sphere, coated with a viscoelastic layer, as it is rolling on a rigid plane. Steady-state results generated by the proposed model were verified by comparison to those obtained from running dynamic simulations on a three-dimensional finite element model of a coated sphere, rolling on a rigid plane, beyond the transient. A detailed application example includes a verification of convergence and illustrated the dependence of the resisting torque on various parameters, such as the applied load, the thickness of the coating, and the rolling velocity.

7

Simplified approaches to viscoelastic rolling resistance

7.1 Preamble

Modeling approaches yielding rolling resistance estimates for rigid spheres (and cylinders) on viscoelastic layers of finite thicknesses are introduced as lower-cost alternatives to more comprehensive solution-finding strategies. Detailed examples are provided to illustrate the capabilities of the different approaches over their respective ranges of validity.

7.2 Background

A full three-dimensional model of a rigid sphere, rolling in steady-state, with or without friction, on a viscoelastic foundation of finite thickness is presented in Chapter 4 (Zéhil and Gavin, 2013e). The candidate contact surface is discretized in a coordinate system that is traveling along with the moving object and the foundation's behavior described using a three-dimensional boundary element formulation, yielding

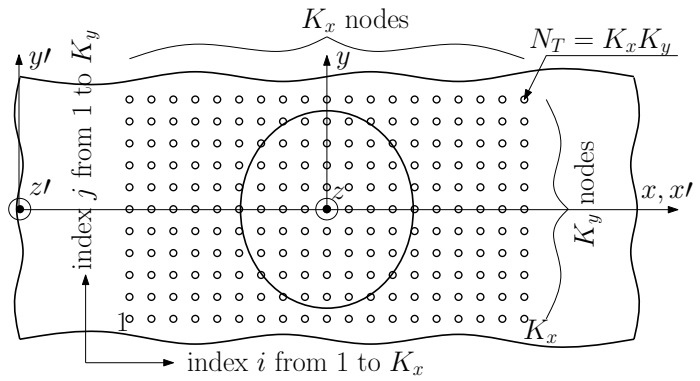

FIGURE 7.1: Discretization of the candidate contact surface.

a constitutive model for the layer of the following form

$$\mathbf{CF} = \mathbf{D}, \tag{7.1}$$

where $\mathbf{F}$ is a nodal surface force vector, $\mathbf{D}$ the corresponding nodal surface displacement vector and $\mathbf{C}$ the foundation's compliance matrix. Full results are then obtained by solving the rolling contact problem at the interface between the rigid sphere and the viscoelastic layer described by equation (7.1). Efficient means of solving the rolling contact problem are described in Chapter 3 (Zéhil and Gavin, 2013c).

The practical implementation of the full three-dimensional model involves determining matrix $\mathbf{C}$, or at least relevant parts of it, depending on each problem's particular assumptions and goals. Assuming that the candidate contact surface is descretized into K_x and K_y nodes in directions x and y respectively (see Figure 7.1), the total number of nodes is $N_T = K_x K_y$ and the full resulting square compliance matrix $\mathbf{C}$ is of dimension $3N_T = 3K_x K_y$. Taking advantage of existing configurational similarities between pairs of nodes, less than six columns of $\mathbf{C}$ (i.e. about $18K_x K_y$ terms) need to be formed explicitly (see Zéhil and Gavin (2013e), or Chapter 4).

In the absence of friction and provided that no horizontal displacements are wanted as part of the solution, only $1/9^{th}$ of the matrix $\mathbf{C}$ is required, from which

less than two columns need to be formed explicitly, which adds up to about $2K_xK_y$ terms. This number remains relatively high considering the fact that each matrix entry results from the addition of a sufficient number of terms from a double Fourier series. The computational cost of building compliance matrices increases quadratically with the number of discretization nodes and the truncation order. For reference, in the absence of surface friction, the computational time of building $1/9^{th}$ of a 3D compliance matrix corresponding to $N_T = 41 \times 41 = 1681$ nodes and including $N_{tx} = N_{ty} = 500$ Fourier terms on an Intel® Core™ i7 M620 CPU with 4 MB of cache memory and a clock speed of 2.66 GHz is approximately two minutes. In comparison, solving a frictionless rolling contact problem in 3D, using the same hardware, requires roughly 1.33 seconds. Consequently, the total computational time needed to evaluate the rolling resistance for 23 different values of rolling speed V_s and 15 different values of the applied load P, as we do in Sections 7.3.4 and 7.4.6 of this chapter, adds up to almost 54 minutes. This is considered as the reference case.

In many circumstances however, a complete and perfectly accurate solution is not necessary, hence justifying the search for cheaper computational means. This is particularly the case when only an estimate of the rolling resistance is sought. The present work considers alternative approaches to the full three-dimensional model, providing rolling resistance estimates with an accuracy that is suitable for many engineering purposes. According to Qiu (2006), and to Zéhil and Gavin (2013e) (see Chapter 4), the contribution of surface friction to the total rolling resistance is relatively small in comparison with viscoelastic energy dissipation and will therefore be neglected. Experimental evidence strongly supporting this assumption, for the rolling and lubricated sliding of rigid cylinders and spheres on rubber, date back to the 1950's (e.g. Greenwood and Tabor, 1958; Tabor, 1955).

7.3 2D cylinder based approaches to a 3D rolling resistance problem

Although configurational similarities afford significant increases of efficiency in three-dimensional solutions, the computational cost remains high in comparison with a similar implementation of a two-dimensional model originally presented by Qiu (2006). We have thus sought approximate solutions for the rolling resistance on a sphere (which is a 3D problem) based on a two-dimensional model of a rolling cylinder.

7.3.1 Shared principle

The idea is quite simple: a sphere of radius R moving in direction x at a given speed V_s, as depicted in Figure 7.2, is conceptually divided, along the transverse direction y, into an odd number of thin vertical cylindrical elements of thickness dy, such that one slice is centered in the middle with a symmetrical discretization on both sides. A cylindrical slice whose middle layer is centered at y has radius $R_c(y)$ and penetration $d_c(y)$. In particular, the middle slice is centered at $y = 0$ and its radius $R_c(0)$ is equal to R. The behavior of each cylindrical element is then approached using a two-dimensional model where the underlying subbase is in a state of plane strain (which is where the approximation lies). The vertical load P that is applied to the sphere gets distributed among the cylindrical slices. At equal thickness, the middle slice supports the largest part of the load and thus incurs the largest penetration $d_c(0)$. However, due to the plane stain assumption that is made on the layer in two-dimensions, $d_c(0)$ is typically smaller than the actual penetration of the sphere (d), as determined from a 3D model.

The total rolling resistance on the sphere is estimated by summing the rolling resistances incurred by each of its cylindrical elements, taking advantage of symmetry. Three variant algorithms (named “PD”, “PP” and “SP”) based on these common principles were implemented and tested against 3D results. The additional

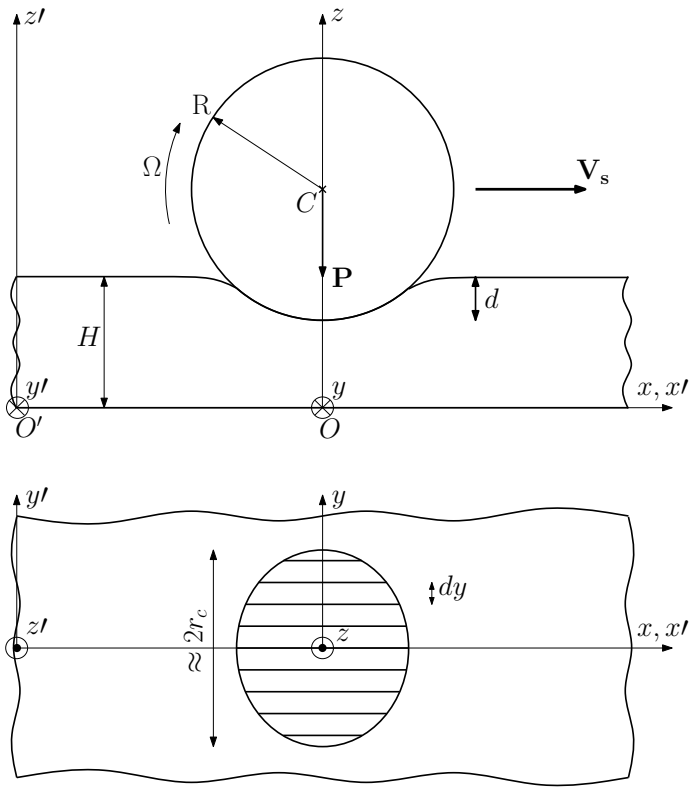

FIGURE 7.2: Discretization of the sphere into cylindrical elements (section in plane Oxz and projection on plane Oxy).

assumptions specific to each algorithm are presented in the sequel.

7.3.2 Algorithms PD and PP

Common Core of Algorithms PD and PP

The half-width of the actual contact surface r_c is considered to be roughly equal to the contact radius of a perfectly centered and circular one

$$r_c = \sqrt{d_o(2R - d_o)}, \tag{7.2}$$

where the penetration of the middle cylindrical slice $d_o = d_c(0)$ is approximated by the vertical distance between the bottom of the sphere and the contact boundary. It is further assumed that the marginal distribution $p_c(y)$ of the total vertical load P, among the cylindrical slices, is quadratic in y, transversally symmetric and

continuous at the edges, i.e.

$$p_c(y) = \frac{r_c^2 - y^2}{2R_p}, \tag{7.3}$$

where R_p is an unknown parameter characterizing the distribution $p_c(y)$ and corresponding to its radius of curvature, at the apex. The equilibrium of vertical forces may be written in analytical form as

$$P = \int_{-r_c}^{+r_c} p_c(y)dy. \tag{7.4}$$

Plugging (7.3) into (7.4) yields the following relation between R_p and r_c

$$r_c^3 = \frac{3}{2}PR_p. \tag{7.5}$$

Since parameters d_o, r_c and R_p are related by (7.2) and (7.5), one of them, say d_o, is chosen to serve as a state variable. The partial load per unit thickness applied to the middle slice $p_c(0)$, may hence be expressed in terms of the state variable d_o as follows

$$p_c(0) = \frac{3P}{4\sqrt{d_o(2R - d_o)}}. \tag{7.6}$$

Let $p_c^{alg}(d_o)$ be the vertical load per unit length returned by a 2D cylinder-based algorithm for a given penetration d_o of the middle slice. Based on equation (7.6), the problem is redefined as finding the penetration d_o such that (7.7) is satisfied

$$p_c^{alg}(d_o) = \frac{3P}{4\sqrt{d_o(2R - d_o)}}. \tag{7.7}$$

The left-hand-side of equation (7.7) corresponds to an implicit function of d_o which is evaluated by calling a 2D cylinder-based algorithm. Hence, starting with an initial guess for d_o, successive 2D cylinder-based iterations are performed on the middle slice only, until vertical load equilibrium is achieved.

One way to determine an initial guess for d_o is through an elastic estimate of the contact radius r_c^H, using an analytical result by Hertz (1881), where Poisson's ratio is taken equal to 0.5 and the shear modulus is approximated by the storage modulus $G'(\omega_m)$, where $\omega_m = 2\pi V_s/L_x$ is the angular frequency corresponding to the periodic length L_x in the direction of movement

$$r_c^H = \left(\frac{3PR}{16G'(\frac{2\pi V_s}{L_x})} \right)^{\frac{1}{3}}. \tag{7.8}$$

Algorithm PD

After d_o has been determined, algorithm PD will enforce geometrical consistency based on the lower profile of the sphere: a cylindrical slice whose middle layer is centered at y is subjected to a penetration $d_c(y)$ given by

$$d_c(y) = d_o - R + \sqrt{R^2 - y^2}. \tag{7.9}$$

As a result, geometrical consistency is strictly enforced while vertical load equilibrium remains approximate.

Algorithm PP

After d_o has been determined, algorithm PP will enforce vertical load equilibrium based on the applied load P: a cylindrical slice whose middle layer is centered at y is subjected to a vertical load per unit length $p_c(y)$ given by the following equation obtained by combining (7.2), (7.3) and (7.5)

$$p_c(y) = \left(\frac{3P}{4} \right) \left(\frac{d_o(2R - d_o) - y^2}{(d_o(2R - d_o))^{\frac{3}{2}}} \right). \tag{7.10}$$

Hence conversely, vertical load equilibrium is strictly enforced while geometrical consistency remains approximate.

7.3.3 Algorithm SP

Algorithm SP makes fewer assumptions and is more computationally involved than algorithms PD and PP, but still within reasonable bounds when compared with the computational cost of 3D results. The previous estimate for the half-width of the contact surface, as given by equation (7.2), is maintained. However, the assumption pertaining to the marginal transverse distribution of the load (i.e. equation (7.3)) which previously allowed performing iterations on the middle slice only, is now dropped.

Let $P_c^{alg}(d_o)$ correspond to the total vertical load obtained by adding all partial loads $p_c^{alg}(y)dy$ supported by each cylindrical element when subjected to a penetration $d_c(y)$ given by (7.9). For the purposes of algorithm SP, the problem is redefined as finding d_o such that $P_c^{alg}(d_o)$ is equal to the applied load P

$$P_c^{alg}(d_o) = \sum \left[p_c^{alg}(y)dy \right] = P. \tag{7.11}$$

The left-hand-side of equation (7.11) corresponds to an implicit function of d_o which is evaluated by calling a 2D cylinder-based algorithm as many times as there are slices centered at $y > 0$. Hence, starting with an initial guess for d_o, algorithm SP performs successive 2D cylinder-based iterations involving all cylindrical slices (taking advantage of symmetry), until it finds a global solution satisfying vertical load equilibrium as well as geometrical consistency.

In order to minimize the number of iterations involving multiple cylindrical elements, a good initial guess for d_o is sought by using the common core of algorithms PD and PP.

7.3.4 Example and results

The performances of algorithms PD, PP and SP are evaluated on the following example: a rigid sphere of radius $R = 2$ cm is rolling at a constant speed V_s, on

a viscoelastic foundation of thickness H, under the influence of a horizontal force Q applied at the top, with an intensity such that a steady-state is achieved. The value of Q is therefore not specified. A vertical load P is concomitantly applied at the center of the sphere. The foundation's material is modeled by a three-parameter viscoelastic solid defined by the following master curves

$$\begin{aligned} G'(\omega) &= G_0(1+f)\frac{(1+f)+\omega^2\tau^2}{(1+f)^2+\omega^2\tau^2}, \\ G''(\omega) &= G_0(1+f)\frac{f\omega\tau}{(1+f)^2+\omega^2\tau^2}, \end{aligned} \tag{7.12}$$

where $G_o = G'(0) = 3.0$ MPa is the static shear modulus, $\tau = 0.25$ s is the creep time and $f = G'(0)/G'(\infty) - 1 = 1$.

Three foundation thicknesses are considered: a relatively thin foundation ($H = 2$ mm), a foundation of intermediate thickness ($H = 5$ mm) and a relatively thick foundation ($H = 30$ mm). For each value of H, the vertical load P and the linear speed V_s are varied over appropriate ranges.

Discretization parameters of two and three-dimensional compliance matrices are set based on practical convergence results presented in Chapter 4 (Zéhil and Gavin, 2013e). The current example setting being an aperiodic one, the spatial periods are set to $L = L_x = L_y = 20$ cm, i.e. large enough to allow for sufficient creep recovery of the viscoelastic foundation between two successive sphere arrivals, at any given point. The nodal spacings retained are $a = a_x = a_y = 0.25$ mm. According to Table 4.1 in Chapter 4 (Zéhil and Gavin, 2013e, table 1), given the choices for a and L, a Fourier series truncation order of $N_t = 500$ terms is appropriate for the purposes of this work and is therefore adopted.

Regarding algorithms PD, PP and SP, the portion of the sphere that is above the contact surface is sliced into 21 cylindrical divisions. In order to test the level of convergence of these algorithms for $N_t = 500$ terms and 21 cylindrical divisions,

Table 7.1: Average computational times recorded for algorithms PD, PP and SP. The reference case, including minimal computations for 23 values of V_s and 15 values of P, is compared to a full solution time of 54 minutes (see Section 7.2).

Algorithm	Single run	Reference case	Speed factor
PD	0.21 s	21 s	153
PP	0.18 s	20 s	161
SP	0.56 s	107 s	30

tests were performed using a higher truncation order of 2000 terms and as many as 201 cylindrical divisions instead. The corresponding results were found to be well within 0.5% of each other.

Neglecting surface frictions, the rolling resistance estimates given by algorithms PD, PP and SP are plotted against the reference solution resulting from the full three-dimensional model. Furthermore, variations of the mean relative error between the reference solution and its estimate are plotted versus V_s and versus P. Results obtained from the best fitting algorithms are presented in Figures 7.3, 7.4 and 7.5, for $H = 2$, 5 and 30 mm respectively. Average computational times for the three algorithms are given in Table 7.1. In the case of reference involving minimal computations for 23 different values of rolling speed and 15 different values of the load, rolling resistance estimates are obtained using algorithms PD, PP and SP respectively 153, 161 and 30 times faster than the high fidelity solution given by the full 3D model.

When the foundation strip is relatively thin (i.e. $H = 2$ mm), algorithm SP yields rolling resistance estimates that are the closest to the reference solution given by the full 3D model. Figure 7.3(b) reveals that the average relative error of algorithm SP over the specified ranges of loading and speed is about -7.3%. Over the same ranges of P and V_s, the average errors of algorithms PP and PD are -9.6% and -27.0% respectively. Hence for relatively thin foundations, the lower computational

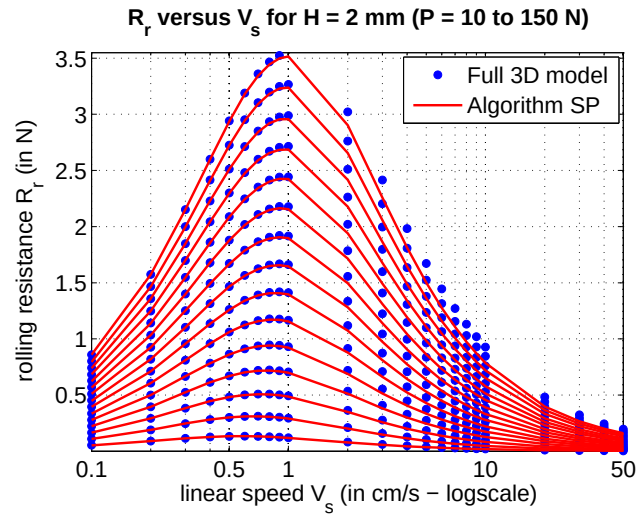

(a) Algorithm SP versus full 3D model

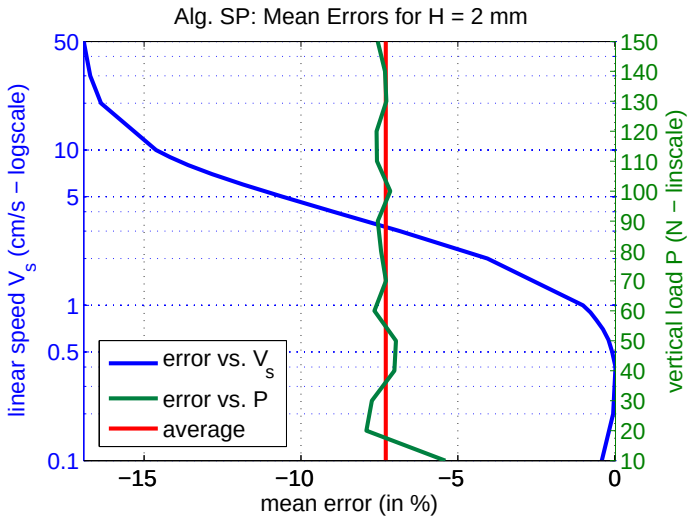

(b) %-errors versus V_s and P

FIGURE 7.3: Best results for $H = 2$ mm achieved by Algorithm SP.

cost of algorithm PP results in a slightly weaker performance than SP's. However, algorithm PD performs rather poorly in this range of foundation thickness.

Algorithm SP yields the best rolling resistance estimates for foundations of intermediate thickness as well. Its average relative error on the specified ranges of P and V_s is about -3.3% as given by Figure 7.3(b) for $H = 5$ mm. Algorithms PP and PD have average percentage errors of -4.6% and -18.9% respectively, over

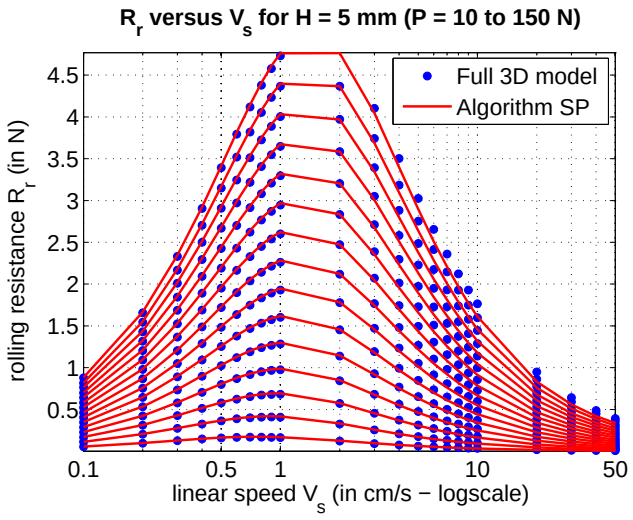

(a) Algorithm SP versus full 3D model

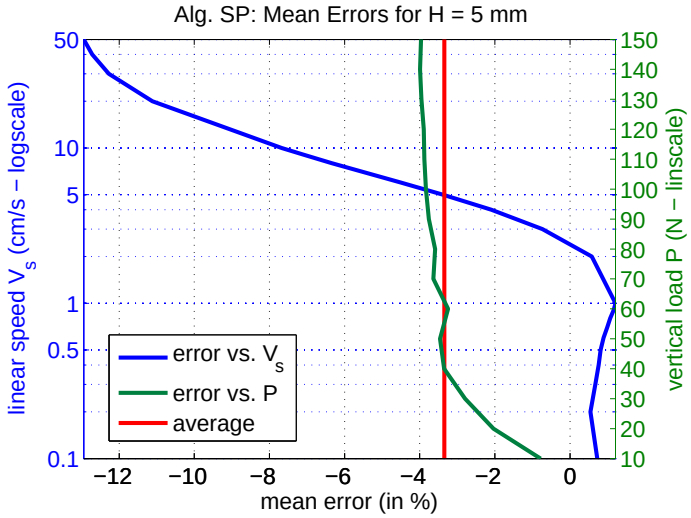

(b) %-errors versus V_s and P

FIGURE 7.4: Best results for $H = 5$ mm achieved by Algorithm SP.

the same ranges of loading and speed. The ranking of algorithms PP, PD and SP remains the same for thin and intermediate foundation thicknesses, while in both cases, the rolling resistance is mainly approached from below. However, the overall performance of the three algorithms is higher when the foundation is of intermediate thickness.

In the case of thick foundations, algorithm PD performs the best since it over-

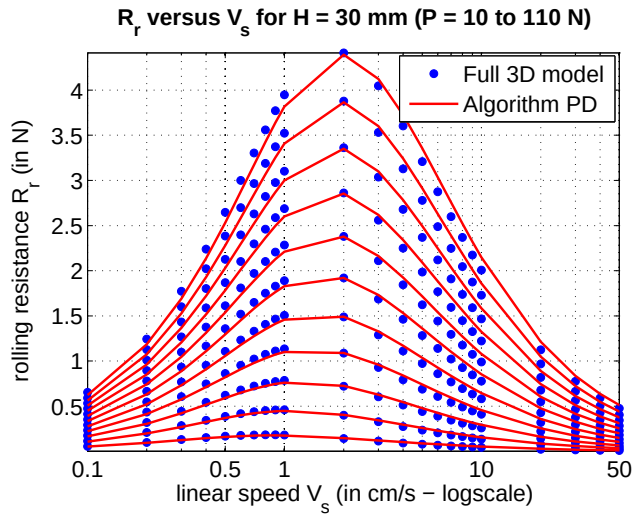

(a) Algorithm PD versus full 3D model

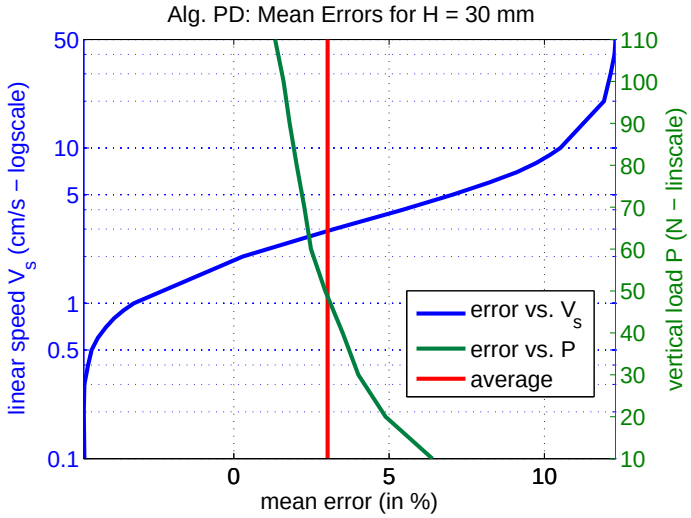

(b) %-errors versus V_s and P

FIGURE 7.5: Best results for $H = 30$ mm achieved by Algorithm PD.

estimates the rolling resistance, on average, by 3.0%, as given by Figure 7.5(b) for $H = 30$ mm, over the specified ranges of loading and speed. In the same conditions, algorithms PP and SP have average relative errors of 9.3% and 9.7% respectively. The performance ranking for thick foundations is hence PD > PP > SP. The same ordering would result if it were based on their computational cost (SP being the most expensive).

Figures 7.3(b), 7.4(b) and 7.5(b) reveal that in all three cases of foundation thickness and regardless of the estimating algorithm, the average percentage error remains rather constant at low rolling velocities then increases (algebraically) with a fairly constant slope (V_s is given on a logarithmic scale) passing through a best performance point (i.e. 0% error) located in the neighborhood of the speed corresponding to the peak of rolling resistance. At higher rolling velocities, the relative error endergoes a change in curvature and tends towards stabilizing.

Alternatively, the error varies less with the vertical loading than the moving speed. For $H = 2$ mm, it oscillates with a rapidly decreasing amplitude about its global average. For $H = 5$ mm the error slowly increases with the load while behaving oppositely for $H = 30$ mm. In all cases however, it remains fairly close to its global average.

It may be concluded that both algorithms SP and PP yield good rolling resistance estimates for foundations of intermediate thickness (e.g. $H = 5$ mm). Poorer performances are obtained as the foundation thins (e.g. $H = 2$ mm) or thickens (e.g. $H = 30$ mm). The higher computational cost of algorithm SP results in a moderate gain of accuracy in comparison with algorithm PP. Alternatively, algorithm PD yields good rolling resistance estimates for thick foundations (e.g. $H = 30$ mm). In general, the relative error depends less on the loading than it does on the speed. The best performances are obtained in the neighborhood of the moving velocity corresponding to the peak in rolling resistance, which is to the advantage of engineering applications where such a peak is of particular importance.

7.4 A direct Fourier series approach

7.4.1 Motivation

Section 7.3 introduced simplified approaches to estimating the viscoelastic rolling resistance on a sphere at a reduced computational cost as compared to the cost

of the full three-dimensional model given in Chapter 4 (Zéhil and Gavin, 2013e). Algorithms PD, PP and SP were based on a transverse summation of two-dimensional rolling cylinder contributions, without further relation to the full 3D model. In the second part of this chapter, we derive an alternative approach, directly stemming from the full 3D model itself, by introducing simplifying assumptions to it. As we will see, the methodology applies equally to deriving a simplified alternative to the full two-dimensional model of a rolling cylinder presented by Qiu (2006).

The simplified approach developed herein was inspired by the recent works of Persson (2010) and Jaffar (2008), as well as older works by Jaffar (1988, 1997). In Persson's simplified approach to rolling resistance, the effects of viscoelastic dissipation on the contact stress distribution are neglected. Persson's general theory is developed within the mathematical framework of continuous Fourier transforms and results in infinite integral expressions of the rolling resistance involving oscillatory Bessel functions. The method's efficiency hence depends on the practical implementation of such numerical integration. Efficient integration approaches applicable to this type of integrand are discussed for instance by Lucas and Stone (1995). Persson's method is applied to rigid cylinders and spheres rolling on a viscoelastic half-space assuming that the contact stress distribution is of Hertz's form. Alternatively, Jaffar's work provides valuable numerical approaches as well as asymptotic solutions to stationary contact problems between rigid bodies and elastic foundations of finite thickness. Jaffar's work may hence be used, in combination with suitable compliance matrices given by Carbone and Mangialardi (2008); Carbone et al. (2009), to apply Persson's approach to foundations of finite thickness.

Instead, retaining appropriate assumptions, the rolling resistance is directly expressed hereafter in the form of an infinite sum involving Fourier series coefficients of the normal contact stress distribution (i.e. $\sigma_{mn}(z = H)$) as well as Fourier coefficients of the vertical surface displacement field (i.e. $w_{mn}(z = H)$). Using existing

equations relating $\sigma_{mn}(z = H)$ to $w_{mn}(z = H)$ from the full 3D boundary element formulation presented in Chapter 4 (Zéhil and Gavin, 2013e), the latter is eliminated yielding an expression of the rolling resistance depending solely on the Fourier series expansion of the normal contact stress. Finally, neglecting the effects of viscoelasticity on $\sigma_z(x, y, z = H)$, it is assumed to keep a stationary elastic profile depending on the foundation thickness, which yields the σ_{mn}'s and hence the rolling resistance.

In comparison with the full 2D and 3D model requirements, the present 'simplified' and 'direct' approach to rolling resistance fully avoids solving the rolling contact problem by making a simplifying assumption on the distribution of normal contact pressure. It also circumvents forming the entire compliance matrix by directly summing terms contributing to the rolling resistance, which constitutes a substantial computational cost reduction. The series furthermore converges very rapidly: for instance, in the example of Section 7.4.6, approximately 99.4% accuracy (with respect to the limit value) is achieved using 50 terms only, for an average computational time of 0.85 seconds. In addition, the method can be implemented in vectorized form to compute the rolling resistance for multiple values of the same parameter: using 50 terms, rolling resistance estimates for 15 different values of the load P are obtained simultaneously for an additional time of 0.14 seconds. The computational time for the reference case including 23 values of V_s and 15 values of P adds up to less than 23 seconds, which is roughly 141 times faster than the full solution (see Section 7.2).

7.4.2 General Fourier series for the rolling resistance

Let A_c designate the contact area. With appropriate simplifying assumptions[1], a suitable expression of the rolling resistance may be derived from the power associated

[1] It is assumed that the foundation is subjected to small deformations, in the absence of surface friction, such that surface tractions act in the vertical direction.

with vertical stress and displacement fields

$$R_r = \frac{1}{V_s}\iint_{A_c} \sigma_z(x,y,z=H)\frac{\partial w}{\partial t}((x,y,z=H))dxdy, \tag{7.13}$$

which, given the fact that $\frac{\partial w}{\partial t} = -V_s\frac{\partial w}{\partial x}$ becomes

$$R_r = -\iint_{A_c} \sigma_z(x,y,z=H)\frac{\partial w}{\partial x}(x,y,z=H)dxdy. \tag{7.14}$$

For shortness of notation we will drop the argument $z = H$ since all quantities are evaluated at the contact interface. Vertical stress and deformation fields are then written in Fourier series as follows

$$\sigma_z(x,y) = \sum_{m_1,n_1=-\infty}^{+\infty} \sigma_{m_1n_1} e^{i\frac{2\pi m_1}{L_x}x} e^{i\frac{2\pi n_1}{L_y}y}, \tag{7.15}$$

$$w(x,y) = \sum_{m_2,n_2=-\infty}^{+\infty} w_{m_2n_2} e^{i\frac{2\pi m_2}{L_x}x} e^{i\frac{2\pi n_2}{L_y}y}. \tag{7.16}$$

Differentiating (7.16) with respect to x we get

$$\frac{\partial w}{\partial x}(x,y) = \sum_{m_2,n_2=-\infty}^{+\infty} i\frac{2\pi m_2}{L_x} w_{m_2n_2} e^{i\frac{2\pi m_2}{L_x}x} e^{i\frac{2\pi n_2}{L_y}y}. \tag{7.17}$$

Substituting (7.15) and (7.17) into (7.14) and integrating under the summation sign the following expression is obtained

$$R_r = -\sum_{m_1,n_1,m_2,n_2=-\infty}^{+\infty} \left(i\frac{2\pi m_2}{L_x}\sigma_{m_1n_1}w_{m_2n_2} \iint_{A_c} e^{i\frac{2\pi(m_1+m_2)}{L_x}x} e^{i\frac{2\pi(n_1+n_2)}{L_y}y} dxdy \right). \tag{7.18}$$

Since the vertical stress field $\sigma_z(x,y)$ is equal to zero outside of the contact surface we may integrate on the periodic domain $\left[-\frac{L_x}{2},+\frac{L_x}{2}\right] \times \left[-\frac{L_y}{2},+\frac{L_y}{2}\right]$ using the following

result

$$\int_{-\frac{L_x}{2}}^{+\frac{L_x}{2}} e^{i\frac{2\pi(m_1+m_2)}{L_x}x}dx \int_{-\frac{L_y}{2}}^{+\frac{L_y}{2}} e^{i\frac{2\pi(n_1+n_2)}{L_y}y}dy = \begin{cases} 0 & \text{if } (m_1+m_2)(n_1+n_2)=0, \\ L_xL_y & \text{otherwise.} \end{cases} \tag{7.19}$$

Hence, the only remaining terms in (7.18) are the ones for which $m_2 = -m_1 \equiv -m$ and $n_2 = -n_1 \equiv -n$. Noting further that $w_{-m-n} = \bar{w}_{mn}$, $\bar{w}_{-mn} = w_{mn}$ and $\sigma_{-mn} = \bar{\sigma}_{mn}$, expression (7.18) simplifies to

$$R_r = \sum_{m,n=-\infty}^{+\infty} i\,(2\pi m L_y)\,\sigma_{mn}\bar{w}_{mn} = -(4\pi L_y)\sum_{m\geq 1}\left(m\sum_{n=-\infty}^{+\infty}\Im\left(\sigma_{mn}\bar{w}_{mn}\right)\right), \tag{7.20}$$

where $\Im(z)$ corresponds to the imaginary part of the complex number z.

In Chapter 4 (Zéhil and Gavin, 2013e), we derived the following general solution, relating Fourier coefficients of displacements to Fourier coefficients of surface tractions at the upper boundary of a viscoelastic foundation strip

$$\mathbf{d}_{mn} = \mathbf{T}_{mn,12}\mathbf{T}_{mn,22}^{-1}\mathbf{f}_{mn}, \tag{7.21}$$

where the array quantities were defined as below

$$\mathbf{d}_{mn} = \langle w_{mn}, u_{mn}, v_{mn}\rangle^T,$$

$$\mathbf{f}_{mn} = \langle \sigma_{z,mn}, \tau_{xz,mn}, \tau_{yz,mn}\rangle^T,$$

$$\mathbf{T}_{mn}(z) = \exp(\mathbf{A}_{mn}H).$$

$\mathbf{A}_{mn}$ is a complex valued matrix given by

$$\mathbf{A}_{mn} = \begin{bmatrix} 0 & -i\nu_x & -i\nu_y & 0 & 0 & 0 \\ -i\nu_x & 0 & 0 & 0 & G_m^{*^{-1}} & 0 \\ -i\nu_y & 0 & 0 & 0 & 0 & G_m^{*^{-1}} \\ -\rho V_s^2\nu_x^2 & 0 & 0 & 0 & -i\nu_x & -i\nu_y \\ 0 & \alpha & \gamma & -i\nu_x & 0 & 0 \\ 0 & \gamma & \beta & -i\nu_y & 0 & 0 \end{bmatrix}, \tag{7.22}$$

where ρ is the material's density, $G_m^* = G'(\omega_m) + iG''(\omega_m)$ is the dynamic shear modulus and the following shorthand parameters have been used

$$\begin{aligned}
&\nu_x = 2\pi m/L_x \ ; \ \nu_y = 2\pi n/L_y, \\
&\beta_x = (4\nu_x^2 + \nu_y^2)G_m^* - \rho V_s^2 \nu_x^2, \\
&\beta_y = (\nu_x^2 + 4\nu_y^2)G_m^* - \rho V_s^2 \nu_x^2, \\
&\beta_{xy} = 3\nu_x \nu_y G_m^*.
\end{aligned} \tag{7.23}$$

Assuming frictionless contact conditions, we may write $\tau_{xz,mn} = \tau_{yz,mn} = 0$ and thus, regarding the vertical displacement, expression (7.21) reduces to

$$w_{mn} = T_{mn}\sigma_{mn}, \tag{7.24}$$

where $\sigma_{z,mn} \equiv \sigma_{mn}$ and T_{mn} is the upper left scalar entry of matrix $\mathbf{T}_{mn,12}\mathbf{T}_{mn,22}^{-1}$ that is, using the unit vector $\mathbf{e}_1 =< 1, 0, 0 >^T$

$$T_{mn} = \mathbf{e}_1^T \mathbf{T}_{mn,12}\mathbf{T}_{mn,22}^{-1}\mathbf{e}_1. \tag{7.25}$$

Substituting (7.24) into (7.20) leads to

$$R_r = (4\pi L_y) \sum_{m\geq 1} \left(m \sum_{n=-\infty}^{+\infty} |\sigma_{mn}|^2 \Im(T_{mn}) \right). \tag{7.26}$$

Fourier coefficients for the vertical surface traction are given by

$$\sigma_{mn} = \frac{1}{L_x L_y} \int_{-\frac{L_x}{2}}^{+\frac{L_x}{2}} \int_{-\frac{L_y}{2}}^{+\frac{L_y}{2}} \sigma_z(x,y) e^{-i\frac{2\pi m_1}{L_x}} e^{-i\frac{2\pi n_1}{L_y}} dydx, \tag{7.27}$$

and may be expressed in polar form as

$$\sigma_{mn} = \frac{1}{L_x L_y} \int_0^{2\pi} \int_0^{r_c} \sigma_z(r,\theta) e^{-iqr\cos\theta} r dr d\theta, \tag{7.28}$$

where $q = |\mathbf{q}|$, $\mathbf{q} = \left\langle \frac{2\pi m}{L_x}, \frac{2\pi n}{L_y} \right\rangle^T$, $r = |\mathbf{x}|$, $\mathbf{x} = \langle x, y \rangle^T$ and $\theta = \angle(\mathbf{q}, \mathbf{x})$.

Note about cylinders: the same approach equally applies to the case of a two - dimensional plane strain representation of a rigid cylinder rolling on a viscoelastic foundation of finite thickness. Expression (7.20) for the rolling resistance, stated per unit cylinder's length, becomes

$$R_r = -4\pi \sum_{m\geq 1} [m\Im(\sigma_m \bar{w}_m)], \tag{7.29}$$

where σ_m and w_m are the complex coefficients of single-variable exponential Fourier series expansions of the vertical traction distribution and displacement field across the foundation's surface. Letting L be the spatial period in one dimension, σ_m is given by

$$\sigma_m = \frac{1}{L}\int_{-\frac{L}{2}}^{+\frac{L}{2}} \sigma_z(x) e^{-i\frac{2\pi m}{L}} dx. \tag{7.30}$$

The foundation's constitutive equations relating σ_m to w_m were derived by Qiu (2006) in real form and may hence be used to eliminate w_m from (7.29). The following developments pertain to the case of a sphere knowing that the same principles apply to the cylinder.

7.4.3 Sphere on a thick foundation

According to Jaffar (2008), in frictionless and stationary conditions, provided that the half-width of the contact area (or equivalently, the contact radius r_c) does not exceed roughly 90% of an elastic foundation's thickness H (i.e. $\gamma = r_c/H \leq 0.9$) the contact pressure distribution keeps Hertz's form, i.e.

$$\sigma_z(r) = \frac{3P}{2\pi r_c^2}\sqrt{1-\left(\frac{r}{r_c}\right)^2}, \tag{7.31}$$

and the total vertical load P is given by the following expression

$$P = \frac{4\pi E r_c^3}{RD(1-\nu^2)}, \tag{7.32}$$

where E and ν are Young's modulus and Poisson's ratio respectively and D is defined as follows

$$D = 3\pi + 8\gamma^3 \left(b_1 + \frac{2}{5} b_2 \gamma^2 \right), \tag{7.33}$$

with coefficients b_m expressed (for $m = 1, 2$) as

$$b_m = \left(-\frac{1}{4} \right)^m \int_0^\infty \left(1 - L(\omega) \right) \omega^{2m} d\omega. \tag{7.34}$$

For a foundation bonded to its substrate $L(w)$ is given by

$$L(\omega) = \frac{2\kappa \sinh(2\omega) - 4\omega}{2\kappa \cosh(2\omega) + 4\omega^2 + \kappa^2 + 1}, \text{ with } \kappa = 3 - 4\nu. \tag{7.35}$$

Assuming that (7.31) and (7.32) are suitable approximations for steady state moving conditions on a viscoelastic layer, the contact radius may be evaluated by solving (7.32) for ${r_c}^2$. Following a similar approach to the one presented by Persson (2010), we may further plug (7.31) into (7.28) and write

$$\begin{aligned} \sigma_{mn} &= \frac{1}{L_x L_y} \frac{3P}{2\pi r_c^2} \int_0^{2\pi} \int_0^{r_c} r \sqrt{1 - \left(\frac{r}{r_c} \right)^2} e^{-iqr\cos\theta} dr d\theta \\ &= \frac{1}{L_x L_y} \frac{3P}{2\pi r_c^2} \frac{2\pi r_c^2}{(qr_c)^3} \left[\sin(qr_c) - qr_c \cos(qr_c) \right] \\ &= \frac{1}{L_x L_y} \frac{3P}{(qr_c)^3} \left[\sin(qr_c) - qr_c \cos(qr_c) \right]. \end{aligned} \tag{7.36}$$

Plugging (7.36) into (7.26) and using the fact that $T_{m-n} = T_{mn}$ the following expression for the rolling resistance is obtained

$$R_r = 2\pi \frac{(6P)^2}{L_x L_y} \left[\sum_{m,n \geq 1} I_{mn} + \frac{1}{2} \sum_{m \geq 1} I_{m0} \right], \tag{7.37}$$

[2] in the following Section 7.4.6, the contact radius given by solving (7.32) for r_c will be designated by r_c^{JK}

where

$$I_{mn} = \frac{m}{L_x}\frac{1}{(qr_c)^6}\left[\sin(qr_c) - qr_c\cos(qr_c)\right]^2 \Im(T_{mn}). \tag{7.38}$$

7.4.4 Sphere on a thin foundation

A similar approach to the one presented in Section 7.4.3 may be developed for very thin foundations (i.e. $\gamma \gg 1$) provided that it is based on appropriate estimates of the contact radius and the distribution of normal tractions. Suitable estimates are provided by Jaffar (1997) for the case of a thin elastic foundation in frictionless and stationary conditions.

Thin incompressible foundation

The contact pressure on a thin elastic and incompressible foundation takes the following form

$$\sigma_z(r) = \frac{3P}{\pi r_c^2}\left(1 - \left(\frac{r}{r_c}\right)^2\right)^2, \tag{7.39}$$

while (R being the radius of the sphere) the contact radius r_c may be expressed as follows[3]

$$r_c = \left(\frac{96PRH^3}{\pi E}\right)^{\frac{1}{6}}. \tag{7.40}$$

Plugging (7.39) into (7.28) we may write

$$\begin{aligned}
\sigma_{mn} &= \frac{1}{L_x L_y}\frac{3P}{\pi r_c^2}\int_0^{2\pi}\int_0^{r_c} r\left(1 - \left(\frac{r}{r_c}\right)^2\right)^2 e^{-iqr\cos\theta} dr d\theta \\
&= \frac{1}{L_x L_y}\frac{3P}{\pi r_c^2}\frac{16\pi r_c^2}{(qr_c)^3}J_3(qr_c) \\
&= \frac{1}{L_x L_y}\frac{48P}{(qr_c)^3}J_3(qr_c),
\end{aligned} \tag{7.41}$$

[3] in the following Section 7.4.6, the contact radius given by (7.45) will be designated by r_c^{JN}

where $J_3()$ is the third order Bessel function of the first kind. We may now plug (7.41) into (7.26) to get the corresponding expression of the rolling resistance

$$R_r = \frac{2\pi(96P)^2}{L_x L_y}\left[\sum_{m,n\geq 1} I_{mn} + \frac{1}{2}\sum_{m\geq 1} I_{m0}\right], \tag{7.42}$$

where I_{mn} becomes

$$I_{mn} = \frac{m}{L_x}\frac{1}{(qr_c)^6} J_3^2(qr_c)\Im(T_{mn}). \tag{7.43}$$

Thin compressible foundation

In the compressible case, the contact pressure on a thin elastic foundation takes the following form

$$\sigma_z(r) = \frac{2P}{\pi r_c^2}\left(1 - \left(\frac{r}{r_c}\right)^2\right), \tag{7.44}$$

and the contact radius may be expressed as follows

$$r_c = \left(\frac{(1+\nu)(1-2\nu)}{1-\nu}\frac{4RH}{\pi E}\right)^{\frac{1}{4}}. \tag{7.45}$$

Plugging (7.44) into (7.28) we may write

$$\begin{aligned}
\sigma_{mn} &= \frac{1}{L_x L_y}\frac{2P}{\pi r_c^2}\int_0^{2\pi}\int_0^{r_c} r\left(1 - \left(\frac{r}{r_c}\right)^2\right) e^{-iqr\cos\theta} dr d\theta \\
&= \frac{1}{L_x L_y}\frac{2P}{\pi r_c^2}\frac{4\pi}{q^2} J_2(qr_c) \\
&= \frac{1}{L_x L_y}\frac{8P}{(qr_c)^2} J_2(qr_c),
\end{aligned} \tag{7.46}$$

where $J_2()$ is second order Bessel function of the first kind. We may now plug (7.46) into (7.26) to get the corresponding expression of the rolling resistance

$$R_r = \frac{2\pi(16P)^2}{L_x L_y}\left[\sum_{m,n\geq 1} I_{mn} + \frac{1}{2}\sum_{m\geq 1} I_{m0}\right], \tag{7.47}$$

where I_{mn} becomes

$$I_{mn} = \frac{m}{L_x} \frac{1}{(qr_c)^4} J_2^2(qr_c) \Im(T_{mn}). \tag{7.48}$$

7.4.5 Foundations of intermediate thickness[4]

To the author's knowledge, there are no closed form or even approximate analytical expressions of the normal contact pressure between rigid objects and foundation layers of intermediate thicknesses (i.e. for $\gamma = \mathcal{O}(1)$ and $\gamma > 0.9$) that may be used at a low computational cost in expression (7.26) of the rolling resistance, in similar ways to the ones presented in previous Sections 7.4.3 and 7.4.4.

In axisymmetric problems[5], a numerical strategy, valid for $0 < \gamma < 20$ and Poisson's ratio $0 \leq \nu \leq 0.5$, is detailed by Jaffar (1988): given the indenter's lower profile, a truncated expansion, in modified Legendre polynomials, of the vertical displacement field is written in terms of the unknown penetration d. Integral equations relating the vertical pressure distribution to the vertical displacement field over the contact surface are transformed, using quadrature rules as well as the orthogonality property of modified Legendre polynomials, into a linear system of equations to be solved for the unknown coefficients of a similar truncated expansion of $\sigma_z(r, H)$. The edge condition $\sigma_z(r_c, H) = 0$ yields one additional equation for the unknown penetration d.

The aforementioned system of equations remains linear provided that the contact radius r_c is known, in which case the applied load P is deduced, using vertical force equilibrium, by integrating $\sigma_z(r, H)$ over the contact surface. However, if the vertical load P is given instead, which is practically the case, the system to be solved becomes nonlinear, which increases its numerical cost.

[4] unlike the methodologies presented in Sections 7.4.3 and 7.4.4, the one outlined here was not explicitly implemented and tested, as part of the present work.

[5] in an axisymmetric context, the radial position is denoted by $r = \sqrt{x^2 + y^2}$

The obtained solution for $\sigma_z(r, H)$, which corresponds to a truncated expansion in terms of modified Legendre polynomials, may then be plugged into (7.28) yielding similar order truncated expansions of the σ_{mn}'s. The latter can be used in turn in (7.26) yielding an estimate of the rolling resistance.

7.4.6 Example

Let us consider again the case of a rigid sphere, of radius $R = 2$ cm, rolling on a viscoelastic layer of thickness H in similar conditions to the ones described in Section 7.3.4. Three values of H are considered here: $H = 30$ mm and $H = 5$ mm will serve to illustrate the methods behavior over the range of thick foundations, while $H = 10$ μm will allow for checking its accuracy on a very thin layer.

The rolling resistance estimates given by the direct series approach (plain line) are plotted against the reference solution resulting from the full three-dimensional model[6] (round markers) in Figure 7.6(a), for a foundation of thickness $H = 30$ mm. In all cases on Figure 7.6(a), the stationary contact radius remains below 5.15 mm, which corresponds to $\gamma \leq 0.17$ and is therefore well within the thick foundation range. Consequently, the approximate solution closely follows the reference one.

Variations of the mean relative error between the reference solution and its estimate are plotted versus V_s and versus P on Figure 7.6(b). It may be seen that the mean errors remains positive and below 2.8% with a global average of 1.8%. The approximate solution hence approaches the reference one from above, with good accuracy. However, unlike for the 2D cylinder-based approaches presented in Section 7.3, the error depends equally on the loading and the speed: although not monotonically, the mean relative error seems to increase with the vertical load. It first increases than decreases with speed, reaching its 2.8% peak slightly before the peak in rolling resistance. Consequently, the minimum relative error (on the "error vs. V_s" curve)

[6] without friction

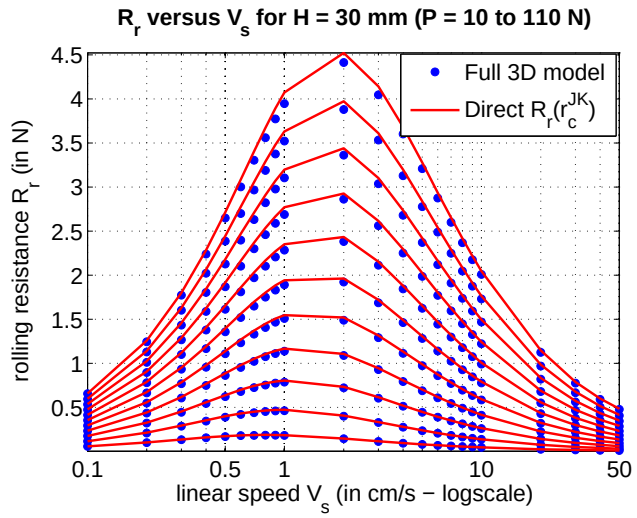

(a) Direct $R_r(r_c^{JK})$ versus full 3D model

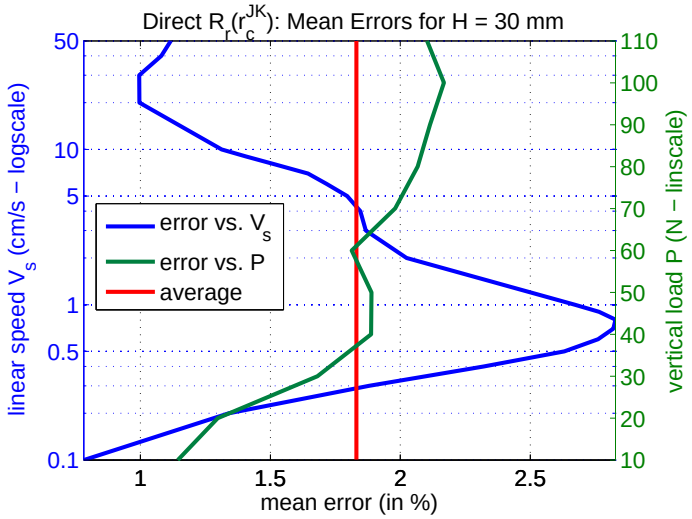

(b) %-errors versus V_s and P

FIGURE 7.6: Direct approach to R_r versus full 3D model for $H = 30$ mm.

does not seem to occur in the neighborhood of the peak in rolling resistance, as was previously the case.

Figure 7.7(a) compares the rolling resistance estimates provided by the direct approach, in the thick foundation range, to the full 3D model reference solution, for $H = 5$ mm. It may be noted that, up to $P = 120$ N, both solutions match extremely well. Starting $P = 130$ N, an increasing gap can be distinguished between the round

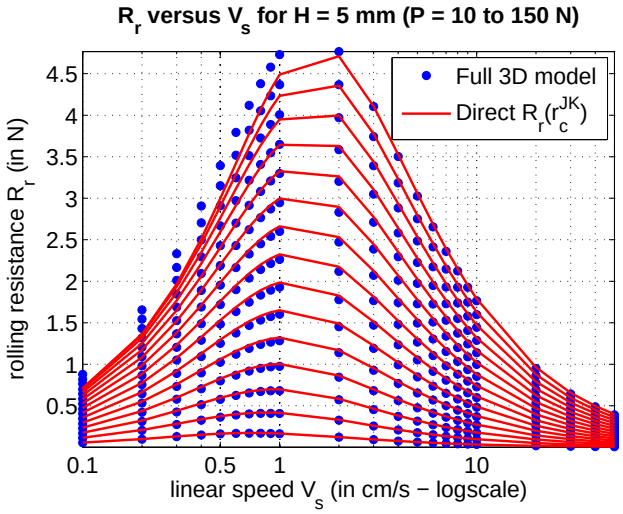

(a) Direct $R_r(r_c^{JK})$ versus full 3D model

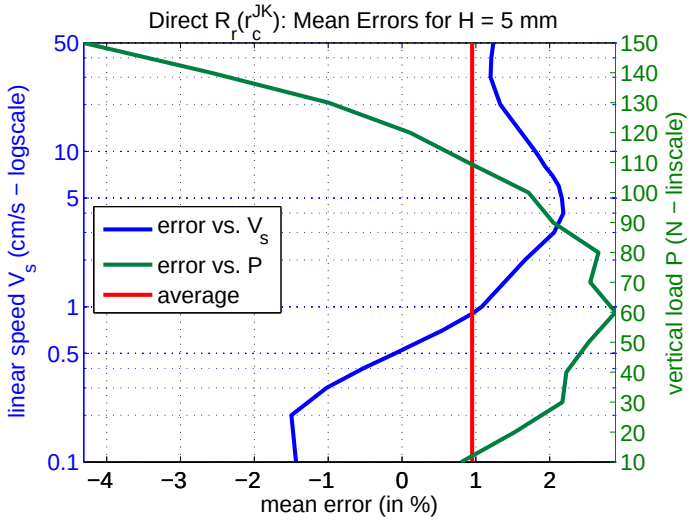

(b) %-errors versus V_s and P

FIGURE 7.7: Direct approach to R_r versus full 3D model for $H = 5$ mm.

markers and the plain curves, mainly on the left side of the peak in rolling resistance. In fact, for $P \leq 120$ N, the stationary contact radius remains below 4.87 mm, which corresponds to $\gamma \leq 0.97$ indicating that H is reaching beyond the lower bound of the thick foundation range (Section 7.4.3) into the intermediate range (Section 7.4.5).

Figure 7.7(b) reveals that the mean relative errors computed over the specified ranges of loading and speed remain below 4.3% with a global average of 0.95%. It

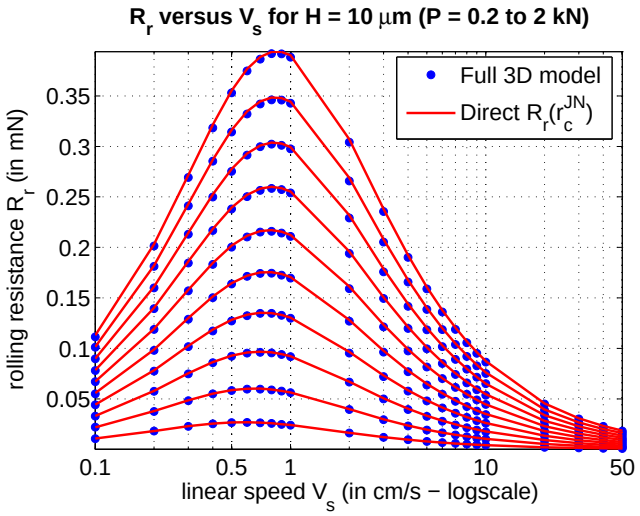

(a) Direct $R_r(r_c^{JN})$ versus full 3D model

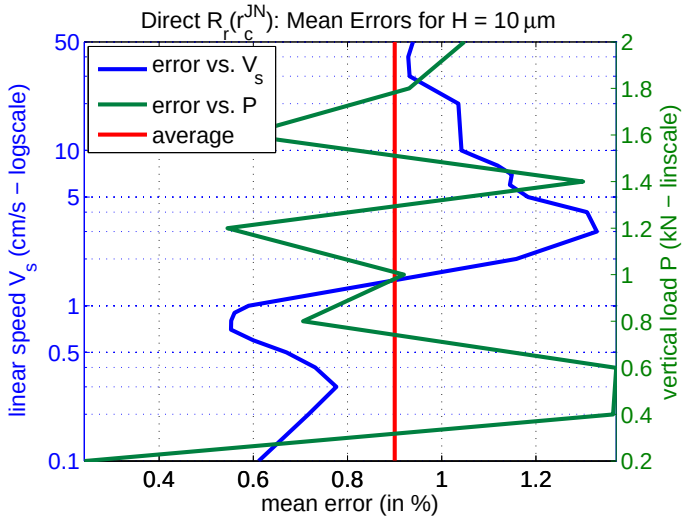

(b) %-errors versus V_s and P

FIGURE 7.8: Direct approach to R_r versus full 3D model for $H = 10$ μm.

can be noted that the "error vs. P" curve crosses the zero error axis at $P = 120$ N and monotonocally increases as greater loads drive γ out of the thick foundation range. The mean relative error remains positive up to $P = 120$ N, which indicates that, over its domain of validity, the simplified approach slightly overestimates the rolling resistance.

In order to generate a setting whereby $H \ll r_c$ while keeping the 3D model dis-

cretization unchanged as well as the same range of linear speed, the layer's thickness is reduced to $H = 10$ μm and the sphere's radius increased to $R = 2000$ m. It is further determined that a suitable loading range corresponds to $0.2 \leq P \leq 2$ kN. Indeed, the associated range of stationary contact radius is $3.33 \leq r_c \leq 4.88$ mm, which is large enough while remaining within the 1×1 cm^2 candidate contact surface. Moreover, the chosen parameters are such that $333 \leq \gamma \leq 488$, which is well within the thin foundation range.

Figure 7.8(a) indicates that, at the drawing's scale, the rolling resistance estimates given by the direct approach are in perfect agreement with the reference results from the full 3D model. This appears to be true over the entire ranges of loading and speed.

Figure 7.8(b) reveals that the simplified direct approach very slightly overestimates the rolling resistance. The mean errors remain positive but below 1.4% with a global average of 0.9% which may be considered to be an excellent results.

7.5 Summary

Simplified approaches to the rolling resistance of a rigid sphere on a viscoelastic layer of finite thickness were introduced throughout this chapter. The method presented in Section 7.4 applies equally to the case of a two-dimensional plane strain representation of a rigid cylinder on a viscoelastic foundation. Although based on simplifying assumptions and therefore yielding approximate rolling resistance estimates, the methods were tested and found to be quite accurate on their respective domains of application. Any comprehensive solution-finding strategy would necessarily involve modeling the viscoelastic layer as well as solving a three-dimensional rolling contact problem between the moving sphere and its foundation, both of which imply conceptual challenges as well as substantial computational costs. In a reference case involving minimal computations for 23 different values of rolling speed

and 15 different values of the load, rolling resistance estimates were obtained using algorithms PD, PP, SP and the 'direct' method, respectively 153, 161, 30 and 141 times faster than the high fidelity solution given by the full 3D model of Chapter 4 (Zéhil and Gavin, 2013e). The simplified approaches presented in this chapter hence constitute quite appealing alternatives in that they provide cheaper rolling resistance estimates of suitable accuracy to many engineering applications.

8

Experimental study of the resistance to motion incurred by a hard sphere rolling between two sheets of rubber: influence of material and geometric nonlinearities on the viscoelastic rolling resistance.

8.1 Preamble

An experimental apparatus is designed and assembled to measure the resisting force resulting from viscoelastic energy losses during motion, and to study the influence of material and geometric nonlinearities on rolling resistance. Using this setup, rolling resistance experiments are conducted on steel balls between sheets of a Urethane rubber, and a Neoprene rubber. The tests involve two ball diameters, two sheet thicknesses, and several loading levels and rolling speeds. Principal sources of measurement error, specific to the device, are discussed. The elastomers are described by linear viscoelastic models and characterized by: (i) High Frequency Thermo-Viscoelastic Spectroscopy, under very small strain amplitudes, and (ii) Dynamic Mechanical Analysis under relatively larger deformations. In both cases, rolling re-

sistance predictions are obtained using the computational tools presented in Chapters 3 and 4 (Zéhil and Gavin, 2013e,c), and compared to the measurements. Interesting conclusions are drawn regarding the fundamental influence of the Payne effect on predictions.

8.2 Experimental setup

8.2.1 Description

We have independently designed and assembled an experimental apparatus, somewhat similar to that proposed by Persson (2010), capable of measuring the resistance incurred by:

- a rigid sphere rolling between two rubber sheets, or alternatively, between one sheet of rubber and a flat rigid plate,
- a solid rubber sphere, or a rigid sphere with rubber coatings, rolling between flat and rigid plates.

The setup uses the shake table available in the Structural Dynamics and the Seismic Response Control Laboratory at Duke University, to prescribe the desired motion to the lower plate. An ALM (`http://www.americanlinear.com`) linear bearing, model P(A)-4-8-2, mounted vertically, insures that the load applied to the upper plate is entirely transmitted to the sphere. The schematic of the experimental setup is presented in Figure 8.1. A photograph of the assembled apparatus is shown in Figure 8.2.

8.2.2 About the load cell

The axial force in the system is measured between the linear bearing and the upper plate with an Interface (`http://www.interfaceforce.com`) 5210XYZ-1K multi-axis

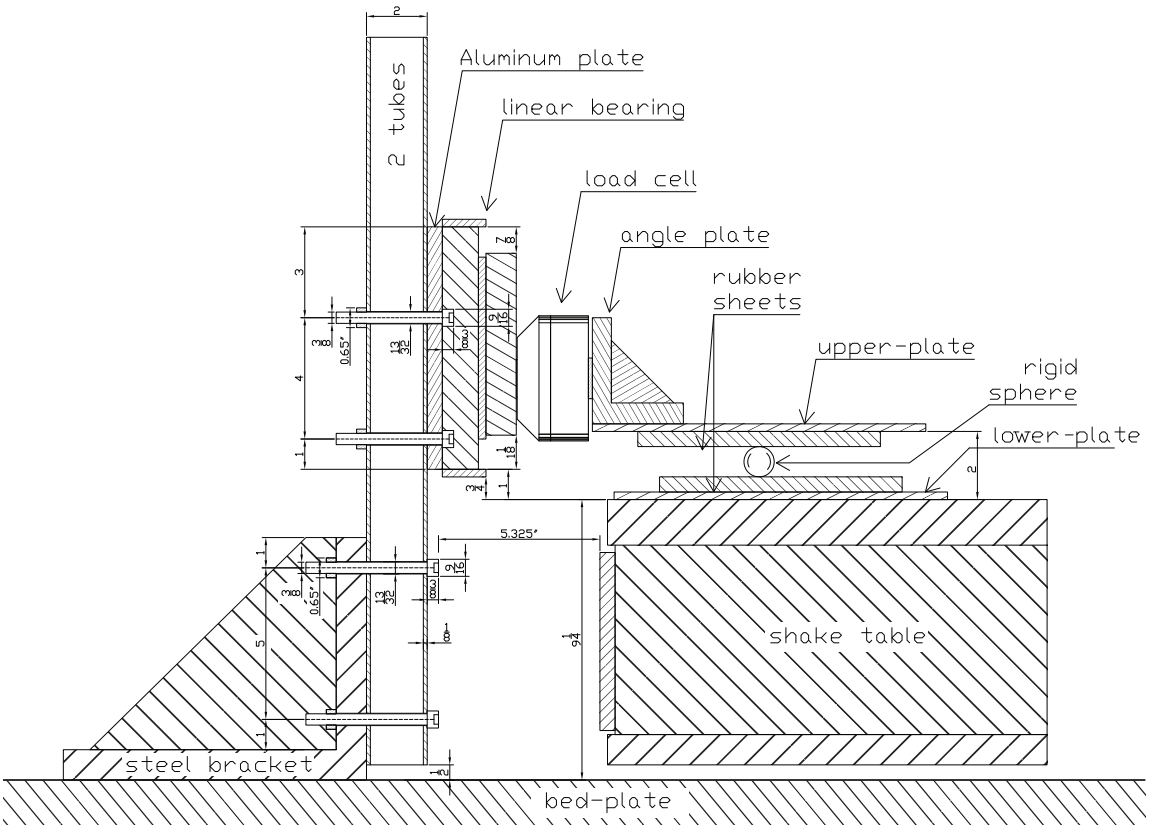

FIGURE 8.1: Schematic of the experimental apparatus designed to measure the rolling resistance of a sphere between two horizontal planes, using a fixed load cell connected to the upper plane. The sphere is subjected to a known vertical force applied by adding weights on top of this upper plane. The horizontal displacement of the lower plane is controlled by prescribing the motion of the shake table.

load cell. Main characteristics of the load cell relevant to the thrust axis are reproduced in Table 8.1. It is assumed that the different sources of measurement error originating from the load cell are uncorrelated. The square of the global error is therefore estimated as the sum of the squares of individual contributions. The shifts in zero and in signal output at room temperature are negligible, so are the net side-loads. The zero balance is accounted for by measuring the output in the absence of loading and considering this measurement as an offset. The static error band, which comprises nonlinearity and hysteresis, corresponds to $\pm 0.04\%$ of the "full scale" out-

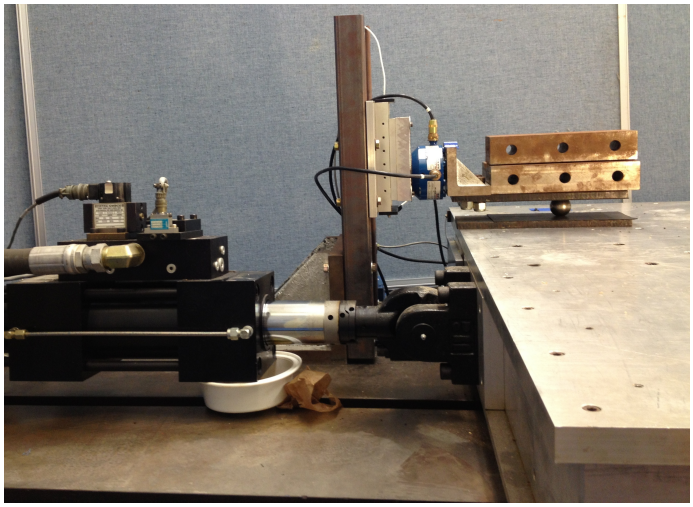

FIGURE 8.2: Photograph of the experimental rolling resistance apparatus. Sheets of rubber are bonded to the parallel steel plates. Due to the linear bearing, the upper part of the device can be lifted vertically and a rigid sphere inserted between the two rolling planes. A constant vertical load can be applied to the rolling sphere by adding weights on top of the upper plate.

put (F.S.), or equivalently in this case, of the maximum rolling resistance measured during a test. Non-repeatability amounts to $\pm 0.01\%$ of the rated output, or equivalently, of the load cell's capacity. The measurement error due to the eccentricity of rolling resistance is within $\pm 0.01\%$ per millimeter of eccentricity. The latter corresponds to the vertical distance between the upper rolling interface and the axis of the load cell, which is roughly equal to 25.4 mm plus the thickness of the upper sheet of rubber. Based on the above, the measurement error $\Delta R_r^{(1)}$ originating from the load cell is estimated to be within ± 0.45 N to ± 0.55 N, depending on the rolling resistance R_r measured during a test. The latter varies roughly between 2.1 N and 62 N, for an applied load P ranging from 86 N to 1083 N. The coefficient of variation on R_r corresponding to $\Delta R_r^{(1)}$ hence varies between 21.4% and 0.9%. Alternatively, the ratio $\Delta R_r^{(1)}/P$, which lies roughly between 0.5% and 0.05%, may be compared to the ratio R_r/P, ranging from 6.2% to 2.4%. These numbers reveal that measurement errors originating from the load cell are significant in the lower portion of the range

in which P is varied, in this experiment.

Table 8.1: Main thrust axis specifications of the Interface 5210XYZ-1K load cell.

Property	**Value(s)**
Capacity [N]	$4,448$
Rated output (R.O.) [mV/V]	2.214
Maximum D.C. input voltage [V]	20
Static error band [% F.S.]	± 0.04
Non-linearity [% F.S.]	± 0.04
Hysteresis [% F.S.]	± 0.03
Non-repeatability [% R.O.]	± 0.01
Side load sensitivity [%]	± 0.25
Eccentric load sensitivity [%/mm]	± 0.01
Compensated temperature range [°C]	-10 to $+45$
Operating temperature range [°C]	-55 to $+90$
Zero shift due to temperature [% R.O./°C - Max.]	± 0.0015
Output shift due to temperature [% R.O./°C - Max.]	± 0.0015
Zero balance [% R.O.]	± 1.0
Deflection at R.O. [mm]	0.03
Natural frequencies [kHz]	3.9; 5.0; 6.9; 9.8

8.3 Methods

Rolling resistance experiments are conducted using different sheets of initially virgin rubber-like materials:

- 1.6 mm thick Urethane rubber sheets ($\mathcal{U}_{1.6}$), provided by WorkSafe Technologies (`http://www.worksafetech.com/`). The company produces a rolling isolation platform (ISO-Base$^{\text{TM}}$) for the seismic protection of critical equipment. $\mathcal{U}_{1.6}$ rubber sheets are incorporated into the platform to generate viscoelastic rolling resistance, as a source of energy dissipation. This additional form of 'soft' damping improves the performances of the seismic isolation device (Harvey et al., 2013),

- 0.8 mm thick ($\mathcal{N}_{0.8}$) and 1.6 mm thick ($\mathcal{N}_{1.6}$) WFP-N2RS Neoprene rubber sheets of 50A durometer hardness, provided by Fairprene (`http://www.fairprene.com/`). The influence of thermo-oxidative aging on the mechanical behavior of $\mathcal{N}_{1.6}$ sheets was studied by Ha-Anh (2008) (see also Ha-Anh and Vu-Khanh, 2005a,b).

Three sets of rolling resistance experiments are performed by rolling: (i) a 38.1 mm steel ball between two $\mathcal{U}_{1.6}$ rubber sheets, (ii) a 25.4 mm steel ball between two $\mathcal{N}_{0.8}$ rubber sheets, and (iii) a 25.4 mm steel ball between two $\mathcal{N}_{1.6}$ rubber sheets.

The shake table is controlled to track slightly smoothed triangular displacement waves, each wave comprising five cycles. The influence of rolling speed on rolling resistance is explored by retaining six different periods for the prescribed motion: $T = 1$, 2, 5, 10, 15 and 20 seconds. Different load levels are used to investigate the effect of vertical load on rolling resistance: $P = 86$, 226, 297, 509, 649, 720, 901 and 1083 N for the $\mathcal{U}_{1.6}$ rubber sheets, and $P = 86$, 114, 157, 226 and 297 N for the $\mathcal{N}_{0.8}$ and the $\mathcal{N}_{1.6}$ rubber sheets. Between successive load levels, the ball is manually shifted, perpendicular to the center line of motion, so that the it would be rolling, initially, on a virgin material.

To explore the system's behavior without rubber sheets, one additional set of rolling resistance experiments is conducted by rolling a 25.4 mm steel ball between two bare steel plates, under the five load levels: $P = 86$, 114, 157, 226 and 297 N. In the absence of viscoelastic components, the response of the metallic setup is time-independent. Thus, tests on bare steel plates are performed at the intermediate period $T = 5$ s only.

The experimental setup is equipped with an array of sensors:

- the load cell, located between the angle-plate and the linear bearing, measures the axial force along the thrust axis, but also two moments perpendicular to

this axis,

- an accelerometer placed on top of the angle plate confirms that vertical accelerations in the upper part of the frame are not significant during the tests,
- the hydraulic actuator has a linear variable differential transformer (LVDT) that senses the displacement of the shake table. The table's velocity is deduced by differentiation of the LVDT output signal.

The table's displacement is limited to 95% of the actuator's stroke, which is of 152.4 mm. All measurements are anti-alias filtered at 200 Hz and collected at 400 samples per second.

8.4 Experimental data analysis procedures

8.4.1 Rolling resistance

The steady-state rolling resistance is estimated, from the time-history of the measured force resisting motion, following the procedure described below:

1. A sigmoidal wave function characterized by four parameters is fit to the rolling resistance measurements, after detrending. The fitted wave function can be defined over one period (i.e. for $t \in [u, u+T_s]$) as follows:

$$\hat{R}_r(t) = \begin{cases} -\bar{R}_r \tanh\left(\frac{t-u}{\tau_s}\right) & \text{for} \quad u \leq t < u + \frac{T_s}{4}, \\ +\bar{R}_r \tanh\left(\frac{t-u-\frac{T_s}{2}}{\tau_s}\right) & \text{for} \quad u + \frac{T_s}{4} \leq t < u + \frac{3T_s}{4}, \\ -\bar{R}_r \tanh\left(\frac{t-u-T_s}{\tau_s}\right) & \text{for} \quad u + \frac{3T_s}{4} \leq t \leq u + T_s, \end{cases} \tag{8.1}$$

where T_s is the wave's period, $\bar{R}_r$ is a limit peak-value, u is a time-shift, and τ_s corresponds to a characteristic time.

2. The estimated value of rolling resistance, in steady-state, is taken as

$$R_r = \max_{t \in [u, u+T_s]} \hat{R}_r(t). \tag{8.2}$$

Typical examples of sigmoidal wave functions fitted to time histories of experimental rolling resistance measurements on $\mathcal{U}_{1.6}$, $\mathcal{N}_{1.6}$ and $\mathcal{N}_{0.8}$ rubber sheets are shown in figures (8.3)-(8.8), for a selection of periods (T = 1, 5 and 20 s) and for the extremal values of the applied load P. To improve the legibility of these figures, and to limit their size, the original sets of data points are downsampled by a factor of T, for plotting purposes only.

Alternative models

Other mathematical representations may be used, as alternatives to that given by expression (8.1), to model rolling resistance. We briefly mention a couple of options below:

- A simple dynamic model, known as Dahl's model (Dahl, 1968, 1976), which expresses rolling resistance as a function of displacement. The Dahl model may be formulated as

$$\frac{d\hat{R}_r(t)}{dt} = \sigma \left(1 - \frac{\hat{R}_r(t)}{\bar{R}_r} \operatorname{sgn}(V_s(t)) \right)^{\alpha} V_s(t), \tag{8.3}$$

  where $\bar{R}_r$, σ and α are empirical fitting parameters. For friction modeling, the parameter α is typically set to 1.

- A simple analytic expression relating rolling resistance to rolling speed, such as

$$\hat{R}_r(t) = \bar{R}_r \tanh \left(\frac{V_s(t)}{V_o} \right), \tag{8.4}$$

  where $\bar{R}_r$ and V_o are two parameters to be fit.

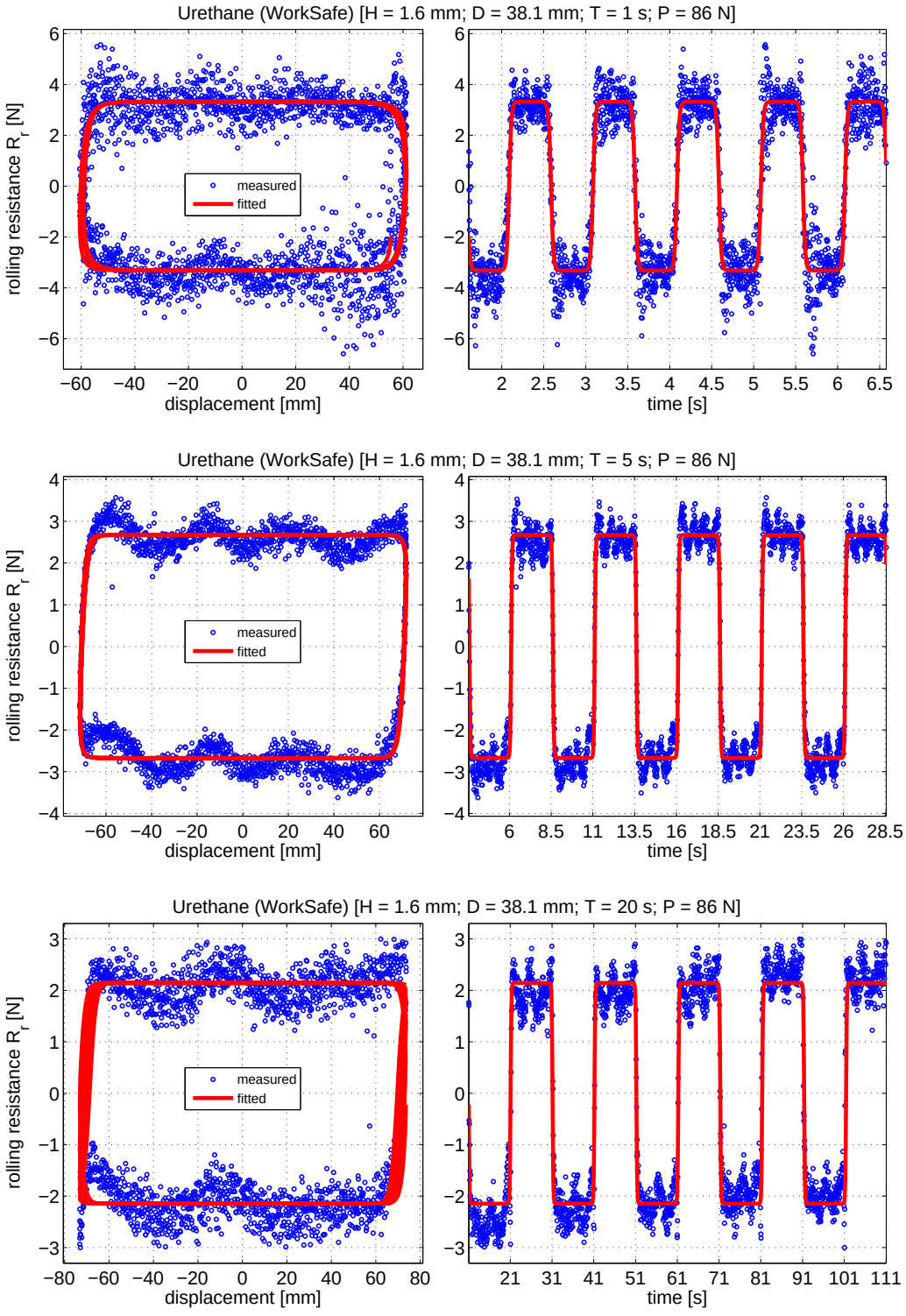

FIGURE 8.3: Examples of sigmoidal waves fitted to experimental rolling resistance results on $\mathcal{U}_{1.6}$ sheets under $P = 86$ N, for $T = 1$, 5 and 20 seconds.

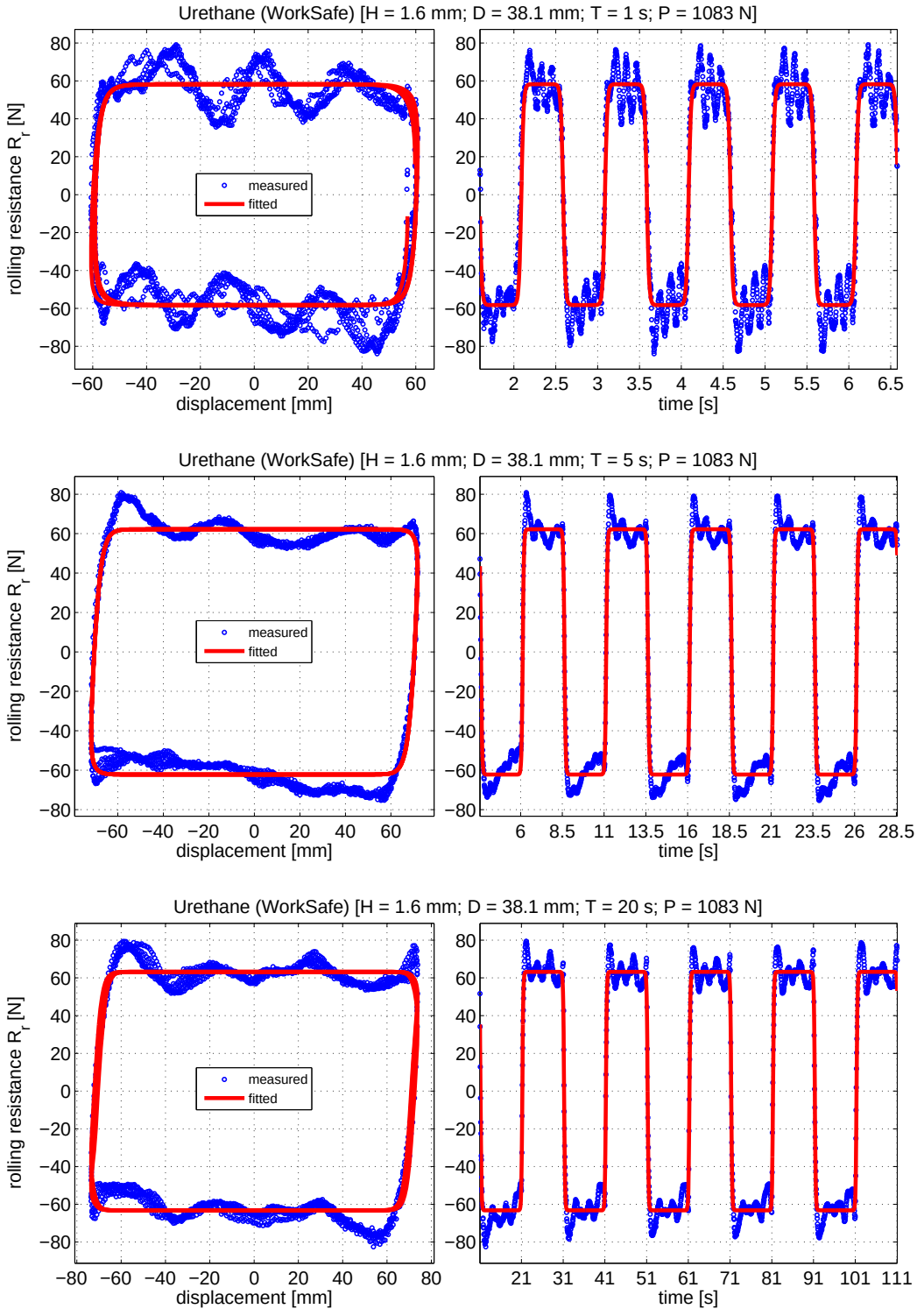

FIGURE 8.4: Examples of sigmoidal waves fitted to experimental rolling resistance results on $\mathcal{U}_{1.6}$ sheets under $P = 1083$ N, for $T = 1$, 5 and 20 seconds.

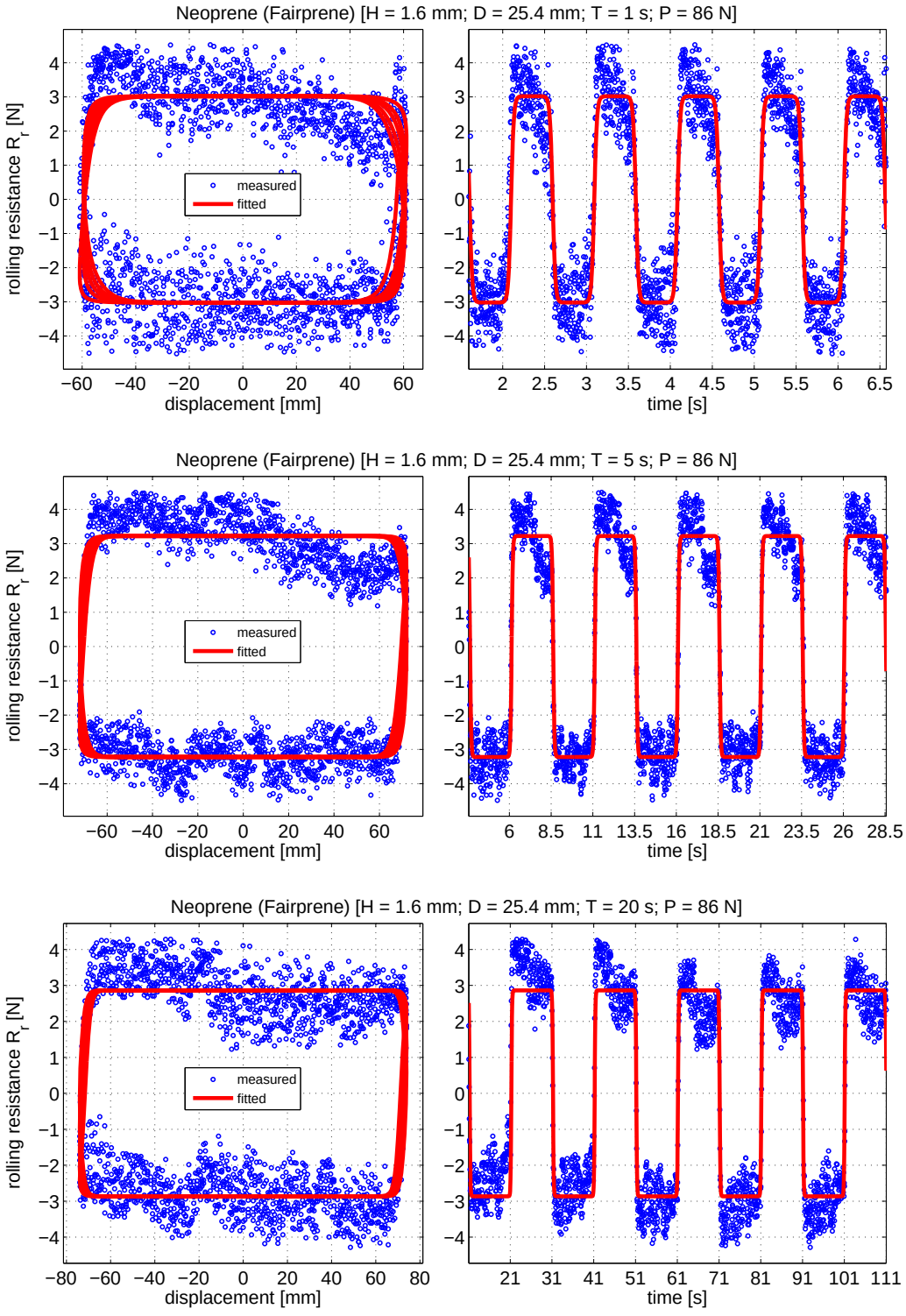

FIGURE 8.5: Examples of sigmoidal waves fitted to experimental rolling resistance results on $\mathcal{N}_{1.6}$ sheets under $P = 86$ N, for $T = 1$, 5 and 20 seconds.

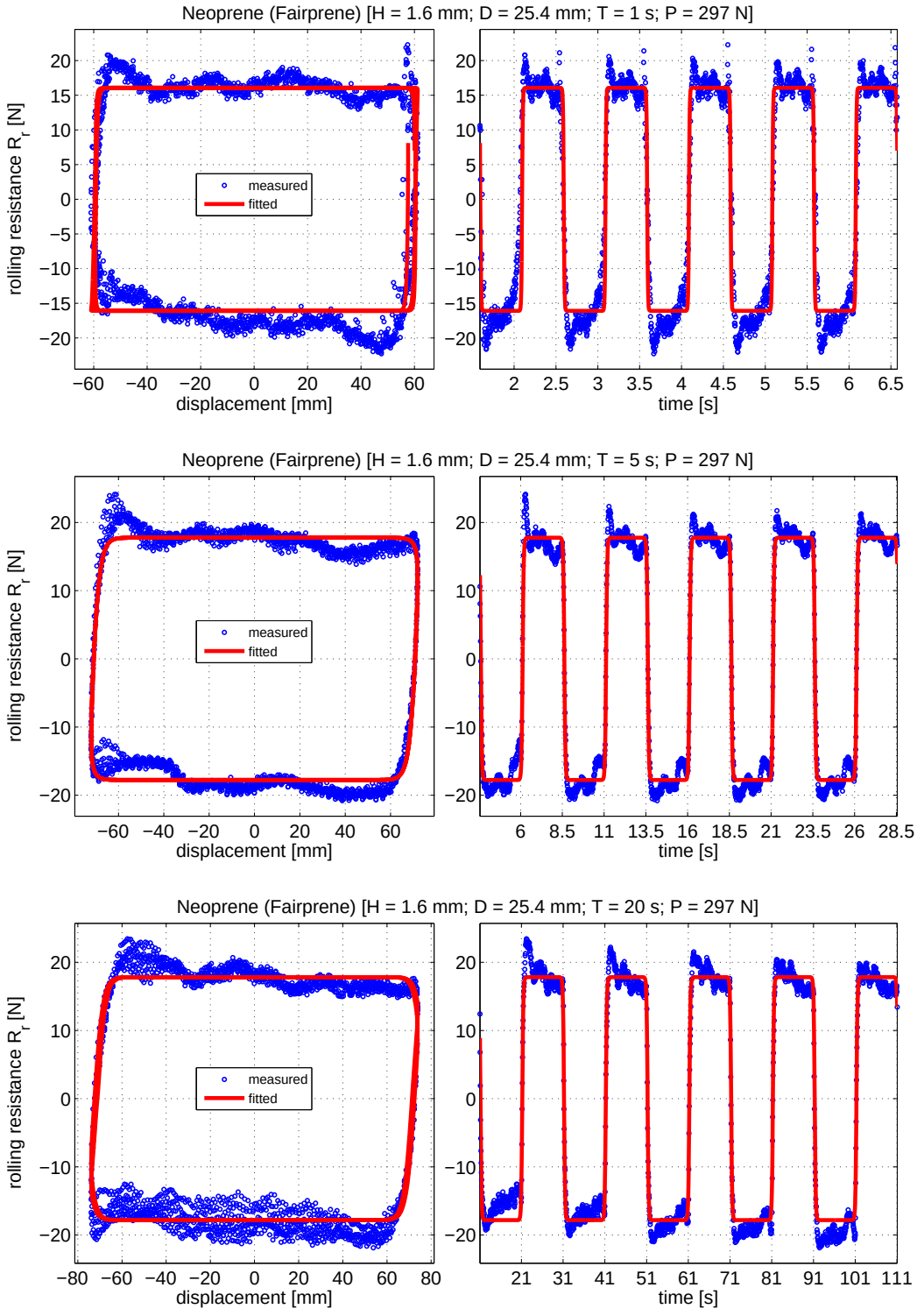

FIGURE 8.6: Examples of sigmoidal waves fitted to experimental rolling resistance results on $\mathcal{N}_{1.6}$ sheets under $P = 297$ N, for $T = 1$, 5 and 20 seconds.

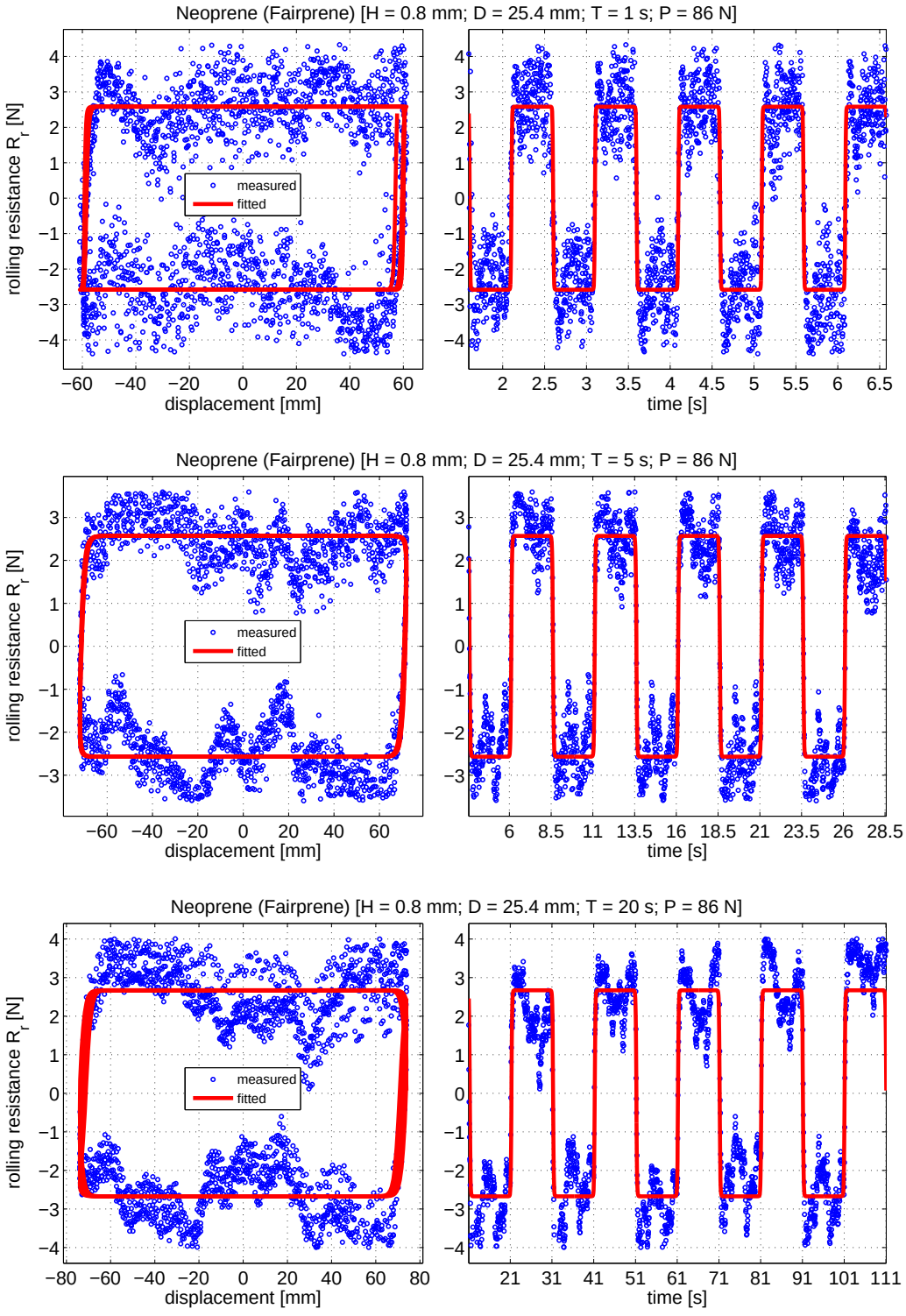

FIGURE 8.7: Examples of sigmoidal waves fitted to experimental rolling resistance results on $\mathcal{N}_{0.8}$ sheets under $P = 86$ N, for $T = 1$, 5 and 20 seconds.

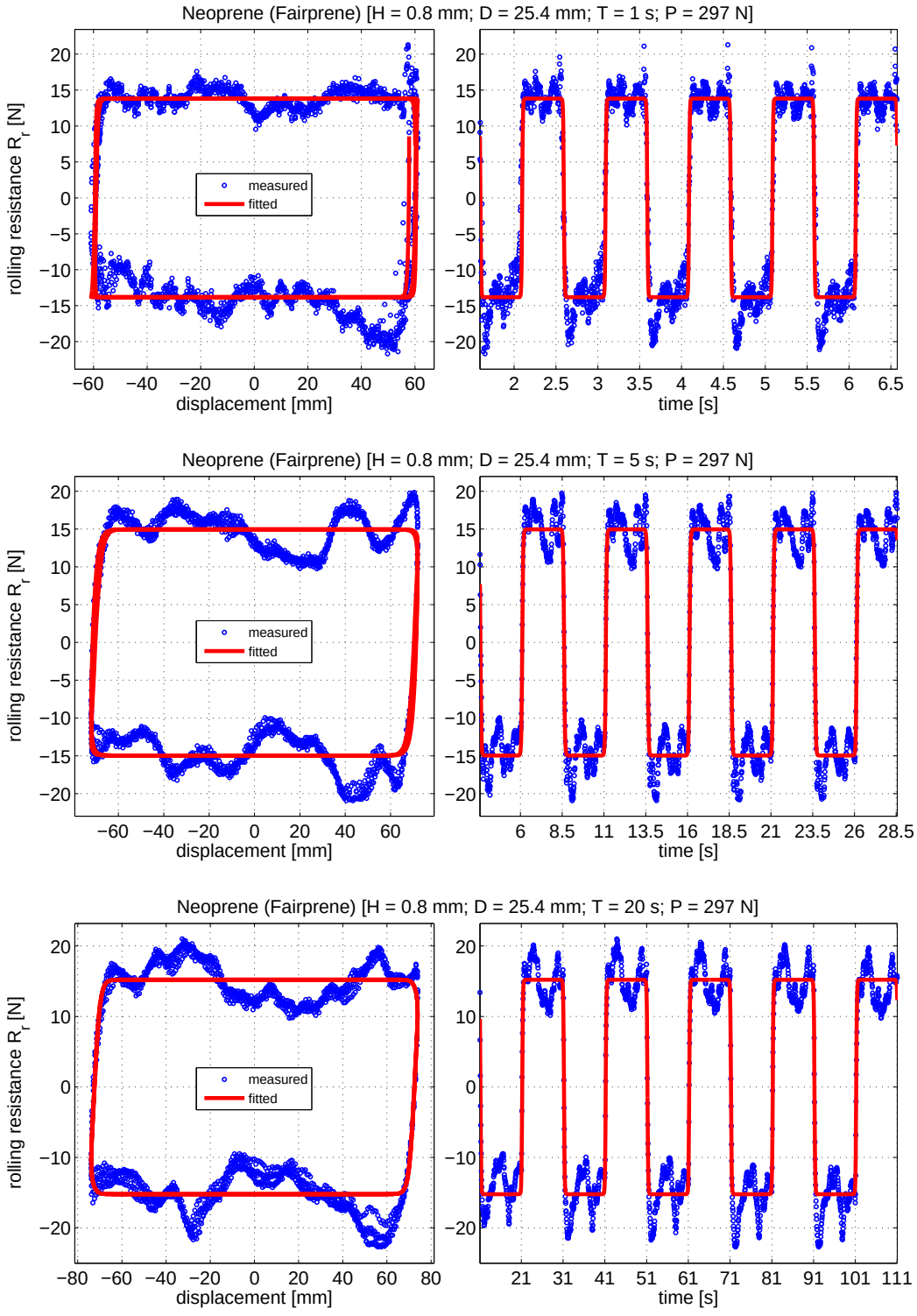

FIGURE 8.8: Examples of sigmoidal waves fitted to experimental rolling resistance results on $\mathcal{N}_{0.8}$ sheets under $P = 297$ N, for $T = 1$, 5 and 20 seconds.

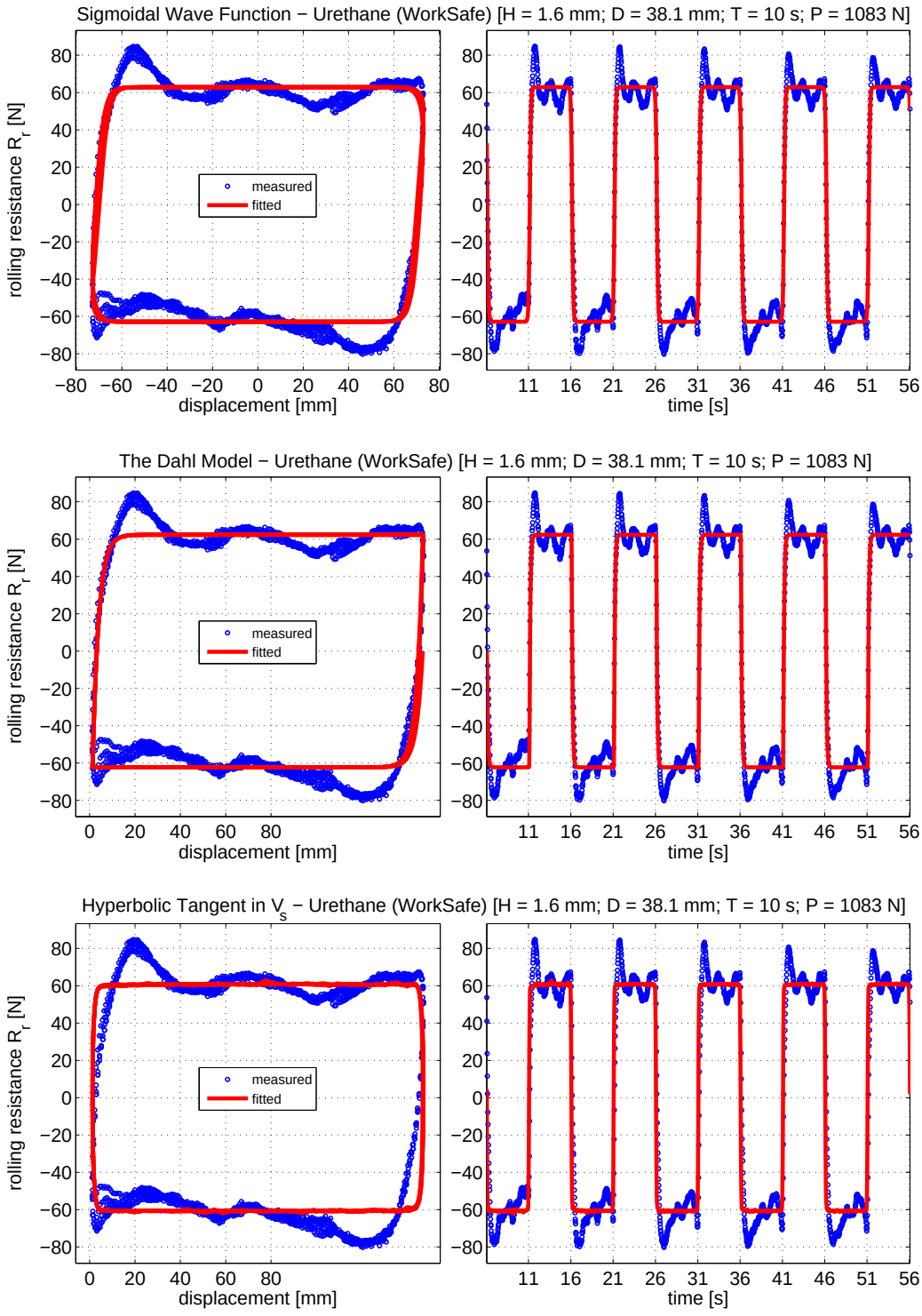

FIGURE 8.9: Comparison between the models given by expressions (8.1), (8.3) and (8.4): all three models agree on the estimate of rolling resistance in steady state.

Figure 8.9 illustrates, for comparison, the performances of the models given by equations (8.1), (8.3) and (8.4) on a typical case corresponding to $\mathcal{U}_{1.6}$ rubber sheets for $T = 10$ s and $P = 1083$ N. Fitting the Dahl model (8.3) requires solving an ordinary differential equation iteratively, and is therefore significantly more computationally expensive than fitting analytical expressions such as (8.1) and (8.4). Expression (8.4) does not capture the transient as well as (8.1) and (8.3). It is however sufficient to determine a good estimate of the rolling resistance in steady-state, which is the quantity of interest all three models agree on, fairly well. It is perhaps interesting to note that, as opposed to the model retained in this study (8.1), the alternative approaches corresponding to expressions (8.3) and (8.4) rely on the measured speed, which is practically obtained by differentiating the measured displacement, and is therefore noisy. These methods hence require some smoothing, which model (8.1) does not.

High-frequency noise

The high-frequency measurement noise is an artifact that is primarily due to the combination of a certain number of electronic effects, in the data acquisition system. In most cases, the signal to noise ratio appears relatively large, despite tentative measures taken to increase the gain on the signal. Nevertheless, the high sampling rate retained generates a large number of data points, resulting in very narrow confidence intervals on the parameters of the sigmoidal wave function fitted to the output signal, and thus, on the rolling resistance. Interval bounds for the coefficients of variation of rolling resistance (equation (8.2)) are given in Table 8.2.

Low-frequency noise

The low-frequency changes in rolling resistance, in the intervals of constant rolling speed, are clearly independent from measurement noise. These variations may es-

Table 8.2: Interval bounds for the coefficients of variation of R_r (equation (8.2)).

	$\mathcal{U}_{1.6}$ rubber sheets	$\mathcal{N}_{1.6}$ rubber sheets	$\mathcal{N}_{0.8}$ rubber sheets
Upper bound	0.66%	0.83%	0.93%
Lower bound	0.05%	0.05%	0.08%

sentially be attributed to:

1. mechanical oscillations of components of the experimental apparatus, and

2. surface imperfections or material inhomogeneities.

Oscillations of the setup: The upper components of the setup oscillate vertically, most likely in bending, since no significant vertical accelerations are detected by the accelerometer on top of the angle plate. These oscillations occur, at the same frequency as the prescribed motion, as the position of the viscoelastic support constituted by the rubber in contact with the rolling sphere changes. As illustrated in Figure 8.10, the angle α_2 between the upper steel plate and the horizontal plane modifies the horizontal component of the contact resultant, and therefore the axial force measured by the load cell.

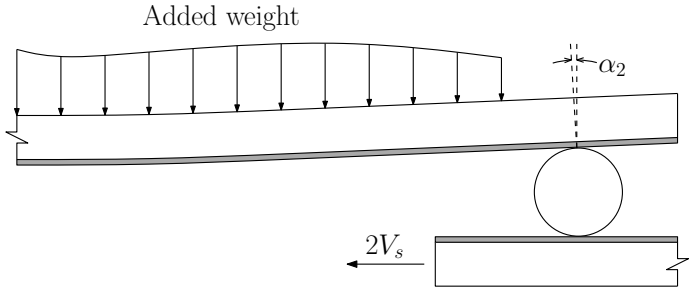

FIGURE 8.10: The sphere rolling between rubber sheets constitutes a viscoelastic 'spring' acting as a shifting support to the upper part of the setup, which bends under the combination of its own weight and the added weight. The angle α_2 between the upper steel plate and the horizontal plane modifies the horizontal component of the contact resultant, and therefore the axial force measured by the load cell.

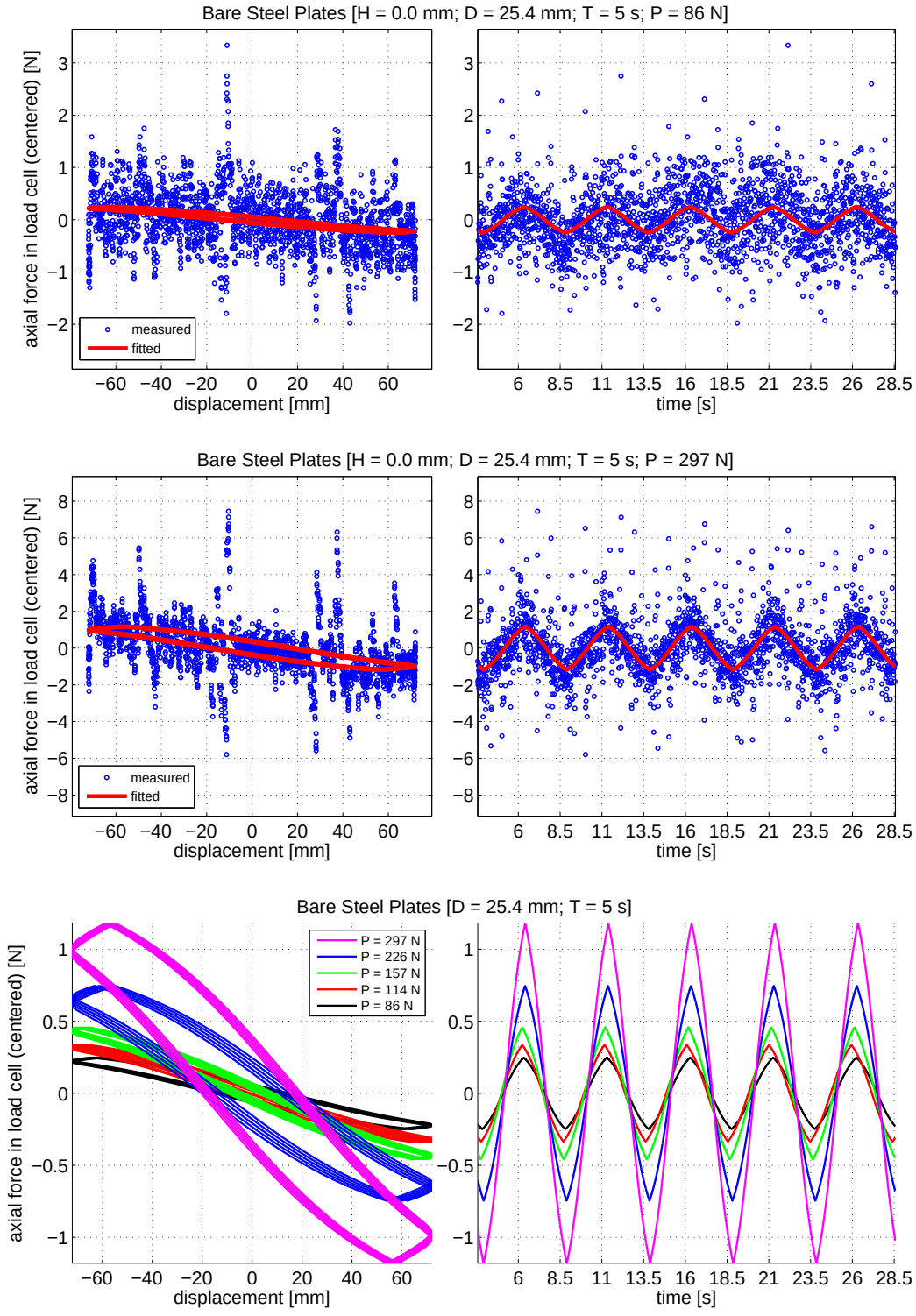

FIGURE 8.11: Sigmoidal wave functions fitted to the axial force in the load cell upon rolling a 25.4 mm steel ball between bare steel plates, at $T = 5$ s, under several P.

This behavior is confirmed by the set of rolling resistance measurements performed on bare steel plates. The top and the middle frames in Figure 8.11 show two examples of sigmoidal wave functions, of the type defined by equation (8.1), fitted to the histories of the axial force in the load cell, as measured upon rolling a 25.4 mm steel ball between bare steel plates, at $T = 5$ s, under $P = 86$ N and $P = 297$ N, respectively. Similar fits are obtained under intermediate values of the weight, i.e. $P = 114$, 157 and 226 N, and all fitted models are plotted on top of each other in the bottom frames of Figure 8.11. The fitted parameters are such that the waves are essentially triangular, presenting no steady-state value, and hence no measurable rolling resistance. In this case, the axial force in the load cell is essentially determined by the position of the ball. Indeed, the force decreases continuously as the sphere rolls away from the free end of the upper plate, and gets closer to the angle plate (see Figure 8.1). During this part of the cycle of motion, the angle α_2 shown in Figure 8.10, which is essentially due to bending, decreases gradually and thus reduces the horizontal component of the sphere's reaction on the upper plate, measured by the load cell. The hysteresis loops in the force-displacement planes of Figure 8.11 are essentially due to the slipping of the ball as the shake table's velocity changes sign: although the shake table has reached its peak displacement and has begun to move in the opposite direction, the force in the load cell keeps on varying monotonically for a short period of time (a fraction of a second), revealing that the ball has not yet started to follow the table's motion.

The peak-amplitude of axial force variations due to low-frequency oscillations of the setup in bending (see Figure 8.11) is designated by $\Delta R_r^{(2)}$. This quantity is plotted against the load P in Figure 8.12. It is well fitted by a cubic polynomial, in the particular case of this experiment. A simple physical model based, for instance, on the bending of a beam clamped at one end and simply supported at the other end, subjected to a uniformly distributed weight, would have resulted in a quadratic

dependence of $\Delta R_r^{(2)}$ on P, as well as on the span of the beam. The apparent deviation of $\Delta R_r^{(2)}(P)$ from such model may be attributed to the fact that the set of weights used to load the upper plate do not have similar distributions. The rightmost position of the ball (see Figures 8.1 8.2 8.10) may also have shifted between tests due to the slipping phenomenon noted above. Figure 8.12 reveals that the absolute error on the axial force measured by the load cell due to oscillations in bending of the experimental setup varies roughly between 0.3% and 0.4% of P, as P increases from 86 N to 297 N. Extrapolating, for what it is worth, to $P = 1083$ N, which is the heaviest weight used in the tests conducted on the $\mathcal{U}_{1.6}$ sheets, yields $\Delta R_r^{(2)}/P \approx 3.3\%$. It is important to note that such errors are of the same order of magnitude as the rolling resistance being measured. Indeed, the ratios R_r/P reported in this experiment range approximately from 2.4% to 6.2%.

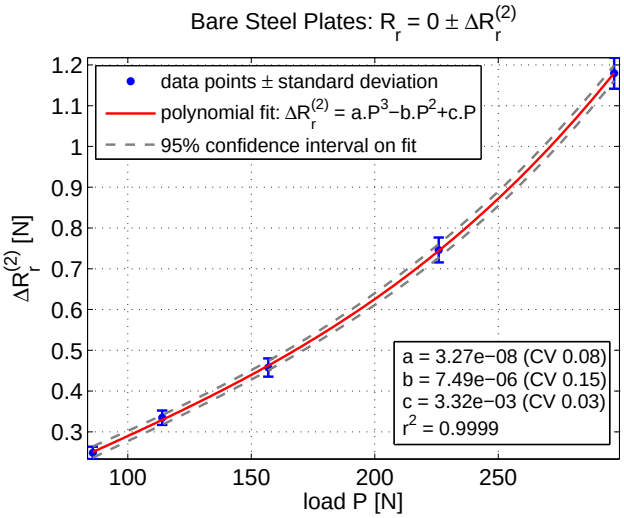

FIGURE 8.12: Dependence on the load P of the peak-amplitude $\Delta R_r^{(2)}$ of variations in rolling resistance measured between bare steel plates, under a triangular displacement history of period $T = 5$ s.

Surface imperfections and material inhomogeneities: The observed low-frequency variations in R_r occurring at a higher rate than that of the prescribed motion may be

due to the influence on surface flatness of an uneven distribution of the bonding glue applied between the rubber sheets and the steel plates, of surface irregularities in the steel plates, or to possible material inhomogeneities in the rubber sheets. To illustrate certain aspects of this problem, Figure 8.13 shows a rigid sphere rolling at constant speed V_s on an uneven surface corresponding to a quadratic spline of period $4l$ and peak-to-peak amplitude 2δ. Assuming for simplicity that the contact occurs at a single point, in the absence of slipping and friction, the contact force is normal to the surfaces of the contacting bodies. Because the vertical component of this contact force must balance the applied load P, at all times, its horizontal component, interfering with load cell measurements, follows a triangular wave whose peak-amplitude $\Delta R_r^{(3)}$ is given by

$$\Delta R_r^{(3)} = 2P\frac{\delta}{l}. \tag{8.5}$$

It is interesting to note, from a quantitative point of view, that imperfections in surface flatness corresponding to a ratio δ/l as small as 1% can result in an absolute error on the measured force as large as 2% of the applied load P which, again, is the order of magnitude of rolling resistance itself. A rapid inspection of the rolling resistance measurements shown in Figures 8.3 to 8.8 reveals that l varies roughly between 1 mm and 10 mm. An absolute error on the ratio R_r/P of 2% can hence be generated by a value of δ as small as 10 microns.

8.4.2 Rolling speed

The velocity of the shake table is obtained by using the central difference of its actual displacement history, which amplifies the noise in the measurements. The steady-state rolling speed of the ball is hence estimated following a similar procedure to that described in Section 8.4.1 for rolling resistance:

1. A sigmoidal wave function characterized by four parameters is fit to half of the

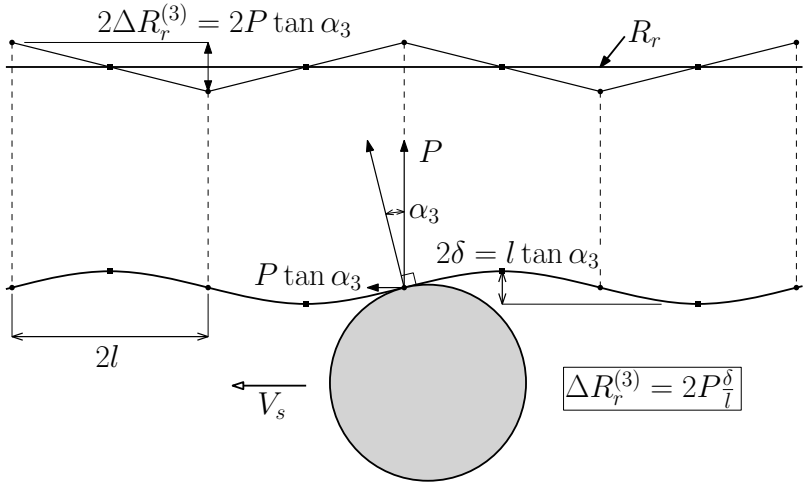

FIGURE 8.13: Sphere rolling on an uneven surface: the horizontal component of the sphere's reaction interferes with rolling resistance measurements.

table's velocity. The fitted wave function is defined over one period (i.e. for $t \in [u, u + T_s]$) as follows:

$$\hat{V}_s(t) = \begin{cases} -\bar{V}_s \tanh\left(\frac{t-u}{\tau_s}\right) & \text{for} \quad u \leq t < u + \frac{T_s}{4}, \\ +\bar{V}_s \tanh\left(\frac{t-u-\frac{T_s}{2}}{\tau_s}\right) & \text{for} \quad u + \frac{T_s}{4} \leq t < u + \frac{3T_s}{4}, \\ -\bar{V}_s \tanh\left(\frac{t-u-T_s}{\tau_s}\right) & \text{for} \quad u + \frac{3T_s}{4} \leq t \leq u + T_s, \end{cases} \tag{8.6}$$

where T_s is the wave's period, $\bar{V}_s$ is a limit peak-value, u is a time-shift, and τ_s corresponds to a characteristic time.

2. The estimated value of rolling speed, in steady-state, is taken as

$$V_s = \max_{t \in [u, u+T_s]} \hat{V}_s(t). \tag{8.7}$$

Typical examples of sigmoidal wave functions fitted to time histories of rolling speed on $\mathcal{U}_{1.6}$ rubber sheets are shown in figure 8.14, for a selection of periods ($T = 1$, 5 and 20 s) and for the extremal values of the applied load P. The original sets of

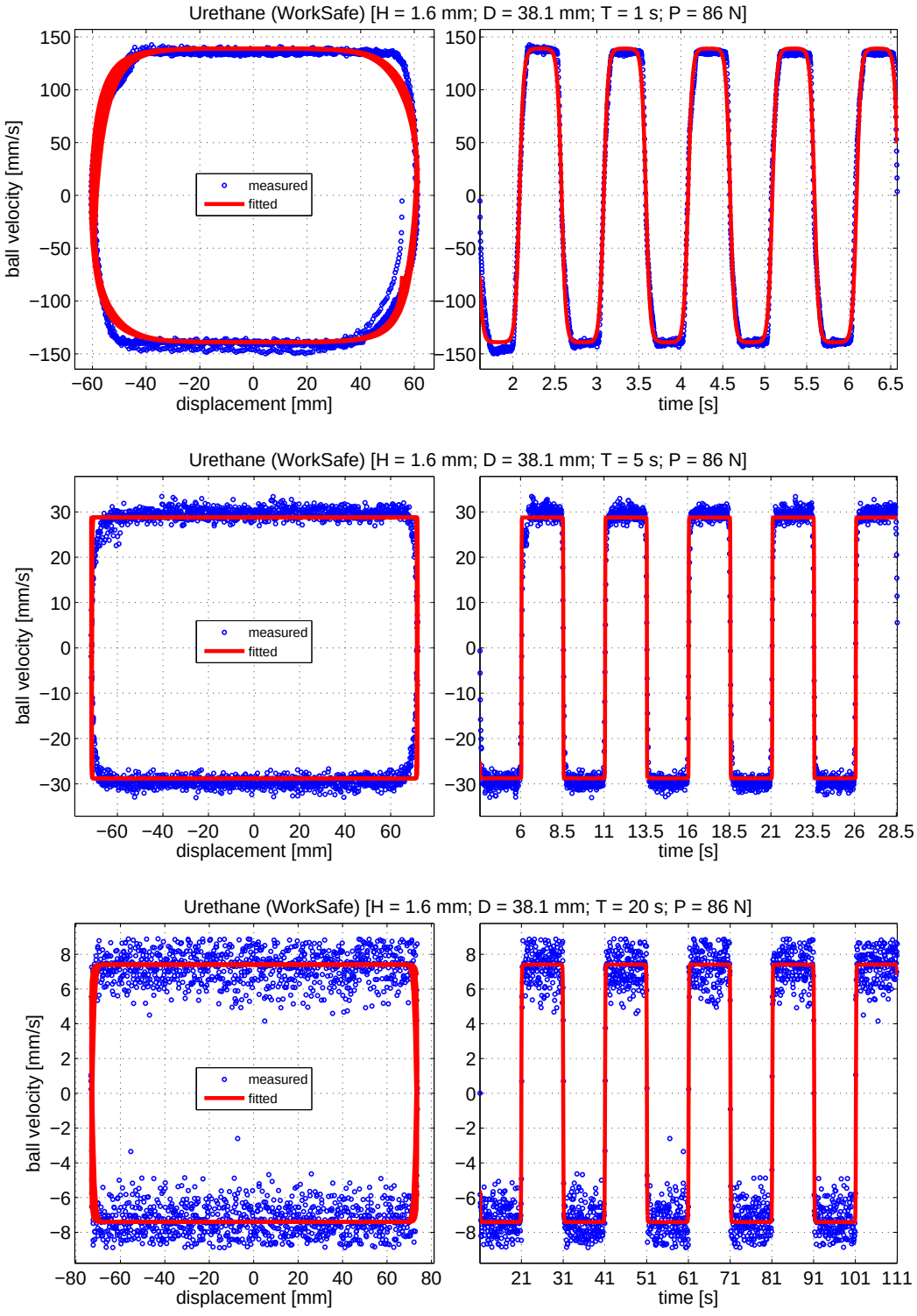

FIGURE 8.14: Examples of sigmoidal waves fitted to experimental rolling speed results on $\mathcal{U}_{1.6}$ sheets under $P = 86$ N, for $T = 1$, 5 and 20 seconds.

data points are downsampled by a factor of T, for plotting purposes only. Despite the significant level of noise appearing in some of the plots, especially those corresponding to $T = 20$ s, the large number of data points, which is due to the high sampling rate retained in the measurements, results in very narrow confidence intervals on the rolling speed. Interval bounds for the coefficients of variation of rolling speed (equation (8.7)) are given in Table 8.3.

Table 8.3: Interval bounds for the coefficients of variation of V_s (equation (8.7)).

	$\mathcal{U}_{1.6}$ rubber sheets	$\mathcal{N}_{1.6}$ rubber sheets	$\mathcal{N}_{0.8}$ rubber sheets
Upper bound	0.22%	0.21%	0.21%
Lower bound	0.04%	0.04%	0.04%

8.5 Summary of experimental results

Experimental rolling resistance results are presented in Figures 8.15, 8.16 and 8.17, for the $\mathcal{U}_{1.6}$, the $\mathcal{N}_{1.6}$ and the the $\mathcal{N}_{0.8}$ rubber sheets, respectively. Rolling resistance is plotted against rolling speed in frames 8.15(a), 8.16(a) and 8.17(a), for the different values taken by the applied load P, in each case. In frames 8.15(b), 8.16(b) and 8.17(b), rolling resistance is plotted, alternatively, against P, for the different values taken by the rolling velocity V_s. Frames 8.15(c), 8.16(c) and 8.17(c) show three-dimensional plots of rolling resistance versus both V_s and P. Over the range of the data, rolling resistance appears to be roughly independent from rolling speed, for the three types of rubber sheets. As shown in frames 8.15(d), 8.16(d) and 8.17(d), the dependence, on the applied load P, of average rolling resistance values over speed, is well fitted by a power law of the form

$$R_r = aP^b. \tag{8.8}$$

It is interesting to note that, in all three cases, the exponent of P (i.e. b) is fairly close to the value of 4/3 suggested by classical theory (see, for instance, equations (1.1)-(1.3)), and that the coefficient of variation on this fitted parameter is less than 2%.

8.6 High Frequency Viscoelastic Spectroscopy

8.6.1 Methods

High Frequency Viscoelastic Spectroscopies (HFVS) were performed on four samples (U1, U2, U3 and U4) of the Urethane rubber provided by WorkSafe Technologies, and four samples (N1, N2, N3 and N4) of the Neoprene rubber provided by Fairprene. The samples were cut from $\mathcal{U}_{1.6}$ and $\mathcal{N}_{1.6}$ rubber sheets, respectively. The experimental procedure was carried out by Rheolution (`http://www.rheolution.com/`) on its RheoSpectris$^{\text{TM}}$C500 instrument.

A horizontal cantilever beam geometry (length 26 mm; height 1.6 mm; width 3.4 mm) was retained by Rheolution to characterize the eight samples of rubber. In this configuration, the instrument applies pulse wave signals at the fixed end of the beam, in the vertical direction, perpendicular to the beam's axis, and measures the displacements generated by the excitation at the free end of the beam. The viscoelastic moduli are determined, at a very small strain amplitude ($\epsilon_{max} \ll 1\%$), over the range of frequencies between 10 Hz and 1000 Hz, at temperatures increasing from room temperature, by steps of 10 °C, up to 150 °C.

Average test results over the four samples of each rubber are presented in Figure 8.18: the storage modulus $E'(f)$ and the loss modulus $E''(f)$ of Urethane and Neoprene are plotted against frequency, at the various temperatures T = 20, 30, ..., 150 °C. As expected, the storage moduli increase with frequency and decrease with rising temperature. Furthermore, since both materials undergo a transition to a glassy state at a temperature below the range considered in the tests, the loss moduli

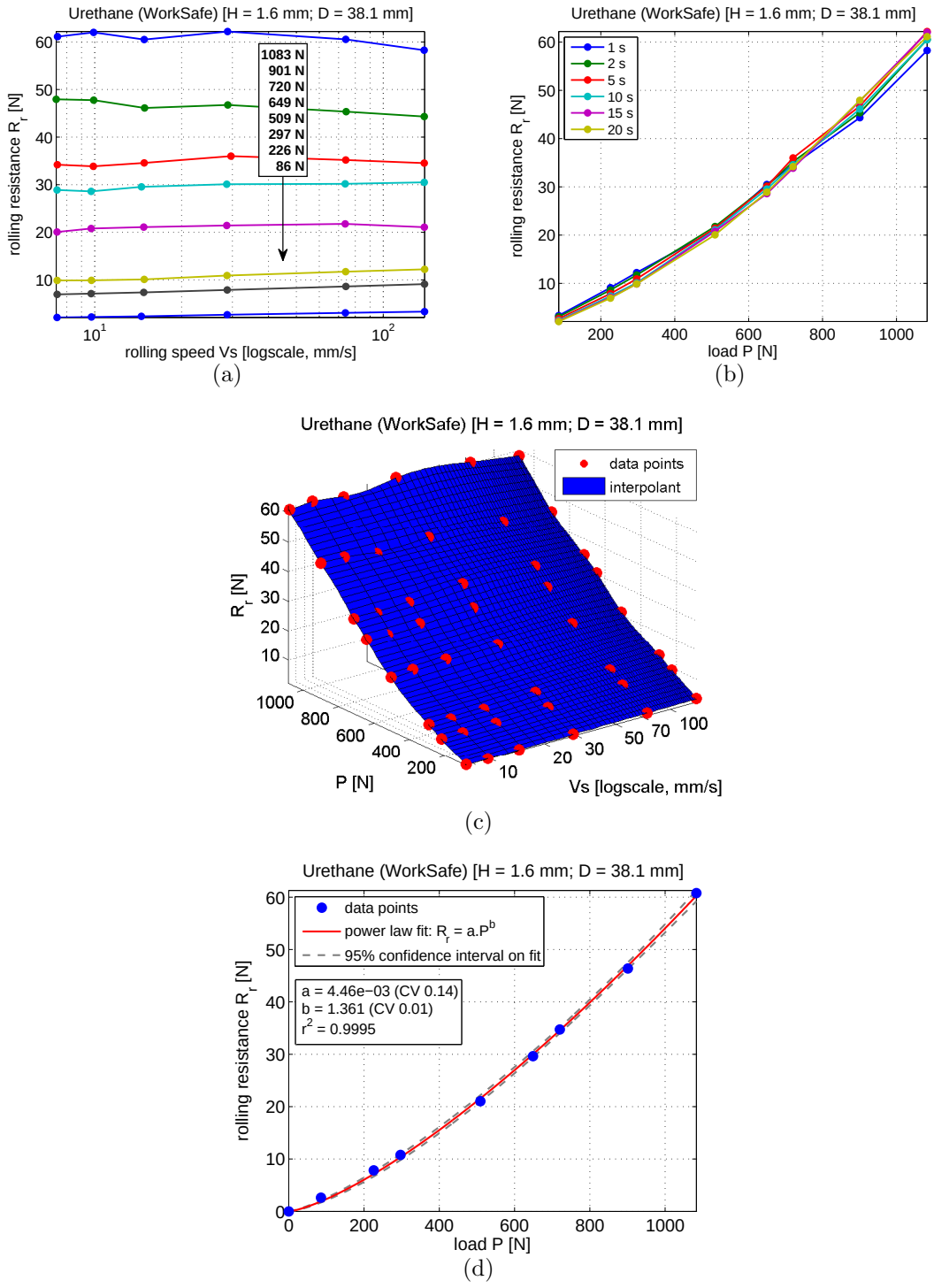

FIGURE 8.15: Experimental rolling resistance results for the $\mathcal{U}_{1.6}$ rubber sheets: (a) versus rolling speed, (b) versus load, and (c) versus both V_s and P. The dependence of R_r on P is well fitted by a power law (d).

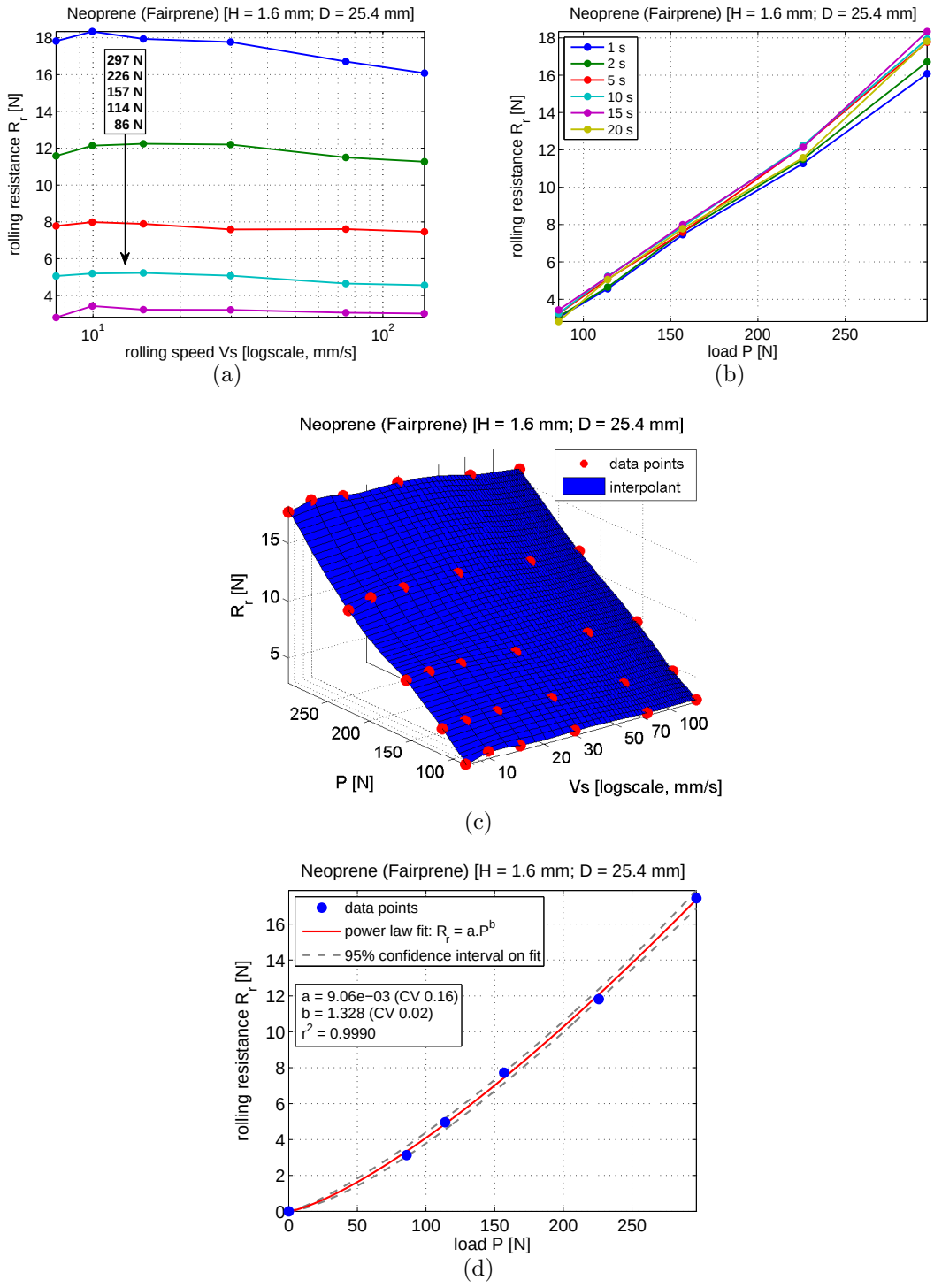

FIGURE 8.16: Experimental rolling resistance results for the $\mathcal{N}_{1.6}$ rubber sheets: (a) versus rolling speed, (b) versus load, and (c) versus both V_s and P. The dependence of R_r on P is fitted fairly by a power law (d).

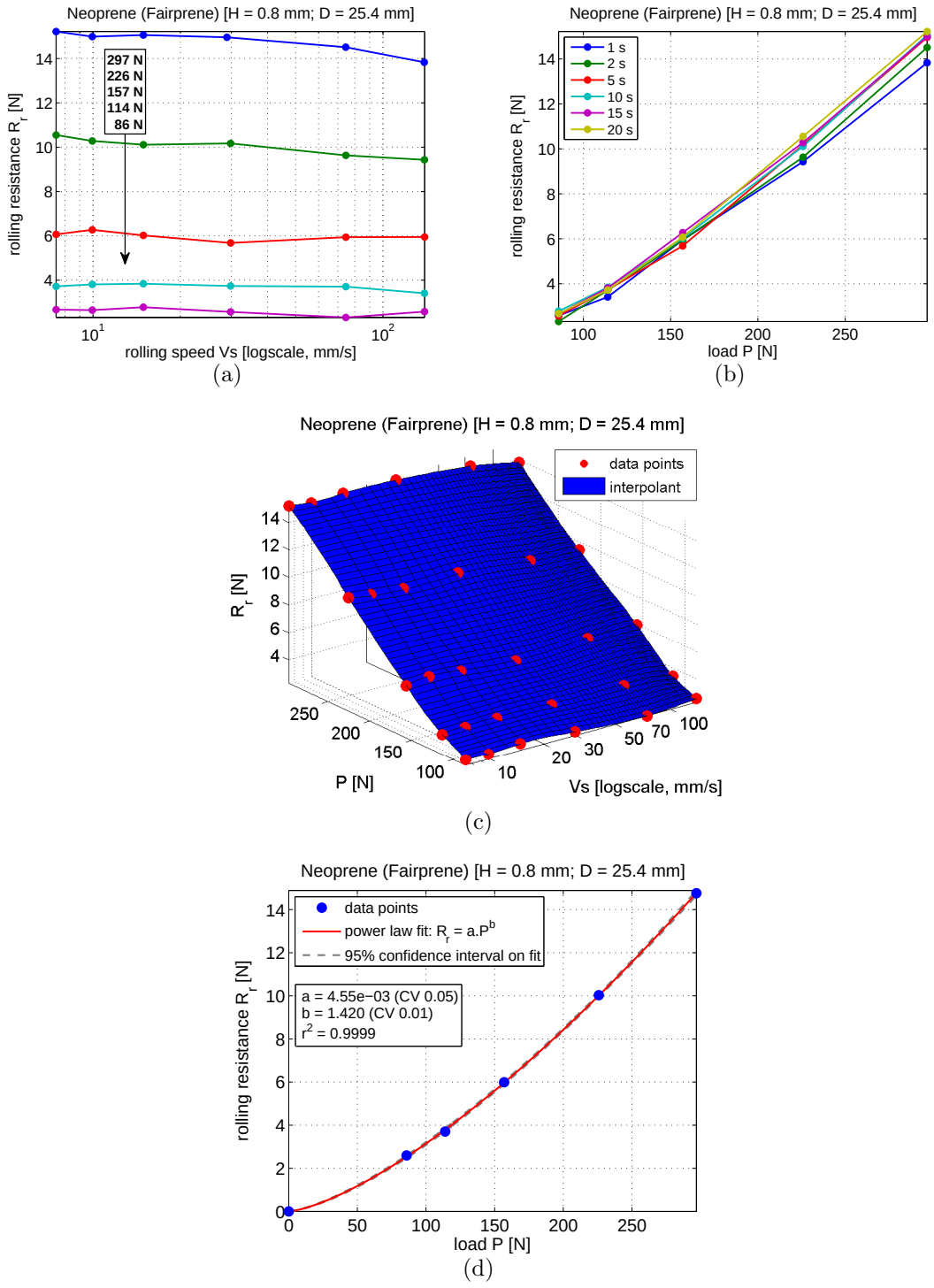

FIGURE 8.17: Experimental rolling resistance results for the $\mathcal{N}_{0.8}$ rubber sheets: (a) versus rolling speed, (b) versus load, and (c) versus both V_s and P. The dependence of R_r on P is well fitted by a power law (d).

also increase with frequency and decrease with heat.

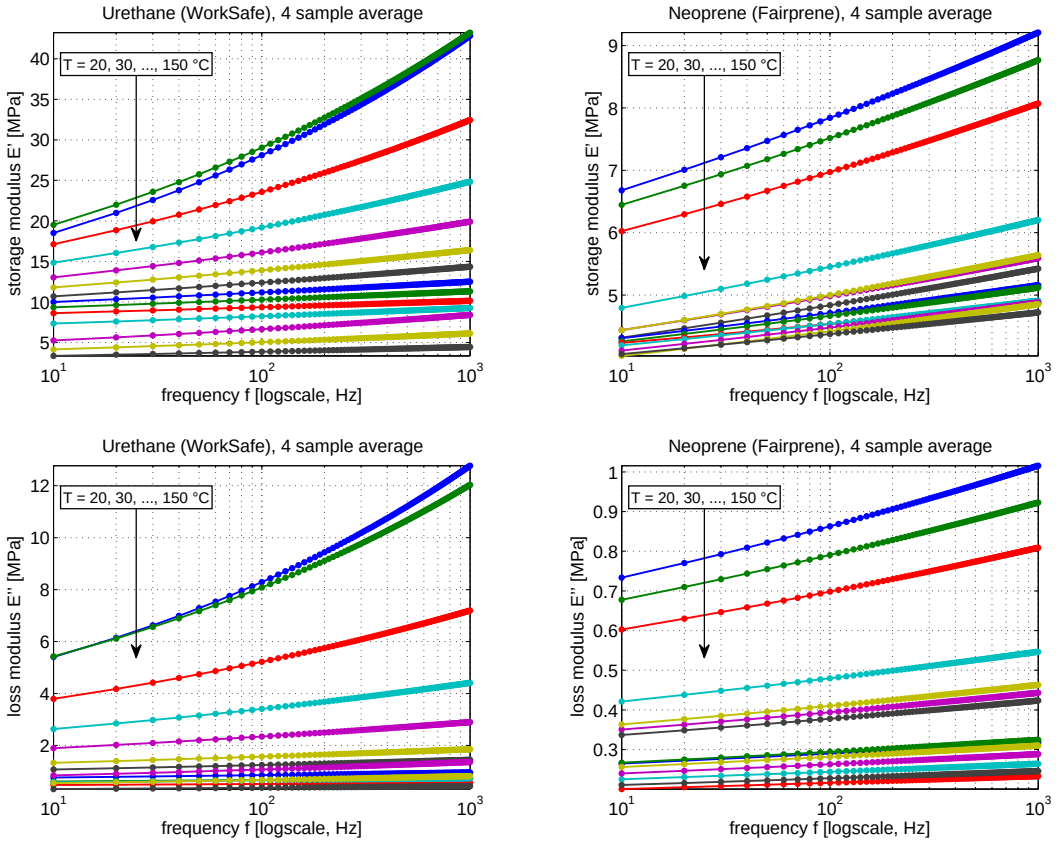

FIGURE 8.18: Average HFVS data for four samples (U1,U2,U3,U4) of Urethane rubber (left) and four samples (N1,N2,N3,N4) Neoprene rubber (right).

8.6.2 The time-temperature superposition principle

The relaxation modulus $E(t, T)$ of a viscoelastic material can be seen as a function of both time t and temperature T. When all the transformation processes contributing to viscoelasticity are equally affected by heat, the relaxation modulus satisfies the so-called *time-temperature superposition principle* (TTS), which can be expressed by a relation of the form (e.g. Lakes, 2009):

$$E(t, T) = E(t_r, T_r), \tag{8.9}$$

where T_r is a temperature of reference and t_r is the corresponding *reduced time*. Viscoelastic materials obeying equation (8.9) are said to be *thermo-rheoligically simple*. For instance, at a temperature T greater than T_r, the relaxation of such a material is accelerated such that $t < t_r$. The ratio $a_T = t/t_r$ is called the *shift factor*.

When studying the dynamic behavior of a viscoelastic material, the time temperature superposition principle may be expressed in the frequency domain, in terms of the complex modulus $E^*(f, T)$, by taking the Fourier transform of equation (8.9) and multiplying both sides by $i\omega$, which yields

$$E^*(f, T) = E^*(f_r, T_r), \tag{8.10}$$

where f_r is the *reduced frequency*. In this case, the shift factor corresponds to $a_T = f_r/f$.

According to equations (8.9) and (8.10), the long-term or low-frequency response of thermo-rhelogically simple viscoelastic materials can be determined by studying their behavior on a shorter term, or at higher frequencies, when subjected to higher temperatures, and vice versa. Such materials can hence be characterized, at a given temperature of reference T_r, over a long period of time, or a wide frequency range, by shifting horizontally, along the abscissa, curve segments $E(t, T)$, or $E^*(f, T)$, obtained at different temperatures T. The full curves constructed by joining such shifted and coinciding segments are called the viscoelastic *master-curves*.

It is interesting to note that, although thermo-rheological simplicity, i.e. the compliance of a given material with equations (8.9) and (8.10), is a sufficient condition for curve segments obtained at different temperatures to coincide upon shifting, it is not a necessary one, meaning that the ability to form a master-curve by the shifting of curve segments does not necessarily imply a thermo-rhelogically simple behavior.

The Arrhenius law

At a fixed temperature of reference T_r and pressure, the shift factor $a_T(T)$ of a given material, is function of the temperature T. For many materials, in certain ranges of temperature, mainly above a characteristic temperature where weak molecular interactions result in exponentially fast responses (e.g. Roland, 2011), $a_T(T)$ tends to follow the expression below resulting from the Arrhenius law

$$\ln\left(a_T\right) = \frac{E_a}{R}\left(\frac{1}{T} - \frac{1}{T_r}\right), \tag{8.11}$$

where E_a is the *activation energy* and the *universal gas constant* is given by $R = 8.3144621$ J/mol/K.

The WLF equation

For many polymers, roughly between the glass transition temperature T_g and $T_g + 100\,^{\circ}\mathrm{C}$ (Sullivan, 1990; Williams et al., 1955), the shift factor $a_T(T)$ tends to follow the WLF equation proposed by Williams, Landell, and Ferry

$$\log_{10}\left(a_T\right) = \frac{-C_1\left(T - T_r\right)}{C_2 + \left(T - T_r\right)}, \tag{8.12}$$

where C_1 and C_2 practically serve as empirical fitting parameters. Equation (8.12) is based on the assumption that molecular velocities are governed by the amount of free space in the material, and that this available volume increases linearly with temperature (e.g. Roland, 2011).

8.6.3 Construction of master-curves

For each sample of Urethane rubber (U1,U2,U3 and U4), and Neoprene rubber (N1,N2,N3 and N4), on which high frequency viscoelastic spectroscopies are performed, the experimental curves $E'(f)$ and $E''(f)$, obtained at different tempera-

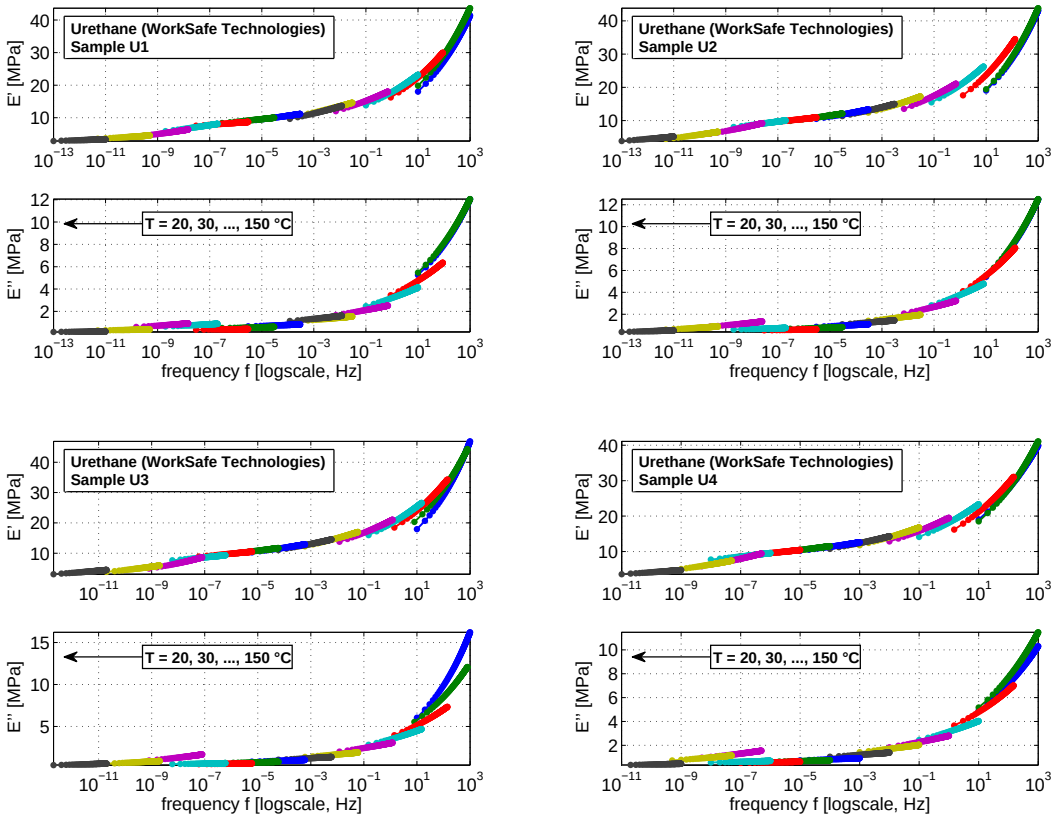

FIGURE 8.19: Shifted HFVS master-curves for the four samples of Urethane.

tures, are shifted horizontally[1], along the frequency axis, in an attempt to construct master-curves, at $T_r = 20\,^{\circ}\mathrm{C}$, extending over several decades of frequency. The resulting master-curves are shown in Figure 8.19, for the Urethane rubber samples, and in Figure 8.20, for the samples of Neoprene rubber. It is interesting to note that, for both types of rubber samples, not all shifted curve segments coincide perfectly. Curve segments corresponding to temperatures above roughly $120\,^{\circ}\mathrm{C}$ in the case of Urethane, and $80\,^{\circ}\mathrm{C}$ in the case of Neoprene, are less congruent to others. Furthermore, the master-curves corresponding to the Urethane rubber samples appear to present more global 'structure' than those constructed from the Neoprene rubber samples. Based on these observations, it is possible to conclude that the

[1] The same shift factor must be applied to both moduli.

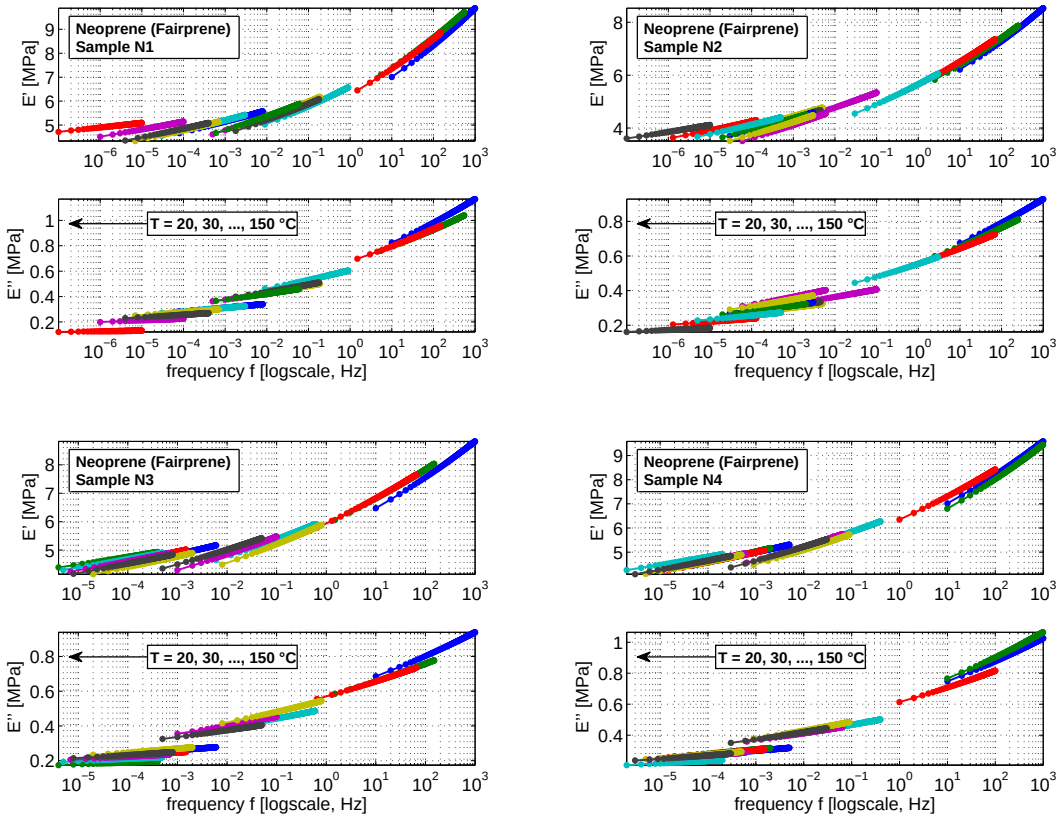

FIGURE 8.20: Shifted HFVS master-curves for the four samples of Neoprene.

time-temperature superposition principle does not apply between room temperature and temperatures above 120 °C for the Urethane rubber, and 80 °C for the Neoprene rubber. It should however be stressed that, as previously noted in Section 8.6.2, the ability to construct master-curves with an acceptable level of 'structure' from curve segments obtained in certain ranges of temperature does not necessarily warrant a thermo-rheologically simple behavior within those ranges.

The shift factors $a_T(T) = f_r/f$ resulting from the constructions of the master-curves shown in Figures 8.19 and 8.20, for each sample of rubber, are plotted against temperature in Figure 8.21. The Arrhenius law is fitted to the shift factors in the upper two frames. The poorness of the Arrhenius fits reveals that both tested materials

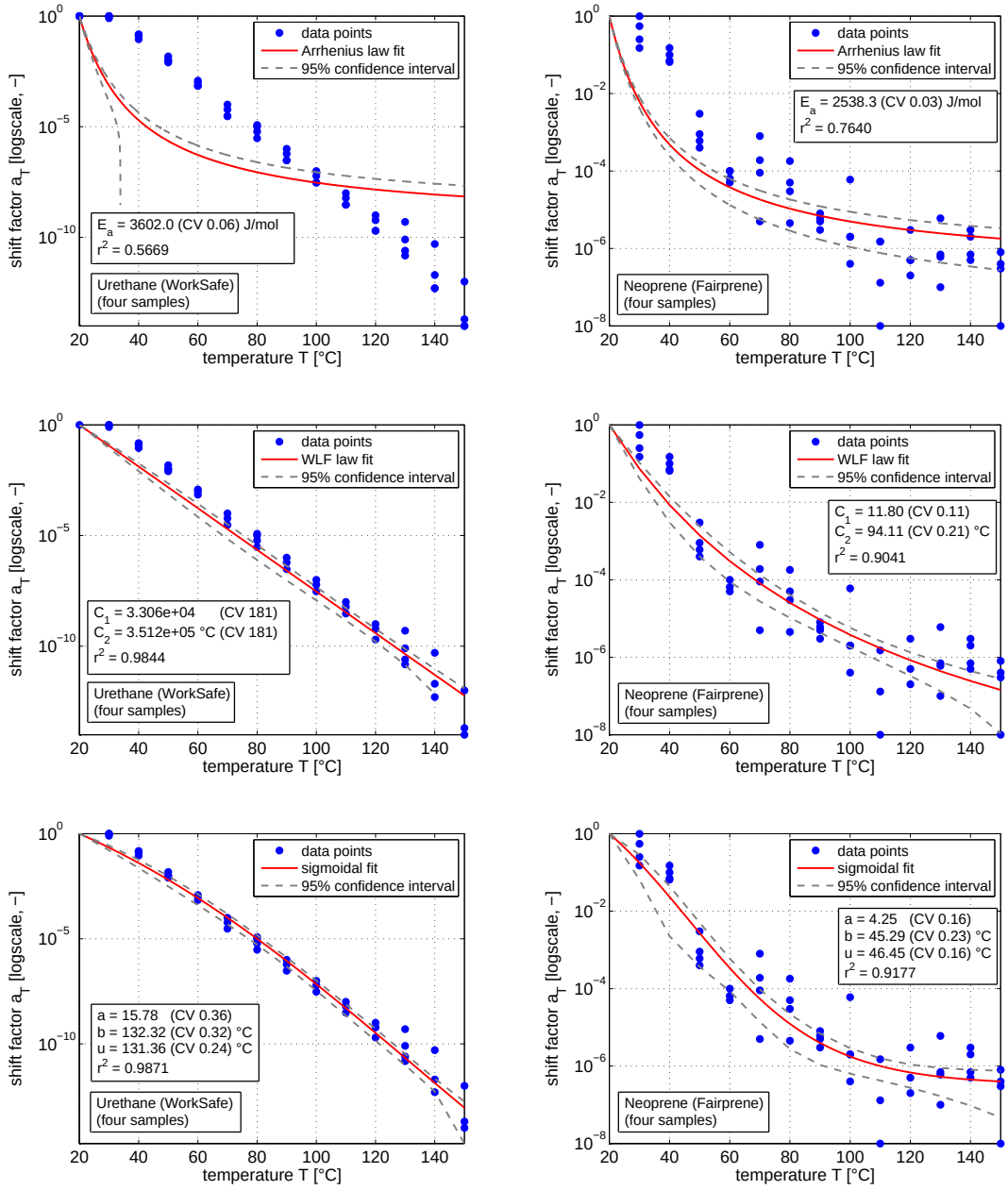

FIGURE 8.21: Tentative fits of the Arrhenius law (top), of the WLF equation (middle), and of a sigmoidal function (bottom), to the shift factors determined from the four samples of Urethane (left) and the four samples of Neoprene (right). The Arrhenius fits are poor. The sigmoidal function best fits the data; however, it may not be worth the additional parameter, in comparison to the WLF equation.

present a non-Arrhenius behavior in the range of temperatures under consideration. Alternatively, the WLF equation is fitted to the shift factors in the middle two frames of Figure 8.21: the goodness of the WLF fits is clearly better than that of the Arrhenius law. The general features of polymer behavior, briefly noted in Section 8.6.2, with respect to the TTS principle, are hence confirmed. It is also interesting to note that the WLF equation fits the shift factor of the Urethane rubber slightly better than that of the Neoprene rubber. This is consistent with the fact that the master-curves of the former (see 8.19) appear to have somewhat more 'structure' than those of the latter (see Figure 8.20). In the bottom two frames of Figure 8.21, an attempt is made to improve the model for the shift factors, on phenomenological grounds, by fitting a sigmoidal function of the form

$$\log_{10}(a_T) = a\left(\tanh\left(\frac{T_r - u}{b}\right) - \tanh\left(\frac{T - u}{b}\right)\right), \tag{8.13}$$

where a, b, and u are three empirical fitting parameters. The model given by equation (8.13) fits the shift factors of Neoprene and Urethane slightly better than the WLF equation. The level of improvement seems however not to be worth the additional parameter.

8.6.4 Fitting of the HFVS data

Linear viscoelastic models, in the form of Prony series (equations (8.14)), are fitted to the shifted HFVS master-curves constructed in Section 8.6.3, for the four samples (U1,U2,U3 and U4) of the Urethane rubber, and the four samples (N1,N2,N3 and N4) of the Neoprene rubber

$$E'(\omega) = E_o\left(g_\infty + \sum_{k=1}^{n} \frac{g_k \omega^2 \tau_k^2}{1 + \omega^2 \tau_k^2}\right) \qquad \text{(storage modulus)}, \tag{8.14a}$$

$$E''(\omega) = E_o \sum_{k=1}^{n} \frac{g_k \omega \tau_k}{1 + \omega^2 \tau_k^2} \qquad \text{(loss modulus)}, \tag{8.14b}$$

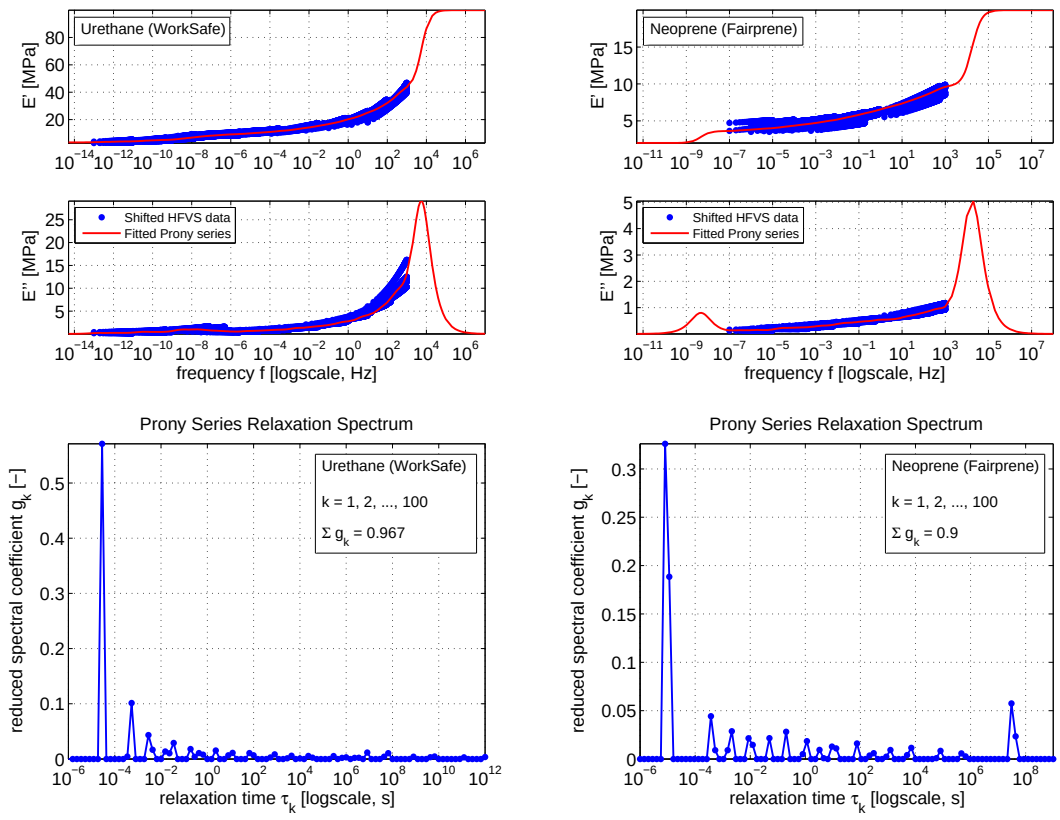

FIGURE 8.22: Prony series fitted to the shifted HFVS moduli (top) and corresponding relaxation spectra (bottom) for the four samples of Urethane (left) and Neoprene (right).

where $\omega = 2\pi f$ is the angular frequency, the material parameters τ_k correspond to internal relaxation times, and the associated 'weights', or *reduced spectral coefficients*, g_k satisfy

$$g_\infty + \sum_{k=1}^{n} g_k = 1. \tag{8.15}$$

The fitted models, comprising (initially) 100 relaxation times each, are shown in the upper frames of Figure 8.22, superimposed to the shifted data: clearly, the models fit the data fairly well. The Prony series relaxation spectra (i.e. g_k versus τ_k) are shown in the bottom two frames of Figure 8.22. These plots reveal that, out of the

100 terms retained initially in the series, less than 30 are necessary to replicate most of the observed behavior.

8.7 Dynamic Mechanical Analysis

8.7.1 The Payne effect

High frequency viscoelastic spectroscopy characterizes the dynamic behavior of viscoelastic materials in the linear range, in particular, at very small strain amplitudes: these are typically well below 1%. In many static and dynamic applications however, rubber-like materials incur fairly large deformations and do not behave linearly under the corresponding levels of strain. In fact, many elastomers, such as natural rubber filled with carbon black, present material nonlinearities appearing under fairly small deformations. A typical manifestation of such nonlinearities is the *Payne effect* (Payne, 1962), also known as the *Fletcher-Gent effect* (Fletcher and Gent, 1953, 1954). This effect is characterized by the dependence of the dynamic moduli on strain amplitude, often starting at very small (i.e. on the order of 0.1%) or even undetectably small levels of strain. Typically, the storage modulus decreases rapidly from its asymptotic value under vanishing deformations to a lower bound at larger strain amplitudes; the loss modulus presents a peak in that region where the storage modulus decreases.

8.7.2 DMA testing and results

To characterize the dependence of the dynamic moduli on strain amplitude, for the studied materials, Dynamic Mechanical Analyzes (DMA) are performed using the RSA3 micro-strain analyzer, from TA Instruments (`http://www.tainstruments.com/`), available at the Shared Materials Instrumentation Facility (SMIF) at Duke University (`http://smif.lab.duke.edu`). A rectangular sample of the Neoprene rubber mounted on the micro-strain analyzer is shown in Figure 8.23.

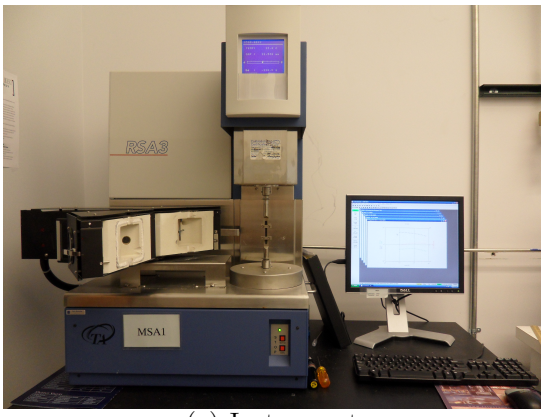

(a) Instrument

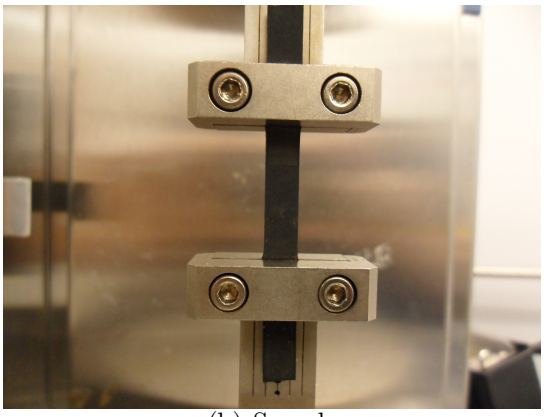
(b) Sample

FIGURE 8.23: Sample of the Urethane rubber mounted on the RSA3 micro-strain analyzer: (a) photo of the instrument, and (b) close-up on the mounted sample. End effects resulting from the clamping of the sample at the fixtures are limited.

Urethane (WorkSafe)

Frequency sweep tests are run, in uniaxial extension, between 0.01 Hz and roughly 15.85 Hz, on a rectangular sample (length 20 mm; width 3.2 mm) cut from a $\mathcal{U}_{1.6}$ rubber sheet. The tests are performed at different strain amplitudes ranging from 0.1% up to 2.0%. To insure that the sample remains in tension throughout the tests, the static force is set to automatically follow the dynamic force, and to exceed this force by 20%.

The experimental results for the storage modulus E', the loss modulus E'', and the loss factor $\tan\delta$ of the Urethane rubber are plotted in Figure 8.24: (i) against frequency, for different values of strain amplitude, in the upper frames, and (ii) against strain amplitude, for different values of frequency, in the lower frames. Three-dimensional plots of E', E'' and $\tan\delta$ against frequency (f) and strain amplitude (ϵ_{max}) are presented in the left frames of Figure 8.26, for the Urethane rubber.

Over the ranges retained for the independent variables, both moduli E' and E'' increase with increasing frequency and decrease with increasing strain amplitude,

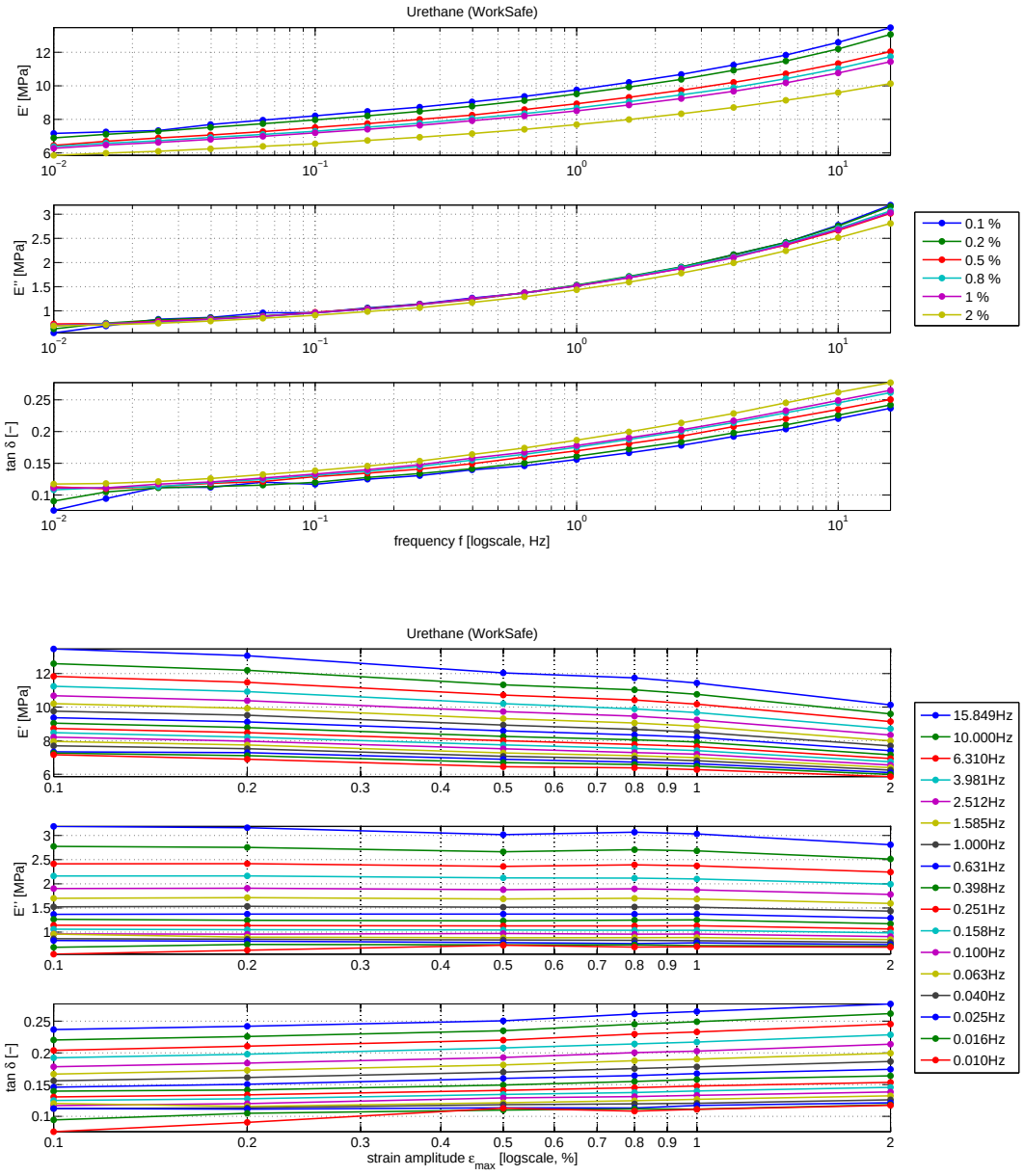

FIGURE 8.24: DMA results for Urethane.

whereas the loss factor increases with increasing frequency and strain amplitude. More energy dissipation is hence to be expected at larger strain amplitudes. Whether E'' presents a peak (at $\epsilon_{max} \approx 0.8\%$), as one would expect for the Payne effect, is rather unclear. It is interesting to note that changes in the quantities of interest, over the limited range of strain amplitudes (i.e. $[0.1\%, 2.0\%]$) these were measured on, are significant: roughly, E', E'' and $\tan\delta$ vary by up to 30%, 35% and 20%, respectively.

Neoprene (Fairprene)

Stain amplitude sweep tests are run, in uniaxial extension, between 0.1% and roughly 6.3%, on a rectangular sample (length 20 mm; width 5.4 mm) cut from a $\mathcal{N}_{1.6}$ rubber sheet. The tests are performed at different frequencies ranging from 0.01 Hz up to 10 Hz. The static force is set to automatically follow and exceed the dynamic force by 10%.

The experimental results for the storage modulus E', the loss modulus E'', and the loss factor $\tan\delta$ of the Neoprene rubber are plotted in Figure 8.25: (i) against frequency, for different values of strain amplitude, in the upper frames, and (ii) against strain amplitude, for different values of frequency, in the lower frames. Three-dimensional plots of E', E'' and $\tan\delta$ against frequency (f) and strain amplitude (ϵ_{max}) are presented in the right frames of Figure 8.26, for the Neoprene rubber.

Over the range of the data, both moduli and the loss factor increase with increasing frequency. Regarding dependencies on strain amplitude, the typical features of the Payne effect, as briefly outlined in Section 8.7.1, are clearly apparent in the behavior of the Neoprene rubber: the storage modulus decreases with increasing strain amplitude whereas the loss modulus shows a peak at roughly $\epsilon_{max} \approx 0.7\%$. The loss factor appears to peak at a strain amplitude increasing with frequency. For the Neoprene rubber, the quantities of interest were measured over a wider range of strain

amplitudes than for the Urethane rubber. Although this range (i.e. $[0.1\%, 6.3\%]$) remains limited, E', E'' and $\tan\delta$ vary roughly by up to 60%, 45% and 35%, respectively.

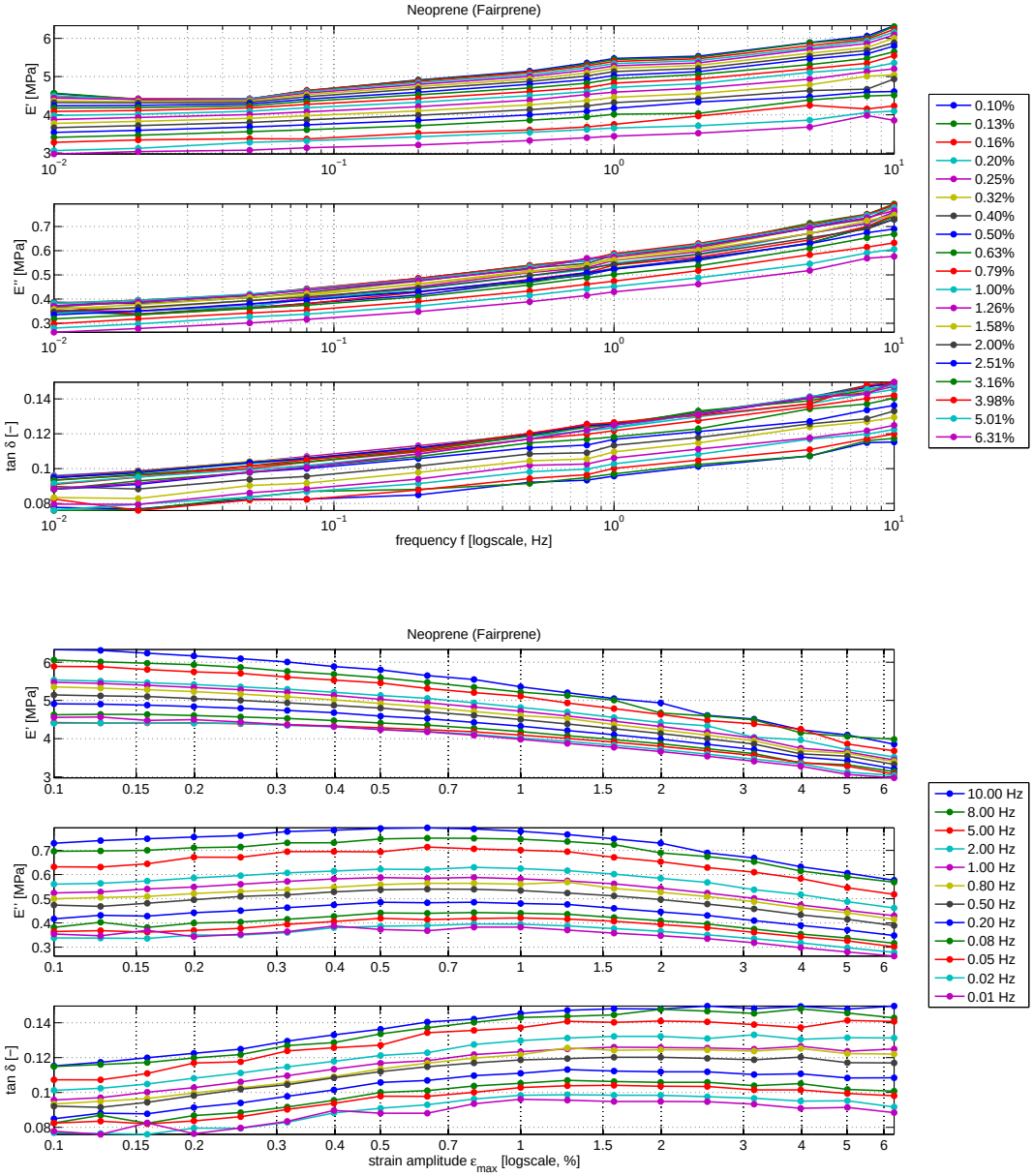

FIGURE 8.25: DMA results for Neoprene.

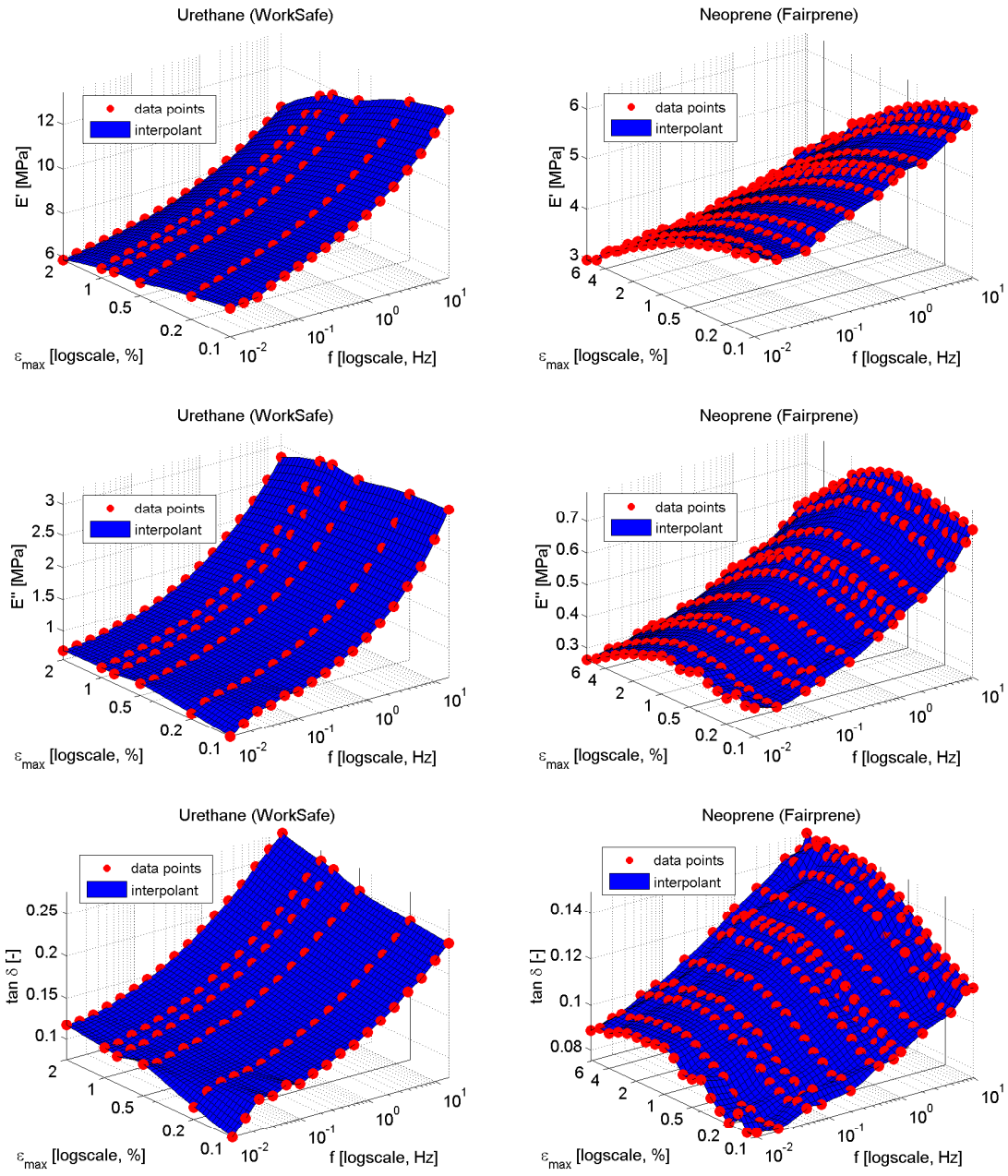

FIGURE 8.26: 3D plots of DMA results for Urethane (left) and Neoprene (right).

8.7.3 The Kraus model

The Payne effect is often modeled using the so-called *Kraus model* (e.g. Lion et al., 2003), which is characterized, at fixed frequency f, and temperature T, by the equations below

$$E'(\bar{\epsilon}, f, T) = E'(\infty, f, T) + \frac{E'(0, f, T) - E'(\infty, f, T)}{1 + \left(\frac{\bar{\epsilon}}{\bar{\epsilon}_c}\right)^{2m}}, \tag{8.16a}$$

$$E''(\bar{\epsilon}, f, T) = E''(\infty, f, T) + \frac{2\left(E''(\bar{\epsilon}_c, f, T) - E''(\infty, f, T)\right)\left(\frac{\bar{\epsilon}}{\bar{\epsilon}_c}\right)^{m}}{1 + \left(\frac{\bar{\epsilon}}{\bar{\epsilon}_c}\right)^{2m}}, \tag{8.16b}$$

where m, $\bar{\epsilon}_c$, $E'(0, f, T)$, $E'(\infty, f, T)$, $E''(\bar{\epsilon}_c, f, T)$ and $E''(\infty, f, T)$ are six empirical fitting parameters, and $\bar{\epsilon} = \epsilon_{max}$ is the strain amplitude.

8.7.4 Attempted extrapolation of DMA measurements to larger strain amplitudes

A shortcoming of the Kraus equations (8.16) is that they only model the marginal dependence of the dynamic moduli on the strain amplitude $\bar{\epsilon}$, i.e. they do not explicitly describe their joint dependence on strain amplitude and frequency. The Kraus model is nevertheless useful to capture the dynamic response of certain materials at constant frequency.

The dynamic moduli of the tested materials are reported in Section 8.7.2 in relatively narrow ranges of strain amplitude. This is due to limitations of the RSA3 micro-strain analyzer available at the SMIF, which is mainly designed to perform viscoelastic spectroscopies of soft materials under small deformations. An attempt is made to extrapolate the data to larger strain amplitudes by fitting the Kraus model to DMA measurements, at fixed frequencies. Figure 8.27 shows typical fits of the Kraus model obtained at four different frequencies for the Urethane rubber (upper frames), and the Neoprene rubber (lower frames). Globally, the model fits the data fairly well, except in a limited number of cases, such as the case corresponding to $f = 10$ Hz

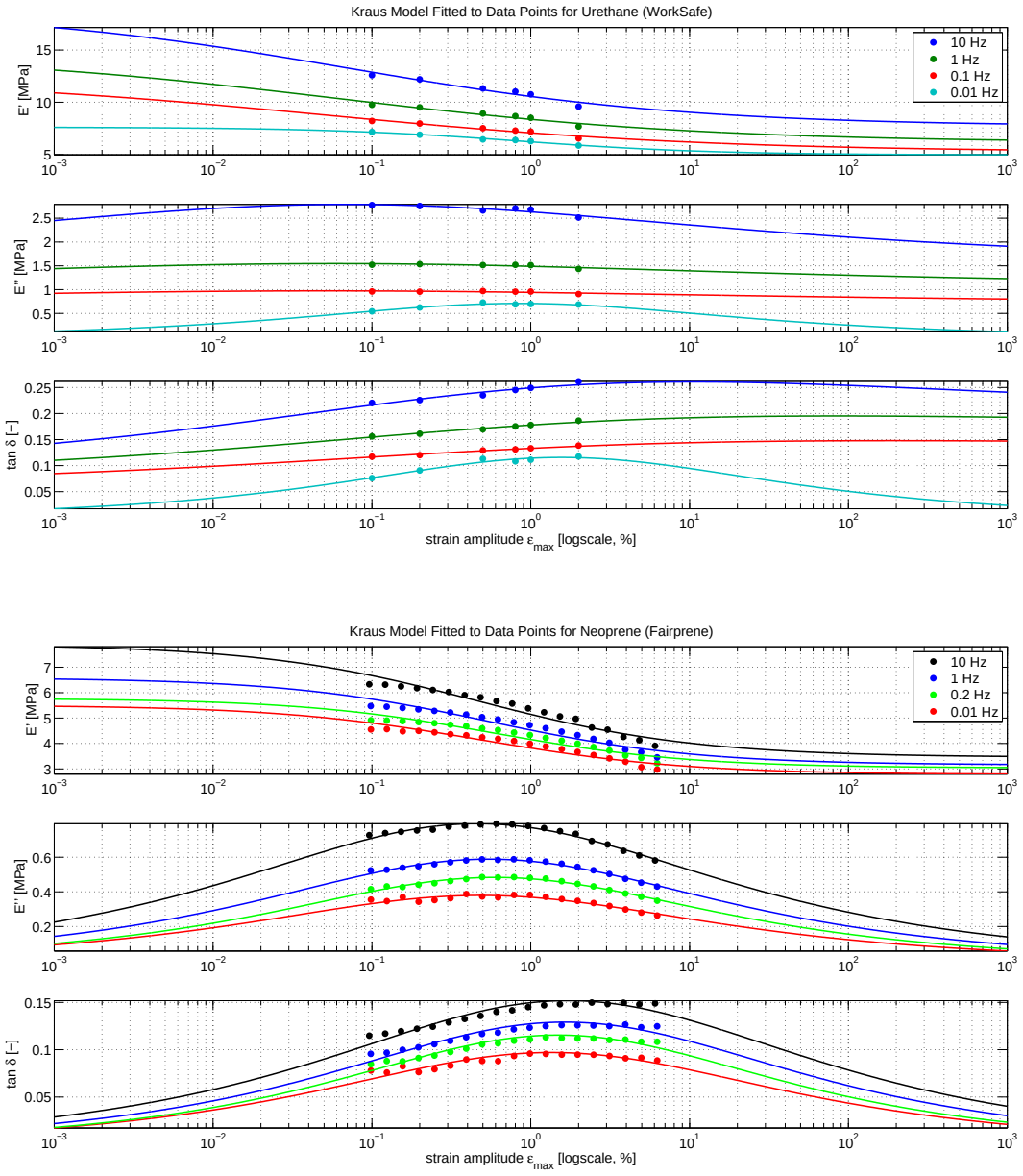

FIGURE 8.27: Kraus model fitted to the DMA data.

for the Neoprene rubber, where the fit appears to be relatively poor. Unfortunately, due to the fewness and concentration of available measurements, confidence intervals on the fitted parameters are rather wide, which renders the predictive ability of the fitted models, beyond the range of the data, very poor.

8.7.5 Fitting of the DMA data versus frequency

To study the influence of the Payne effect on rolling resistance, in the absence of reliable estimates of the dynamic moduli beyond the ranges of strain amplitude over which the material samples were tested, simple and well suited models are fit to DMA data corresponding to strain amplitudes chosen on the upper side of these ranges, i.e. $\epsilon_{max} = 2.00\%$ for the Urethane rubber, and $\epsilon_{max} = 5.53\%$ for the Neoprene rubber. The fits are shown in Figure 8.28 superimposed on the DMA and the shifted HFVS data points, for the Urethane rubber (upper frames), and the Neoprene rubber (lower frames). The increasing difference between the HFVS results corresponding to very small deformations and the DMA results obtained at larger strain amplitudes is quite striking. It stresses the fact that linear viscoelastic characterizations of materials presenting a significant Payne effect are strain amplitude dependent, which raises the question of whether, for such materials, linear viscoelastic models can be of any practical interest.

In Figure 8.28, the storage moduli are fit by a sigmoidal function of the form

$$E'(f) = a \tanh\left(\frac{1}{b}\log_{10}\left(\frac{f}{f_o}\right)\right) + c, \tag{8.17}$$

whereas the loss moduli are fit by a Gaussian function, i.e.

$$E''(f) = a \exp\left(-\left(\frac{1}{b}\log_{10}\left(\frac{f}{f_o}\right)\right)^2\right). \tag{8.18}$$

The fitting parameters a, b, c and f_o appearing in equations (8.17) and/or (8.18) are not the same. These two expressions are in fact unconnected and do no satisfy

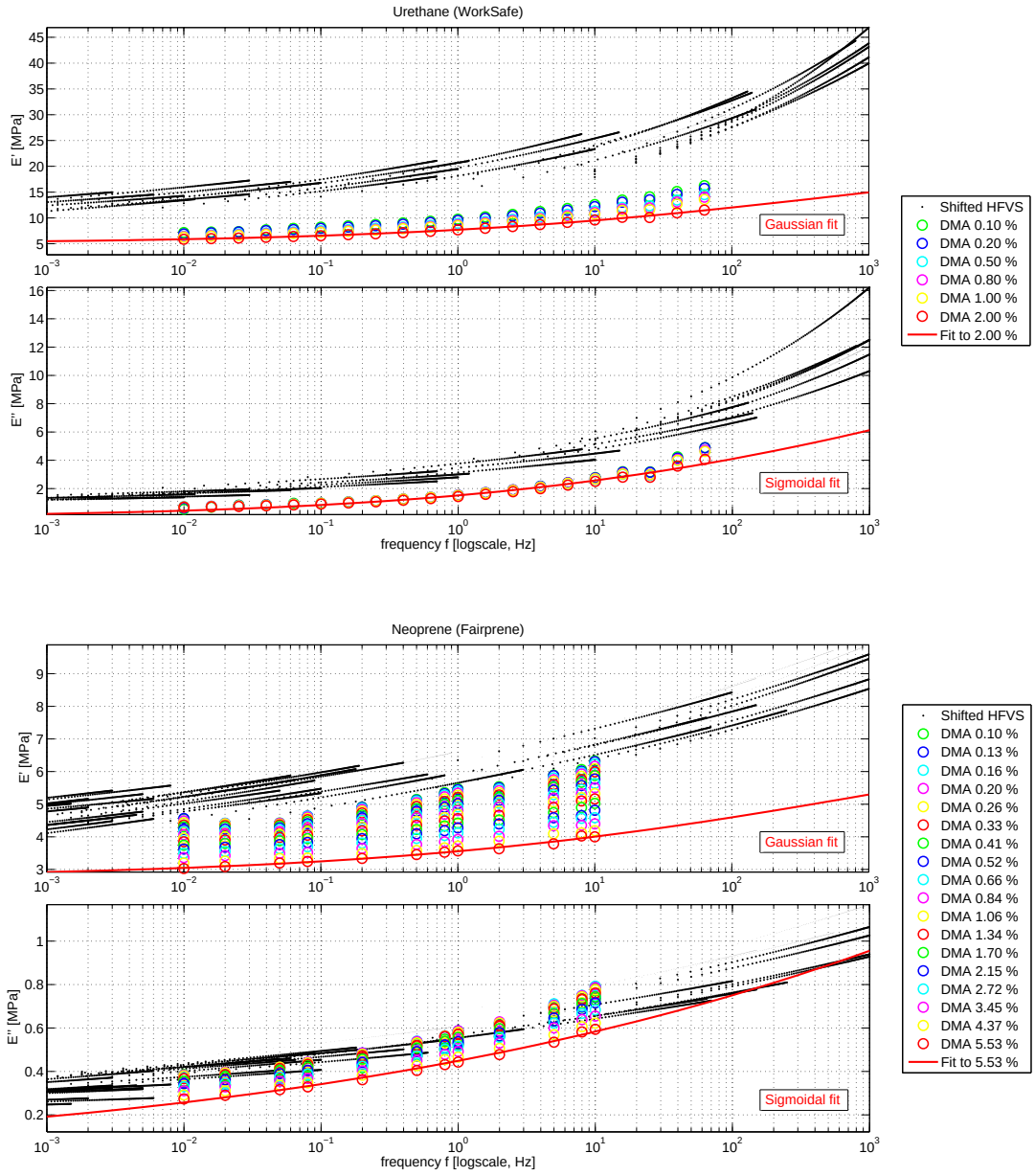

FIGURE 8.28: Sigmoidal and Gaussian functions fitted to the largest available strain-amplitude DMA data for the storage moduli and the loss moduli, respectively, for Urethane (top) and Neoprene (bottom).

the *Kramers–Kronig relations*, which relate the real part and the imaginary part of any complex function that is analytic in the upper half-plane, such as the response of a causal linear system to a harmonic excitation (see e.g. Lakes, 2009; Tschoegl, 1989). Nevertheless, as noted in Section 8.8 below, the viscoelastic rolling resistance, at velocities relevant to the experiment discussed in this chapter, is influenced by the values taken by the dynamic moduli in a limited frequency range, including that of the collected data. Consequently, the modeling of $E'(f)$ and $E''(f)$ by unrelated expressions such as (8.17) and (8.18) relies on the plausible assumption that a complex and analytic function, whose real and imaginary parts coincide with these expressions over the limited frequency range relevant to the application, exists. Such a function could for instance result from a Prony series (8.14) comprising a sufficient number of terms (i.e. of relaxation times), which may however be difficult to fit in practice, due to the inevitable curse of dimensionality.

8.8 Rolling resistance predictions versus experiment

8.8.1 Predictions: method, convergence, and relevant frequency range

Method

The linear viscoelastic material models fitted to the HFVS data points in Section 8.6.4 (see Figure 8.22) and the analytical models fitted to the DMA data points in Section 8.7.5 (see Figure 8.28) are introduced into the three-dimensional boundary element formulation proposed in Chapter 4 (Zéhil and Gavin, 2013e), which is used in combination with the 3D rolling contact algorithm presented in Chapter 3 (Zéhil and Gavin, 2013c), to generate steady-sate rolling resistance predictions from parameters reflecting the conditions under which the rolling resistance setup is operated, as reported in Section 8.3 regarding ball radius R, rubber sheet thickness H, and applied load P, and as determined in Section 8.4.2 regarding rolling speed V_s.

Convergence and relevant frequency range

The level of convergence of rolling resistance calculations performed as outlined in Section 8.8.1 depends on: (i) the number of terms N_{t_x} and N_{t_y} retained in the Fourier series of the boundary element formulation, and (ii) the fineness of the spatial mesh discretizing the candidate contact surface, which is determined by the nodal spacings a_x and a_y. Given the ranges over which parameters vary in the rolling resistance experiment, truncation orders corresponding to $N_{t_x} = N_{t_x} = 1500$ terms, and nodal spacings of $a_x = a_y = 0.25$ mm, provide a satisfactory level of convergence.

In an other vein, rolling resistance is usually governed by material properties in a limited range of relevant frequencies, depending on the rolling speed. It is determined, following a heuristic approach, that the angular frequencies relevant to the experiment lie, roughly, between $\omega_{min} = 10^{-3}$ rad/s and $\omega_{max} = 10^{3}$ rad/s. Values taken by the dynamic moduli outside this range have a negligible influence on rolling resistance predictions.

The two claims formulated above regarding the level of convergence and the frequency range relevant to the experiment are supported by the comparison shown in Figure 8.29, between three sets of rolling resistance predictions, obtained from the linear viscoelastic models fitted to the HFVS data points (Figure 8.22), in the conditions listed below:

- **(a)** Predictions obtained using a truncation order corresponding to $N_{t_x} = N_{t_x} = 750$ terms in the Fourier series, and a relatively coarse mesh characterized by the nodal spacings $a_x = a_y = 0.5$ mm. This first set of predictions it termed "(a) coarse", in reference to the coarse mesh and to the relatively low truncation order retained.

- **(b)** Predictions obtained using a truncation order corresponding to $N_{t_x} = N_{t_x} = 1500$ terms in the Fourier series, and a fine mesh characterized by the

nodal spacings $a_x = a_y = 0.25$ mm. This second set of predictions it termed "(b) fine", in reference to the finer spatial mesh and to the higher order of truncation retained.

- **(c)** Predictions obtained in the same condition as in case (b), with an additional 'saturation' applied to the dynamic moduli, as defined in the expressions below

$$E'_{sat}(\omega) = \begin{cases} E'(\omega_{min}) & \text{if} \quad \omega < \omega_{min}, \\ E'(\omega) & \text{if} \quad \omega_{min} \leq \omega \leq \omega_{max}, \\ E'(\omega_{max}) & \text{if} \quad \omega_{max} < \omega, \end{cases} \tag{8.19a}$$

$$E''_{sat}(\omega) = \begin{cases} E''(\omega_{min}) & \text{if} \quad \omega < \omega_{min}, \\ E''(\omega) & \text{if} \quad \omega_{min} \leq \omega \leq \omega_{max}, \\ E''(\omega_{max}) & \text{if} \quad \omega_{max} < \omega. \end{cases} \tag{8.19b}$$

This third set of predictions it termed "(c) fine, with E_{sat}", in reference to the conditions of case (b) and to the saturation applied to the moduli outside the frequency range of interest.

8.8.2 Comparing experiment to predictions

The experimental results[2] ("EXP") for steady-state rolling resistance, determined by processing load cell measurements according to the procedure described in Section 8.4.1, are compared in Figures 8.30, 8.31 and 8.32, to two sets of predictions obtained by setting $N_{t_x} = N_{t_x} = 1500$ terms and $a_x = a_y = 0.25$ mm, and applying the saturation defined by equations (8.19) to:

- the linear viscoelastic models fitted to the HFVS data points (Figure 8.22) corresponding to very small strain amplitudes. This first set is equivalent to set (c) "fine, with E_{sat}" of Section 8.8.1. It is renamed "HFVS" in reference to the fact that it is based on material characterizations obtained by High Frequency Viscoelastic Spectroscopy,

[2] See Figures 8.15, 8.16 and 8.17, for $\mathcal{U}_{1.6}$, $\mathcal{N}_{1.6}$, and $\mathcal{N}_{0.8}$ rubber sheets, respectively.

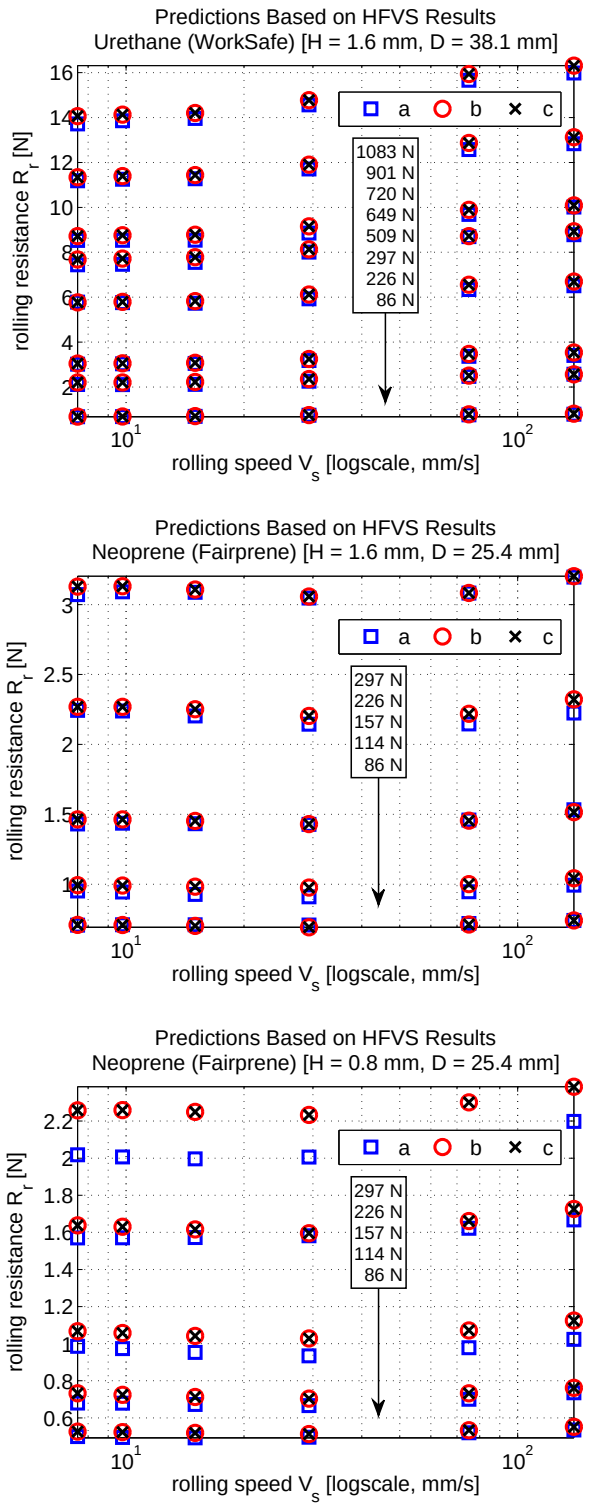

FIGURE 8.29: Verification of convergence and determination of the effective frequency range for predictions: (a) coarse, (b) fine, and (c) fine, with E_{sat}.

- the analytical functions fitted to the DMA data points (Figure 8.28) corresponding to larger strain amplitudes. This second set of rolling resistance predictions is termed "DMA" in reference to the Dynamic Mechanical Analyzes on which it relies.

In Figure 8.30, experimental and predicted rolling resistance results (R_r) are plotted against rolling speed (V_s), for the various levels of loading (P). The ratios of experimental to predicted values are plotted against P in Figure 8.31, and against V_s in Figure 8.32.

The differences between experimental values and predictions are significant. The ratio of experimental to predicted rolling resistance varies roughly between 1.6 and 6.7. The fact that it is always larger than 1 indicates that the real amount of viscoelastic friction, in the conditions of this experiment, is underestimated by the predictions. The "HFVS" predictions are clearly poorer than the "DMA" predictions, the latter corresponding to material models determined under larger strain amplitudes. The inspection of global trends reveals that the prediction error increases with the applied load and decreases with the rolling velocity. In this vein, it is interesting to note that the sphere's penetration into the rubber sheets is an increasing function of the load, but a decreasing function of the speed.

In addition to uncertainties associated with calculations and measurement errors (see Sections 8.2.2 and 8.4.1), the aforementioned observations can be attributed to a combination of the two main factors listed below:

- The self-weight of the upper part of the experimental setup, comprising the upper steel plate and the rubber sheet that is attached to it, the angle plate, the load cell, the moving part of the linear bearing and their connections, added to that of the steel ball, is such that the minimal vertical load applicable to the rolling sphere is roughly $P = 86$ N. This weight produces relatively

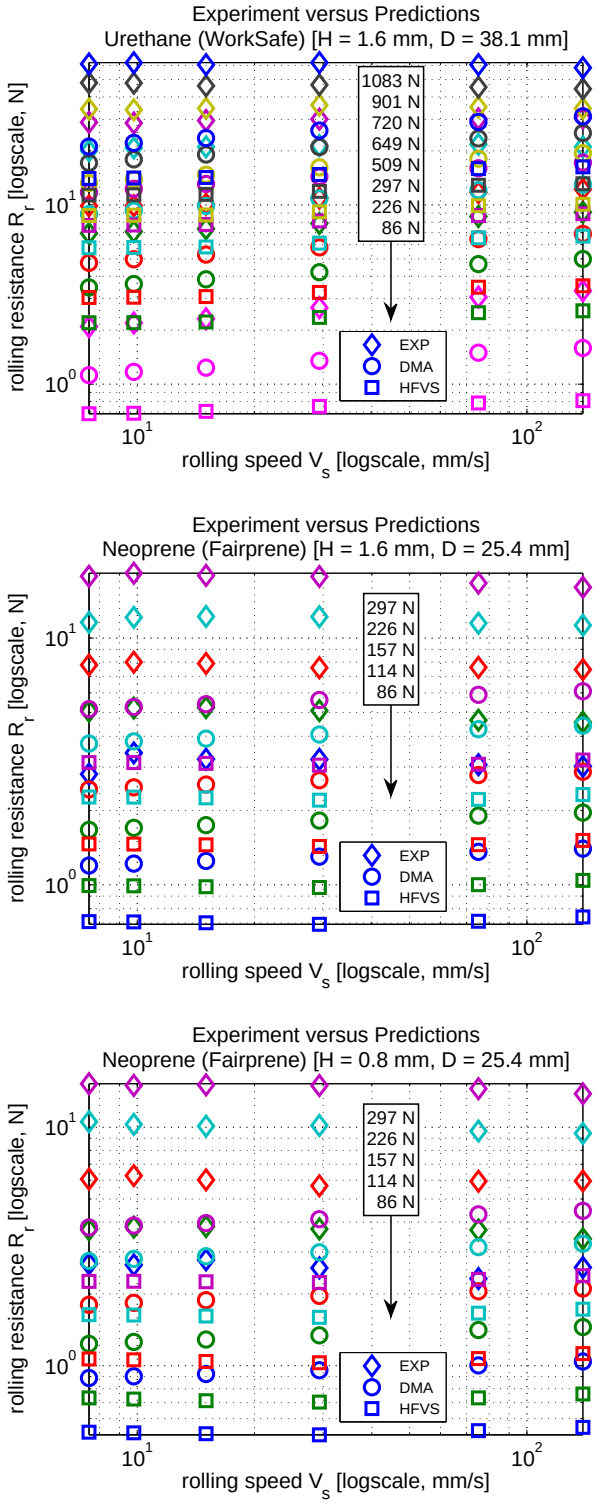

FIGURE 8.30: Comparison between experimental and predicted values of rolling resistance.

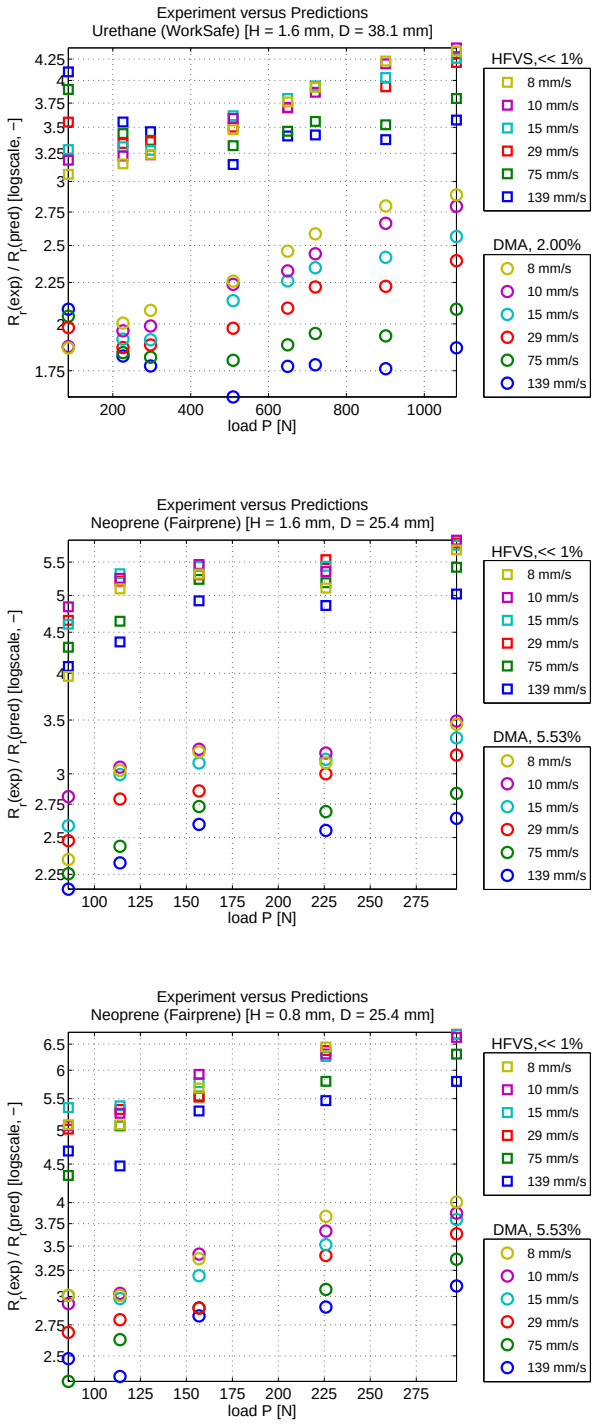

FIGURE 8.31: Ratio of experimental to predicted values of rolling resistance, plotted versus P.

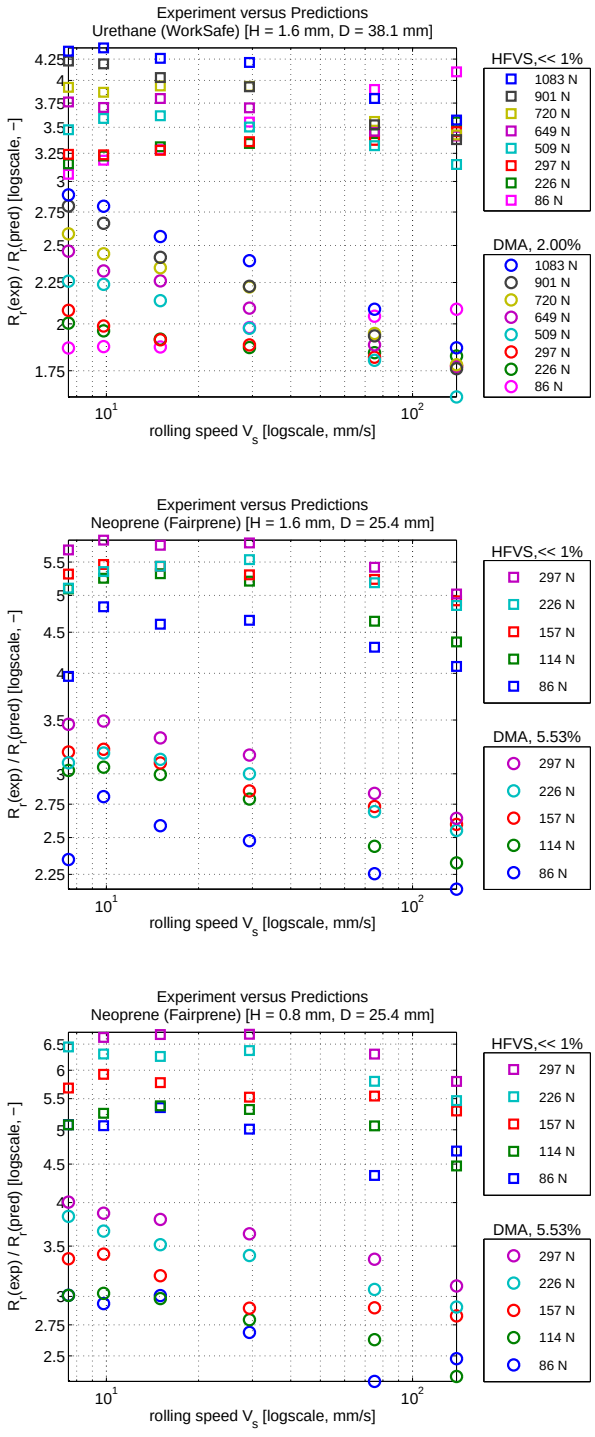

FIGURE 8.32: Ratio of experimental to predicted values of rolling resistance, plotted versus V_s.

large deformations in the rubber sheets tested, which are not compatible with the assumption of small deformations on which rely the computational tools that were developed and used, as well as the material model retained, for the predictions.

- As previously described in Section 8.7, both materials tested present a substantial Payne effect, which cannot be accounted for by material models that are independent of strain amplitude.

8.8.3 Comparison to recent tribometer results

In a recent publication, Carbone and Putignano (2013) report experimental results for the sliding of a fixed (rigid) sphere, made of Polytetrafluoroethylene (PTFE), on a rotating disk of Styrene-Butadiene Rubber (SBR). The rubber sample has a diameter of 50 mm and a thickness of 4 mm. We were unable to establish contact with the authors to determine the size of the ball, which is not specified in their paper. Nevertheless, from the picture shown in figure 14 of the paper, and after contacting the manufacturer (CSM Instruments) of the tribometer used by the authors to perform their experiment, we were able to estimate the diameter of the ball to roughly 10 mm. Indeed, according to the manufacturer, the rubber disk is maintained along its perimeter by a fastening ring whose internal diameter is equal to 50 mm; this dimension seems roughly five times larger than the diameter of the ball appearing on the photograph. Regarding boundary conditions: whether the rubber disk can be considered as being perfectly bonded to its rigid support is rather unclear. Furthermore, the radial position of the ball, and hence its distance to the fastening ring, is not specified. Based on the photograph, we estimate the distance from the center of the ball to the axis of rotation of the rubber disk to approximately 15 mm. According to the authors, the angular speed of the rotating disk is adjusted so that the sliding velocity of the ball is set to 6 mm/s, to avoid significant heating and wear. The co-

efficient of rolling friction $\mu(P) = R_r(P)/P$ is measured for $P = 1$, 2, 3, 4, and 5 N. To isolate the viscoelastic contribution to $\mu(P)$ and eliminate the effect of surface friction, which is assumed proportional to P, the increase in the friction coefficient defined as $\Delta\mu(P) = \mu(P) - \mu(1\text{ N})$ is determined and plotted against P. The authors compare these experimental results to the predictions of their model, obtained after fitting a Prony series to DMA data for the SBR, and find a satisfactory match.

The plot shown in Carbone and Putignano (2013, fig. 13) is digitized and a Prony series comprising 50 terms is fit to the DMA data. The fit and the corresponding spectrum of relaxation times are shown in Figure 8.33. It is furthermore assumed that the tested rubber is incompressible, or nearly so. Based on this material model, two different sets of predictions are sought for $\Delta\mu(P)$, as described below:

1. The first set of predictions (P1) is obtained using the three-dimensional boundary element formulation developed in Chapter 4 (Zéhil and Gavin, 2013e), in combination with the 3D contact solver presented in Chapter 3 (Zéhil and Gavin, 2013c). The truncation order and the nodal spacing are set to $N_{t_x} = N_{t_y} = 1750$ terms and $a_x = a_y = 50$ μm, respectively. A spatial period of $L_x = L_y = 100$ mm is retained, which is fairly close to the estimated perimeter of the ball's circular trajectory, in the experiment. In fact, increasing or decreasing the spatial period by 50% does not result in noticeable changes in the predictions. This observation is due to characteristics of the relaxation spectrum shown in Figure 8.33, i.e. most dominant terms in the Prony series correspond to relaxation times that are much smaller than the characteristic time of the experiment, which is of the order of 15 s.

2. The second set of predictions (P2) is obtained by running three-dimensional dynamic finite element simulations, on the commercial software ABAQUS. A

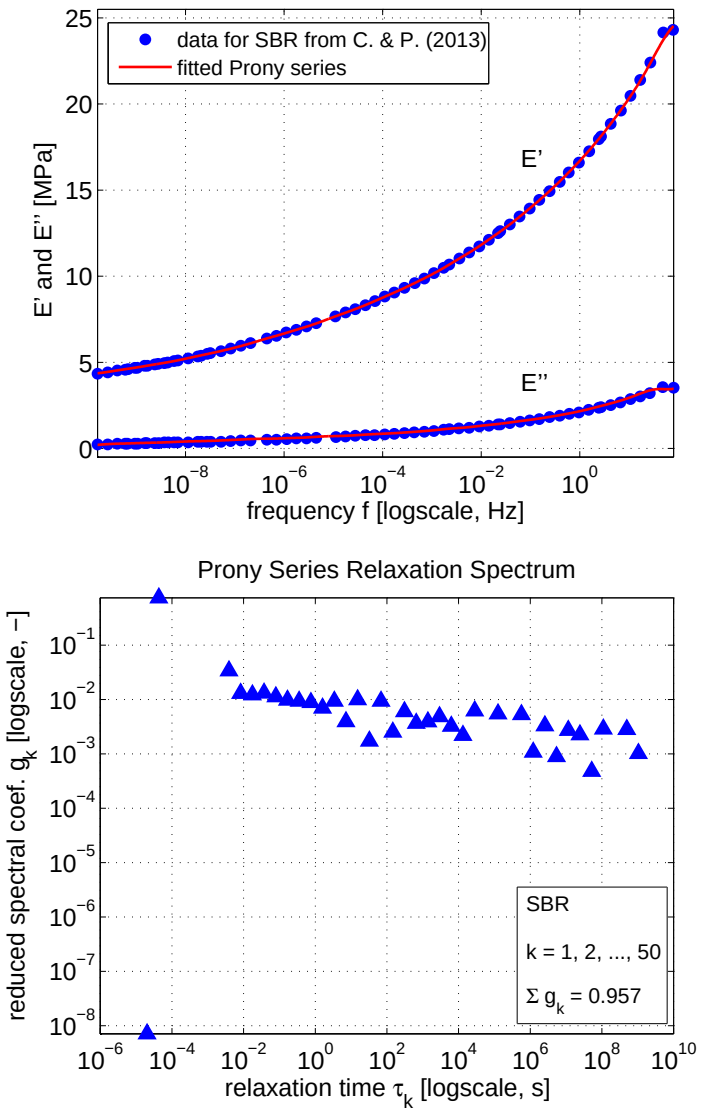

FIGURE 8.33: Prony series fitted to the DMA data digitized from in Carbone and Putignano (2013, fig. 13): fit superimposed on the data (top), and spectrum of relaxation times (bottom).

10 mm analytically rigid sphere is slid on a 10 mm wide[3] and 4 mm thick viscoelastic layer characterized by the material model shown in Figure 8.33. A hybrid formulation is used to avoid volumetric locking (e.g. Hughes, 2000): the strip is discretized using 8-node linear brick elements, with constant pressure. Inertial forces and geometric nonlinearities are accounted for in the solution scheme, and surface-to-surface (frictionless) normal contact is implemented using the "hard" contact pressure-overclosure relationship. In each simulation, the sphere is first loaded by a vertical force P. A sliding velocity of 6 mm/s is then applied, instantaneously. All simulations are run until a steady-state is reached.

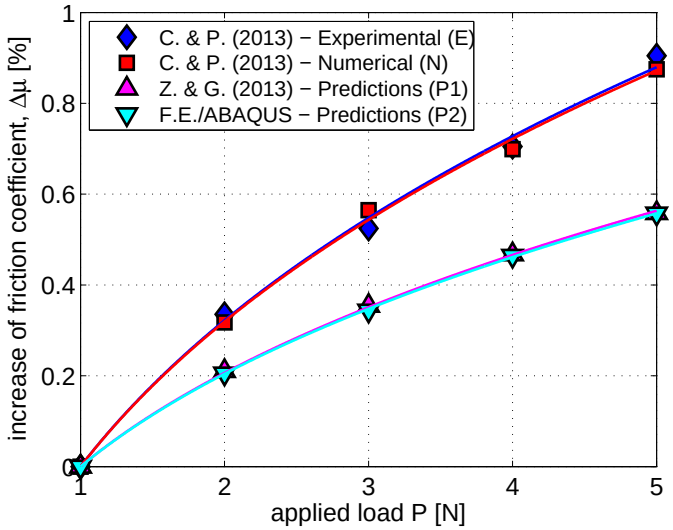

FIGURE 8.34: Increase in the viscoelastic friction coefficient $\Delta\mu(P) = \mu(P) - \mu(1\text{ N})$ plotted verus P. The sets of predictions (P1) and (P2) are superimposed on the experimental (E) and numerical (N) results reported by Carbone and Putignano (2013, fig. 15).

Both sets of predictions (P1) and (P2), are shown in Figure 8.34 and compared to the experimental (E) and numerical (N) results reported by Carbone and Putignano

[3] In comparison, the contact radius under the maximum load of 5 N is roughly equal to 1 mm.

(2013, fig. 15). Figure 8.34 reveals that, although the sets of predictions (P1) and (P2) match perfectly well, they differ appreciably from the values related by these authors. Whether the rubber they used (provided by Pirelli Tyre S.p.A.) presents a significant Payne effect is uncertain, but likely (see e.g. Ramorino et al., 2003), depending on its filler content. The strain amplitude at which the DMA was performed on the material is furthermore unknown. A noticeable Payne effect would perhaps explain the difference between the predictions (P1) and (P2) and the experimental results (E), the latter presenting a higher friction coefficient. The exceptional match between the authors' predictions (N) and the experiments (E) is rather surprising, unless these predictions are based on different assumptions than those retained in (P1) and (P2). For instance, assuming the ball has a diameter of 5 mm (instead of the estimated 10 mm) in (P1) would roughly match the experimental results (E).

8.9 The Mullins effect

Uniaxial extension tests are performed, at a constant strain rate of 0.125 mm/s, on rectangular samples cut form virgin $\mathcal{U}_{\infty./}$(length 30 mm; width 3.05 mm) and $\mathcal{N}_{\infty./}$ (length 50 mm; width 4.9 mm) rubber sheets. The virgin samples are subjected to a first loading cycle with a strain amplitude of 50%, followed immediately by a second loading cycle with a strain amplitude of 100%.

The nominal stress is plotted against the nominal strain in Figure 8.35, for the two samples. The Mullins effect is noticeable in both materials tested, i.e. the virgin samples soften significantly under deformation. However, despite this fact, no clear sign of a potential influence of the Mullins effect on the steady-state rolling resistance is detected in this study. Indeed, although the rolling resistance experiments described in Section 8.3 are performed on virgin rubber sheets, and the ball is shifted between successive tests so that it travels an initially virgin path, the loops traced in the force-displacement plane during successive cycles of motion, in any given test,

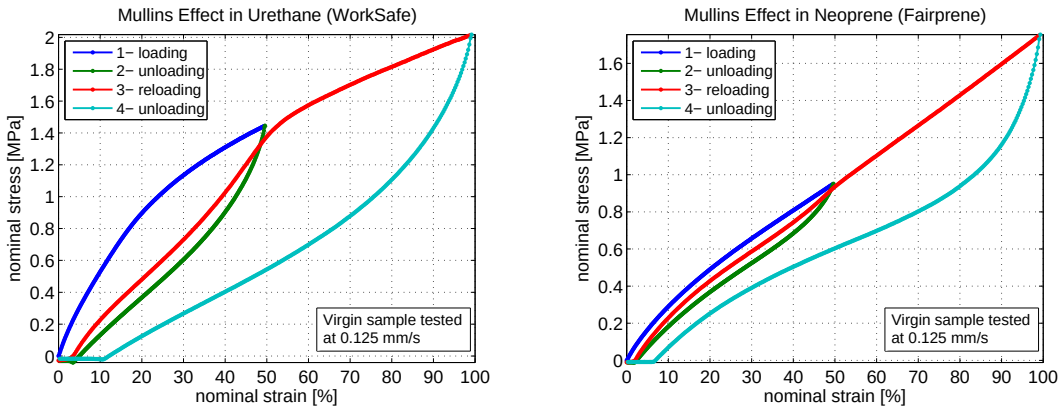

FIGURE 8.35: The Mullins effect in Urethane (left) and Neoprene (right).

appear to overlap fairly well (see Figure 8.3-8.8).

8.10 Summary

The experimental setup shown in Figures 8.1 and 8.2 is designed and assembled to measure the resistance incurred by rigid spheres rolling between identical sheets of rubber, and to study the influence of material and geometric nonlinearities on the viscoelastic rolling resistance. Two different materials (a Urethane rubber and a Neoprene rubber), two sheet thicknesses (0.8 mm and 1.6 mm), two ball diameters (25.4 mm and 38.1 mm), multiple weight levels (varying between 86 N and 1083 N), and several rolling velocities (ranging from 8 mm/s to 139 mm/s) are involved in the tests. Principal sources of measurement error, such as the precision of the load cell ($0.05\% \leq \Delta R_r^{(1)}/P \leq 0.5\%$), the mechanical compliance of components in the setup ($0.3\% \leq \Delta R_r^{(2)}/P \leq 3.3\%$), and surface imperfections ($\Delta R_r^{(3)}/P \approx 2\delta/l$) are examined. It is shown that, in the conditions of this experiment, measurement errors have the same order of magnitude as rolling resistance ($2.4\% \leq R_r/P \leq 6.2\%$). High frequency Thermo-Viscoelastic Spectroscopies (HFVS) are performed to characterize the linear viscoelastic behavior of the materials involved in a wide frequency range,

but under very small strain amplitudes ($\epsilon_{max} \ll 1\%$). Dynamic Mechanical Analyzes (DMA) are also performed on samples of the Urethane rubber ($0.1\% \leq \epsilon_{max} \leq 2.0\%$) and the Neoprene rubber ($0.1\% \leq \epsilon_{max} \leq 6.3\%$) to characterize their linear viscoelastic behavior at moderately larger strain amplitudes, but in a more limited frequency range (0.01 Hz $\leq \epsilon_{max} \leq$ 10 Hz). It is shown that both materials present a significant Payne effect. The Kraus model is fitted to DMA results in an attempt to extrapolate the observed Payne effects to larger strain amplitudes than can be obtained with the micro-strain analyzer, consistent with the levels of deformation involved in the rolling resistance experiment. The fitting procedures however result in very poor confidence intervals on the parameters. To evaluate the influence of the Payne effect on rolling resistance predictions, linear viscoelastic material models are fit to the sets of HFVS data ($\epsilon_{max} \ll 1\%$), and to sets of DMA data corresponding to larger available strain amplitudes ($\epsilon_{max} = 2\%$ for the Urethane rubber, and $\epsilon_{max} = 5.53\%$ for the Neoprene rubber). These material models are then introduced in the computational tools presented in Chapter 3 (Zéhil and Gavin, 2013c) and Chapter 4 (Zéhil and Gavin, 2013e) to obtain corresponding sets of rolling resistance predictions, termed "HFVS" and "DMA" predictions, respectively. Experimental values of rolling resistance are found to be 1.6 to 6.7 times larger than the predictions. Nevertheless, the "DMA" predictions are significantly closer to the measurements, although the substantial Payne effect in the materials involved cannot rigorously be accounted for by linear viscoelastic models, which are independent of strain amplitude. The prevailing influence of strain amplitude is confirmed by the predictions becoming poorer under larger loads and smaller velocities, i.e. when the actual deformations in the rubber sheets are larger. It is concluded that (even) the (smallest) deformations involved in the experiment are not compatible with the assumptions (of linear behavior under small strains) behind the computational tools and the material models used to make the predictions. Nevertheless, the ratio of measurements to predictions approaches

1 as these assumptions come closer to being satisfied. It is finally determined that both rubbers tested present a significant Mullins effect. However, no clear sign of a potential influence of this effect on rolling resistance is detected in this study.

9

On the structural behavior of casing-infill composite tubes: theory and experiment

9.1 Preamble

In this chapter, we touch on the mechanical behavior of casing-infill composite tubes, as potential new lightweight structural elements. For simplicity, the axial behavior of general composite circular tubes, comprising a casing and an infill, is addressed analytically, with the aim of developing physical insight into the mechanical interactions between these two components, in the linear range. The influence of material parameters, such as Young's modulus and Poisson's ratio of the infill, relative to those of the casing, and of geometry, such as the ratio of wall-thickness to diameter of the casing, on the structural stiffness and capacity of the composite are revealed and presented in unpublished graphical form. It is for instance highlighted that, the capacity at yield of a composite column with an incompressible fluid infill is roughly half that of the empty casing alone, without benefit in terms of stability. Alternatively, it is shown that significantly improved overall stiffness and capacity at yield can be obtained by bonding a moderately softer, but highly auxetic, infill to the

casing, which further highlights the need to develop new lightweight auxetic materials, without compromising their stiffness. It is furthermore concluded that limited mechanical synergies can be expected in metal-polymer composite tubes, within the linear range of the materials involved. This prediction is confirmed by a bending experiment conducted on an Aluminum-Urethane composite tube. The experiment however reveals unexpected and quite promising mechanical synergies under large deformations. The composite member appears capable of 'ever-increasing' resistance under large deformations while maintaining a softening behavior. Such properties are suitable for applications involving lightweight protecting structures against shocks and accelerations due to impacts. The potential influence of this novel composite on the design and performance of such structures seems to justify that it be characterized further.

9.2 Analytical approach for the axial behavior of casing-infill composite tubes

9.2.1 The empty tube

Consider an empty tube of circular cross-section. We will often refer to this tube as the "casing". Let D designate the mean diameter of the casing and t its wall-thickness, as shown in Figure 9.1.

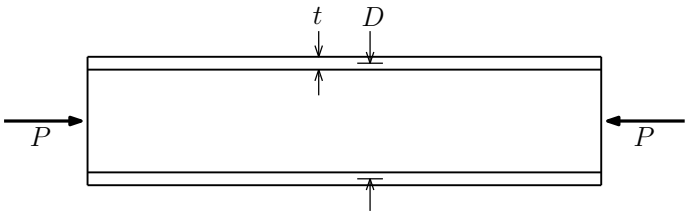

FIGURE 9.1: Empty tube (casing) of circular cross-section.

It is assumed that the material constituting the casing behaves linearly in the elastic range. This material is therefore characterized by its Young modulus E_c, its

Poisson ratio ν_c, and its normal yield stress σ_y. In intermediate sections of the tube where the axial load P is uniformly distributed, the normalized capacity at yield is given by

$$\frac{P_y}{\sigma_y D^2} = \pi \left(\frac{t}{D}\right)\left(1 - \frac{t}{D}\right), \tag{9.1}$$

where P_y is the axial yield load. In the following, we will assume that the wall-thickness t is much smaller than the diameter D of the tube (i.e. $t/D \ll 1$). In this case, expression (9.1) reduces to

$$\frac{P_y}{\sigma_y D^2} = \pi \left(\frac{t}{D}\right). \tag{9.2}$$

9.2.2 The "fluid column"

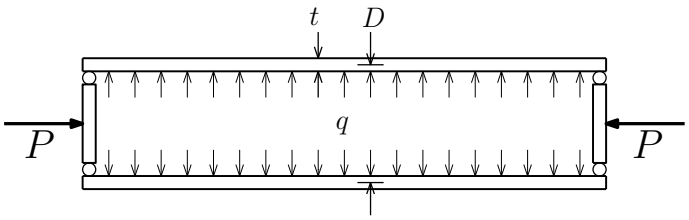

FIGURE 9.2: Tube of circular cross-section filled with an incompressible fluid.

Consider now that the thin-walled casing is filled with an incompressible or nearly incompressible fluid, and that the axial load P is applied to the fluid infill through a sealed piston, as illustrated in Figure 9.2. The hydrostatic pressure q in the fluid, resulting from the axial load P, is given by

$$q = \frac{4P}{\pi D^2}. \tag{9.3}$$

The mean circumferential (hoop) stress σ_r generated in the casing by q is readily deduced from the equilibrium of a half-cylinder of unit length, located on one side

of a longitudinal plane, in a direction perpendicular to that plane

$$\sigma_r = \frac{1}{2}\left(\frac{D}{t}\right) q. \tag{9.4}$$

Substituting equation (9.3) into equation (9.4) and replacing σ_r by σ_y in (9.4) yields the normalized capacity at yield of the fluid column, i.e.

$$\frac{P_y^{fl}}{\sigma_y D^2} = \frac{\pi}{2}\left(\frac{t}{D}\right). \tag{9.5}$$

Comparing expression (9.5) to expression (9.1) reveals that, although yielding and failure of the fluid infill are not of direct concern, the yield capacity of the combined "fluid column" P_y^{fl} is roughly half that of the casing alone, i.e. P_y. Since the fluid column buckles much the same as the empty casing (e.g. Blake D. Mills, 1960), it can be concluded that filling a thin-walled tube with an incompressible fluid results in a poorer structural behavior as compared to the empty tube.

9.2.3 The "solid column"

Consider now that the casing is filled by a solid, rather than a fluid, and that there is no bonding (or friction) between the casing and its content. It is assumed that the infill behaves as a linear elastic material characterized by its Young modulus E_f and its Poisson ratio ν_f, and that the product $P\nu_f$ is greater than or equal to zero, so that normal contact is maintained between the casing and the infill. It is further assumed that, in the range of applied loads, the confined infill does not yield or fail. As in the previous case, the axial load P is applied to the infill through a sealed piston. The system's behavior is considered at a distance from its extremities.

A section of the solid infill is shown in Figure 9.3. Let q refer to the normal contact pressure between the casing and the infill. The state of stress in the infill is homogeneous and it is given by

$$\sigma_r = \sigma_\theta = -q, \tag{9.6a}$$

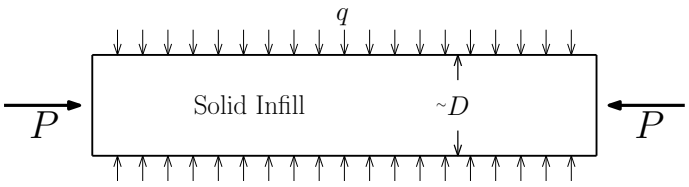

FIGURE 9.3: Section of unbonded solid infill.

$$\sigma_z = -\frac{4P}{\pi D^2}, \tag{9.6b}$$

where σ_r, σ_θ and σ_z are the principal stresses corresponding to the radial, circumferential and axial directions, respectively. The state of strain in the infill is given by

$$\epsilon_r = \epsilon_\theta = -\frac{\nu_f}{E_f}\sigma_z - \frac{1-\nu_f}{E_f}q, \tag{9.7a}$$

$$\epsilon_z = \frac{1}{E_f}\sigma_z + \frac{2\nu_f}{E_f}q, \tag{9.7b}$$

where ϵ_r, ϵ_θ and ϵ_z are the principal strains.

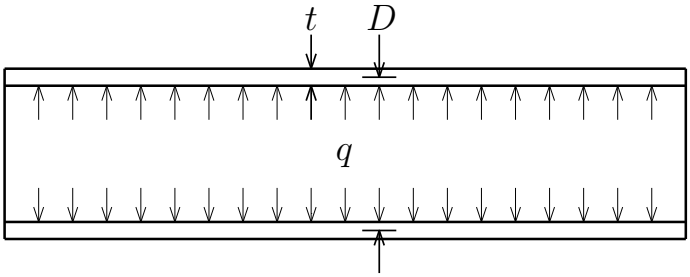

FIGURE 9.4: Section of the casing interacting with an unbonded solid infill.

A section of the casing in contact with the unbonded solid infill is shown in Figure 9.4. The principal stresses in the thin-walled tube are given by

$$\sigma_r = \sigma_z = 0, \tag{9.8a}$$

$$\sigma_\theta = \frac{1}{2}\left(\frac{D}{t}\right)q, \tag{9.8b}$$

while the principal strains corresponds to

$$\epsilon_r = \epsilon_z = -\frac{1}{2}\left(\frac{\nu_c}{E_c}\right)\left(\frac{D}{t}\right)q, \tag{9.9a}$$

$$\epsilon_\theta = \frac{1}{2}\left(\frac{1}{E_c}\right)\left(\frac{D}{t}\right)q. \tag{9.9b}$$

Although there is no tangential bonding between the casing and the solid infill, the circumferential strains in the two materials at the contact interface must be equal. This result is a consequence of the fact that the problem is axisymmetric and that the radial displacements are equal. Consequently, the normal contact pressure q can be determined by simply equating equations (9.7a) and (9.9b), which yields

$$q = -\left(\frac{\nu_f}{(1-\nu_f) + \frac{1}{2}\left(\frac{E_f}{E_c}\right)\left(\frac{D}{t}\right)}\right)\sigma_z. \tag{9.10}$$

Substituting equation (9.10) back into equation (9.8b) and replacing σ_θ by σ_y yields the following expression for the normalized capacity at yield

$$\frac{P_y^{cu}}{\sigma_y D^2} = \frac{\pi}{4\nu_f}\left(\frac{E_f}{E_c} + 2\left(1-\nu_f\right)\left(\frac{t}{D}\right)\right). \tag{9.11}$$

It is noteworthy that, by setting $E_f = 0$ and $\nu_f = 0.5$, equation (9.11) reduces to equation (9.5), which corresponds to the case of an incompressible fluid infill. The ratio of the capacity at yield P_y^{cu} when the load is applied to a confined but unbonded solid infill to the capacity at yield P_y of the casing alone is plotted in Figures 9.5(a) and 9.5(a) against E_f/E_c and ν_f, respectively, for $D/t = 20$. The capacity at yield increases with E_f/E_c because a stiffer infill deforms less under the applied load, which reduces its lateral interaction with the casing. The capacity at yield also becomes larger when $|\nu_f|$ decreases since the lateral repercussions on the casing, of the axial deformation of the infill, are reduced.

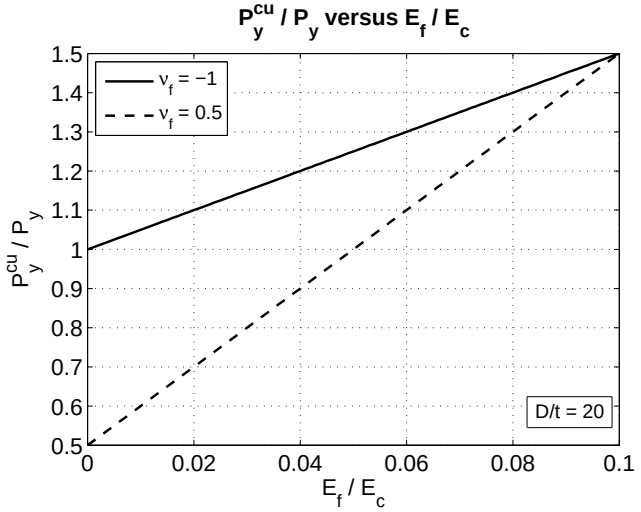

(a) P_y^{cu}/P_y versus E_f/E_c, for $D/t = 20$

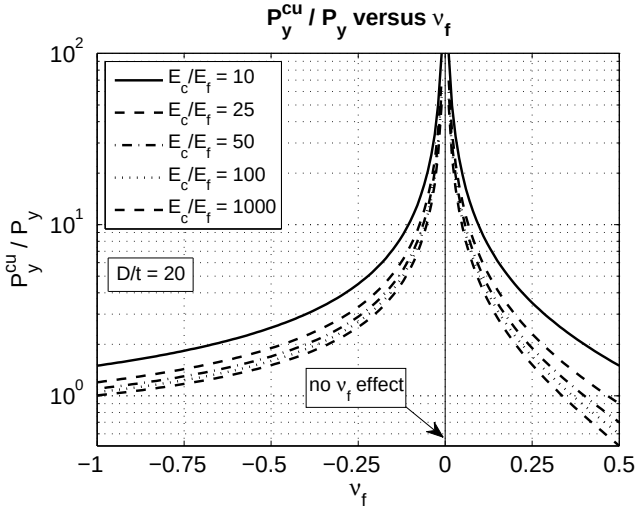

(b) P_y^{cu}/P_y versus ν_f, for $D/t = 20$

FIGURE 9.5: Ratio of the capacity at yield P_y^{cu} when the load is applied to a confined but unbonded solid infill to the capacity at yield P_y of the casing alone.

The ratio of the confined, unbonded axial stiffness K_f^{cu} to the unconfined axial stiffness K_f of the solid infill is readily obtained following the substitution of (9.10) into (9.7b)

$$\frac{K_f^{cu}}{K_f} = \left(1 - \frac{4\nu_f^2}{2\left(1-\nu_f\right) + \left(\frac{E_f}{E_c}\right)\left(\frac{D}{t}\right)} \right)^{-1}. \tag{9.12}$$

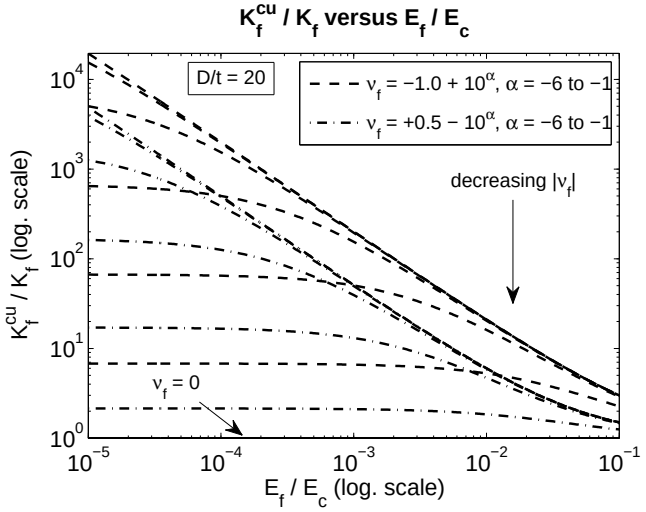

(a) K_f^{cu}/K_f versus E_f/E_c, for $D/t = 20$

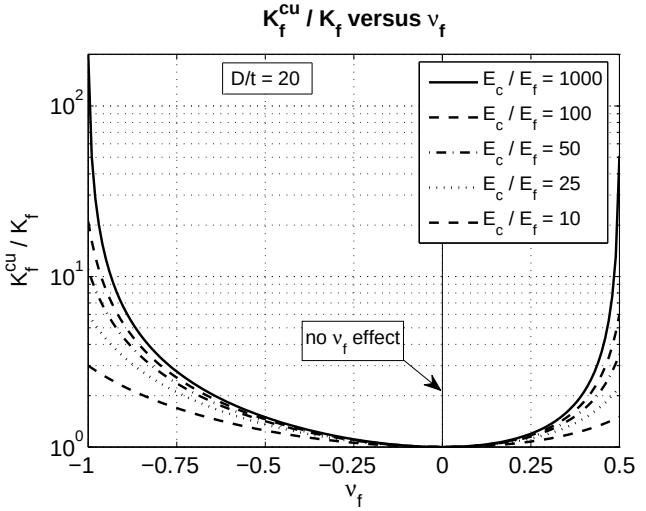

(b) K_f^{cu}/K_f versus ν_f, for $D/t = 20$

FIGURE 9.6: Ratio of the axial stiffness K_f^{cu} of the confined, unbonded solid infill to its unconfined stiffness K_f.

The left-hand-side of equation 9.12 is plotted against E_f/E_c and ν_f, for $D/t = 20$, in Figures 9.6(a) and 9.6(b), respectively. These figures show that the axial stiffness of the solid infill increases when the infill is confined. Naturally, the relative influence of the confinement is more apparent on softer infills. It is furthermore significant when the Poisson ratio of the infill is close to 0.5, or -1, with better results in the

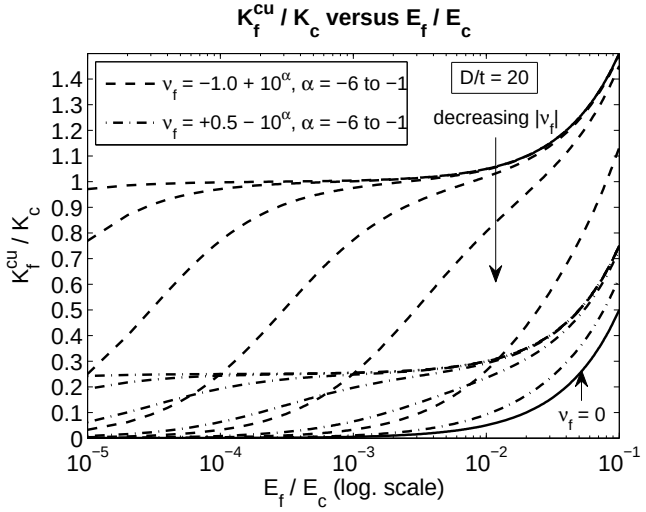

(a) K_f^{cu}/K_c versus E_f/E_c, for $D/t = 20$

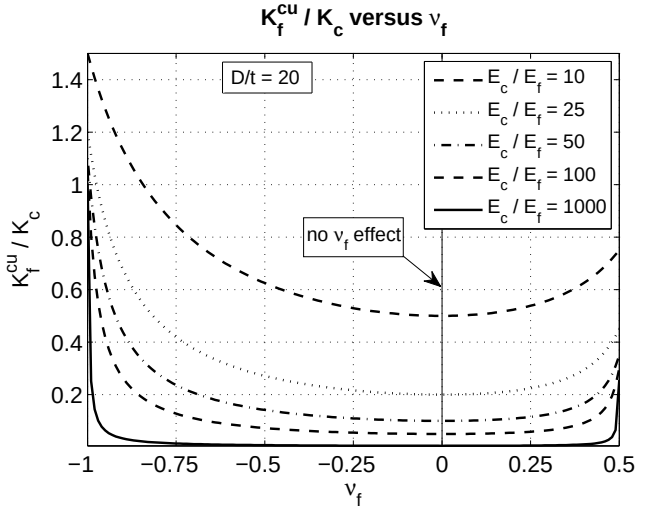

(b) K_f^{cu}/K_c versus ν_f, for $D/t = 20$

FIGURE 9.7: Ratio of the axial stiffness K_f^{cu} of the confined, unbonded solid infill to the axial stiffness K_c of the empty tube.

auxetic case.

On the other hand, the ratio of the axial stiffness K_f^{cu} of the confined, unbonded solid infill to the axial stiffness K_c of the empty casing is given by

$$\frac{K_f^{cu}}{K_c} = \frac{1}{4}\left(1 - \frac{4\nu_f^2}{2\left(1-\nu_f\right) + \left(\frac{E_f}{E_c}\right)\left(\frac{D}{t}\right)}\right)^{-1}\left(\frac{E_f}{E_c}\right)\left(\frac{D}{t}\right). \tag{9.13}$$

The left-hand-side of equation 9.13 is plotted against E_f/E_c and ν_f, for $D/t = 20$, in Figures 9.7(a) and 9.7(b), respectively. According to Figure 9.7(a), K_f^{cu}/K_c is an increasing function of E_f/E_c, as opposed to K_f^{cu}/K_f (see, Figure 9.6(a)). The ratio K_f^{cu}/K_c is more relevant when the behavior of the empty tube is taken as a reference. In this vein, comparing Figures 9.5(b) and 9.7(b) shows that the best improvements in the capacity at yield and in stiffness do not occur in the same ranges of ν_f: the former is obtained for $\nu_f \to 0$ while the latter occurs when $\nu_f \to -1$, or possibly when $\nu_f \to 0.5$ for stiffer infills. Nevertheless, Figures 9.5 and 9.7 reveal that, under particular circumstances, namely when E_f/E_c is sufficiently large and ν_f is close to -1, the ratios P_y^{cu}/P_y and K_f^{cu}/K_c can be both larger than one. For instance, retaining (mathematically) $E_f = E_c/10$ and $\nu_f = -0.97$ yields $P_y^{cu} = 1.531P_y$ and $K_f^{cu} = 1.365K_c$. However, most existing auxetic materials are highly porous and therefore relatively soft (e.g. Liu, 2006); hence, in practice, E_f is much smaller than E_c. Improving axial stiffness with very soft (unbonded) infills requires that the Poisson ratio of the infill be very close to -1, as can be seen on the left-hand-side of Figure 9.7(b). Figure 9.5(b) shows that, in such conditions, possible improvements in the capacity at yield are very limited. These observations clearly highlight the need to develop stiffer lightweight auxetic materials.

9.2.4 The composite tube

We now assume that the solid infill is bonded to the thin-walled tube. In this case, the exact way by which the axial load P is applied at both ends of the composite element does not really matter beyond a certain distance from those ends, where contact shear stresses vanish. An intermediate section of the composite tube, away from its extremities, is shown in Figure 9.8. The normal tractions along the axial direction in the infill and in the casing are denoted by σ_z^f and σ_z^c, respectively.

Following a similar approach to that presented in Section 9.2.3 for the unbonded

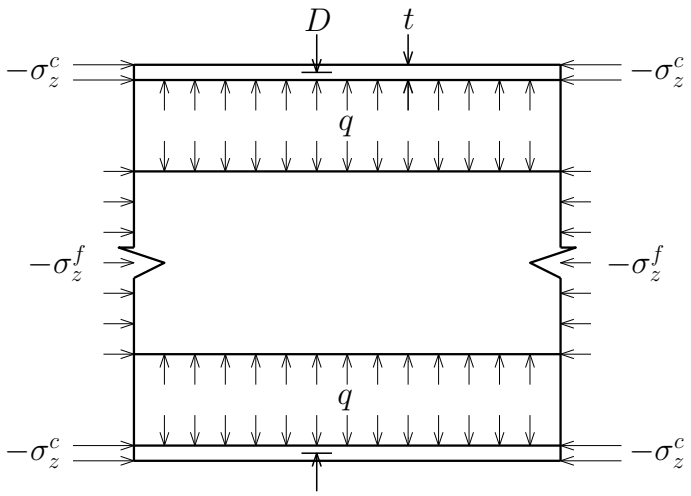

FIGURE 9.8: Intermediate section of the composite tube.

case, we write the states of stress and strain in the bonded solid infill. The principal stresses in the infill are given by

$$\sigma_r = \sigma_\theta = -q, \tag{9.14a}$$

$$\sigma_z = \sigma_z^f, \tag{9.14b}$$

The principal strains in the infill corresponding to those stresses write

$$\epsilon_r = \epsilon_\theta = -\frac{\nu_f}{E_f}\sigma_z^f - \frac{1-\nu_f}{E_f}q, \tag{9.15a}$$

$$\epsilon_z = \frac{1}{E_f}\sigma_z^f + \frac{2\nu_f}{E_f}q. \tag{9.15b}$$

We also write the states of stress and strain in the thin-walled casing. The principal stresses in the casing are given by

$$\sigma_r = 0, \tag{9.16a}$$

$$\sigma_\theta = \frac{1}{2}\left(\frac{D}{t}\right)q, \tag{9.16b}$$

$$\sigma_z = \sigma_z^c, \tag{9.16c}$$

while the principal strains resulting from those stresses are

$$\epsilon_r = -\frac{\nu_c}{E_c}\left(\frac{1}{2}\left(\frac{D}{t}\right)q + \sigma_z^c\right), \tag{9.17a}$$

$$\epsilon_\theta = \frac{1}{E_c}\left(\frac{1}{2}\left(\frac{D}{t}\right)q - \nu_c\sigma_z^c\right), \tag{9.17b}$$

$$\epsilon_z = -\frac{1}{E_c}\left(\frac{\nu_c}{2}\left(\frac{D}{t}\right)q + \sigma_z^c\right). \tag{9.17c}$$

The problem features three unknown quantities, i.e. q, σ_z^f and σ_z^c, and therefore requires three equations to be solved. The first equation results from the compatibility of radial displacements, or of circumferential strains, at the contact interface. Equating expressions 9.15a and 9.17b yields

$$\left((1-\nu_f) + \frac{1}{2}\left(\frac{E_f}{E_c}\right)\left(\frac{D}{t}\right)\right)q + \nu_f\sigma_z^f - \left(\frac{E_f}{E_c}\right)\nu_c\sigma_z^c = 0. \tag{9.18}$$

The second equation falls out from the compatibility of axial displacements and strains, which is due to shear bonding, at the interface between the solid infill and the casing. Equating expressions 9.15b and 9.17c yields

$$\left(2\nu_f + \frac{1}{2}\nu_c\left(\frac{E_f}{E_c}\right)\left(\frac{D}{t}\right)\right)q + \sigma_z^f - \left(\frac{E_f}{E_c}\right)\sigma_z^c = 0. \tag{9.19}$$

The third equation corresponds to the equilibrium of forces in the axial direction

$$\frac{\pi D^2}{4}\sigma_z^f + \pi Dt\sigma_z^c = -P. \tag{9.20}$$

Solving the linear system comprising equations 9.18, 9.19 and 9.20 for the three unknown quantities yields

$$q = \frac{8}{\pi\mathcal{B}}\left(\frac{E_f}{E_c}\right)\left(\frac{t}{D}\right)(\nu_f - \nu_c)\frac{P}{D^2}, \tag{9.21a}$$

$$\sigma_z^f = -\frac{4}{\pi\mathcal{B}}\left(\frac{E_f}{E_c}\right)\left(\left(\frac{E_f}{E_c}\right)\left(1-\nu_c^2\right) + 2\left(\frac{t}{D}\right)\left(1-\nu_f\left(1+2\nu_f\right)\right)\right)\frac{P}{D^2}, \tag{9.21b}$$

$$\sigma_z^c = -\frac{4}{\pi\mathcal{B}}\left(\left(\frac{E_f}{E_c}\right)\left(1-\nu_f\nu_c\right) + 2\left(\frac{t}{D}\right)\left(1-\nu_f\left(1+2\nu_f\right)\right)\right)\frac{P}{D^2}, \tag{9.21c}$$

where the dimensionless shorthand parameter $\mathcal{B}$ is given by

$$\mathcal{B} = \left(\frac{E_f}{E_c}\right)^2 \left(1-\nu_c^2\right) + 2\left(\frac{E_f}{E_c}\right)\left(\frac{t}{D}\right)\left(3-\nu_f\left(1+4\nu_c\right)\right)$$
$$+ 8\left(\frac{t}{D}\right)^2 \left(1-\nu_f\left(1+2\nu_f\right)\right). \tag{9.22}$$

It is noteworthy that, for a solid infill characterized by the same Poisson ratio as that of the casing ($\nu_f = \nu_c$), the normal pressure at the contact interface vanishes ($q = 0$) and the axial load is distributed between the two components proportionally to their axial stiffness, i.e. $\sigma_z^f/E_f = \sigma_z^c/E_c$, as one would expect.

The Von Mises yield criterion for the casing, expressed in cylindrical coordinates with $\sigma_r = 0$ (9.16a), writes (e.g. Fung and Tong, 2001)

$$\sigma_\theta^2 + \sigma_z^2 + \sigma_\theta\sigma_z \leq \sigma_y^2. \tag{9.23}$$

The capacity at yield P_y^p of the composite element is obtained, in normalized form, by plugging equations 9.21a and 9.21c into equations 9.16b and 9.16c and applying inequality (9.23) to get

$$\frac{P_y^p}{\sigma_y D^2} = \frac{\pi}{4}\frac{\mathcal{B}}{\mathcal{C}}, \tag{9.24}$$

where the dimensionless shorthand parameter $\mathcal{C}$ is given by

$$\mathcal{C}^2 = \left(\frac{E_f}{E_c}\right)^2 \left(\left(1+\nu_f\left(1+\nu_f\right)\right)\left(1+\nu_f^2\right) - \nu_c\left(1+\nu_f\left(4+\nu_f\right)\right)\right)$$
$$+ 2\left(\frac{E_f}{E_c}\right)\left(\frac{t}{D}\right)\left(\nu_f - \nu_c + 2\left(1-\nu_f\nu_c\right)\right)\left(1-\nu_f\left(1+2\nu_f\right)\right) \tag{9.25}$$
$$+ 4\left(\frac{t}{D}\right)^2 \left(1-\nu_f\left(1+2\nu_f\right)\right)^2.$$

The ratio of the axial capacity at yield P_y^p of the composite tube to the axial capacity at yield P_y of the empty casing is plotted in Figures 9.9(a) and 9.9(b) against

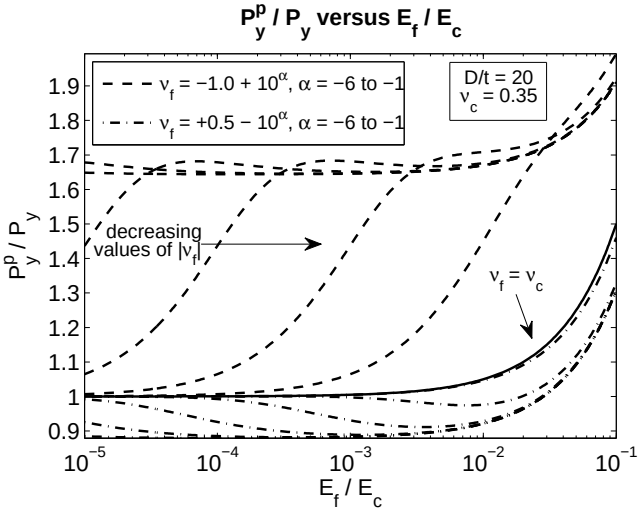

(a) P_y^p/P_y versus E_f/E_c, for $\nu_c = 0.35$ and $D/t = 20$

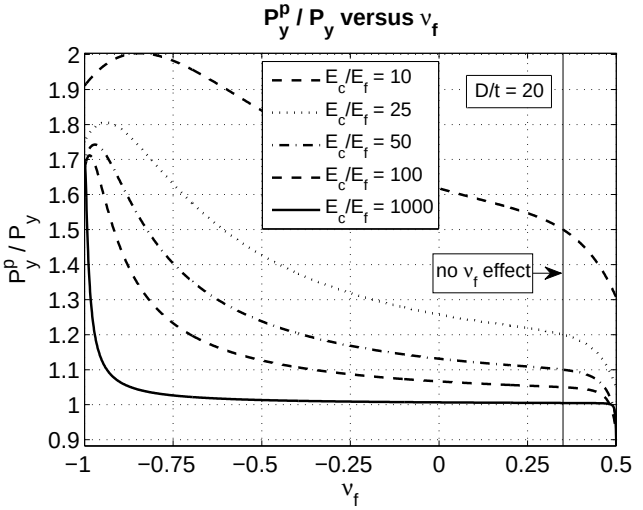

(b) P_y^p/P_y versus ν_f, for $\nu_c = 0.35$ and $D/t = 20$

FIGURE 9.9: Ratio of the capacity at yield P_y^p of the composite tube to the capacity at yield P_y of the casing alone.

E_f/E_c and ν_f respectively, for $\nu_c = 0.35$ and $D/t = 20$. These figures show that the best improvement in the axial capacity at yield of an empty tube can be obtained by filling the tube with a moderately soft solid material, bonded to the tube, and characterized by a strongly negative Poisson ratio (e.g. $E_f = E_c/10$ and $\nu_f \approx -0.85$). This observation reveals that sufficiently stiff and auxetic materials or meta-materials

are needed. Nevertheless, it seems possible to achieve some improvement using softer infills (e.g. $E_f = E_c/1000$ and $\nu_f \to -1$). More limited results can be expected from stiffer non-auxetic infills with $\nu_f < \nu_c$. It is however important to note that, for the softer infills, the load capacity of the composite element drops very sharply as ν_f differs from -1. The high sensitivity of P_y^p to a material parameter such as ν_f may be problematic, especially as ν_f varies, for instance, with temperature, or with the level of strain.

An equivalent axial modulus E_f^{eq} for the bonded solid infill can be defined as $E_f^{eq} = \sigma_z/\epsilon_z$, where σ_z and ϵ_z are given by equations 9.14b and 9.15b, respectively. Working out the expression of E_f^{eq} in terms of material characteristics and geometry yields

$$E_f^{eq} = \frac{E_f}{1 - \left(\frac{4\nu_f\left(\nu_f - \nu_c\right)}{2\left(1-\nu_f(1+2\nu_c)\right)+\left(\frac{E_f}{E_c}\right)\left(\frac{D}{t}\right)(1-\nu_c^2)} \right)}. \tag{9.26}$$

It is worth noting that, when the bonded solid infill and the casing have the same Poisson ratio, the equivalent axial modulus of the infill is equal to its Young's modulus, i.e. $E_f^{eq} = E_f$. This is explained by the fact that, when $\nu_f = \nu_c$, there are no mechanical interactions between the two materials in intermediate sections of the composite element since, according to equation 9.21a, $q = 0$.

The ratio of the axial stiffness K_p of the composite tube to the axial stiffness K_c of the empty casing is readily expressed in terms of E_f^{eq}, E_c, D and t

$$\frac{K_p}{K_c} = 1 + \frac{1}{4}\left(\frac{D}{t}\right)\left(\frac{E_f^{eq}}{E_c}\right). \tag{9.27}$$

The left-hand-side of equation (9.27) is plotted against E_f/E_c and ν_f in Figures 9.10(a) and 9.10(b), respectively, for $\nu_c = 0.35$ and $D/t = 20$. These figures reveal that predominantly, except in the case of limited interest where $\nu_f \in [0, \nu_c]$, the ratio K_p/K_c increases with $|\nu_c - \nu_f|$, which is the greatest for highly auxetic infills. As for

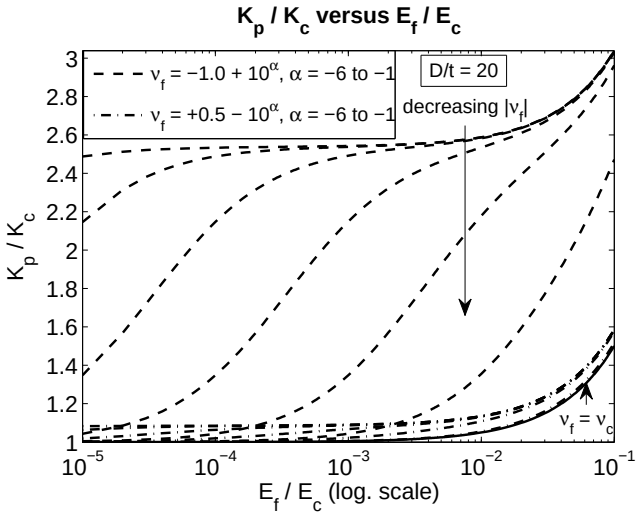

(a) K_p/K_c versus E_f/E_c, for $\nu_c = 0.35$ and $D/t = 20$

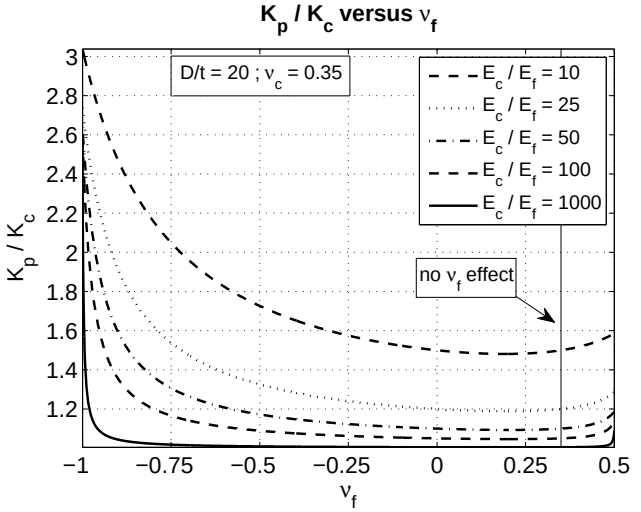

(b) K_p/K_c versus ν_f, for $\nu_c = 0.35$ and $D/t = 20$

FIGURE 9.10: Ratio of the axial stiffness K_p of the composite tube to the axial stiffness K_c of the empty casing.

the capacity at yield, the axial stiffness of the composite is highly sensitive to small changes in Poisson's ratio, especially in cases where the infill is much softer than the casing. These observations further highlight the need to develop new lightweight auxetic materials without compromising their stiffness.

9.2.5 Metal-rubber and metal-polymer composite tubes

The Young modulus of the most commonly used structural metals lies between 60 GPa and 210 GPa, while that of rubbers and polymers ranges roughly from 500 KPa to 3 GPa (see e.g. Lakes, 2009, figure 7.1). The stiffness ratio E_f/E_c for metal-rubber and metal-polymer composites therefore varies in a fairly wide range, approximately between $1/420,000$ and $1/20$. However, on the other hand, Poisson's ratio lies between 0.20 and 0.35 for common structural metals, while it ranges from 0.3 to 0.5 for most polymers and rubbers (see e.g. Mott et al., 2008, figure 1). Clearly, the difference $|\nu_c - \nu_f|$ is rather small, and hence, according to Figures 9.9 and 9.10, only limited mechanical synergies can be expected in metal-rubber and metal-polymer composite tubes, within the linear range of the materials involved.

9.3 Three-point bending experiment on an Aluminum-Urethane composite tube

9.3.1 Materials and methods

Two 762 mm long 6061-T6 Aluminum alloy tube samples of square cross-section (side $b = 25.4$ mm and wall thickness $t = 1.6$ mm) were tested under three-point-bending using an ad-hoc rigid supporting arrangement installed on a Tinius Olsen H50KS load frame (capacity of 50 kN). The experimental setup can be seen in Figures 9.11 and 9.12. One Aluminum tube was partially filled (asymmetrically) with a TASK® 9 high performance Urethane casting resin, and the other tube was left empty to serve as a control sample. The partially filled tube had empty sections at both ends: 251 mm on one side and 171 mm on the other side of the filled section. The main relevant characteristics of the TASK® 9 Urethane, as given by the manufacturer, are reproduced in Table 9.1. The polymer is obtained by mixing an equal volume of two liquid components, part A and part B, whose compositions

Table 9.1: Main relevant characteristics of the TASK® 9 Colormatch Urethane casting resin, as given by the manufacturer (`http://www.smooth-on.com/tb/files/TASK_9_TB.pdf`). (*) properties measured after 7 days at 23°C.

TASK® 9 Colormatch - Technical properties		
Property, Unit	Value	Standard
Mixed viscosity, Pa.s	0.3	ASTM D-2393
Specific gravity, kg/m^3	1140	ASTM-D-1475
Cure time	1 hour at 23°C	-
Shore D hardness	85	ASTM-D-2240
Ultimate tensile strength, MPa	53.8	ASTM-D-638*
Tensile modulus, MPa	2,551	ASTM-D-638*
Elongation at break	6%	ASTM D-638*
Flexural strength, MPa	81.7	ASTM D-790*
Flexural modulus, MPa	2,413	ASTM-D-790*
Compressive strength, MPa	75.8	ASTM D-695*
Compressive modulus, MPa	675.7	ASTM D-695*
Shrinkage	0.9%	ASTM D-2566*

are reproduced in Table 9.2. The low mixed viscosity of the product combined with slow and steady mixing precautions ensured minimal bubble entrapment. To prevent excessive heating of the cast Urethane, the sample was allowed to cure for 22 hours outdoors, under cover, at a mean temperature of 9.1°C (min. 0.7°C; max. 17.1°C) and a mean relative humidity of 67.8% (min. 40%; max. 91%). The sample was then cured indoors, at room temperature, for seven additional days before the bending experiments were conducted. The experimental setup is shown in Figure 9.11, at the beginning and at the end of the bending experiment performed on the composite beam. All tests were conducted under displacement control, at a constant rate of 10 mm per minute. The vertical load was applied to the beam by means of a rigid 38.1 mm diameter cylindrical punch, located right below the load cell.

9.3.2 Observations and results

During each bending experiment, the history of the applied load and that of the cross-head's displacement were stored in a data file. These experimental results were then plotted for both specimens, as shown in Figure 9.14. The main experimental

Table 9.2: TASK® 9 Colormatch Urethane: chemical compositions of part A, and part B, as given by the manufacturer.

	TASK® 9 Colormatch - Composition	
	Chemical component	Weight Percent (%)
Part A	4,4 Methylene bis (phenylisocyanate) (MDI)	80-90
	Butyl benzyl phthalate	10-20
Part B	Butyl benzyl phthalate	10-20
	Phenylmercuric neodecanoate	0.3-0.5

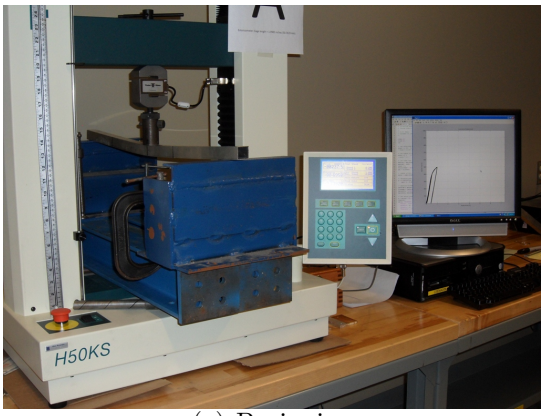

(a) Beginning

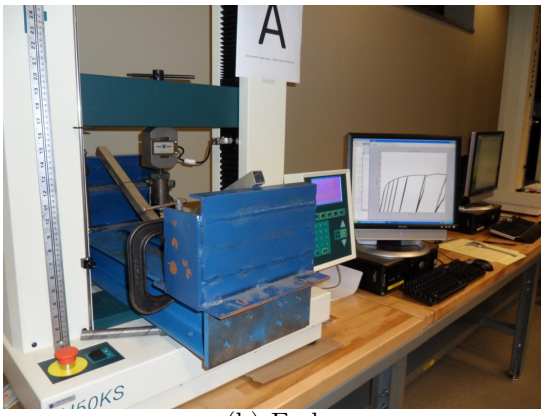

(b) End

FIGURE 9.11: Experimental setup for the composite beam at the beginning and at the end of the bending experiment. The applied load is plotted versus the cross-head displacement instantaneously, on the computer's screen.

observations are listed below:

- The two specimens have a comparable stiffness, in the linear range. The stiffness of the composite specimen is only slightly larger than that of the empty tube due to the presence of the Urethane infill.

- The initial proportional limit of the composite specimen (roughly 1735 N) is slightly larger than that of the empty tube (approximately 1645 N).

- The load-displacement curves show no significant mechanical synergies between the Aluminum casing and the Urethane infill, in the linear range of the ma-

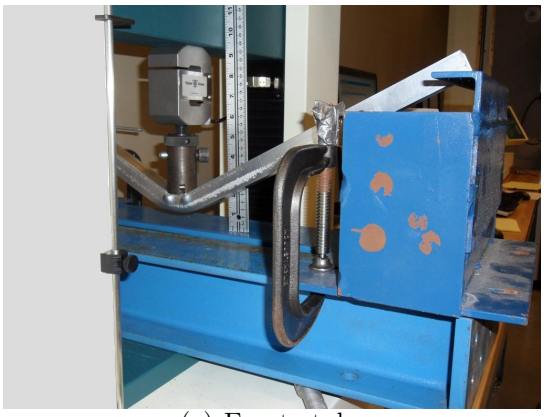

(a) Empty tube

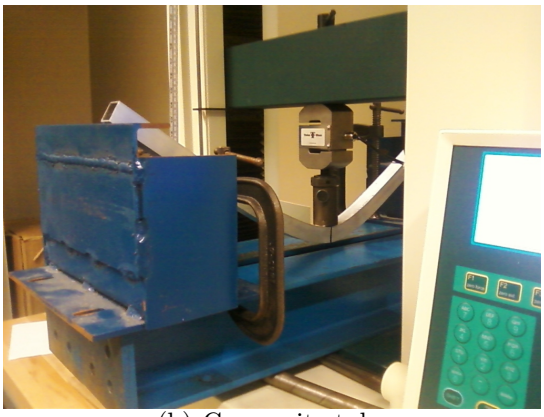

(b) Composite tube

FIGURE 9.12: Photos of the empty tube and of the composite beam taken right after the bending experiments. (a) Empty tube: two plastic hinges as well as significant local buckling of the walls can be seen right below the edges of the punch. (b) Composite tube: local buckling of the walls is prevented by the infill. Plastic deformations are better distributed along the length of the composite tube.

terials involved. This observation is consistent with the conclusions stated in Section 9.2.5. Hence, as predicted analytically, confining Urethane in an Aluminum tube does not result in a significantly larger elastic stiffness, or capacity, as compared to the empty tube.

- During both bending experiments, no particular observations, whether visual or auditive, called into question the integrity of the Urethane infill, nor the nature of the bonding between the two materials of the composite tube. Furthermore, the distances between the edges of the infill and the edges of the Aluminum casing measured before the experiment remained the same after the composite specimen was tested, i.e. 251 mm on one side and 171 mm on the other side.

- A control sample of Urethane cast in a 5 cm section of Aluminum tube and later pulled out, after a cure of eight days at room temperature, appeared to be covered by a thin layer of lubricating fluid. This may be an intended feature of the Urethane compound that was used, to facilitate demolding. The degree to

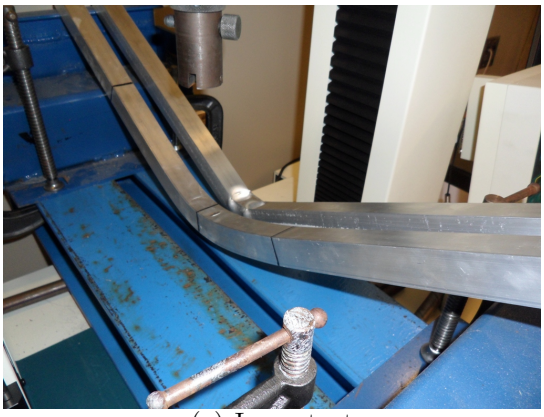

(a) In context

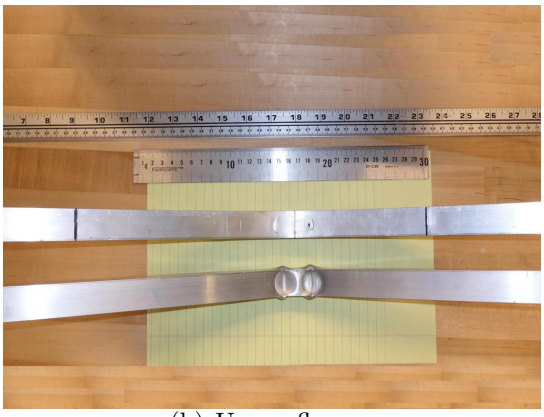

(b) Upper flanges

(c) Lateral walls

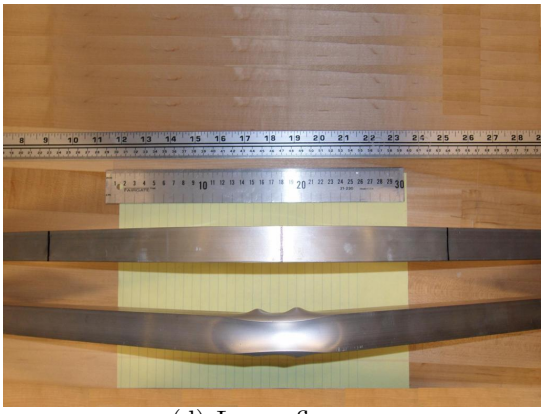

(d) Lower flanges

FIGURE 9.13: Comparing tube deformations after bending. The boundaries of the filled section of the composite tube and the point of application of the load are marked in black. Permanent bending deformations and local buckling of the walls can be seen in the middle section of the empty tube, in the vicinity of the region where the concentrated load was applied. Despite incurring very large deformations, the composite tube does not show signs of local wall-buckling. Furthermore, permanent deformations are better distributed along its length.

which the cast Urethane is actually bonded to the Aluminum tube is therefore unknown, at this stage of this research.

- A subtle change in slope, corresponding to an increase in stiffness, was observed for both specimens at a load of approximately 710 N. This observation was concomitant with a shift of the actual support lines towards the edges of the steel abutments, and therefore with a reduction of the effective length in

bending.

- The empty tube showed a significant local buckling of its walls, accompanied by large plastic deformations, in the vicinity of the applied load. In fact, two plastic hinges were observed at the edges of the (finite-dimensional) punch used to apply the load.

- The walls of the Urethane-filled tube did not buckle at all; in comparison with the empty specimen, plastic deformations were better distributed across the filled-section of the composite beam.

- The unfilled sections of the composite specimen remained straight after the test showing no sign of plastic deformations.

- The bending experiments induced a limited hardening of the empty tube: its linear range was increased roughly up to 1910 N. A more significant hardening was induced in the composite specimen, i.e. roughly up to 2890 N.

- Hysteresis loops were observed when loading/unloading both specimens. Their width increased with deformation amplitude, especially in the range of large deformations. This observation was concomitant with clearly observable sliding of both tubes on the abutments. It is hence suspected that the bulk of the dissipated energy is due to friction on the supports, although the possible contribution of the Urethane's viscoelasticity is unclear at this stage.

- Past a peak at roughly 1910 N, the load capacity of the empty tube decreases monotonically as the deformation increases. In contrast, the load capacity of the composite tube keeps on increasing with deformation, with a suspected peak at roughly 2890 N. At a displacement of 186.8 mm, the load capacity of the composite specimen is 2.18 times that of the empty tube.

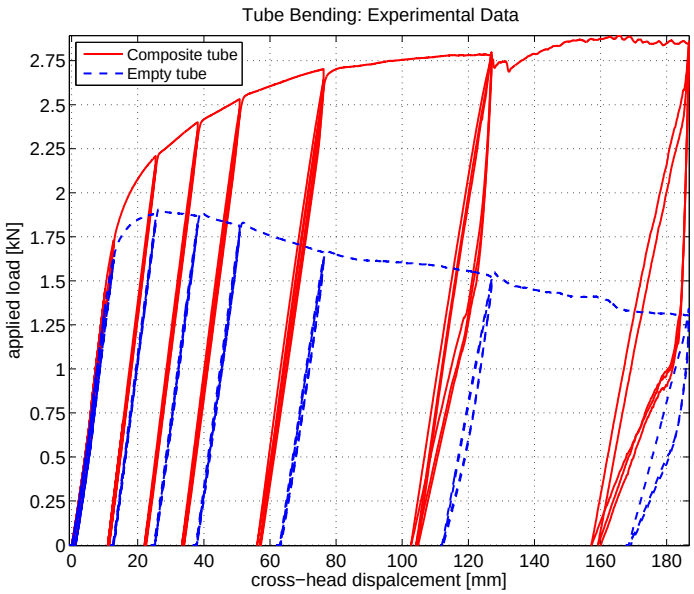

FIGURE 9.14: Experimental results: plot of the applied load versus the cross-head displacement for the two specimens. The proportional limit of the composite tube is slightly larger than that of the empty tube.

9.3.3 Discussion

Had the bending experiments been conducted under *load control*, which is often the case, for instance, in real structural settings, the empty Aluminum tube would have failed under a load of 1910 N, corresponding to a deflection of 26.5 mm (see Figure 9.14). In contrast, the Urethane-filled Aluminum tube would have resisted the applied load up to 2890 N, and perhaps even further. Indeed, although it was incurring very large deflections (up to 186.8 mm), the composite beam maintained a monotonously increasing resistance, i.e. plastic load capacity. This fact reveals that the Urethane infill plays a significant role in allowing the beam to reach and exploit its structural capacity resources further away from the point of application of the load. As a result, the ductile behavior of the composite beam is significantly improved. Indeed, the experiments show that, for the empty Aluminum tube, the

ratio of the ultimate load ($\approx$ 1910 N at 26.5 mm) to the 'elastic limit' ($\approx$ 1645 N at 13.0 mm), is relatively small (roughly 1.16); so is the ratio of the corresponding deflections (roughly 2.04). In contrast, the ratio of the ultimate capacity of the composite tube ($>$ 2890 N at 165.6 mm) to its 'elastic limit' ($\approx$ 1735 N at 13.0 mm) is significantly larger (roughly 1.67); the ratio of the corresponding deflections is even more so (roughly 12.74). Hence, filling Aluminum tubes with Urethane seems to result in a very ductile and therefore structurally safe material, capable of 'ever-increasing' resistance at very large deformations. Furthermore, although its plastic load capacity increases with deformation, the composite clearly shows a softening behavior, i.e. a decreasing stiffness under larger loads. This additional feature could play a key role in the attenuation of shock intensities and accelerations resulting from impacts.

9.4 Summary

To develop physical insight into the behavior of composite structural elements comprising a tubular casing and an infill, and to explore potential mechanical synergies between the materials involved, the axial behavior of filled circular tubes was studied and characterized analytically, in the linear range. The influences of the main, dimensionless, geometrical and material parameters on the structural performances of the composite were revealed and presented in a yet unpublished graphical form.

It was shown that significant improvements in structural stiffness and capacity at yield can be obtained by filling a relatively rigid tubular casing by a moderately softer, highly auxetic solid infill, bonded to the tube. This result emphasizes the importance of developing more auxetic materials without compromising their stiffness.

It was also shown that limited mechanical synergies can be expected between a metallic casing and a rubber-like or a polymeric infill. A three-point bending experiment conducted on an Aluminum-Urethane composite beam confirmed the latter

prediction in the elastic domain. However, interestingly and quite unexpectedly, significant improvements in ductility and in ultimate capacity were observed under large deformations. The resisting capacity of the composite increased monotonically with increasing deformations, up to very large deflections, while maintaining a softening behavior.

Based on the experimental results reported and discussed in this chapter, it may be concluded that the combination of lightweight metallic casings, such as an Aluminum tube, and lightweight polymeric infills, such as cast Urethane, could result in promising composites which may be of use in applications where structural elements are driven into the range of very large deformations and pushed up to their capacity at break, such as impacts. Such composite members could be used, for instance, in the design of novel, lightweight, and efficient vehicle retaining barriers, bumpers or safety frames in vehicles, as well as in other civil and defensive military applications.

The potential influence of such lightweight high-performance elements on the design, and on the structural and energetic efficiencies of future vehicles, structures and shields seems to justify that they be studied further. Future experiments on Aluminum-Urethane composite tubes will aim at investigating and characterizing: (i) the bonding between the two materials, (ii) the amount of structural damping added by the Urethane, (iii) the structural behavior of the composite under loads of alternating sign, such as earthquakes, (iv) temperature and loading rate response dependencies of the composite, and (v) its overall fatigue resistance. Future work will also focus on developing suitable models yielding accurate predictions of the composite's behavior under various loading conditions and in different ranges of the parameters involved. The formulation of simple methodologies for practical design will also be attempted.

10

Summary, conclusions, and future work

10.1 Summary and conclusions

The work presented in this dissertation draws upon and impacts the fields of computational mechanics, contact mechanics, material modeling, in small and in finite strain, linear and nonlinear viscoelasticity, material damage, damage induced anisotropy, rolling resistance, and the elastic and plastic behavior of composite structures. We briefly review below the main contributions presented in the previous chapters.

Most existing material models for elastomers are valid under specific loading regimes and in narrow ranges of loading parameters. Their predictive capabilities are also limited within these ranges; hence, much remains to be done in the modeling of rubbers. As a contribution to addressing this gap, we have developed in Chapter 2 (Zéhil and Gavin, 2013f) a new, unified, three-dimensional constitutive model for elastomers based on hyperelasticity, nonlinear viscoelasticity with multiple timescales, and a probabilistic description of damage. The proposed model is capable of replicating several aspects of the nonlinear behavior of rubber-like materials under

diverse loading conditions, including in finite strain and at high strain rates, while accounting for their softening under deformation (i.e. the Mullins effect) and for the anisotropy induced by their degradation.

Simple, novel and computationally efficient moving contact algorithms, in two and three dimensions, were presented in Chapter 3 (Zéhil and Gavin, 2013c). In many practical instances, these (frictional) contact solvers constitute appealing alternatives to existing solution strategies, based on constrained optimization, which are more cumbersome to implement.

A novel and computationally efficient three-dimensional boundary element formulation of an incompressible viscoelastic layer of arbitrary thickness was presented in Chapter 4 (Zéhil and Gavin, 2013e). The formulation is readily specialized to two-dimensional settings in plane stress, or in plane strain. These semi-analytical modeling techniques are based on Fourier series and can accommodate any viscoelastic model described, in the most general way, by frequency domain master-curves. The formulations result in a compliance matrix characterizing the mechanical behavior of the layers upper boundary, including the effects of steady-state motion. These characterizations can be used as model components in various problem settings, such as rolling or sliding contact problems, involving multiple indenters and layers, to generate sequences of high fidelity solutions for varying input parameters.

The abovementioned moving contact solving strategies (Chapter 3) and viscoelastic modeling techniques (Chapter 4) were successfully applied in two and three dimensions to determine, with high efficiency and accuracy, the rolling/sliding resistances incurred by rigid cylinders and spheres rolling on viscoelastic layers of arbitrary thickness, including hysteretic effects in the bulk and surface friction. In many instances however, the only quantity of interest is the viscous resistance to motion. In such cases, a comprehensive modeling of the viscoelastic component and the full resolution of a frictional moving contact problem can be avoided. To this aim, novel and highly

cost efficient computational tools were developed in Chapter 7 (Zéhil and Gavin, 2013d). These alternative modeling and solving strategies are based on simplifying assumptions, and yet provide rolling resistance estimates of suitable accuracy for most engineering applications.

New boundary element formulations of compressible isotropic, transversely isotropic and fully orthotropic viscoelastic layers were developed in Chapter 5 (Zéhil and Gavin, 2014c). These formulations involve an increasing number of frequency-dependent parameters and are intended to model naturally compressible or polar anisotropic materials such as cork and rubber-cork composites, or man-made materials, such as auxetic composites made of rubber-filled re-entrant honeycombs for instance, which are often characterized by different mechanical properties in three orthogonal directions. By applying these directional models to rolling/sliding resistance, it was shown that (i) the level of dissipation varies with the direction of motion, and that (ii) the moving object is subjected to a lateral force which tends to deviate it from its initial course. We discussed potential impacts of broader significance of these observations on the design of metamaterials and the engineering of systems to achieve motion control and optimize directional energy transfers in various applications (e.g. triage and velocity based sorting, vehicle handling and safety, and damping of seismic isolation systems) and fields (e.g. industry, transport, aerospace, defense, and risk mitigation).

A new boundary element formulation for the modeling of a rotating spherical coating composed of multiple viscoelastic layers was also developed in Chapter 6 (Zéhil and Gavin, 2013b). This formulation raised more difficulties than those corresponding to flat layers, mainly because of the particular nature of inertial effects in a spherical configuration, and to the coupling induced by the coordinate system in the frequency-domain equilibrium equations. These and other complexities described in Chapter 6 were overcome through appropriate choices of mathematical assumptions,

and tools, such as the theory of linear time-varying systems. The proposed model was applied, in combination with an adapted moving contact solving strategy (also described in Chapter 6), to the problem of the viscoelastic resistance incurred by a coated sphere rolling on a rigid plane, which, to our knowledge, had never been addressed in the scientific literature.

A novel experimental device, specifically designed and assembled to measure rolling resistance, was described in Chapter 8. The setup uses a controlled shake table to prescribe the horizontal motion, a vertical linear bearing to insure that the prescribed weight is applied to the rolling object, a load cell to measure the resisting force, and a data acquisition and processing system. Experiments were conducted on rigid spheres rolling at different velocities between sheets of rubber, while subjected to various weights. The primary sources of measurement error were discussed. It was shown that extreme care must be given to the design, and the choice of components, of any setup intended to measure viscoelastic friction. Experimental results were compared to rolling resistance predictions based on linear viscoelastic material models, characterized at different strain amplitudes. It was shown that the the Payne effect in filled elastomers has a significant influence on rolling resistance, which, in most practical cases, cannot be accounted for by computational tools based on the assumption of small deformations, and on linear viscoelastic material models.

In Chapter 9 (Zéhil and Gavin, 2014b), we presented theoretical and experimental work with the aim to explore and characterize the main conditions under which noticeable mechanical synergies occur when materials of different properties are combined in structural elements. An analytical study of the axial behavior of general casing-infill composite tubes was conducted and its results were presented in novel graphical forms. The study revealed that significant improvements in the performances of structural tubes could be obtained by filling those tubes with lightweight, but sufficiently stiff, and highly auxetic materials. It is however important to note

that the resulting performances would be highly sensitive to the Poisson ratio of the infill. Because most existing auxetic materials are too soft for such applications, new metamaterials must be developed. The analytical study also predicted that metal-polymer composite tubes would not present noticeable mechanical synergies, in the elastic range, due to their relative compressibility and stiffness. This prediction was confirmed by a bending experiment conducted on an Aluminum-Urethane composite tube. The experiment however revealed interesting properties of this composite element in the plastic range, i.e. a monotonically increasing capacity, combined with a highly ductile and progressively softening behavior, up to very large deformations. These properties, which seem suitable for lightweight impact-attenuation structures, justify that Aluminum-Urethane composite tubes be characterized further.

10.2 Directions for future research

This research led to the development of highly accurate and cost efficient modeling techniques and solving strategies for dynamic problems involving viscoelastic materials, under the assumption of linearity. The experimental work presented in Chapter 8 however revealed the challenges of modeling certain elastomers, in dynamic conditions, under relatively large deformations, such as those encountered in a fair proportion of practical cases of rolling resistance. These challenges mainly result from material nonlinearities occurring at moderate strain levels, such as the Payne effect, and from other material (e.g. the Mullins effect) and geometric nonlinearities resulting from larger deformations. Accurate predictions involving such materials and loading conditions must rely on nonlinear behavioral characterizations, such as the model proposed in Chapter 2, and on problem formulations capable of handling material and geometrical nonlinearities, such as finite element formulations.

A three-dimensional constitutive model for rubber-like materials, with even broader predictive capabilities than the model presented in Chapter 2 could be sought.

This projected material description would account for finite strain viscoelasticity in a wide range of strain-rates, plasticity, continuum damage, the Mullins effect, the Payne effect, the Mullins effect induced anisotropy, and the permanent set. Such a comprehensive model would most likely involve additional parameters. Practical procedures would need to be defined for the proper identification of all parameters from experimental data. Experimental procedures for validating the model would also need to be set, independently. Given their widespread use, the provision of a fully comprehensive multi-regime constitutive law for rubber-like materials would have a positive impact on design efficiency in different areas of engineering and result in considerable savings of resources. By reducing the need for approximations, the unified model would also improve the achievable accuracy in modeling actual systems. If successful, the projected task would provide the scientific and engineering communities worldwide with a powerful tool that would stimulate a broad range of innovative multi-regime applications. It would hence contribute to achieving resilient and sustainable infrastructures and systems. The projected model would also apply to many biological materials and ultimately benefit to human health.

The moving contact algorithms presented in Chapter 3 could be extended to problems comprising material nonlinearities. Such extensions would involve replacing the linear systems embedded in the solution processes by their nonlinear counterparts. The latter would be handled using suitable iterative solving schemes, rooted in the contact subroutines. The moving contact algorithms could be extended further to handle problems involving large deformations. These projected extensions would involve accounting for the horizontal displacements of the nodes while checking for and resolving geometrical conflicts.

According to the US department of energy, a nearly 30% difference in rolling friction transforms into an approximately 4.5% difference in fuel consumption for vehicles. This research had laid building blocks towards the predictive modeling of

rolling resistance. The modeling techniques and the solving strategies described in this dissertation could be extended for application to both vehicle tires and road pavements. One may furthermore choose to build on the results presented in Chapter 5 regarding rolling resistance directionality and lateral effects in anisotropic materials to explore new tire and pavement designs with the ultimate goal of developing safer and more energy-efficient vehicles.

The steady-state boundary element formulations of viscoelastic components presented in Chapters 4, 5 and 6, as well as the simplified approaches to rolling resistance proposed in Chapter 7, are semi-analytical modeling techniques relying on the combination of Fourier series expansions of physical fields and their spatial discretization. It would be interesting and useful to develop new approaches in truncation error analysis, specific to such modeling techniques, to study the propagation of truncation errors to relevant quantities of interest and outputs, such as rolling resistance results.

A novel Aluminum-Urethane structural composite exhibiting promising performances was introduced in Chapter 9. The structural properties and capabilities of this new material must be explored and characterized further, both in the elastic and the plastic domains. Future work would aim at investigating, for instance: (i) the bonding between the Aluminum tube and the Urethane infill, (ii) the structural damping-to-weight ratio of the composite, in comparison to that of the empty tube, (iii) the seismic behavior of the composite, (iv) the influence of temperature and loading rate on its structural response, and (v) its fatigue resistance. Future work would also focus on developing suitable predictive models for the composite, and on the formulation of simple methodologies for practical design.

In Harvey et al. (2013), we discussed the benefits of the added (rolling resistance-based) damping obtained by adhering thin viscoelastic rubber sheets to the bowl-shaped steel plates of the Ball-N-Cone^{TM}rolling seismic isolation system. This partic-

ular arrangement may however exhibit a few shortcomings. Indeed, under long-term static loading, creep in the rubber sheets may result in undesirable depressions below the ball-bearings. Furthermore, with the aging of the rubber material and of the bonding agent, the rubber sheets may pose a greater risk of rapid wear, tear, or delamination, in the event of an earthquake. An alternative solution would be to replace (or possibly cover) the steel bowls of such rolling seismic isolation systems by a cast material composed of a mixture of a possibly recycled polymer, or copolymer[1], and a hard filler, such as sand for instance, in appropriate proportions, so as to achieve an optimal balance between resistance, stiffness, durability and damping. The molds in which such dished components would be cast could be easily adapted to produce specific bowl shapes so as to optimize the dynamic performances of the rolling isolator in particular seismic environments and setup configurations. The exploration of suitable material compositions and bowl shapes constitute two interesting research directions that could be perused in the future.

From another perspective, it is interesting to note that, although added damping can improve the dynamic performances of rolling seismic isolation systems, fitting a source of damping, such as rubber sheets, right into the rolling mechanisms, between the ball-bearings and their dishes, is practically constraining and raises some difficulties, such as those mentioned above. Other cost-efficient solutions may be found by setting damping devices, which may comprise viscoelastic elements, or simply viscous dashpots, in parallel to the isolating and restoring mechanisms. The exploration of potential alternatives of this type is yet another direction of research that one may choose to follow.

[1] This component could be derived, for instance, from ground or crumb vehicle tires, which would contribute to the treatment of this large and problematic source of waste.

Appendix A

Supplemental materials

A.1 On the convergence of the boundary element formulations

We touch briefly upon the limiting behavior of the boundary element formulations developed in this work, as the spatial mesh is refined. For simplicity and without prejudice to the generality of this analysis, we consider the problem in two dimensions, as depicted in Figure A.1.

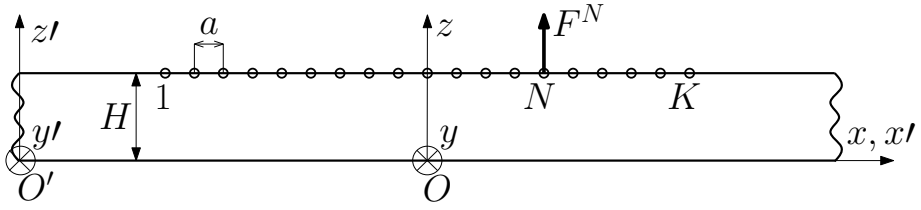

FIGURE A.1: Two-dimensional setting: discretized boundary.

First, we briefly review the case corresponding to a finite spacing a between nodes. A unit point load F^N is applied at a given node N of the grid. The surface stress

distribution associated with F^N is defined as

$$\sigma^N(x, z = H) = \begin{cases} \frac{F^N}{a}, & \text{if } x^N - \frac{a}{2} \leq x \leq x^N + \frac{a}{2} \\ 0, & \text{otherwise.} \end{cases} \tag{A.1}$$

The stress field in expression A.1 is then expanded into a trigonometric Fourier series of the form

$$\sigma^N(x, z = H) = \sum_{m=-\infty}^{\infty} \sigma_m^N(H)\, e^{i\nu_m x}, \tag{A.2}$$

where $\nu_m = 2\pi m/L$, L being the spatial period in the variable x. Fourier coefficients appearing in A.2 write

$$\begin{aligned} \sigma_m^N(H) =& \frac{1}{L} \int_{-\frac{L}{2}}^{\frac{L}{2}} \frac{F^N}{a} e^{-i\nu_m x} dx, \\ =& \frac{1}{L} \int_{x^N - \frac{a}{2}}^{x^N + \frac{a}{2}} \frac{F^N}{a} e^{-i\nu_m x} dx, \\ =& \frac{F^N}{L} \operatorname{sinc}(\nu_m a/2)\, e^{-i\nu_m x^N}. \end{aligned} \tag{A.3}$$

Fourier coefficients of displacements are deduced from equation A.3 using the analytical expression below

$$\mathbf{d}_{mn}(H) = \mathbf{T}_{mn,12}(H)\, \mathbf{T}_{mn,22}^{-1}(H)\, \mathbf{f}_{mn}(H). \tag{A.4}$$

We now examine the limiting case as the nodal spacing a tends to zero. At first sight, expression A.1 may seem to 'blow up' (i.e. tend to infinity) as a approaches zero. In fact, when $a \to 0$, the surface stress field corresponding to F^N may be written as

$$\sigma^N(x, z = H) = F^N \delta\left(x^N\right), \tag{A.5}$$

where $\delta(\xi)$ is a "delta" distribution. Consequently, the Fourier coefficients appearing in A.2 become

$$\sigma_m^N(H) = \frac{1}{L} \int_{-L/2}^{L/2} F^N \delta(x^N) e^{-i\nu_m x} dx,$$

$$= \frac{F^N}{L} e^{-i\nu_m x^N}. \tag{A.6}$$

Hence, when the nodal spacing tends to zero, expression A.3 reduces to A.6, which is consistent with the fact that $\operatorname{sinc}(0) = \lim_{\xi \to 0} \sin(\xi)/\xi = 1$.

In fact, equation A.6 corresponds to the exact Fourier series expansion of the surface stress field resulting from a point load applied at node N. Since expression A.4 is analytical, it is also exact. We may therefore conclude that the numerical solution approaches the exact solution as the spatial mesh is refined: the method is convergent.

A.2 Intermediate steps between equations (2.6) and (2.7)

Intermediate steps between equations (2.6) and (2.7) are detailed hereafter: equation (2.6) is pushed forward to the current configuration, in the usual way, to yield

$$\boldsymbol{\sigma}_j = \mathbf{F}_j \frac{\partial U_j}{\partial \mathbf{E}_j} \mathbf{F}_j^T + p_j \mathbf{I}. \tag{A.7}$$

The chain rule is then applied to $\partial U_j / \partial \mathbf{E}_j$, for instance in terms of the first two invariants of $\mathbf{C}_j$, i.e. $I_{\mathbf{C}_j} = \operatorname{trace}(\mathbf{C}_j)$ and $II_{\mathbf{C}_j} = \frac{1}{2}\left(I_{\mathbf{C}_j}^2 - \operatorname{trace}(\mathbf{C}_j^2)\right)$, as follows

$$\begin{aligned}
\frac{\partial U_j}{\partial \mathbf{E}_j} = 2\frac{\partial U_j}{\partial \mathbf{C}_j} &= 2\frac{\partial U_j}{\partial I_{\mathbf{C}_j}} \frac{\partial I_{\mathbf{C}_j}}{\partial \mathbf{C}_j} + 2\frac{\partial U_j}{\partial II_{\mathbf{C}_j}} \frac{\partial II_{\mathbf{C}_j}}{\partial \mathbf{C}_j} \\
&= 2\frac{\partial U_j}{\partial I_{\mathbf{C}_j}} \mathbf{I} + 2\frac{\partial U_j}{\partial II_{\mathbf{C}_j}} \left(I_{\mathbf{C}_j} \mathbf{I} - \mathbf{C}_j\right) \\
&= 2\left(\frac{\partial U_j}{\partial I_{\mathbf{C}_j}} + I_{\mathbf{C}_j} \frac{\partial U_j}{\partial II_{\mathbf{C}_j}}\right) \mathbf{I} - 2\frac{\partial U_j}{\partial II_{\mathbf{C}_j}} \mathbf{C}_j.
\end{aligned} \tag{A.8}$$

Recalling that tensors $\mathbf{b}_j$ and $\mathbf{C}_j$ have the same invariants, equation (2.7) is readily obtained by substituting expression (A.8) into (A.7) and rearranging terms.

A.3 Two-variable periodicity of physical fields in a spherical coordinate system

Consider a generic physical field $\hat{f}(r, \phi, \theta)$ in the continuum of the sphere's viscoelastic coating, where the spherical coordinates r, ϕ and θ designate the radius, the azimuth (or longitude) and the inclination (or latitude), respectively. The vertical projection of the sphere's center-point C onto the hard plane corresponds to the angular coordinates $\phi = \pi/2$ and $\theta = \pi/2$. In practice, contact occurs for values of ϕ and θ over a small surface in the neighborhood of $\pi/2$.

The azimuth ϕ belongs to the interval $]-\pi, +\pi]$. The function of the single variable ϕ denoted by $\hat{f}_{r,\theta}(\phi) = \hat{f}(r, \phi, \theta)$, for fixed values of r and θ, can be extended to a 2π-periodic function in ϕ over the real line $\mathbb{R}$, by defining $f_{r,\theta}(\phi + 2k\pi) = \hat{f}_{r,\theta}(\phi)$ for any $\phi \in]-\pi, +\pi]$ and any integer k.

The latitude θ belongs to the interval $[0, +\pi]$. The function of the single variable θ denoted by $\hat{f}_{r,\phi}(\theta) = \hat{f}(r, \phi, \theta)$ for fixed values of r and ϕ can be extended to a 2π-periodic function in θ over $\mathbb{R}$, in two steps:

1. from $[0, +\pi]$ to $]-\pi, +\pi]$, by defining

$$\tilde{f}_{r,\phi}(\theta) = \begin{cases} \hat{f}_{r,\phi}(\theta), & \text{for } \theta \in [0, +\pi], \\ 0, & \text{for } \theta \in]-\pi, 0[, \end{cases} \tag{A.9}$$

2. then, from $]-\pi, +\pi]$ to $\mathbb{R}$: by defining $f_{r,\phi}(\theta + 2k\pi) = \tilde{f}_{r,\phi}(\theta)$ for any $\theta \in]-\pi, +\pi]$ and any integer k.

For any admissible value of the variable r, the functions $f_{r,\theta}(\phi)$ with $\phi \in \mathbb{R}$, and $f_{r,\phi}(\theta)$ with $\theta \in \mathbb{R}$, are the restrictions to constant ϕ, and constant θ, respectively, of the 2π-periodic function $f(r, \phi, \theta)$ in the two variables ϕ and θ, which is addressed in Section 6.6.

Bibliography

Ahmad, I., Zhu, Z., and Mirmiran, A. (2008a), "Behavior of Short and Deep Beams Made of Concrete-Filled Fiber-Reinforced Polymer Tubes," *Journal of Composites for Construction*, 12, 102–110.

Ahmad, I., Zhu, Z., and Mirmiran, A. (2008b), "Fatigue Behavior of Concrete-Filled Fiber-Reinforced Polymer Tubes," *Journal of Composites for Construction*, 12, 478–487.

Alderson, A. (1999), "A triumph of lateral thought," *Chemistry & Industry*, 10, 384–391.

Alderson, A. and Alderson, K. L. (2007), "Auxetic materials," *Proceedings of the Institution of Mechanical Engineers, Part G: Journal of Aerospace Engineering*, 221, 565–575.

Alderson, A. and Evans, K. (1995), "Microstructural modelling of auxetic microporous polymers," *Journal of Materials Science*, 30, 3319–3332.

Alderson, A., Alderson, K., Attard, D., Evans, K., Gatt, R., Grima, J., Miller, W., Ravirala, N., Smith, C., and Zied, K. (2010a), "Elastic constants of 3-, 4- and 6-connected chiral and anti-chiral honeycombs subject to uniaxial in-plane loading," *Composites Science and Technology*, 70, 1042 – 1048, Special issue on Chiral Smart Honeycombs.

Alderson, A., Alderson, K., Chirima, G., Ravirala, N., and Zied, K. (2010b), "The in-plane linear elastic constants and out-of-plane bending of 3-coordinated ligament and cylinder-ligament honeycombs," *Composites Science and Technology*, 70, 1034 – 1041, Special issue on Chiral Smart Honeycombs.

Alderson, K. and Evans, K. (1992), "The fabrication of microporous polyethylene having a negative Poisson's ratio," *Polymer*, 33, 4435 – 4438.

Alderson, K. and Evans, K. (1993), "Strain-dependent behaviour of microporous polyethylene with a negative Poisson's ratio," *Journal of Materials Science*, 28, 4092–4098.

Alderson, K., Pickles, A., Neale, P., and Evans, K. (1994), "Auxetic polyethylene: The effect of a negative poisson's ratio on hardness," *Acta Metallurgica et Materialia*, 42, 2261 – 2266.

Alderson, K. L., Simkins, V. R., Coenen, V. L., Davies, P. J., Alderson, A., and Evans, K. E. (2005), "How to make auxetic fibre reinforced composites," *physica status solidi (b)*, 242, 509–518.

Ang, A. and Tang, W. (2007), *Probability concepts in engineering: emphasis on applications in civil & environmental engineering*, Wiley.

Arnold, J. W. (1985), "Predicting vibratory sorting probability of viscoelastic spheres," M.S. dissertation, Ohio State University.

Arruda, E. M. and Boyce, M. C. (1993), "A three-dimensional constitutive model for the large stretch behavior of rubber elastic materials," *Journal of the Mechanics and Physics of Solids*, 41, 389 – 412.

Assidi, M. and Ganghoffer, J.-F. (2012), "Composites with auxetic inclusions showing both an auxetic behavior and enhancement of their mechanical properties," *Composite Structures*, 94, 2373 – 2382.

Atsbha, H. (1993), "Viscoelastic flows around spheres," M.A.S. dissertation, University of Ottawa.

Bahadur, S. and Schwartz, C. J. (2008), *Tribology of Polymeric Nanocomposites*, vol. 55 of *Tribology and Interface Engineering Series*, Elsevier.

Bambusi, D. and Haus, E. (2012), "Asymptotic stability of synchronous orbits for a gravitating viscoelastic sphere," *Celestial Mechanics and Dynamical Astronomy*, 114, 255–277.

Barber, J., Ciavarella, M., Afferrante, L., and Sackfield, A. (2008), "Effect of small harmonic oscillations during the steady rolling of a cylinder on a plane," *International Journal of Mechanical Sciences*, 50, 1344–1353.

Baughman, R. H., Shacklette, J. M., Zakhidov, A. A., and Stafstrom, S. (1998), "Negative Poisson's ratios as a common feature of cubic metals," *Nature*, 392, 362–365.

Bažant, P. and Oh, B. H. (1986), "Efficient Numerical Integration on the Surface of a Sphere," *ZAMM - Journal of Applied Mathematics and Mechanics / Zeitschrift fr Angewandte Mathematik und Mechanik*, 66, 37 – 49.

Berg, M. A. (1999), "A viscoelastic continuum model of nonpolar solvation. III. Electron solvation and nonlinear coupling effects," *The Journal of Chemical Physics*, 110, 8577–8588.

Bezazi, A., Scarpa, F., and Remillat, C. (2005), "A novel centresymmetric honeycomb composite structure," *Composite Structures*, 71, 356 – 364, Fifth International Conference on Composite Science and Technology ICCST/5.

Bir, C. A., Resslar, M., and Stewart, S. (2012), "Skin penetration surrogate for the evaluation of less lethal kinetic energy munitions," *Forensic Science International (Online)*, 220, 126–129.

Blake D. Mills, J. (1960), "The Fluid Column," *American Journal of Physics*, 28, 353–356.

Bogy, D. B. (1968), "Edge-Bonded Dissimilar Orthogonal Elastic Wedges Under Normal and Shear Loading," *Journal of Applied Mechanics*, 35, 460–466.

Bonet, J. and Wood, R. (2008), *Nonlinear Continuum Mechanics for Finite Element Analysis*, Cambridge University Press, 6 edn.

Boresi, A. and Schmidt, R. (2003), *Advanced Mechanics of Materials*, John Wiley & Sons, 6 edn.

Bose, S., Das, S. K., Karp, J. M., and Karnik, R. (2010), "A Semianalytical Model to Study the Effect of Cortical Tension on Cell Rolling," *Biophysical journal*, 99, 3870–3879.

Boucher, M.-A., Smith, C., Scarpa, F., Rajasekaran, R., and Evans, K. (2013), "Effective topologies for vibration damping inserts in honeycomb structures," *Composite Structures*, 106, 1 – 14.

Boyce, M. C. and Arruda, E. M. (2000), "Constitutive models of rubber elasticity: a review," *Rubber Chemistry and Technology*, 73, 504 – 523.

Braun, D., Kennedy, S. J., Kennedy, D. L., and Allen, D. E. (2002), "Sandwich plate system risers for stadia," in *SSRC 2002 Annual Stability Conference*.

Brilliantov, N. V. and Pöschel, T. (1998), "Rolling friction of a viscous sphere on a hard plane," *Europhysics Letters*, 42, 511–516.

Brown, J. D. (1997), "Nonlinear dynamic behavior of filled elastomers at small strain amplitudes," *Graduate Faculty of Rensselaer Polytechnic Institute*, p. Ph.D. dissertation.

Bueche, A. M. and Flom, D. G. (1959), "Surface friction and dynamic mechanical properties of polymers," *Wear*, 2, 168–182.

Caddock, B. D. and Evans, K. E. (1989), "Microporous materials with negative Poisson's ratios. I. Microstructure and mechanical properties," *Journal of Physics D: Applied Physics*, 22, 1877.

Carbone, G. and Mangialardi, L. (2008), "Analysis of the adhesive contact of confined layers by using a Green's function approach," *Journal of the Mechanics and Physics of Solids*, 56, 684–706.

Carbone, G. and Putignano, C. (2013), "A novel methodology to predict sliding and rolling friction of viscoelastic materials: Theory and experiments," *Journal of the Mechanics and Physics of Solids*, 61, 1822 – 1834.

Carbone, G., Lorenz, B., Persson, B., and Wohlers, A. (2009), "Contact mechanics and rubber friction for randomly rough surfaces with anisotropic statistical properties," *The European Physical Journal E*, 29, 275–284.

Chagnon, G., Verron, E., Gornet, L., Marckmann, G., and Charrier, P. (2004), "On the relevance of Continuum Damage Mechanics as applied to the Mullins effect in elastomers," *Journal of the Mechanics and Physics of Solids*, 52, 1627 – 1650.

Chagnon, G., Verron, E., Marckmann, G., and Gornet, L. (2006), "Development of new constitutive equations for the Mullins effect in rubber using the network alteration theory," *International Journal of Solids and Structures*, 43, 6817 – 6831.

Chan, N. and Evans, K. (1997), "Fabrication methods for auxetic foams," *Journal of Materials Science*, 32, 5945–5953.

Chan, N. and Evans, K. E. (1998), "Indentation Resilience of Conventional and Auxetic Foams," *Journal of Cellular Plastics*, 34, 231–260.

Chan, N. and Evans, K. E. (1999a), "The Mechanical Properties of Conventional and Auxetic Foams. Part I: Compression and Tension," *Journal of Cellular Plastics*, 35, 130–165.

Chan, N. and Evans, K. E. (1999b), "The Mechanical Properties of Conventional and Auxetic Foams. Part II: Shear," *Journal of Cellular Plastics*, 35, 166–183.

Chang, X., Huang, C.-K., and Chen, Y.-J. (2009), "Mechanical performance of eccentrically loaded pre-stressing concrete filled circular steel tube columns by means of expansive cement," *Engineering Structures*, 31, 2588 – 2597.

Chen, C. and Lakes, R. (1991), "Holographic study of conventional and negative Poisson's ratio metallic foams: elasticity, yield and micro-deformation," *Journal of Materials Science*, 26, 5397–5402.

Chertok, D. L., Golden, J. M., and Graham, G. A. C. (2001), "Hysteretic Friction for the Transient Rolling Contact Problem of Linear Viscoelasticity," *Journal of Applied Mechanics*, 68, 589–595.

Choi, J. and Lakes, R. (1992a), "Non-linear properties of metallic cellular materials with a negative Poisson's ratio," *Journal of Materials Science*, 27, 5375–5381.

Choi, J. and Lakes, R. (1992b), "Non-linear properties of polymer cellular materials with a negative Poisson's ratio," *Journal of Materials Science*, 27, 4678–4684.

Choi, J. and Lakes, R. (1995), "Analysis of elastic modulus of conventional foams and of re-entrant foam materials with a negative Poisson's ratio," *International Journal of Mechanical Sciences*, 37, 51 – 59.

Chung, K. (2010), "Prediction of pre- and post-peak behavior of concrete-filled circular steel tube columns under cyclic loads using fiber element method," *Thin-Walled Structures*, 48, 169 – 178.

Coghill, P. A. (2012), "The role of cell deformation during selectin-mediated neutrophil rolling," Ph.D. dissertation, University of Oklahoma.

Coleman, B. D. and Gurtin, M. E. (1967), "Thermodynamics with Internal State Variables," *The Journal of Chemical Physics*, 47, 597 – 613.

Coleman, B. D. and Noll, W. (1963), "The thermodynamics of elastic materials with heat conduction and viscosity," *Archive for Rational Mechanics and Analysis*, 13, 167 – 178.

Coulomb, C. (1821), *Théorie des machines simples: en ayant égard au frottement de leurs parties et à la roideur des cordages*, Bachelier.

Dahl, P. R. (1968), "A solid friction model," .

Dahl, P. R. (1976), "Solid Friction Damping of Mechanical Vibrations," *AIAA Journal*, 14, 1675 – 1682.

D'Ambrosio, P., De Tommasi, D., Ferri, D., and Puglisi, G. (2008), "A phenomenological model for healing and hysteresis in rubber-like materials," *International Journal of Engineering Science*, 46, 293 – 305.

Dargazany, R. and Itskov, M. (2009), "A network evolution model for the anisotropic Mullins effect in carbon black filled rubbers," *International Journal of Solids and Structures*, 46, 2967 – 2977.

De Tommasi, D., Puglisi, G., and Saccomandi, G. (2006), "A micromechanics-based model for the Mullins effect," *Journal of Rheology*, 50, 495 – 512.

Deng, Y., Tuan, C., Zhou, Q., and Xiao, Y. (2011), "Flexural strength analysis of non-post-tensioned and post-tensioned concrete-filled circular steel tubes," *Journal of Constructional Steel Research*, 67, 192 – 202.

Diani, J., Brieu, M., and Vacherand, J. (2006), "A damage directional constitutive model for Mullins effect with permanent set and induced anisotropy," *European Journal of Mechanics - A/Solids*, 25, 483 – 496.

Diani, J., Fayolle, B., and Gilormini, P. (2009), "A review on the Mullins effect," *European Polymer Journal*, 45, 601 – 612.

Dirrenberger, J., Forest, S., Jeulin, D., and Colin, C. (2011), "Homogenization of periodic auxetic materials," *Procedia Engineering*, 10, 1847 – 1852, 11th International Conference on the Mechanical Behavior of Materials (ICM11).

Dirrenberger, J., Forest, S., and Jeulin, D. (2012), "Elastoplasticity of auxetic materials," *Computational Materials Science*, 64, 57 – 61, Proceedings of the 21st International Workshop on Computational Mechanics of Materials (IWCMM 21).

Dorfmann, A. and Ogden, R. (2004), "A constitutive model for the Mullins effect with permanent set in particle-reinforced rubber," *International Journal of Solids and Structures*, 41, 1855 – 1878.

Dorfmann, A. and Pancheri, F. (2012), "A constitutive model for the Mullins effect with changes in material symmetry," *International Journal of Non-Linear Mechanics*, 47, 874 – 887.

Drapaca, C. S., Sivaloganathan, S., and Tenti, G. (2007), "Nonlinear Constitutive Laws in Viscoelasticity," *Mathematics and Mechanics of Solids*, 12, 475 – 501.

Drozdov, A. D. and Dorfmann, A. (2004), "A Constitutive Model in Finite Viscoelasticity of Particle-reinforced Rubbers," *Meccanica*, 39, 245 – 270.

Eakasit, S., Gunasekaran, S., and Lakes, R. S. (2009), "Broadband Viscoelastic Spectroscopy: A New Technique for Characterizing Rheological Behavior of Solid Foods," *International Journal of Food Properties*, 12, 102–113.

Els, D. N. J. (2009), "The Effectiveness of Particle Dampers under Centrifugal Loads," Ph.D. dissertation, University of Stellenbosch.

Esat, I. I. and Ozada, N. (2010), "Articular human joint modelling," *Robotica*, 28, 321–339.

Evans, K. (1990), "Tailoring the negative Poisson's ratio," *Chemistry and Industry*, pp. 654–657.

Evans, K. and Alderson, K. (1992), "The static and dynamic moduli of auxetic microporous polyethylene," *Journal of Materials Science Letters*, 11, 1721–1724.

Evans, K. E. (1989), "Tensile network microstructures exhibiting negative Poisson's ratios," *Journal of Physics D: Applied Physics*, 22, 1870.

Evans, K. E. and Alderson, A. (2000), "Auxetic Materials: Functional Materials and Structures from Lateral Thinking!" *Advanced Materials*, 12, 617–628.

Evans, K. E. and Caddock, B. D. (1989), "Microporous materials with negative Poisson's ratios. II. Mechanisms and interpretation," *Journal of Physics D: Applied Physics*, 22, 1883.

Fam, A. and Cole, B. (2007), "Tests on reinforced-concrete-filled, fiber-reinforced-polymer circular tubes of different shear spans," *Canadian Journal of Civil Engineering*, 34, 311–322.

Fam, A. and Rizkalla, S. (2002), "Flexural Behavior of Concrete-Filled Fiber-Reinforced Polymer Circular Tubes," *Journal of Composites for Construction*, 6, 123–132.

Fan, Z., Shen, J., Lu, G., and Ruan, D. (2013), "Dynamic lateral crushing of empty and sandwich tubes," *International Journal of Impact Engineering*, 53, 3 – 16, Special issue based on contributions at the 3rd International Conference on Impact Loading of Lightweight Structures.

Fletcher, W. P. and Gent, A. N. (1953), "Non-Linearity in the Dynamic Properties of Vulcanised Rubber Compounds," *Transactions of the Institution of the Rubber Industry*, 29, 266 – 280.

Fletcher, W. P. and Gent, A. N. (1954), "Nonlinearity in the Dynamic Properties of Vulcanized Rubber Compounds," *Rubber Chemistry and Technology*, 27, 209 – 222.

Flom, D. G. (1960), "Rolling friction of polymeric materials. I. Elastomers," *Journal of Applied Physics*, 31, 306–314.

Flom, D. G. and Bueche, A. M. (1959), "Theory of Rolling Friction for Spheres," *Journal of Applied Physics*, 30, 1725–1730.

Flügge, W. (1975), *Viscoelasticity*, Springer-Verlag.

Fozdar, D. Y., Soman, P., Lee, J. W., Han, L.-H., and Chen, S. (2011), "Three-Dimensional Polymer Constructs Exhibiting a Tunable Negative Poisson's Ratio," *Advanced Functional Materials*, 21, 2712–2720.

Friis, E., Lakes, R., and Park, J. (1988), "Negative Poisson's ratio polymeric and metallic foams," *Journal of Materials Science*, 23, 4406–4414.

Fung, Y. and Tong, P. (2001), *Classical and Computational Solid Mechanics*, Advanced Series in Engineering Science Series, World Scientific.

Galin, L. and Gladwell, G. (2008), *Contact Problems: The Legacy of L.A. Galin*, Solid Mechanics and Its Applications, Springer.

Gaspar, N., Smith, C. W., and Evans, K. E. (2003), "Effect of heterogeneity on the elastic properties of auxetic materials," *Journal of Applied Physics*, 94, 6143–6149.

Gent, A. N. (1996), "A new constitutive relation for rubber," *Rubber Chemistry and Technology*, 69, 59 – 61.

Gillibert, J., Brieu, M., and Diani, J. (2010), "Anisotropy of direction-based constitutive models for rubber-like materials," *International Journal of Solids and Structures*, 47, 640 – 646.

Golden, J. and Graham, G. (2001), "The problem of a viscoelastic cylinder rolling on a rigid half-space," *Mathematical and Computer Modelling*, 34, 1363–1397.

Greaves, G. N., Greer, A. L., Lakes, R. S., and Rouxel, T. (2011), "Poisson's ratio and modern materials," *Nature Materials*, 10, 823–837.

Greenwood, J. A. and Tabor, D. (1958), "The Friction of Hard Sliders on Lubricated Rubber: The Importance of Deformation Losses," *Proceedings of the Physical Society*, 71, 989.

Greenwood, J. A., Minshall, H., and Tabor, D. (1961), "Hysteresis Losses in Rolling and Sliding Friction," *Proceedings of the Royal Society of London. Series A, Mathematical and Physical Sciences*, 259, 480–507.

Grima, J. N., Alderson, A., and Evans, K. E. (2005), "Auxetic behaviour from rotating rigid units," *physica status solidi (b)*, 242, 561–575.

Grima, J. N., Zammit, V., Gatt, R., Alderson, A., and Evans, K. E. (2007), "Auxetic behaviour from rotating semi-rigid units," *physica status solidi (b)*, 244, 866–882.

Grima, J. N., Cauchi, R., Gatt, R., and Attard, D. (2013), "Honeycomb composites with auxetic out-of-plane characteristics," *Composite Structures*, 106, 150 – 159.

Ha-Anh, T. (2008), *Influence of thermo-oxidative aging on the mechanical behaviors of polychloroprene*, Library and Archives Canada.

Ha-Anh, T. and Vu-Khanh, T. (2005a), "Effects of thermal aging on fracture performance of polychloroprene," *Journal of Materials Science*, 40, 5243–5248.

Ha-Anh, T. and Vu-Khanh, T. (2005b), "Prediction of mechanical properties of polychloroprene during thermo-oxidative aging," *Polymer Testing*, 24, 775 – 780.

Hall, D. E. (2001), "Fundamentals of rolling resistance," *Rubber Chemistry and Technology*, 74, 525–525.

Hall, L. J., Coluci, V. R., Galvo, D. S., Kozlov, M. E., Zhang, M., Dantas, S. O., and Baughman, R. H. (2008), "Sign Change of Poisson's Ratio for Carbon Nanotube Sheets," *Science*, 320, 504–507.

Han, L.-H. (2004), "Flexural behaviour of concrete-filled steel tubes," *Journal of Constructional Steel Research*, 60, 313 – 337.

Harvey, Jr., P. S., Zéhil, G.-P., and Gavin, H. P. (2013), "Experimental validation of simplified models for rolling isolation systems," *Earthquake Engineering and Structural Dynamics*, (in print).

Hertz, H. (1881), "Über die Berührung fester elastischer Körper (On contact between elastic bodies)," *Journal für die reine und angewandte Mathematik*, 92, 156–171.

Holzapfel, G. (2000), *Nonlinear solid mechanics: a continuum approach for engineering*, Wiley.

Hoo Fatt, M. S. and Ouyang, X. (2007), "Integral-based constitutive equation for rubber at high strain rates," *International Journal of Solids and Structures*, 44, 6491 – 6506.

Hoo Fatt, M. S. and Ouyang, X. (2008), "Three-dimensional constitutive equations for Styrene Butadiene Rubber at high strain rates," *Mechanics of Materials*, 40, 1 – 16.

Horgan, C. O., Ogden, R. W., and Saccomandi, G. (2004), "A theory of stress softening of elastomers based on finite chain extensibility," *Proceedings of the Royal Society of London. Series A: Mathematical, Physical and Engineering Sciences*, 460, 1737 – 1754.

Hou, X., Hu, H., and Silberschmidt, V. (2012), "A novel concept to develop composite structures with isotropic negative Poisson's ratio: Effects of random inclusions," *Composites Science and Technology*, 72, 1848 – 1854.

Huber, N. and Tsakmakis, C. (2000), "Finite deformation viscoelasticity laws," *Mechanics of Materials*, 32, 1 – 18.

Hughes, T. (2000), *The finite element method: linear static and dynamic finite element analysis*, Dover Civil and Mechanical Engineering Series, Dover Publications.

Hunter, S. (1961), "The Rolling Contact of a Rigid Cylinder With a Viscoelastic Half Space," *Journal of Applied Mechanics*, 28, 611–617.

Hunter, S. C. (1968), "The motion of a rigid sphere embedded in an adhering elastic or viscoelastic medium," *Proceedings of the Edinburgh Mathematical Society (Series 2)*, 16, 55–69.

Itskov, M., Haberstroh, E., Ehret, A., and Vhringer, M. (2006), "Experimental observation of the deformation induced anisotropy of the Mullins effect in rubber," *Kautschuk Gummi Kunststoffe*, 3, 93 – 96.

Jaffar, M. (1988), "A numerical solution for axisymmetric contact problems involving rigid indenters on elastic layers," *Journal of the Mechanics and Physics of Solids*, 36, 401–416.

Jaffar, M. (1997), "A general solution to the axisymmetric frictional contact problem of a thin bonded elastic layer," *Proceedings of the Institution of Mechanical Engineering*, 211, 549–558.

Jaffar, M. (2008), "On the frictionless axi-symmetric contact of a thick elastic layer and the associated squeeze film problem," *Proceedings of the Institution of Mechanical Engineering Part J, Journal of Engineering Tribology*, 222, 61–68.

Johnson, K. (1985), *Contact mechanics*, Cambridge University Press, Cambridge.

Kachanov, L. (1986), *Introduction to Continuum Damage Mechanics*, vol. 10 of *Mechanics of Elastic Stability*, Dordrecht, Boston: M. Nijhoff.

Kalker, J. J. (1979), "The computation of three-dimensional rolling contact with dry friction," *International Journal for Numerical Methods in Engineering*, 14, 1293–1307.

Kennedy, S., Bond, J., Braun, D., Noble, P., and Forsyth, J. (2003), "An Innovative "No Hot Work" Approach to Hull Repair on In-Service FPSOs Using Sandwich Plate System Overlay (OTC 15315)," in *Offshore Technology Conference 2003 (OTC 03)*, pp. 2129–2135, Curran Associates, Inc., Red Hook, NY 12571.

Kumar, P., Sarkar, D., and Gupta, S. C. (1988), "Rolling resistance of elastic wheels on flat surfaces," *Wear*, 126, 117 – 129.

Kuznetsov, Y. (1978), "The superposition principle in the solution of contact friction stress problems," *Wear*, 50, 183 – 189.

Lakes, R. (1993a), "Advances in negative Poisson's ratio materials," *Advanced Materials*, 5, 293–296.

Lakes, R. (1993b), "Design Considerations for Materials with Negative Poissons Ratios," *Journal of Mechanical Design*, 115, 696–700.

Lakes, R. (2009), *Viscoelastic Materials*, Cambridge University Press.

Lakes, R. and Wineman, A. (2006), "On Poissons Ratio in Linearly Viscoelastic Solids," *Journal of Elasticity*, 85, 45–63.

Lakes, R. S. (2004), "Viscoelastic measurement techniques," *Review of Scientific Instruments*, 75, 797–810.

Langus, J., Sustaric, P., and Rodic, T. (2011), "Impact response of polymer-coated grinding spheres," *Engineering Computations*, 28, 792–801.

Laursen, T. A. and Stanciulescu, I. (2006), "An algorithm for incorporation of frictional sliding conditions within a steady state rolling framework," *Communications in Numerical Methods in Engineering*, 22, 301–318.

Lee, J., Choi, J., and Choi, K. (1996), "Application of homogenization FEM analysis to regular and re-entrant honeycomb structures," *Journal of Materials Science*, 31, 4105–4110.

Lee, T., Lakes, R. S., and Lal, A. (2000), "Resonant ultrasound spectroscopy for measurement of mechanical damping: Comparison with broadband viscoelastic spectroscopy," *Review of Scientific Instruments*, 71, 2855–2861.

Lee, W., Cho, K., and Jang, H. (2009), "Molecular Dynamics Simulation of Rolling Friction Using Nanosize Spheres," *Tribology Letters*, 33, 37–43.

Lekhnitskiĭ, S. (1963), *Theory of elasticity of an anisotropic elastic body*, Holden-Day series in mathematical physics, Holden-Day.

Lemaître, J. (1996), *A course on damage mechanics*, Springer.

Lin, R. and Schomburg, U. (2003), "A finite elastic-viscoelastic-elastoplastic material law with damage: theoretical and numerical aspects," *Computer Methods in Applied Mechanics and Engineering*, 192, 1591 – 1627.

Lion, A. (1996), "A constitutive model for carbon black filled rubber: Experimental investigations and mathematical representation," *Continuum Mechanics and Thermodynamics*, 8, 153 – 169.

Lion, A., Kardelky, C., and Haupt, P. (2003), "On the Frequency and Amplitude Dependence of the Payne Effect: Theory and Experiments," *Rubber Chemistry and Technology*, 76, 533 – 547.

Lira, C., Innocenti, P., and Scarpa, F. (2009), "Transverse elastic shear of auxetic multi re-entrant honeycombs," *Composite Structures*, 90, 314 – 322.

Liu, M. (2010), "Constitutive equations for the dynamic response of rubber," *The Graduate Faculty of The University of Akron*, p. Ph.D. dissertation.

Liu, M. and Hoo Fatt, M. S. (2011), "A constitutive equation for filled rubber under cyclic loading," *International Journal of Non-Linear Mechanics*, 46, 446 – 456.

Liu, Q. (2006), "Literature Review: Materials with Negative Poisson's Ratios and Potential Applications to Aerospace and Defence," .

Liu, Y. and Hu, H. (2010), "A review on auxetic structures and polymeric materials," *Scientific Research and Essays*, 5, 1052–1063.

Logan, J. D. (2006), *Applied Mathematics*, Wiley-Interscience, 3 edn.

Love, A. E. H. (1927), *A Treatise on the Mathematical Theory of Elasticity*, Cambridge University Press, 4 edn.

Lucas, S. and Stone, H. (1995), "Evaluating infinite integrals involving Bessel functions of arbitrary order," *Journal of Computational and Applied Mathematics*, 64, 217–231.

Lygeros, J. and Ramponi, F. (2010), *Lecture notes on linear system theory*, Automatic Control Laboratory, ETH Zurich.

Machado, G., Chagnon, G., and Favier, D. (2010), "Analysis of the isotropic models of the Mullins effect based on filled silicone rubber experimental results," *Mechanics of Materials*, 42, 841 – 851.

Machado, G., Chagnon, G., and Favier, D. (2012), "Induced anisotropy by the Mullins effect in filled silicone rubber," *Mechanics of Materials*, 50, 70 – 80.

Marckmann, G. and Verron, E. (2006), "Comparison of hyperelastic models for rubberlike materials," *Rubber Chemistry and Technology*, 79, 835 – 858.

Marckmann, G., Verron, E., Gornet, L., Chagnon, G., Charrier, P., and Fort, P. (2002), "A theory of network alteration for the Mullins effect," *Journal of the Mechanics and Physics of Solids*, 50, 2011 – 2028.

Martz, E. O., Lee, T., Lakes, R. S., Goel, V. K., and Park, J. B. (1996), "Re-entrant transformation methods in closed cell foams," *Cellular Polymers*, 15, 229–249.

May, W. D., Morris, E. L., and Atack, D. (1959), "Rolling Friction of a Hard Cylinder over a Viscoelastic Material," *Journal of Applied Physics*, 30, 1713–1724.

May, W. D., Morris, E. L., and Atack, D. (1963), "Dynamics of a Viscoelastic Wear Particle between Sliding Surfaces," *Journal of Applied Physics*, 34, 1920–1928.

Menard, K. P. (2008), *Dynamic Mechanical Analysis : A Practical Introduction*, Taylor & Francis.

Miehe, C. and Keck, J. (2000), "Superimposed finite elasticviscoelasticplastoelastic stress response with damage in filled rubbery polymers. Experiments, modelling and algorithmic implementation," *Journal of the Mechanics and Physics of Solids*, 48, 323 – 365.

Milton, G. W. (1992), "Composite materials with poisson's ratios close to -1," *Journal of the Mechanics and Physics of Solids*, 40, 1105 – 1137.

Morland, L. W. (1967), "Exact Solutions for Rolling Contact Between Viscoelastic Cylinders," *The Quarterly Journal of Mechanics and Applied Mathematics*, 20, 73–106.

Morland, L. W. (1968), "Rolling Contact Between Dissimilar Viscoelastic Cylinders," *The Quarterly Journal of Mechanics and Applied Mathematics*, 25, 363–376.

Mott, P., Dorgan, J., and Roland, C. (2008), "The bulk modulus and Poisson's ratio of incompressible materials," *Journal of Sound and Vibration*, 312, 572 – 575.

Mullins, L. (1969), *Softening of Rubber by Deformation*, Rubber chemistry and technology, Rubber Division, American Chemical Society.

Munisamy, R., Hills, D., and Nowell, D. (1991), "Brief note on the tractive rolling of dissimilar elastic cylinders," *International Journal of Mechanical Sciences*, 33, 225–228.

Murray, G., Gandhi, F., and Hayden, E. (2012), "Polymer-filled honeycombs to achieve a structural material with appreciable damping," *Journal of Intelligent Material Systems and Structures*, 23, 703–718.

Murray, G. J. (2009), "Two novel uses of cellular structures," .

Naguib, W. and Mirmiran, A. (2002), "Flexural Creep Tests and Modeling of Concrete-Filled Fiber Reinforced Polymer Tubes," *Journal of Composites for Construction*, 6, 272–279.

Niknejad, A., Assaee, H., Elahi, S. A., and Golriz, A. (2013), "Flattening process of empty and polyurethane foam-filled E-glass/vinylester composite tubes - An experimental study," *Composite Structures*, 100, 479 – 492.

Nolle, A. W. (1950), "Dynamic mechanical properties of rubberlike materials," *Journal of Polymer Science*, 5, 1–54.

Nowell, D. and Hills, D. (1988), "Tractive rolling of dissimilar elastic cylinders," *International Journal of Mechanical Sciences*, 30, 427 – 439.

Obrecht, H., Rosenthal, B., Fuchs, P., Lange, S., and Marusczyk, C. (2006), "Buckling, postbuckling and imperfection-sensitivity: Old questions and some new answers," *Computational Mechanics*, 37, 498–506.

Oden, J. and Lin, T. (1986), "On the general rolling contact problem for finite deformations of a viscoelastic cylinder," *Computer Methods in Applied Mechanics and Engineering*, 57, 297–367.

Ogden, R. W. and Roxburgh, D. G. (1999), "A pseudoelastic model for the Mullins effect in filled rubber," *Proceedings of the Royal Society of London. Series A: Mathematical, Physical and Engineering Sciences*, 455, 2861 – 2877.

Oyadiji, S. O. (1996), "Damping of vibrations of hollow beams using viscoelastic spheres," Proc. SPIE 2720, Smart Structures and Materials 1996: Passive Damping and Isolation, 89 (May 1).

Oyawa, W. O. (2007), "Steel encased polymer concrete under axial compressive loading: Analytical formulations," *Construction and Building Materials*, 21, 57 – 65.

Oyawa, W. O., Sugiura, K., and Watanabe, E. (2001), "Polymer concrete-filled steel tubes under axial compression," *Construction and Building Materials*, 15, 187 – 197.

Oyawa, W. O., Sugiura, K., and Watanabe, E. (2004), "Flexural response of polymer concrete filled steel beams," *Construction and Building Materials*, 18, 367 – 376.

Pasternak, E. and Dyskin, A. (2012), "Materials and structures with macroscopic negative Poisson's ratio," *International Journal of Engineering Science*, 52, 103 – 114.

Payne, A. R. (1962), "The dynamic properties of carbon black-loaded natural rubber vulcanizates. Part I," *Journal of Applied Polymer Science*, 6, 57 – 63.

Persson, B. (2010), "Rolling friction for hard cylinder and sphere on viscoelastic solid," *The European Physical Journal E Soft Matter*, 33, 327–33.

Persson, B. N. J. (2001), "Theory of rubber friction and contact mechanics," *The Journal of Chemical Physics*, 115, 3840–3861.

Pioletti, D. P., Rakotomanana, L. R., Benvenuti, J. F., and Leyvraz, P. F. (1998), "Viscoelastic constitutive law in large deformations: application to human knee ligaments and tendons," *Journal of Biomechanics*, 31, 753 – 757.

Pöschel, T., Schwager, T., and Brilliantov, N. (1999), "Rolling friction of a hard cylinder on a viscous plane," *The European Physical Journal B - Condensed Matter and Complex Systems*, 10, 169–174.

Prall, D. and Lakes, R. (1997), "Properties of a chiral honeycomb with a poisson's ratio of -1," *International Journal of Mechanical Sciences*, 39, 305 – 314.

Prawoto, Y. (2012), "Seeing auxetic materials from the mechanics point of view: A structural review on the negative Poissons ratio," *Computational Materials Science*, 58, 140 – 153.

Pritz, T. (2000), "Measurement methods of complex Poisson's ratio of viscoelastic materials," *Applied Acoustics*, 60, 279–292.

Qiu, X. (2006), "Full two-dimensional model for rolling resistance: hard cylinder on viscoelastic foundation of finite thickness," *Journal of Engineering Mechanics*, 132, 1241–1251.

Qiu, X. (2009), "Full Two-Dimensional Model for Rolling Resistance. II: Viscoelastic Cylinders on Rigid Ground," *Journal of Engineering Mechanics*, 135, 20–30.

Rammohan Rao, B. and Ganapathy, S. (1979), "Linear time-varying systemsstate transition matrix," *Electrical Engineers, Proceedings of the Institution of*, 126, 1331–1335.

Ramorino, G., Vetturi, D., Cambiaghi, D., Pegoretti, A., and Ricco, T. (2003), "Developments in dynamic testing of rubber compounds: assessment of non-linear effects," *Polymer Testing*, 22, 681 – 687.

Rand, O., Rovenski, V., and Rovenski, V. (2005), *Analytical Methods in Anisotropic Elasticity: With Symbolic Computational Tools*, Birkhäuser Boston.

Reddy, T. and Wall, R. (1988), "Axial compression of foam-filled thin-walled circular tubes," *International Journal of Impact Engineering*, 7, 151 – 166.

Roland, C. M. (2006), "Mechanical Behavior of Rubber at High Strain Rates," *Rubber Chemistry and Technology*, 79, 429 – 459.

Roland, C. M. (2011), *Viscoelastic Behavior of Rubbery Materials*, Oxford University Press.

Rosa, M. and Fortes, M. (1991), "Deformation and fracture of cork in tension," *Journal of Materials Science*, 26, 341–348.

Sabey, B. E. (1959), "Skidding friction The effect of hysteresis losses in tyre tread rubber," *Contemporary Physics*, 1, 56–61.

Sadd, M. (2009), *Elasticity: Theory, Applications, and Numerics*, Elsevier Science.

Scarpa, F., Giacomin, J., Zhang, Y., and P., P. (2005), "Mechanical Performance of Auxetic Polyurethane Foam for Antivibration Glove Applications," *Cellular Polymers*, 24, 253–268.

Scheibert, J., Prevost, A., Debrgeas, G., Katzav, E., and Adda-Bedia, M. (2009), "Stress field at a sliding frictional contact: Experiments and calculations," *Journal of the Mechanics and Physics of Solids*, 57, 1921 – 1933.

Seitzberger, M., Rammerstorfer, F., Gradinger, R., Degischer, H., Blaimschein, M., and Walch, C. (2000), "Experimental studies on the quasi-static axial crushing of steel columns filled with aluminium foam," *International Journal of Solids and Structures*, 37, 4125 – 4147.

Shao, Y. and Mirmiran, A. (2005), "Experimental Investigation of Cyclic Behavior of Concrete-Filled Fiber Reinforced Polymer Tubes," *Journal of Composites for Construction*, 9, 263–273.

Sharp, A. (2009), "Rolling resistance: Part 1 of fuel consumption," *Fleet Equipment*, 35, 10–10.

Simkins, V., Alderson, A., Davies, P., and Alderson, K. (2005), "Single fibre pullout tests on auxetic polymeric fibres," *Journal of Materials Science*, 40, 4355–4364.

Slawinski, M. (2010), *Waves and Rays in Elastic Continua*, World Scientific.

Soman, P., Fozdar, D. Y., Lee, J. W., Phadke, A., Varghese, S., and Chen, S. (2012), "A three-dimensional polymer scaffolding material exhibiting a zero Poisson's ratio," *Soft Matter*, 8, 4946–4951.

Stanciulescu, I. and Laursen, T. A. (2006), "On the interaction of frictional formulations with bifurcation phenomena in hyperelastic steady state rolling calculations," *International Journal of Solids and Structures*, 43, 2959–2988.

Strano, M., Villa, A., and Mussi, V. (2013), "Design and manufacturing of anti-intrusion bars made of aluminium foam filled tubes," *International Journal of Material Forming*, 6, 153–164.

Subramaniam, D. R., Gee, D. J., and King, M. R. (2013), "Deformable cell-cell and cell-substrate interactions in semi-infinite domain," *Journal of Biomechanics*, 46, 1067.

Sullivan, J. (1990), "Creep and physical aging of composites," *Composites Science and Technology*, 39, 207 – 232.

Tabor, D. (1952), "CV. The mechanism of rolling friction," *Philosophical Magazine Series 7*, 43, 1055–1059.

Tabor, D. (1955), "The Mechanism of Rolling Friction. II. The Elastic Range," *Proceedings of the Royal Society of London. Series A, Mathematical and Physical Sciences*, 229, 198–220.

Teixeira de Freitas, S., Kolstein, H., and Bijlaard, F. (2010a), "Composite bonded systems for renovations of orthotropic steel bridge decks," *Composite Structures*, 92, 853 – 862.

Teixeira de Freitas, S., Kolstein, H., and Bijlaard, F. (2010b), "Sandwich system for renovation of orthotropic steel bridge decks," *Journal of Sandwich Structures and Materials*.

Teixeira de Freitas, S., Kolstein, H., and Bijlaard, F. (2012a), "Parametric Study on the Interface Layer of Renovation Solutions for Orthotropic Steel Bridge Decks," *Computer-Aided Civil and Infrastructure Engineering*, 27, 143–153.

Teixeira de Freitas, S., Kolstein, H., and Bijlaard, F. (2012b), "Structural monitoring of a strengthened orthotropic steel bridge deck using strain data," *Structural Health Monitoring*, 11, 558–576.

Teixeira de Freitas, S., Kolstein, H., and Bijlaard, F. (2013), "Fatigue behavior of bonded and sandwich systems for strengthening orthotropic bridge decks," *Composite Structures*, 97, 117 – 128.

Tsai, C., Lin, Y.-C., Chen, W.-S., and Su, H. (2010), "Tri-directional shaking table tests of vibration sensitive equipment with static dynamics interchangeable-ball pendulum system," *Earthquake Engineering and Engineering Vibration*, 9, 103–112.

Tschoegl, N. (1989), *The phenomenological theory of linear viscoelastic behavior: an introduction*, Springer-Verlag.

Vince, S. and Shepherd, A. (1785), "On the motion of bodies affected by friction," *Philosophical Transactions of the Royal Society of London*, 75, 165–189.

Vollebregt, E. A. H. (2012), *The Finite Element Method for Solid and Structural Mechanics*, VORtech Computing, Delft, The Netherlands.

Wang, G. and Knothe, K. (1993), "Stress Analysis for Rolling Contact Between Two Viscoelastic Cylinders," *Journal of Applied Mechanics*, 60, 310–317.

Warren, T. L. (1990), "Negative Poisson's ratio in a transversely isotropic foam structure," *Journal of Applied Physics*, 67, 7591–7594.

Wei, G. and Edwards, S. (1998a), "Auxeticity windows for composites," *Physica A: Statistical Mechanics and its Applications*, 258, 5 – 10.

Wei, G. and Edwards, S. F. (1998b), "Poisson ratio in composites of auxetics," *Phys. Rev. E*, 58, 6173–6181.

Williams, M. L., Landel, R. F., and Ferry, J. D. (1955), "The Temperature Dependence of Relaxation Mechanisms in Amorphous Polymers and Other Glass-forming Liquids," *Journal of the American Chemical Society*, 77, 3701–3707.

WorkSafe Technologies, I. (2012), "ISO-Base platform 2012," .

Wu, C.-W. and Hwang, C.-K. (2008), "A novel spherical wheel driven by Omni wheels," in *Machine Learning and Cybernetics, 2008 International Conference on*, vol. 7, pp. 3800–3803.

Wu, C.-W., Qiu, Z.-W., Wang, Y.-H., Hsu, P.-H., and Hwang, C.-K. (2011), "Modeling of a spherical robot driven by Omni wheels," in *Machine Learning and Cybernetics (ICMLC), 2011 International Conference on*, vol. 3, pp. 1256–1260.

Xu, G. and Shao, J.-Y. (2008), "Human neutrophil surface protrusion under a point load: location independence and viscoelasticity," *American Journal of Physiology - Cell Physiology*, 295, C1434–C1444.

Xu, Y., Yung, K. L., and Ko, S. M. (2007), "A classroom experiment to measure the speed-dependent coefficient of rolling friction," *American Journal of Physics*, 75, 571–574.

Yang, S. and Qi, C. (2013), "Multiobjective optimization for empty and foam-filled square columns under oblique impact loading," *International Journal of Impact Engineering*, 54, 177 – 191.

Yang, W., Li, Z.-M., Shi, W., Xie, B.-H., and Yang, M.-B. (2004), "Review on auxetic materials," *Journal of Materials Science*, 39, 3269–3279.

Yeoh, O. H. (1990), "Characterization of Elastic Properties of Carbon-Black-Filled Rubber Vulcanizates," *Rubber Chemistry and Technology*, 63, 792 – 805.

Yung, K. and Xu, Y. (2003), "Non-Linear Expressions for Rolling Friction of a Soft Ball on a Hard Plane," *Nonlinear Dynamics*, 33, 33–41.

Yung, K. L., Xu, Y., and Ng, H. P. (2007), "Modelling method for studying solid conveying process in inclined plastication unit." *Plastics, Rubber & Composites*, 36, 56 – 61.

Zéhil, G.-P. and Gavin, H. P. (2012), "Full three-dimensional model for rolling resistance: hard sphere on viscoelastic foundation of finite thickness," Joint Conference of the Engineering Mechanics Institute and 11th ASCE Joint Specialty Conference on Probabilistic Mechanics and Structural Reliability, University of Notre Dame, Indiana, USA, June 17–20.

Zéhil, G.-P. and Gavin, H. P. (2013a), "New three-dimensional boundary element formulation of a viscoelastic layer of finite thickness applied to the rolling resistance of a rigid sphere," 12^{th} U.S. National Congress on Computational Mechanics, Raleigh, North Carolina, USA, July 22–25.

Zéhil, G.-P. and Gavin, H. P. (2013b), "Rolling resistance of a rigid sphere with viscoelastic coatings," *International Journal of Solids and Structures*, (in print).

Zéhil, G.-P. and Gavin, H. P. (2013c), "Simple algorithms for solving steady-state frictional rolling contact problems in two and three dimensions," *International Journal of Solids and Structures*, 50, 843–852.

Zéhil, G.-P. and Gavin, H. P. (2013d), "Simplified approaches to viscoelastic rolling resistance," *International Journal of Solids and Structures*, 50, 853–862.

Zéhil, G.-P. and Gavin, H. P. (2013e), "Three-dimensional boundary element formulation of a viscoelastic layer of finite thickness applied to the rolling resistance of a rigid sphere," *International Journal of Solids and Structures*, 50, 833–842.

Zéhil, G.-P. and Gavin, H. P. (2013f), "Unified constitutive modeling of rubber-like materials under diverse loading conditions," *International Journal of Engineering Science*, 62, 90–105.

Zéhil, G.-P. and Gavin, H. P. (2013g), "Unified constitutive modeling of rubber-like materials under diverse loading conditions," 12^{th} U.S. National Congress on Computational Mechanics, Raleigh, North Carolina, USA, July 22–25.

Zéhil, G.-P. and Gavin, H. P. (2014a), "Experimental study of the resistance to motion incurred by a hard sphere rolling between two sheets of rubber: influence of material and geometric nonlinearities on the viscoelastic rolling resistance," .

Zéhil, G.-P. and Gavin, H. P. (2014b), "On the structural behavior of casing-infill composite tubes: theory and experiment," *Composite Structures*, (under review).

Zéhil, G.-P. and Gavin, H. P. (2014c), "Two and three-dimensional boundary element formulations of compressible isotropic, transversely isotropic and orthotropic viscoelastic layers of arbitrary thickness, applied to the rolling resistance of rigid cylinders and spheres," *European Journal of Mechanics - A/Solids*, 44, 175–187.

Zhang, R., Yeh, H.-L., and Yeh, H.-Y. (1998), "A Preliminary Study of Negative Poisson's Ratio of Laminated Fiber Reinforced Composites," *Journal of Reinforced Plastics and Composites*, 17, 1651–1664.

Zheng, Q., Zhu, H., and Yu, A. (2011), "Finite element analysis of the rolling friction of a viscous particle on a rigid plane," *Powder Technology*, 207, 401 – 406.

Zhou, Y., Wright, B., Yang, R., Xu, B., and Yu, A. (1999), "Rolling friction in the dynamic simulation of sandpile formation," *Physica A: Statistical Mechanics and its Applications*, 269, 536 – 553.

Zienkiewicz, O. C. and Taylor, R. L. (2005), *The Finite Element Method for Solid and Structural Mechanics*, Butterworth-Heinemann, 6 edn.

Biography

Gérard-Philippe Zéhil was born on September 10, 1976 in Limassol, Cyprus. He is a Lebanese and French national. He received his M.S. degrees in Civil and Environmental Engineering, and graduated with the highest distinction in Infrastructure and Transport, from the École Supérieure d'Ingénieurs de Beyrouth, faculty of engineering of Université Saint-Joseph (Beirut, Lebanon), in 2002. Gérard-Philippe also holds a post-graduate degree in Structural Engineering (with focus on Reinforced and Prestressed Concrete) which he received, along with the highest ranking graduate award, from the Centre des Hautes Études de la Construction (Paris, France) in 2003. He worked as a professional bridge design engineer in Paris, from 2003 to 2010. During this period, he was promoted to positions of increasing technical, financial and managerial responsibility. He gained technical experience in the practical implementation of construction materials and composites in structures such as bridges, footbridges, cut and cover constructions, tunnels, earth and water retaining structures, and their foundations. He contributed to the design and construction of several technically challenging structures around the world, including the famous Trois Bassins bridge, on the French Island of Réunion. Gérard-Philippe has co-authored nine journal articles (Zéhil and Gavin, 2013b,c,d,e,f, 2014a,b,c; Harvey et al., 2013) and three conference abstracts (Zéhil and Gavin, 2012, 2013a,g) through the course of his doctoral research, which he started in 2010. He received his Ph.D. degree in Civil and Environmental Engineering from Duke University in December 2013.